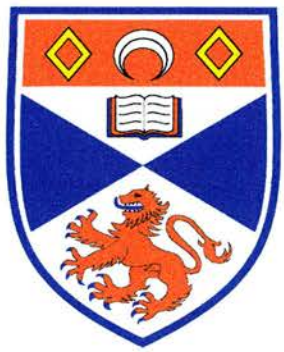

SYNTHESIS AND CHARACTERISATION OF ALUMINOPHOSPHATE-BASED MATERIALS PREPARED WITH NICKEL COMPLEXES AS STRUCTURE DIRECTING AGENTS

A thesis presented for the degree of

Doctor of Philosophy

in the faculty of science of the University of St. Andrews

by Raquel Garcia Salas, B.Sc.

December 2003

DECLARATIONS

I, Raquel García Salas, hereby certify that this thesis, which is approximately 42000 words in length, has been written by me, that it is the record of work carried out by me and that it has not been submitted in any previous application for a higher degree.

I was admitted as a research student in May 2000 and as a candidate for the degree of Doctor of Philosophy in May 2001; the higher study for which this is a record was carried out in the University of St Andrews between 2000 and 2003.

In submitting this thesis to the University of St Andrews I understand that I am giving permission for it to be made available for use in accordance with the regulations of the University Library for the time being in force, subject to any copyright vested in the work not being affected thereby. I also understand that the title and abstract will be published, and that a copy of the work may be made and supplied to any *bona fide* library or research worker.

Date 16/12/03 Raquel García-Salas (Candidate)

I hereby certify that the candidate has fulfilled the conditions of the Resolution and Regulations appropriate for the degree of PhD in the University of St Andrews and that the candidate is qualified to submit this thesis in application for that degree.

Date Paul A. Wright (Supervisor)

16th December 2003

Abstract

Incorporation of metal complexes during crystallisation of aluminophosphate-based solids has been investigated. The addition of nickel to azamacrocycle-directed preparations that in its absence yielded the phases STA-6 (**SAS** framework type) and STA-7 (**SAV** framework type) resulted in the formation of an orthorhombic variant of the STA-6 material. The nickel was shown by EXAFS, magnetic measurements and UV-visible spectroscopy to remain complexed with the macrocycle 1,4,8,11-tetramethyl-1,4,8,11-tetra-azacyclotetradecane and to be located within the cavities of these solids. Calcination of these solids and treatment in hydrogen was monitored with ESR spectroscopy and observed to give isolated nickel(I) species and metallic nickel, sequentially. Modification of the synthesis mixture and the addition of tetraethylammonium cations, has been shown to favour the crystallisation of the STA-7 structure types, with the TEA cation acting as a "co-template". As a result, the compositional range for this framework topology type (SAV), which had only been obtained as CoAlPO and ZnAlPO variants prior to this work, has been broadened. The SAPO version of the STA-7 structure was synthesised in this way. This material is polytypic with SAPO-34 (**CHA** framework type), which is one of the most intensively studied materials for the selective catalytic conversion of methanol to light olefins. Catalytic testing of SAPO-STA-7 revealed it to be a moderately strong solid acid.

The action of the nickel complex $[Ni(diethylenetriamine)_2]^{2+}$ as a structure directing agent in the synthesis of aluminophosphates has also been explored. In the presence of ammonium fluoride two complex-containing phases were prepared: an orthorhombic version of AlPO-5 (Ccc2, a=13.8603(5) Å, b=23.1285(5) Å, c=8.5420(4) Å) and a triclinic version of AlPO-34 ($P\bar{1}$, a=9.283(1) Å, b=9.091(1)Å, c=9.357(1) Å, α=88.35(1)°, β=78.91(1)°, γ=89.21(1)°). In both phases, the fluorine was found in the as prepared materials, modifying the coordination of the aluminium atoms. The orthorhombic AlPO-5 retains its framework topology and achieves hexagonal symmetry upon calcination, due to loss of the fluoride ions, which give rise to the distortion. The triclinic AlPO-34 (UT-6) keeps its framework topology and becomes rhombohedral upon calcination

at 385°C. However, direct calcination of as-prepared $Ni(deta)_2$-UT-6 at temperatures over 500°C results in a reconstructive recrystallisation to AlPO-5, which must be catalysed by interaction of the HF produced during heating and the presence of NiO species in the channels.

The local environment of the nickel in the as-prepared and calcined materials was characterised by Ni K-edge EXAFS spectroscopy. In the case of the STA-6/STA-7 materials this analysis allowed the coordination of the metal cation (Ni^{2+}) occluded within a complex inside the framework to be confirmed. Calcination of materials with charged frameworks (MgAPO, SAPO, etc) leaves charge-balancing Ni^{2+} cations occupying extra framework cation sites. Calcination of aluminophosphate-fluoride frameworks prepared with the $Ni(deta)_2^{2+}$ complex is observed by Ni-K edge EXAFS spectroscopy to give nanoparticles of nickel oxide or nickel metal within neutral aluminophosphate frameworks when calcined under oxygen or nitrogen atmospheres, respectively.

The approach of incorporating metal cations within amines as structure-directing agents has been generalised to other metals that do not prefer tetrahedral framework sites. In particular, copper and rhodium complexes have been included within AlPO-5, STA-6 and STA-7 frameworks. The environment of rhodium was confirmed as complexed with square planar geometry within Rh(TMC)-ZnAlPO-STA-7 by Rh K-edge X-ray absorption spectroscopy and single crystal X-ray diffraction.

Materials synthesised during the course of the project were tested as catalysts for the catalytic selective cracking of butane. A comparison of the nickel-containing and nickel-free materials suggests that nickel(II) is reduced in the hydrocarbon flow and nickel sinters to give highly dispersed nickel metal particles on the exterior surfaces of the microporous solid particles that catalyse the conversion of butane to methane.

Publications arising from this work

1. **On the role of azamacrocycles and metal cations in the syntheses of metallo-aluminophosphates STA-6, -7 and –8**, R. García, E. F. Philp, A.M.Z. Slawin, P.A. Wright and Paul A. Cox, *Stud. Surf. Sci. Catal.*, 135 (*Zeolites and Mesoporous Materials at the Dawn of the 21st Century*), 2001.

2. **Nickel complexed within an azamacrocycle as a structure directing agent in the crystallization of the framework metalloaluminophosphates STA-6 and STA-7**, R. García, E. F. Philp, A.M.Z. Slawin, P.A. Wright and Paul A. Cox, *J.Mater.Chem*, 2002, 11, 1421.

3. **Synthesis, structure and thermal transformations of aluminophosphates containing the nickel complex $[Ni(diethylenetriamine)_2]^{2+}$ as a structure directing agent**, R. García, Ian J. Shannon, Alex Slawin, Wuzong Zhou, Paul A. Cox, Paul A Wright, *Microp.Mesop.Materials, 2003,* 58, 91.

4. **Nickel amine complexes as structure-directing agents for aluminophosphate molecular sieves: a new route to supported nickel catalysts**, R. García, T. D. Coombs, Ian J. Shannon, Paul A Wright, Paul A. Cox,*Top. Cat.*, 2003, **24**, 115

5. **Aluminophosphates templated by metal-amine complexes as catalysts precursor**, R. García, T. D. Coombs, M. J. Maple, I. J. Shannon, P.A. Cox and P. A. Wright, *Stud. Surf. Sci. Catal.*, 2004 (accepted).

Acknowledgements

First of all, I would like to thank my supervisor Paul Wright for giving me the opportunity to do this PhD and for his guidance, enthusiasm and patience throughout the project. I must also acknowledge the assistance of other people during the course of this PhD: Dr Alex Slawin for single crystal diffractometry, Dr Paul Cox for the modelling studies with the templates, Dr W. Zhou for collecting the TEM images and Dr Ian J. Shannon for his invaluable advise with the EXAFS analysis. All the departmental technical staff at St. Andrews have been very helpful during this time, but my especial thanks should go to Mrs Silvia Williamson and Mr Ross Blackley for performing the C,H,N analysis and for help with the SEM-EDX microscope, respectively.

My acknowledgement should also go to the past and present members of the Wright group from whom I have learnt so much, especially Alf García Bennett, Martin Maple, Nandini Devi, Jorge Gonzalez and Robert Hodgkins.

I have had the fortune of meeting great people at St Andrews, who made my life enjoyable and have been always there in the good and in the bad times. I must thank Mireia Rodriguez i Zubiri, Anna Hovris, Anita L. Kinney, Alf García Bennett, Naiara Elejalde, Nandini Devi, Luis Villaescusa, Sonia, Dave and Chantal, Fionna Ross, Teresa Crespo, Pascal, the Spanish Inquisition (Jesus, Jorge and Juan Carlos), Pepa, Robbie, Pierrott, las Cristinas, Alvaro, McPiku, Leslie Mines, Tomás Rada, 3 Stanley Smith House and visitors, Mumu, Berni and Julia, Penélope and Fiz, Alix and Lina. I also want to thank the people from Catálisis in Madrid, where I spent an unforgettable year before starting my PhD. Especially to the molecular sieve group members at that time, Carlos, Fede, Isabel, Enrique, Joaquin, Javi and Veronica, for introducing me into the research world and from whom I learned a great deal.

I do not have words to express my gratitude to my dearest friend Raquel Gonzalez, whose friendship all these years has been the most valuable gift.

Last, but most importantly, I could never thank my family enough for their encouragement and support, and to my boyfriend, Jose Angel, for standing by me at all times.

A mis padres,

me sirve tu mirada
que es generosa y firme
y tu silencio franco
sí me sirve

me sirve la medida
de tu vida

me sirve tu futuro
que es un presente libre
y tu lucha de siempre
sí me sirve

me sirve tu batalla
sin medalla

me sirve tu modestia
de tu orgullo posible
y tu mano segura
sí me sirve

me sirve tu sendero
compañero.

Mario Benedetti

Contents

Abreviations

AlPO	Aluminophosphate
Cyclam	1,4,8,11-tetraazacyclotetradecane
$Dec(OH)_2$	Decamethonium hydroxide
dien	Diethylenetriamine
DTA	Differential thermal Analysis
DPA	Di-n-propylamine
EDX	Energy Dispersive X-ray analysis
en	Ethylenediamine or 1,2-diaminoethane
EXAFS	Extended X-ray Absorption Fine Structure
ESR	Electron Spin Resonance
MAPO	Metalloaluminophosphate
MAS	Magic Angle Spinning
Mor	Morpholine
MR	Member ring
NMR	Nuclear Magnetic Resonance
SAPO	Silicoaluminophosphate
SBU	Secondary building unit
SDA	Structure directing agent
SEM	Scanning electron microscopy
TEAOH	Tetraethylammonium hydroxide
TGA	Themogravimetric Analysis
TMAOH	Tetramethylammonium hydroxide
TMC	1,4,8,11-tetramethyl-1,4,8,11-tetraazacyclotetradecane or tetramethylcyclam
TPA	Tripropylamine
TPAOH	Tetrapropylammonium hydroxide
tren	Tris(2-aminoethyl)amine
trien	Triethylenetriamine
XAFS	X-ray Absorption Fine Structure
XRD	X-ray diffraction

1. INTRODUCTION

1.1. ZEOLITES AND ZEOTYPES[1, 2]

McBain[3] introduced the term molecular sieve in order to name materials with selective adsorption properties. These were porous materials with the capability to differentiate between compounds in a mixture on the basis of their size and shape. The family of molecular sieves is made up of amorphous materials such as microporous carbons or silica gels and crystalline solids such as zeolites and related materials.

Rigorously, zeolites are defined as microporous aluminosilicates with a three-dimensionally connected framework and are characterised by large void volumes. A zeolite structure comprises a regular inorganic framework formed by corner-sharing TO_4 tetrahedra (T= Si, Al), each oxygen being shared between two tetrahedra. The replacement of Si (IV) by Al (III) imparts a single negative charge to the framework. This contributes to the stabilisation of the structure through their interaction with the charge balancing cations which can be alkali metal, alkaline-earth or organic R_4N^+(R= H, alkyl, aryl) cations. The framework structure contains channels and cavities with the dimensions of small molecules (3-10 Å), which can host these cations and water or other adsorbed molecules. Removal by heating (calcination) of the adsorbed species renders the microporous volume accessible to other molecules.

The structural formula of a zeolite is therefore

$$M^{n+}_{x/n}[\ Al_xSi_{1-x}O_2]\ .\ y\ H_2O$$

where M is an extra-framework cation with charge *n*, which compensates the negative charge of the framework; *y* is the number of water molecules in the voids and *x* refers to the fraction of tetrahedral silicon replaced by aluminium.

The ratio Si/Al is an important value in determining the zeolite's physical properties, such as stability and cation exchange capacity. The upper limit of this ratio is infinity as observed for silica polymorphs. The lower value of this ratio is dictated by Loewestein's principle[4] to be one. This principle states that Al-O-Al

linkages are energetically unfavourable because they would give rise to adjacent negative charges and the repulsion between them would destabilise the lattice. The maximum amount of aluminium that can be incorporated is therefore 50%, with perfect order.

Incorporation of elements other than silicon and aluminium into the framework has extended the original family of aluminosilicates (and pure silica zeolites), to include aluminophosphates and metalloaluminophosphates, among many others[5] (figure 1.1). Synthesis research continues to successfully explore new compositional domains both to obtain framework materials with novel architectures and also to generate materials of the same framework topology but with different compositions, often possessing different properties[6,7].

Material scientists tend to divide the family of crystalline microporous three-dimensional oxide structures into silicate-based (zeolitic) and phosphate-based (zeotypic) varieties. This sub-division is arbitrary because some structure types can contain both silicon and phosphorus as in the case of the silicoaluminophosphates, or SAPOs.

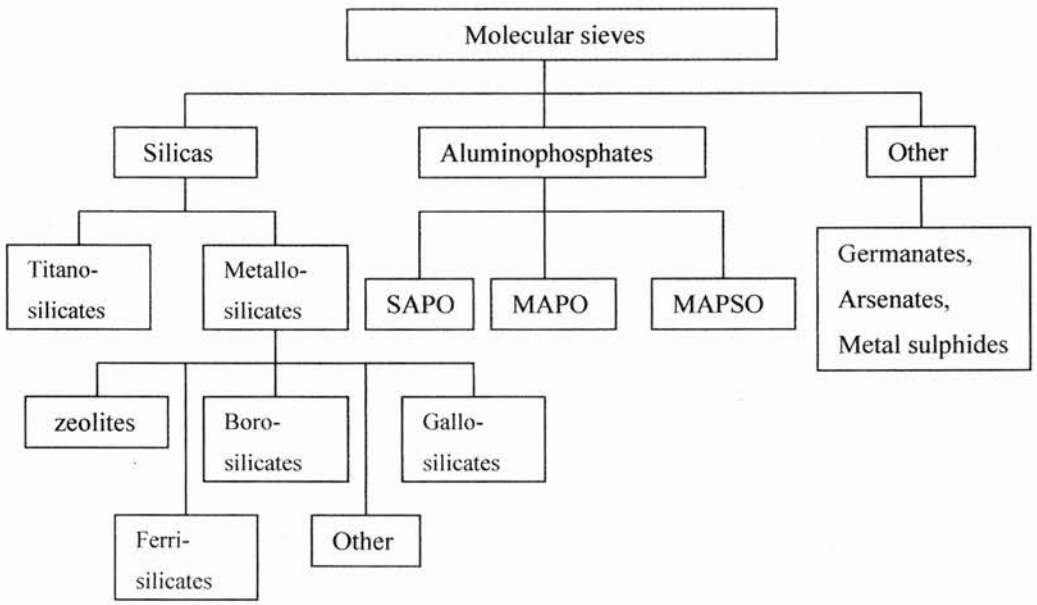

Figure 1.1 Classification of inorganic molecular sieves materials indicating the extensive variation in composition.

The aluminophosphate structures, analogous to zeolites, are denoted with the acronym '$AlPO_4$-n' referring to the three-dimensional oxide frameworks with Al/P ratios of 1. The number 'n' refers to the specific crystallographic structures reported. In these materials, the formal negative charge associated with each $[AlO_{4/2}]^-$ tetrahedron is balanced by the formal positive charge associated with each $[PO_{4/2}]^+$ tetrahedron. There is no need, therefore, for charge-balancing extraframework cations.

Analogous materials containing other elements besides Al and P can be derived from an $AlPO_4$ in which Al, or P, or both, have undergone partial or even complete substitution.

These materials have a framework composition of the general formula:

$$(Al_{1-x-y}M_xSi_y)(P_{1-z}Si_z)O_4$$

Divalent cations which are able to adopt tetrahedral coordination (e.g. M= Mg, Mn, Fe, Co, and Zn)[8,9] can partially substitute in the aluminium site whilst silicon can substitute in both aluminium and phosphorous sites, although this is not desirable. This leads to new series of materials: silicoaluminophosphates[10] (SAPO-n), metal aluminophosphates (MAPO-n) and metal silicoaluminophosphates (MAPSO-n)[11]. The type of substitution is indicated in the acronym, for example SAPO-5 is a silicoaluminophosphate with structure type 5, CoAPO-11 is a cobaltoaluminophosphate with structure type 11, and so on. Introduction of these elements renders the framework negatively charged and therefore, extra-framework cations are required to maintain the electroneutrality of the framework.

Loewenstein´s rule can be extended to the phosphate-based family to prohibit Al-O-Al, P-O-P, P-O-Si, Me-O-Al and Me-O-Me linkages. This rule also limits the structural possibilities of this family since it prevents the occurrence of rings with an odd number of tetrahedra. However, a special feature of phosphate-based molecular sieves is that in these materials aluminium in the framework can exhibit a coordination number higher than four which is not observed in aluminosilicates (although octahedrally-coordinated extra framework aluminium is frequently observed)[12]. In aluminophosphates, aluminium can adopt fivefold

coordination (trigonal bipyramidal) or sixfold coordination (octahedral) where water or anions such as hydroxide or fluoride ions complete its coordination sphere. In these cases, the aluminium polyhedra can share corners or edges through Al-O-Al or Al-F-Al linkages (the balance being compensating by the extra-atom coordinated to the aluminium) and therefore these materials can exhibit an odd numbered rings in their structures as observed in AlPO-21[13].

1.1.1 Structure and Classification

There are several ways to describe the structure of a zeolitic material depending on the particular feature of that structure to be discussed or compared to another structure.

The framework structures of zeolitic materials can usefully be considered as being built up from smaller sub-units. The smallest of such units or "primary building unit" is the TO_4 tetrahedron. Meier[14] derived "secondary building units" (SBU, figure 1.2) subject to the condition that each tetrahedral framework contains only one type of SBU but the definition of SBU can be broadened to include units found in combination. As stated above, zeolite frameworks contain channels and cavities of many kinds. These spaces are frequently polyhedral and many zeolite frameworks can be constructed by stacking one or more types of polyhedron[15]. Some polyhedral cage-like cavities are given in figure 1.3. There are further ways of considering structures, for example, in terms of layers linked to other layer in different sequences, and the frameworks of some zeolites can also be constructed from several kinds of tetrahedral chains[1]. Most of the materials presented in this thesis have structures that are most easily described on the basis of the type of polyhedra forming their cavities and hence, that have been the nomenclature adopted through this work.

The topology of the framework defines a structure type -independently of its composition- and is symbolised by a group of three letters, e.g., MFI for the structural type of zeolite ZSM-5, AFI for AlPO-5, etc. A list of the currently accepted structure types with their type materials, can be found in the Atlas of Zeolite Structure Types[16] and on the web[17].

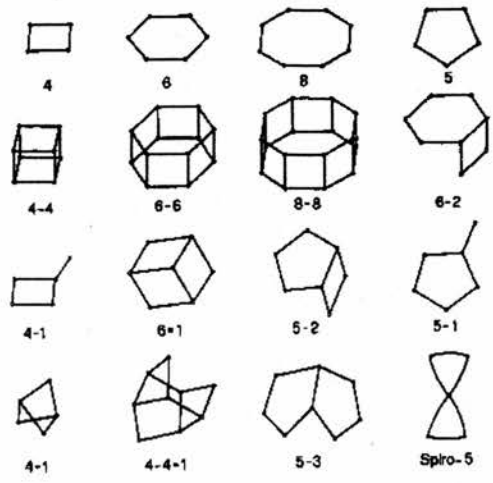

Figure 1.2 Examples of secondary building units found in zeolite frameworks.

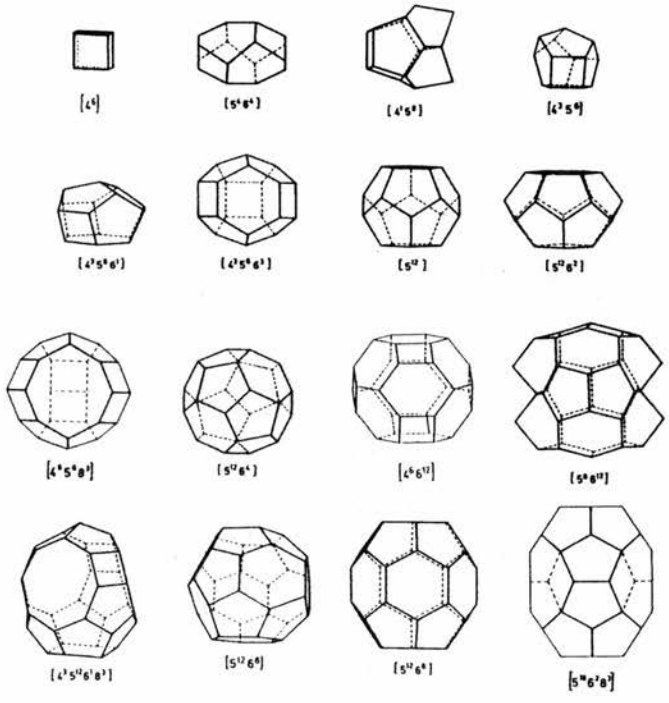

Figure 1.3. Some polyhedra observed as "cages" in zeolite structures. A T atom will lie at each corner of the polyhedron and the oxygen atom linking two T atoms, near the middle point of each edge. The oxygen atoms not engaged in bridges between T atoms are not considered as part of this polyhedron. The notation $[n_i^{m_i}]$ is used, where m is the number of n sided polygons defining the polyhedron and Σm_i is the number of faces of the polyhedron, e.g., $[5^{12}]$ represents a pentagonal dodecahedron.

From the viewpoint of sorption and catalysis, important aspects of the framework type include the type and the free dimensions of the channel system. Zeolitic materials can therefore be classified according to the dimensionality of their channel system as one-dimensional (parallel channels without connections), two-dimensional where the channels are connecting in two dimensions or three-dimensional where the channels are connected in three dimensions.

Another way of classifying molecular sieve structures is according to the number of tetrahedra forming the window openings to the channel system (number of tetrahedra following by MR, member ring). This can indicate the size of the pore openings to the channel system, although the dimensions are only approximate since the free diameter for the window also depends on the precise geometry of the window.

The main categories are:

1. Clathrasils: zeolitic materials where the void space comprises cages connected by very small openings, such as 6MR. The microporous system is only accessible to the smallest of molecules because the free diameter of the windows are very small (~ 2Å)
2. Small pore materials, with 8 or 9 MR windows, free diameter *ca.* 4 Å
3. Medium pore materials, with 10MR windows, free diameter *ca.* 5.5 Å
4. Large pore materials, with 12MR windows, free diameter *ca.* 7- 7.5 Å
5. Extra-large pore zeolitic materials, the windows contain more than 12T atoms, free diameter over 10 Å

In the case of aluminosilicates, extra-large pore materials have only recently been discovered, such as the silicas UTD-1[18] and CIT-5[19] that contains 14 MR openings. However, for the AlPOs family the discovery of very large pore solids was initiated before, with the discovery in 1988 of the extralarge pore aluminophosphate VPI-5 (VFI)[20] which contains 18 MR one-dimensional circular channels. Table 1.1 lists typical (though not all) representatives of extra-large pore materials. Most of them are phosphate-based.

Material	Year reported	Main framework composition	Ring size (MR)
VPI-5	1988	$AlPO_4$	18
AlPO-8	1990	$AlPO_4$	14
Cloverite	1991	$GaPO_4$	20
JDF-20	1992	$AlPO_4$	20
ULM-5	1994	$GaPO_4$	16
UTD-1	1996	SiO_2	14
ULM-16	1996	$GaPO_4$	16
CIT-5	1997	SiO_2	14
ND-1	1999	$ZnPO_4$	24
FDU-4	2001	Ge_xO_y	24
NTHU-1	2001	$GaPO_4$	24

Table 1.1 Representative examples of crystalline materials with ring sizes above 12 MR[21]

Finally, another important characteristic of these microporous framework materials is the framework density (or tetrahedral density) which can be expressed by the number of tetrahedra (TO_4) per 1000 Å. The tetrahedral density decreases as the portion of the volume of the voids increases. These densities range from 12.7 to about 20 tetrahedra/1000Å for zeolite or zeolite-type materials[14].

1.1.2. Properties and uses of zeolite & zeotypes

The large, regular internal surface area, taken together with features of their crystal chemistry, imparts to zeolitic materials several important properties that are not found in amorphous molecular sieves. Furthermore, the variety of composition they can exhibit extends the range of their potential applications, which are traditionally in the fields of gas adsorption and separation, molecular sieving, cation exchange and catalysis[22]. They are also of interest as hosts for other species such as small clusters of semiconductors, coordination complexes and metal clusters for

optical and electronic applications.[23,24] Recently emerging applications and perspectives have been summarised in a recent review by Davis[21].

The adsorption capacity arises from the large internal surface area (typically > 300 m^2g^{-1}) and pore volume (typical values are in the range > 0.1 cm^3/g). The ring size of the windows leading into the cavities determines the size of the molecules that can be adsorbed and the chemical composition of the framework determinates the surface hydrophilicity or hydrophobicity. The hydrophilicity affects their utility in adsorption processes, because the material will differentiate between molecules not only on the basis of their size and form, but also on their polarity.

Cation exchange capacity is only observed in materials with charged frameworks. To maintain the electroneutrality of the framework, they possess charge-compensating cations, M^{n+}, that will exchange with others in a surrounding solution when they can move through the structure. The process results from the establishment of equilibrium between external cations and internal cations. This property makes zeolites highly suitable as water softeners[25].

Charged frameworks can also be employed as acid catalysts when the charge balancing cation is a proton. This generates stable Brϕnsted acid sites as P-OH-M and Si-OH-Al. Lewis acid sites can also be present and they are usually associated with framework connectivity defects.

Microporous frameworks can also be active as redox catalysts when transition metals are incorporated in their frameworks since redox catalytic sites can be achieved by the oxidation of the transition metal. Metallo aluminophosphates are particularly promising materials in this respect since they can easily incorporate divalent transition metal cations (M=Fe, Mn, Co, etc) in their structures and these form redox catalytic sites of the type ($M^{2+} \leftrightarrow M^{3+}$)[26].

One of the most remarkable properties of these solid is that they provide shape selectivity on the processes where they are employed since the size of the channels can control the molecules that can diffuse through the channel system and for that reason they act as molecular sieves. Therefore, as catalysts they present selectivity to the reactants, the products or the transition state that can be formed within the channels.

These properties are general for this type of materials, although every single compositional family has its own particular set. For example, despite their structural similarities, phosphate-based materials are less stable than silicates to high temperatures. They are also easily hydrolysed by contact with steam and these features have reduced their applicability compared to aluminosilicates. However, they are able to accommodate high concentrations of framework heteroatoms, which is more difficult and rarely observed in silicate molecular sieves. Theoretical calculations[27] have attributed these differences in behaviour to the different nature of the bonding between phosphates and silicates. These studies suggest than the bonding in AlPO´s is molecular ionic rather than the continuous semicovalent network present in silica and silicoaluminates and in this sense, the AlPO framework comprise discrete Al^{3+} and PO_4^{3-} ionic units. This ionic bonding nature would be responsible for the lower stability of microporous AlPO´s compared to their isostructural silicates but also permits the inclusion of relatively high concentrations of ions such as magnesium, iron, cobalt, manganese and zinc.

1.1.3 Synthesis of zeolites & zeotypes

Natural zeolites occur as aluminosilicates that are found in volcanogenic sedimentary rocks. They have been known as "zeolites" since Baron Cronstedt[28] described the mineral stilbite in 1756, although they had been used since the Roman times in construction. They have been exploited industrially[29] since the discovery in the late 1950´s of huge beds of zeolite-rich sediments in the western United States and other countries, although only six of the approximate 63 natural zeolites commonly occur in large beds.

The breakthrough in this field of research was the possibility of synthesising these materials in a laboratory, when in the early 1950´s Milton[30] and Barrer[31] found a method to prepare zeolites based on the use of reactive alkaline aluminosilicate gels and low crystallization temperatures (80-150 °C). Many aluminosilicate zeolites with low Si/Al ratio were prepared via this route, such as the commercially significant A, P and X. The discovery in the early 1960's[32] that high silica zeolites could be prepared by the addition of quaternary ammonium cations to alkali aluminosilicate gels produced another major increased in the number of known

types. Zeolite β was the first synthetic high Si/Al ratio zeolite[33]. It was also through the use of quaternary ammonium salts and organic amines that the aluminophosphate family was discovered in the 80's[34, 35]. In total, more than a hundred different types of zeolites or zeolite-like materials have now been synthesised[16] and many varieties, including the important ZSM-5(MFI) structure type, have been and are continuing to be prepared through this route.

1.1.3.1. Mechanism

Generally speaking, tetrahedrally-coordinated framework molecular sieves are almost exclusively synthesised under hydrothermal conditions, i.e. in the presence of water and at temperatures between 80-200°C. The synthesis involves the preparation of a gel mixing tetrahedral cation sources, organic additives or inorganic cations and a mineraliser (OH^- or F^-).

The kinetics and mechanism of crystallisation of a zeolitic phase[36] entails complex chemistry since it is a multicomponent system in which there are interactions, chemical reactions and equilibria as well as crystal nucleation and growth processes taking place throughout the mixture. In the initial stages of the reaction, the solvent allows the dissolution and mixing of the reactants to form an inhomogeneous gel. Nucleation centres are formed with time and subsequently grow to form the final crystalline product. Due to this complex chemistry, there is a lack of understanding of this process, and for example, the precise nature of the precursor species forming the crystals is unknown and it is also thought that they depend or are intimately related to the synthesis conditions.

Some authors have proposed mechanisms of crystallisation of microporous materials. Two main mechanisms have been postulated[36]. The *solution-mediated transport mechanism*[37] considers equilibrium to be stablished between the solid gel and the solution where the nucleation precursor species are formed. Hence, the process of nucleation and growth of the crystalline phase take place at the expenses of the gel that continuously dissolves to feedstock the solution. The *solid hydrogel transformation mechanism*, suggest that the gel transforms directly to the crystalline phase. There are examples to support these theories in both silicate and aluminophosphate systems[36].

There is also a third theory, suggested by Ozin and co-workers[38] for aluminophosphate materials, as a variation of the solution-mediated mechanism. They propose a progenitor chain that could undergo successive hydrolysis and condensation processes to form other chain types, layers and/or three-dimensional structures. The amount of water in the system would be important in determining the degree of hydrolysis and condensation reactions and thereby the final structure formed.

1.1.3.2. Conditions

Factors such as the temperature or composition of the reactant mixture are the main variables that determine the products of such a system but other kinetic factors such as reaction time, reactant sources, tumbling of the autoclaves, etc, also affect the products of reaction in ways that are incompletely understood[39]. Despite these difficulties certain guidelines for the effects of various reaction parameters can be given[40, 41, 42].

The composition of the initial reaction mixture influences the synthesis gel and therefore the final products of crystallisation. This is because syntheses usually consist of a solid and liquid phase and changing the initial composition of the mixture affects both. Small changes in the initial composition or even the way the mixture is made (order of addition of the reactants, temperature of the mixture, etc) can affect the gel and therefore, the structure and composition of the final product. The effects of the order of addition are not well understood but the mixing order can affect the reactivity and the pH; different reactant sources can also have different reactivity.

Time is a very important parameter because zeolitic materials are metastable phases in the reaction medium. The more thermodynamically instable but kinetically favoured phase will be formed in the first place and with time, it will recrystallise to other phases. The system evolves to more stable phases; so denser phases will be formed with time. This is known as Ostwald's rule of successive transformations.

Temperature increases the rate of crystal growth and can influence the phase to be formed. In general, at higher temperature denser phases are formed. *Pressure* is not a critical parameter unless one of the reactants is a volatile agent. It is usually the autogeneous system pressure. *The pH of the reactant mixture* can affect the solubility and nature of the species to be formed in the reactant mixture. In general, for silicate-based systems the synthesis can be made in basic (OH) or in neutral-acid (F) medium. The fluoride medium has been investigated thoroughly in recent years and has allowed numerous new and interesting materials to be obtained[43,44].

1.1.3.3. Role of organic additives: structure direction

Organic additives[45,46] influence the synthesis gel chemistry and they also act as structure-directing agents. Zeolitic materials compensate for their lack of stability with respect to denser phases by the inclusion of inorganic cations, water or organic species. As zeolites are metastable in the reaction media, the organic molecules preferentially stabilise one phase over all the possible structures that could be formed. There is usually a good geometrical fit between the guest molecules and the host framework in order to optimise and maximise the host-guest interactions. That was the origin of the "template effect" since the organic species ("templates") were thought to organise the tetrahedra on their surroundings with a particular geometry. However, there is rarely a one-to-one relationship between the organic molecule and the framework produced and in many cases, one organic molecule can be used to crystallise various zeolitic structures or a zeolitic structure can be produced while using different organic molecules. For this reason, the organic molecules employed in synthesis of zeolitic materials are more accurately referred to as "structure directing agents" (SDAs) which makes clear the crucial role they have in determining the phase that crystallises, without implying the specificity of the term "template".

The structure directing effect has been investigated on pure silica systems[47] with different organic compounds. The results suggest that small globular molecules such as quinuclidine and piperidine favour the crystallisation of clathrasils; linear amines tend to give structures with one-dimensional channel systems (such as ZSM-

48 and ZSM-12) and branched alkylammonium salts tend to give zeolites with interconnecting channels.

Some structures, such as the zeolite ZSM-5 and the aluminophosphate AlPO-5, can be obtained with a great variety of organic molecules. In these cases, the organic acts to stabilise the structure by filling the pores. In a few cases, the relationship between the organic and the structure is unambiguous, for example in the case of the ZSM-18 structure synthesised with $(C_{18}H_{36}N_3)^+$ [48] (figure 1.4). Size, shape and even the symmetry of the structure directing agent influences those of the zeolite channel system.

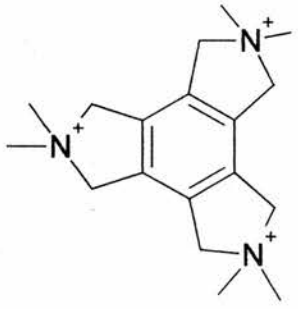

Figure 1.4. Molecule of 2,2,5,5,8,8-hexamethyl-2,3,4,5,6,7,8,9,-octahydro-1H-2,5,8-triazatrindene (triquat), template used in the synthesis of ZSM-18.

1.1.3.4. Synthesis of aluminophosphates

The synthesis of aluminophosphate-based molecular sieves follows broadly the same general principles of gel chemistry, nucleation, structure direction and crystal growth discussed above. However, there are some particularities of this system that need to be underlined.

Aluminophosphates are usually synthesised at neutral or slightly acidic pH conditions, at high temperatures and they usually require shorter crystallisation times than the silicates. Another difference is that they can only be synthesised in the presence of alkylammonium cations or amines, since in their absence or in the presence of alkali metal cations, dense phases are formed. The organic additives in these materials have a key role to play not only as structure directing agents but also

because, as in the case of amines, they modify the pH of the medium and become positively charged under typical reaction conditions.

This complex chemistry makes almost impossible to know *a priori* the result of the synthesis of zeolitic materials with a new SDA or in a new compositional domain. New discoveries on this field of research are based on a *trial and error* methodology by performing a systematic study of the variables of reaction and observing trends in the crystallisation behaviour for each specific system.

1.2 METAL COMPLEXES IN THE SYNTHESIS OF MICROPOROUS MATERIALS

Typical structure directing agents employed in the synthesis of zeolites and zeotypes are organic molecules such as amines and alkylammonium cations. However there are some examples where metal complexes have been employed as structure directing agents. The main problem for the widespread application of such molecules as templates is to fulfil the basic requirements to act as SDAs, namely to be sufficiently stable to remain intact under the conditions of hydrothermal crystallisation and, on a more practical level, to be accessible in quantities large enough to perform detailed synthetic studies.

There have been two main approaches to the incorporation of metal complexes during direct crystallisation of microporous hosts: (1) the addition of the complex to well-defined synthesis of a microporous host that usually crystallised in the absence of the complex and (2) the use of the complex as a "true" template.

The first approach entails the addition of the complex to preparations that are expected to give a certain molecular sieve with the hope that the framework will form around the complex and this will be trapped within it. The preferred host materials for this approach have been the faujasite-type zeolites X and Y. These zeolites are prepared in the presence of small inorganic cations such as sodium and potassium and do not require the presence of an organic additive to crystallise.

Faujasite zeolites also have cavities big enough (~13Å) to include molecules as large as porphyrins.

Bi-Zeng Zhan and Xiao-Yu Li[49] reported a method to encapsulate a metalloporphyrin within zeolite Y during synthesis. The metalloporphyrin molecule was modified with cationic peripherical substituents to favour the inclusion due to the electrostatic interaction with the anionic aluminosilicate species. Hriljac and coworkers[50] were also able to encapsulate a different porphyrin at low concentration in zeolite X and Y and within the aluminophosphate VPI-5 by a similar procedure. The porphyrin used in this work was highly charged and had excellent aqueous solubility. Manganese (III) salen complexes[51] were also encapsulated within the supercages of zeolite X by this method. Again the extent of the encapsulation of the complexes into the zeolite varied with the type of substituent on the aromatic ring.

From these examples, it appears that the incorporation of macrocycles within these solids is promoted by the interactions between the anionic aluminosilicate framework and the cationic complexes. This approach could then be employed to incorporate complexes into materials with negative frameworks and which do not need organic SDAs in their synthesis. However, many of the microporous zeolites and zeolitic materials are synthesised employing organic molecules. The inclusion of complexes in those materials might be more difficult in these cases since there is not obvious chemical reason for the zeolitic host to incorporate the metal complex over the usual structure-directing agent.

In the case of ferrierite, inclusion of copper complexes on this structure has been achieved by taking advantage of the way of synthesising this material. Large crystals of pure silica ferrierite can be synthesised employing propylamine as SDA, using HF as a mobilising agent and with pyridine as a solvent[52]. Such a system provides the opportunity to prepare metal-pyridine complexes *in situ* within the pores of this zeolite when copper was added to the synthesis gel. The $[Cu(py)_2]^{2+}$ complex remained incorporated into the final solid, its charge being balanced by the fluoride and defect sites within the structure. The complex consists of a Cu^{2+} cation located at the centre of the 8-ring window bound to one pyridine molecule residing in the cage that forms part of the 8-ring channel and another pyridine molecule in the main 10-ring channel. The planes of the two pyridine molecules bound to each Cu^{2+} cation are orthogonal with respect to each other (figure 1.5).

A copper (I) complex has also been included in ferrierite by a similar procedure[53]. Composition of the reaction gel was similar to the above case but instead of pyridine, the solvent employed was an ammonium solution. The presence of the propylamine in the reaction medium reduces the Cu(II) to Cu(I) and the ammonia prevents the disproportion to Cu(0) and Cu(II) by stabilising the $[Cu(NH_3)_2]^+$ complex incorporated within the structure. The complex resides within the 10-membered ring channel as a linear complex and is isolated inside the channels. In this case, the dipropylamine is also incorporated within the structure together with the complex.

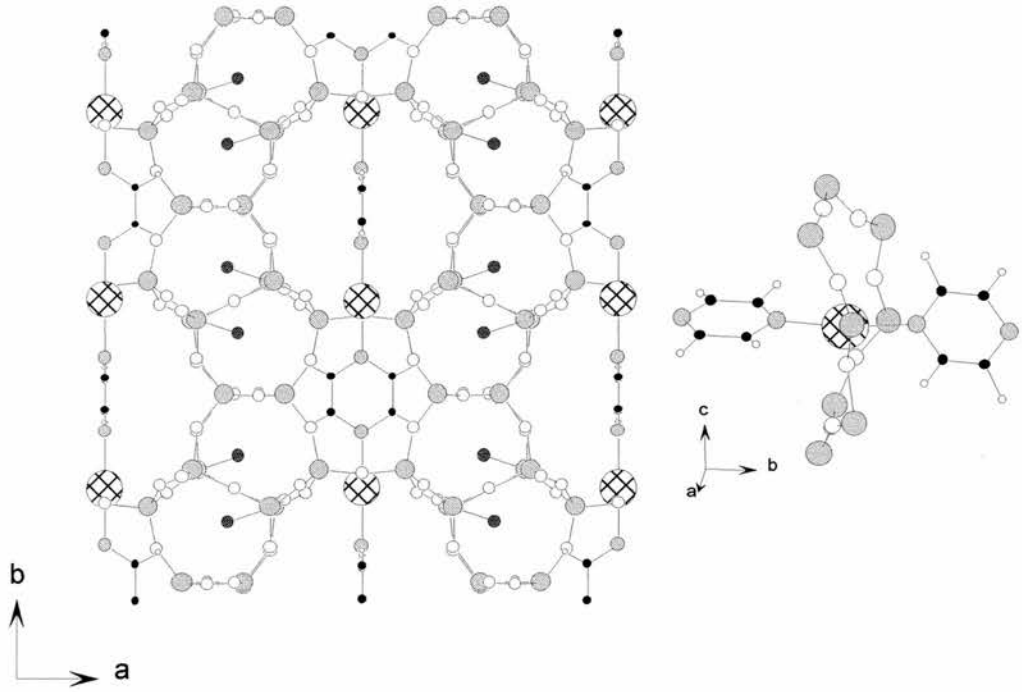

Figure 1.5. Crystal structure of $[Cu(pyr)_2]^{2+}$-containing siliceous ferrierite viewed along the c direction (left) and right, the structure of the complex in the 8-ring of ferrierite (Key: Cu, hatched; Si, grey; O, white; F, black; N, grey smaller; C, black smaller; H, white smaller).

The second approach is the use of the metal complexes as SDAs rather than attempting to incorporate them within a specific material. In this case they have been shown to direct the crystallisation of both known and new structures.

Organometallic complexes[54] have been found to direct the synthesis of several pure silica clathrasils such as nonasil, octadecasil and dodecasil, as well as zeolites such as ZSM-48. A new structure zeolite type, UTD-1[55], was also produced with the permethylcobalticinium complex, which was the first that had not been synthesised before using organic molecules as SDAs and, as previously mentioned, it was the first silicon-rich extra-large pore material. Table 1.2 shows the organometallic cations that have been included and the different frameworks they have directed under different synthesis conditions.

Organometalic cation	**Formula**	**Framework type**
Cobalticinium	$[Co(C_5H_5)_2]^+$	NON; AST; DOH; ZSM-48
1,1'-dimethylcobalticinium	$[Co(C_5H_4CH_3)_2]^+$	DOH
Benzene cyclopentadienyl iron	$[Fe(C_6H_6)(C_5H_5)]^+$	DOH
Decamethylcobalticinium	$[Co(C_5(CH_3)_5)_2]^+$	UTD-1

Table 1.2. Organometallic cations employed as structure directing agents and the framework structures they have directed[54].

Cobalt complexed with linear amines has also been successfully employed to direct the synthesis of layered and three-dimensional frameworks. For instance, tris(1,2-diaminoethane) cobalt (III) in a gallophosphate preparation[56] yielded a material isostructural with AlPO-15 containing the complex. In a preparation with cobalt and the amine diethylenetriamine[57], the complex of cobalt and the amine was formed *in situ* and found to reside in the final CoAlPO-34 (chabazite framework type) structure formed.

Iridium and cobalt complexes based in the ligands 1,2-diaminoethane and trans-1, 2-diaminocyclohexane were employed in aluminophosphate synthesis as structure directing agents[58]. The complexes with the ligand trans-1, 2-diaminocyclohexane direct the synthesis of one AlPO whose structure can be described as aluminophosphate chains running parallel to the crystallographic *a* axis whilst the complex is packed between them. The ethylenediamine complexes yielded layered aluminophosphates with the complexes placed between the layers.

A small number of nickel complexes with linear amines have also been incorporated in aluminophosphate-based materials, mainly in AlPO-5[59] and chabazite frameworks[60]. These are discussed in greater detail in the introduction to chapter 4.

1.2.1 Applications of encapsulated complexes

These examples illustrate that, although examples are limited, metal complexes can be incorporated or act as SDAs in the synthesis of microporous solids, producing materials that could have added functionality over than those prepared with organic amines or quaternary ammonium cations. There are several possible applications of such complex-containing zeolitic materials:

1.2.1.1. Heterogenisation of homogeneous catalysts

When the complexes are themselves catalytically active under single phase conditions incorporation may be attempted in order to 'heterogenize' them.

One of the most desirable properties of homogeneous catalysts is their enantioselectivity. One of the approaches to the design of chiral catalysts entails the heterogenization (or immobilisation) of chiral homogeneous transition metal complexes on a high –area solid support. Inorganic molecular sieves with a three-dimensional pore system and layered materials with a two-dimensional pore system find increasing use as hosts for homogeneous catalysts[61]. Zeolitic hosts might also give additional selectivity by molecular sieving effects.

There are several methods for the heterogenisation of homogeneous catalysts, but probably the most employed is the synthesis of the complex inside the molecular sieve. This is the so-called '*ship in a bottle*' or '*Tea bag*' catalyst: the construction of a chiral entity (the ship) inside a micropore (the bottle). The synthesis of metal-Schiff-base, -porphyrin and –phthalocyanine complexes has been investigated in detail, because they cannot be fixed within the porous structures of zeolites by cation exchange process due to their large size (10-14 Å).

There have been two approaches to these 'ship in a bottle' chelate complexes. In the first approach, a flexible ligand must be able to diffuse freely to

the zeolite pores, but after the complexation with a previously exchanged metal ion, the complex become too large and rigid to escape out of the cages. This approach is well adapted for encapsulated metal-Salen complexes, since the Salen ligand offers the desired flexibility. For example, Corma and coworkers[62] encapsulated a chiral salen complex, Mn(salen), analogous to the Jacobsen catalyst, within the supercages of zeolite Y. This complex showed catalytic activity very similar to the homogeneous complex.

Zeolite-exchanged transition metal ions can easily be chelated by adsorbed amine[63] ligands too. Cyclic amines such as cyclam and triazacyclononane are sufficiently small and flexible to enter the pores of twelve-membered ring zeolites as zeolite Y. For example, a cyclam type complex encapsulated in zeolite Y was tested in the epoxidation of cyclohexene[64]. It showed a higher catalytic potential than its homogeneous analogues, because the zeolites protected the complex against degradation and increased the epoxide yield of the reaction.

A second approach is the template synthesis method and it is exemplified by the preparation of intrazeolite metallophthalocyanines[65]. Initially the metal is introduced, e.g. by ion exchange or vapour deposition of a metal complex, and then the metal-loaded zeolite is reacted with 1,2-dicyanobenzene and tetramerizated by heating. So four dicyanobenzenes are required to diffuse into the zeolite matrix, where they can cyclise around the metal ion to form the tetradentate macrocycle, which is too large to diffuse out.

1.2.1.2. Introduction of transition metals in extra-framework positions

Incorporation of transition metal complexes within zeolite hosts also provides a strategy for immobilising redox-active cations in a solid matrix. After removing the organics by calcination, the active metal remains highly dispersed and evenly distributed within the solids. This route is a potential alternative to the traditional method of introducing metal ions by calcination and aqueous cation exchange. This is especially relevant for aluminophosphate materials whose structure is more easily degraded through hydrolysis of the aluminophosphate framework than for aluminosilicates.

1.2.1.3. Preparation of chiral frameworks

Another possible application, pointed out by Wilkinson[56], could be the preparation of chiral microporous materials. The desirability of preparing chiral catalysts by incorporation of chiral homogeneous catalysts on to zeolitic hosts was mentioned earlier. Another approach to chiral catalysts comes from the synthesis of chiral zeolitic materials that could be used in the preparation of optically pure chiral products. Therefore, much effort has been put on the synthesis of chiral templates with the idea that the template would transfer its chirality to the framework and this has been the reason behind the use of many asymmetric organic molecules on the synthesis of zeolitic materials. Metal complexes are an ideal source of chiral molecules since very simple metal complexes have chiral conformations because of the disposition of the ligands attached to the metallic centre and, therefore, they could potentially "template" chiral frameworks.

1.3. AIMS

The main aim of this project is to explore the use of metal complexes as structure directing agents on the synthesis of aluminophosphate-based materials. The synthetic approach considered in this work has been based in the employment of the azamacrocycles tetramethylacyclam and cyclam to establish the possibility of incorporating metals within the STA-6 and STA-7 framework structures. This approach has been extended to examining the role of linear amine complexes as templates because of their wide availability and lower cost in comparison with the azamacrocycles.

A second aim in this project is to perform a full characterisation of the complex-containing microporous materials, particularly in characterising the included complex and the state of the metal after calcination of the material. The incorporation of catallytically-active complexes could lead to the heterogenisation of these complexes. Also, inclusion of metals that are not readily incorporated in zeolitic materials via occluded complexes offers a route to supported metal or metal oxide catalysts.

1.4. REFERENCES

1. R. Szostack, Molecular Sieves Principles of synthesis and Identification, Van Nostrand Reinhold, 1989.

2. R. M. Barrer, 1978, *Zeolites and Clays Minerals as Sorbents and Molecular Sieves*, Academic Press.

3. J. W. McBain, *The sorption of gases and vapours by solids*, Rutledge and Sons, London, 1932.

4. W. Loewenstein, *Am. Mineral.*, 1954, **39**, 92.

5. A. K. Cheetham, G. Férey, T. Loiseau, *Angew. Chem. Int. Ed.*, 1999, **38**, 3268.

6. G. Férey, *Chem.Mater.*, 2001, **13**, 3084.

7. W. T. A. Harrison, *Curr.Opin.Solid St.Mater.Sci.*,2002, **6**, 407.

8. M. Hartmann, L. Kevan, *Chem. Reviews*, 1999, **99**, 635

9. A. M. Prakash, M. Hartmann, Z. Zhu, L. Kevan, *J. Phys. Chem. B*, 104, 1610.

10. B. M. Lok, C. A. Messina, R. L. Patton, R. T. Gajek, T. R. Cannan, E. M. Flanigen, *J.Am.Chem.Soc.*, 1984,106,6092

11. E. M. Flanigen, B. M. Lok, R. L. Patton, S. T. Wilson, *Pure Appl.Chem.*, 1986, 58, 1351.

12. J. A. van Bokhoven, A. M. J. van der Eerden, D. C. Koningsberger, *Stud. Surf. Sci. Catal.*, 2002, **142**, 1885.

13. J. M. Bennett, J. M. Cohen, G. Artioli, J. J. Pluth, J. W. Richardson Jr, J. V. Smith, *Inorg. Chem.*, 1985, **24**, 188.

14. W. M. Meier, 1968, *Molecular Sieves*, Society for Chemical Industry, London, p10.

15. F. Liebau, H. Gies, R. P. Gunawardane and B. Marler, *Zeolites*, 1986, **6**, 373.

16. W. M. Meier, D. H. Olson and Ch. Baerlocher, Atlas of Zeolite Structures types, 5th Edition, Elsevier, 2001.

17. www.iza-structure.org/databases/

18. R. F. Lobo, M. Tsapatsis, C. C. Freyhardt, S. Khodabandeh, P. Wagner, C.-Y. Chen, K. J. Balkus Jr, S. I. Zones, M. E. Davis, *J.Am.Chem.Soc.*, 1997, **119**, 8474

19. M. Yoshikawa, P. Wagner, M. Lovallo, K. Tsuji, T. Takewak, C.Y. Chen, L. W. Beck, C. Jones, M. Tsapatsis, S. I. Zones, M. E. Davis, *J.Phys.Chem.*, 1998, **102**, 7139

20. M. E. Davies, C. Saldarriaga, C. Montes, J. M. Garces, C. Crowder, *Nature*, 1988, 331, 698.

21. M. E. Davies, *Nature*, 2002, 417, 813.

22. P. B. Venuto, *Microporous Mater.*, 1994, **2**, 297.

23. K. L. Moran, W. T. A. Harrison, I. Kamber, T. E. Gier, X. Bu, D. Herren, P. Behrens, H. Eckert, D. Stucky, *Chem. Mater.*, 1996, **8**, 1930.

24. R. E. Morris and P. A. Wright, *Chemistry & Industry*, 1998, **6**, 256.

25. R. Levanmao, N. T. Vu, S. Y. Xiao, A. Ramsaran, *J.Mater.Chem.*, 1994, **4**, 1143.

26. H. Berndt, A. Martin, Y. Zhang, *Microporous Mater.*, 1996, **6**, 1.

27. F. Corà, C. R. Catlow, *J.Phys.Chem.B*, 2001, **105**, 10278.

28. A. Cronstedt, *Akad.Handl.(Stockholm)*,18, 120

29. F. A. Mumpton, *Proc.Natl.Acad.Sci.USA*, 1999,**96**, 3463.

30. D. W. Breck,W. G. Eversole, R. M. Milton, T. B. Reed,T. L. Thomas, *J.Am.Chem.Soc.*, 1956, **23**, 5963.

31. R. M. Barrer, *J.Chem.Soc.*,1948, 127

32. R. M. Barrer, P. J. Denny, *J.Chem.Soc.*, 1961, 971

33. R. L. Wadlinger, G. T. Kerr, E. J. Rosinski, US Patent 3.308.069, 1967.

34. S. T. Wilson, M. B. Lok, C. A. Messina, T. R. Cannan, E. M. Flanigen, *J.Am.Chem.Soc.*, 1982, **104**,1146.

35. S. T. Wilson, M. B. Lok, E.M. Flanigen, U.S.Patent 4.310.440, 1982.

36. R. J. Francis, D. O'Hare, *J.Chem.Soc., Dalton Trans.*, 1998, 3133.

37. G. T. Kerr, *J.Phys. Chem.*, 1966, **70**, 1047.

38. S. Oliver, A. Kuperman, G. A. Ozin, *Angew.Chem.Int.Ed.Engl.*, 1998, **37**, 46.

39. M. E. Davis, R. F. Lobo, *Chem. Mater.*, 1992, **4**, 756.

40. R. M. Barrer, *Zeolites*, 1981, **1**, 130.

41. H. Van Bekkum, E. M. Flanigen, J. C. Jansen, *Introduction to zeolite science and practice*, p.77-136.

42. S. T. Wilson, *Stud. Surf. Sci. Catal.*, 1991, **58**, 137.

43. M. A. Camblor, M. A. Barret, M. J. Díaz-Cabañas, L. A. Villescusa, *MicroMesoporous Materials*, 2001, **48**, 11.

44. M. Estermann, L. B. McCusker, C. Baerlocher, A. Merrouche, H. Kessler, *Nature*, 1991, **352**, 320

45. B. M. Lok, T. R. Cannan and C. A. Messina, *Zeolites*, 1983, **3**, 282.

46. R. F. Lobo, S. I. Zones, M. E. Davis, *J. Inclus. Phenom. Mol.*, 1995, **21**, 47.

47. H. Gies, B. Marler, *Zeolites*, 12, 42 (1992).

48. S. L. Lawton, W. J. Rohrbaugh, *Science*, 247, 1319 (1990).

49. B. Zhan, X. Li, *Chemm.Comm.*, 1998, 349.

50. T. A. Khan, J. A. Hriljac, *Inorg. Chimica Acta*, 1999, **294**, 179

51. P. S. Varkey, C. Ratnasamy, P. Ratsanamy, *J.Mol.Cat.A-Chemical*, 1998, **135**, 295.

52. M. P. Attfield, S. J. Weigel, F. Taulelle, A. K. Cheetam, *J.Mater.Chem.*, 2000, **10**, 2109.

53. B. Gomez-Lor, M. Iglesias, C. Cascales, E. Gutierrez-Puebla, M. A. Monge, *Chem. Mater.*, 2001, **13**, 1364.

54. P. Behrens, C. Panz, V. Hufnagel, B. Lindlar, C. C. Freyhardt, G. van de Goor, *Solid State Ionics*, 1997, **101-103**, 229

55. R. F. Lobo, M. Tsapatsis, C. C. Freyhardt, S. Khodabandeh, P. Wagner, C.-Y. Chen, K. J. Balkus Jr, S. I .Zones, M. E. Davis, *J.Am.Chem.Soc.*, 1997, **119**, 8474

56. S. M. Stalder, A. P. Wilkinson, *Chem. Mater.*, 1997, **9**, 2168.

57. Y. H. Xu, Z. Yu, X. F. Chen, S. H. Liu, X. Z. You, *J. Solid State Chem..*, 1999, **146**, 157.

58. D. J. Williams, J. S. Kruger, A. F. McLeroy, A. P. Wilkinson and J. C. Hanson, *Chem. Mater.*, 1999, **11**, 2241.

59. N. Rajic, D. Stojakovic, A. Meden, V. Kaucic, *Proc. 12th Int. Zeolite Conf.*, Eds. M. M. J. Treacy, B. K. Marcus, M.E. Bisher, J.B. Higgins, MRS, Warrendale, Pennsylvania, 1999, 1765.

60. N. Rajic, A. Meden, P. Sarv, V. Kaucic, *MicroMesoporous Materials,* 1998, **24**, 83.

61. F. Bedioui, *Coord. Chem. Rev.*, 1995, **144**, 39.

62. M. J. Sabater, A. Corma, A. Domench, V. Fornes and H. Garcia, *Chem. Commun.*, 1997, 1285.

63. D. E. De Vos, D. L. Vanoppen, X. Y. Li, S. Libbrecht, Y. Bruynsaraede, P. P. Knops-Gerrits and P. A. Jacobs, *Chem. Eur. J.*, 1995, **1**, No 2, 144.

64. J. C. Medina, N. Gabriunas, E. Paez-Mozo, *J. Mol. Cat. A*, 1997, **115**, 233.

65. D. E. De Vos, P. A. Jacobs, *Cat. Today*, 2000, **57**, 105.

2. CHARACTERISATION TECHNIQUES

2.1 X-RAY DIFFRACTION[1, 2,3]

This is the most frequently used method for identifying and describing a zeolite and zeotype structure.

Diffraction phenomena result from the interaction of radiation with ordered matter without the absorption of energy. This phenomenon occurs when the repeating dimensions of the diffracting objects (atoms in a crystal) are comparable to the wavelength of the radiation. X-rays have wavelengths on the order of angstroms ($1x10^{-10}$m), which is in the range of typical interatomic distances in crystalline solids. Therefore when a crystal is placed in the path of an X-ray beam its atoms act as secondary sources emitting X-rays due to the the vibrations induced in the electrons by the initial beam. These emitted X-rays have identical frequency and wavelength to those of the incident X-rays and the crystal or atoms are said to "scatter" the X-rays. In certain directions, the individual scattered waves may reconstructively recombine in phase producing a strong reinforced but deviated beam while in other directions, there is no diffracted intensity. This recombination of the scattered waves is the diffraction phenomenon.

In 1912, M. von Laue and W.H. Bragg independently enunciated equivalent explanations of the mechanism by which X-ray diffraction occurs. When a monochromatic beam of X-rays is incident on a crystal, every atom in the crystal scatters the X-ray beam in all directions. The intensity of the scattered X-ray radiation can be thought to depend on the number and type of the atoms located in each plane of the crystal. Reinforcement of the scattered beam will only occur at certain values of the angle between the incident beam and the lattice planes, θ, for every set of atomic planes, depending on the wavelength λ of the incident X-rays and the spacing d between the atomic planes in the crystal lattice (figure 2.1). This is expressed by the Bragg equation:

$$n\lambda = 2d\sin\theta \qquad \text{where n= 1,2,3.....}$$

A diffraction pattern then represents the intensities of diffracted beams from sets of parallel lattice planes *versus* the angle by which the beam has been scattered from the incident beam (2θ).

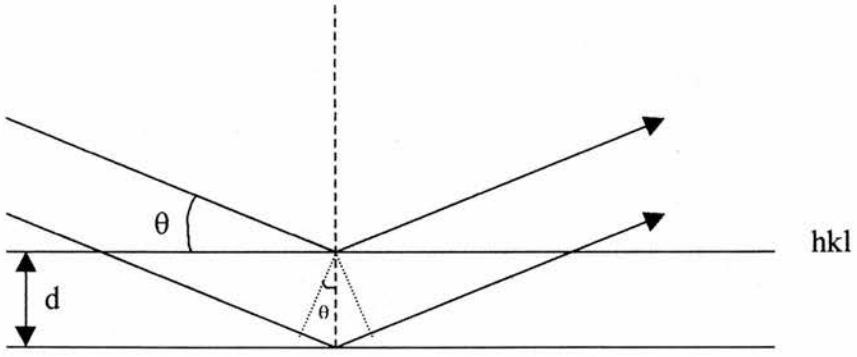

Figure 2.1. Bragg reflection from crystal planes of spacing d_{hkl}

At an atomic level, since the X-rays are scattered by the electrons in the atom, the scattered radiation should be proportional to the particular number of electrons for each atom. However, there are also partial constructive and destructive interferences due to the finite size of the atom. Experimentally, this leads to a fall off of X-ray scattering versus θ. An atomic scattering factor (f_j) is defined for each atom that indicates the effective scattering from the atom and related to the scattering from a single electron.

In a crystal, these set of parallel lattice planes giving rise to the diffraction are called Miller planes and may be described by Miller indices, represented by three integers (h k l) that are the number of times that particular set of planes intercepts the crystallographic axes, *a*, *b* and *c* respectively. It is possible to relate the distance between parallel planes *d* in terms of the Miller Indices (h k l) of the family of planes giving rise to the diffraction and hence, it is possible to identify the family of planes causing the diffraction in a particular direction. For example, the relation for the orthorhombic system is given by the expression:

$$(1/d_{hkl})^2 = h^2/a^2 + k^2/b^2 + l^2/c^2$$

where *a*, *b*, *c*, are the unit cell parameters.

The scattered intensity from each set of atomic planes in the diffraction pattern (I_{hkl}) is related to the position of the atoms in the unit cell (x, y, z) and is expressed for each reflection by the Structure Factor or Structure amplitude, F_{hkl}, which is the resultant of N waves, scattered in the direction of the reflection (h k l) by the N atoms in the unit cell:

$$F_{hkl} = \sum_j f_j \exp\left[2\pi i(hx_j + ky_j + lz_j)\right]$$

where f_j is the atomic scattering factor for each atom in the unit cell.

This is the equation of an addition of waves of amplitude f_j and phase given by the exponential part of this equation. This expression can also be written as:

$$F_{hkl} = \sum_j f_j\left[\cos\left(2\pi(hx + ky + lz)\right) + i\sin\left(2\pi(hx + ky + lz)\right)\right]$$

The structure factor is related to the electron density in the unit cell and so, with coordinates of the atoms in the unit cell (for a structure with a centre of symmetry) by the expression:

$$\rho(xyz) = \frac{1}{V}\sum_h \sum_k \sum_l F_{hkl} \cos\left(2\pi(hx + ky + lz)\right)$$

This illustrates the main problem of X-ray diffraction when applied to solve crystal structures. In a diffraction experiment the intensities of diffraction are measured rather than the structure factors. The intensity of the diffraction from each set of planes is proportional to the product of the structure factor and its complex conjugate:

$$I \propto F\,F^* = |F|^2$$

So, the amplitude of F_{hkl} for each reflection is known, but the phases are lost in the experimental measurement, which is known as "the phase problem". There are several methods to overcome this problem of X-ray diffraction and to allow the

structure of the material, i.e. the atomic coordinates, to be obtained by this technique. These are:

- Direct methods: Statistical trial and error methods. F_{hkl}'s are interdependent so by "guessing" a few it is possible to extrapolate the others.
- Patterson methods: Uses an adapted electron density map where peaks correspond to vectors between atoms.
- Heavy atom Methods: High Z atoms will dominate the electron density map and then they will be easier to locate. The method then use Patterson vectors to find the other atoms.

X-ray diffraction is therefore a powerful tool for determining the structure of materials. The methodology employed consists mainly of the measurement of the diffracted intensities I_{hkl} for many of the hkl reflections from the crystal. The structure factors, F_{hkl}, for each reflection can be obtained from the experimentally measured intensities. Maps of electron density can be generated using the different methods to overcome the phase problem mentioned above (Direct Methods, Patterson, etc.), suggesting the location of the atoms and so the crystal structure may be deduced. The process of solving a crystal structure requires good quality experimental data for many reflections and the aid of computer packages to perform the calculations involved.

Depending on the crystal size, the experimental set up for obtaining the diffraction pattern of a sample can be by single crystal or by powder diffractometry. The characteristics of both are summarised below.

2.1.1. Single Crystal X-ray Diffraction

Single crystal diffraction has long been employed for elucidating the structures of crystalline materials. One needs all the diffracted intensities that can be measured as accurately as possible, since the structure factors are derived from these sets of intensities. The way of achieving this is to collect the diffracted intensities of a single crystal orientated in an X-ray beam, collecting a few reflections at each

time and reorientating the crystal to collect the full data set. Ultimately, this allows the construction of a three-dimensional electron density map from the measured structure factors. Current single crystal diffractometers consist of a computer-controlled goniometer equipped with an area detector which collects several reflections in a single frame, as the one represented schematically in figure 2.2.

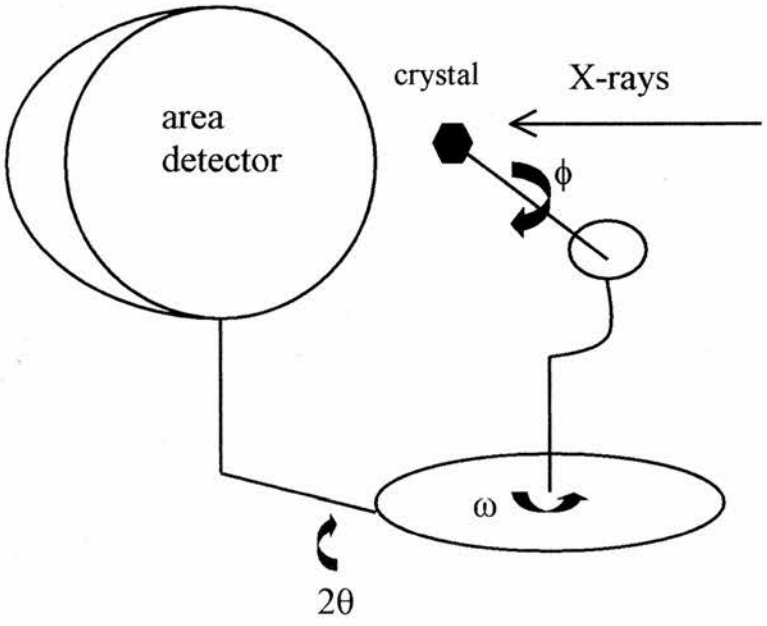

Figure 2.2. Schematic representation of a diffractometer equipped with an area detector.

The experiment involves mounting a crystal on a fine glass capillary, and moving the crystal under computer control during the data collection. In a first stage, the unit cell is determined by randomly rotating the crystal in the X-ray beam to ensure collection of as many reflection intensities as possible and collecting a series of frames in the area detector. One advantage of an area detector rather than a smaller detector is that more reflections can be collected to determine the unit cell, therefore reducing the possibilities of an incorrectly indexed unit cell. Then the full

dataset of reflections is measured with the optimised parameters obtained from the determination of the unit cell and the orientation of the crystal. Once collected, the data can be analysed using different computer sofware packages such as SHELX which require h, k, l, Intensities and unit cell parameters as their primary input. The output is a list of possible atomic positions. The structure is then refined using additional software.

2.1.2. Powder X-ray Diffraction

Powder XRD is a widely available technique to obtain diffraction patterns and it is typically employed as a standard technique for the identification of crystalline materials. A finely divided polycrystalline sample is placed in the X-ray beam. As the powdered sample contains a large number of crystallites randomly arranged, there will be Bragg-type reflection angle from each set of planes. When the X-ray beam with known wavelength λ, is at an incident angle θ to the atomic planes that satisfy the Bragg equation, the reflected beam from the powdered sample will make an angle of 2θ with the incident beam. The detector is rotated varying 2θ during the measurement in order to collect all the reflections. The sample is frequently rotated to obtain more reliable statistics. The intensity of the reflected beam is then measured by the detector and recorded. Reflections from sets of planes of the powder interfere constructively when the Bragg condition is met and lead to the intensities measured at the detector. The set of *d*-spacings data can be obtained from the diffraction pattern based on the Bragg equation.

The XRD pattern of a powdered sample is measured with a stationary X-Ray source (usually Cu K_α) and a movable detector, which scans the intensity of the diffracted radiation as a function of the angle 2θ between the incoming and the diffracted beams. Cones of scattering occur so that effectively the diffraction information contained within a single crystal dataset is compressed into a single dimension, that of 2θ, the diffraction angle (figure 2.3).

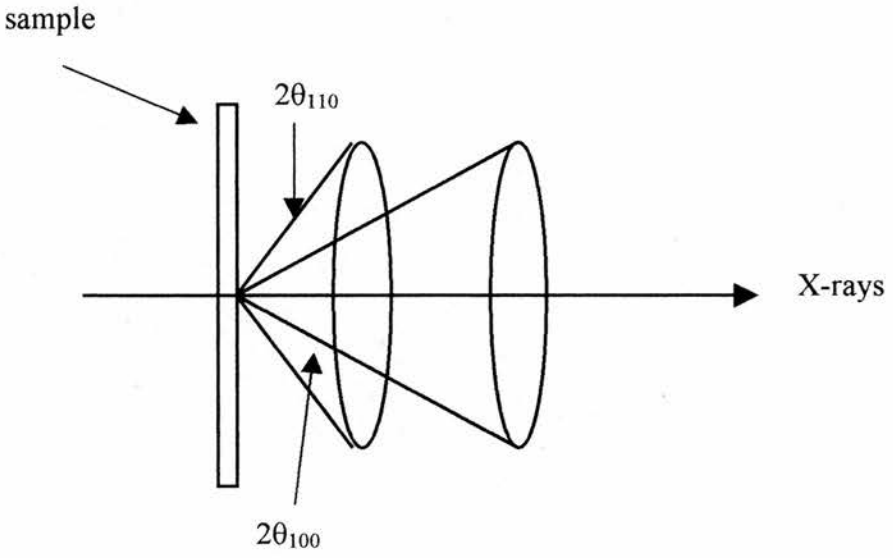

Figure 2.3 . Scattering X-rays into cones by a powder sample

Since in powder diffraction a polycrystalline sample is measured, each of the crystals forming the sample generates its own single-crystal diffraction pattern (each with its own orientation) and hence, the diffraction pattern is a superposition of all of them. As a result, reflections with similar *d* spacings overlap in space and only the sum of their intensities can be measured, obscuring some of the information contained in the pattern. As a result it is not routinely possible to obtain sufficient unambiguous reflection intensity data to enable structure solution from powder data, although this is possible in some cases[4].

2.1.3. The Rietveld Method[5,6,7]

Although structure solution is often difficult from powder diffraction data, it is possible to obtain important structural information by refining a structural model againts the diffraction data. In addition to determining the correctness of a structural model, details of unit cell size, atomic positions and therefore bond lengths can be derived.

One of the most powerful methods to refine a crystal structure from powder data is the Rietveld method. This is a structure refinement technique that fits a calculated powder diffraction profile to the whole experimental pattern. The calculated powder diffraction is based on a structural model and hence, a good starting structural model is required to obtain a good fit. The process of matching is performed by a least square method, minimising the sum $S = \sum w_i |y_{io} - y_{ic}|^2$ where y_{io}, y_{ic} are the observed and calculated intensities and w_i is a weighting factor at the ith step (w_i is normally taken as $1/y_{io}$).

The method permits the refinement of two sets of parameters: instrumental parameters such as the zero point, lattice parameters, background (which may be matched by a cosine series), profile parameters for the peak shape (usually simulated by a pseudovoigt function[8]), and structural or phase dependent parameters such as atomic parameters, fractional occupancies and thermal parameters. All these parameters should be allowed to vary to improve the fit to the experimental data.

A measure of the goodness of fit, i.e. the match between the calculated diffraction powder and the experimental one, is given by the agreement factors, the profile R_p and the weighted profile R_{wp} which are monitored during the course of the refinement. For R values under 0.1 (10%), the structure model is probably correct, although the visual "fit" is often the most informative guide.

$$R_p = \frac{\sum |y_{io} - y_{ic}|}{\sum y_{io}} \qquad \text{(R-profile)}$$

$$R_{wp} = \sqrt{\frac{\sum w_i (y_{io} - y_{ic})^2}{\sum w_i y_{io}^2}} \qquad \text{(weighted R-profile)}$$

The advantage of using the Rietveld method to refine a powder X-ray diffraction pattern is that it entails a whole-profile approach and the intensities of the observed and calculated patterns are compared on a point by point rather than

reflection by reflection basis, avoiding the problem of overlapping reflections, so common in powder X-ray diffraction.

2.2 X-RAY ABSORPTION SPECTROSCOPY[9,10]

The interaction between matter and electromagnetic radiation produces several physical phenomena depending on the wavelength of the radiation. Hence, the radiation can be transmitted, scattered or absorbed by matter. Extended X-ray absorption fine structure spectroscopy (EXAFS) concerns the details of how X-rays are absorbed by an atom at energies near and above the core-level binding energies of that atom.

A XAFS spectrum is the measurement of the energy dependence of the X-ray absorption coefficient (μ) at and above the absorption edge of a known atomic species. It is, therefore, an element specific technique. By analysing the oscillatory modulation in the absorption coefficient (μ) with energy, information about the local atomic and electronic structure of the absorbing atom can be obtained.

2.2.1. The origin of the EXAFS oscillations

X-rays produced on the energy regime of keV can be absorbed by matter through the photoelectric effect (figure 2.4). In this process an X-ray photon is absorbed by an electron in a deep core level (such as 1s or 2p) of an atom. When the photon energy *hv* is larger than the binding energy of a core level electron, one electron of this level can be emitted in the continuum.

At this point, there is sharp rise in absorption called the absorption edge that corresponds to the promotion of this core level to the continuum. This photoelectron propagates as a spherical wave and is scattered by the surrounding atoms. Some of this scattered photoelectron can return towards the absorbing atom where it interferes with the outgoing wave to set up a stationary electron wave. The result of this back scattering from the neighbouring atoms is to modulate the absorption coefficient of the absorbing atom. This modulation will depend on the energy of the absorbed X-rays and also on the local environment of the absorbing atom.

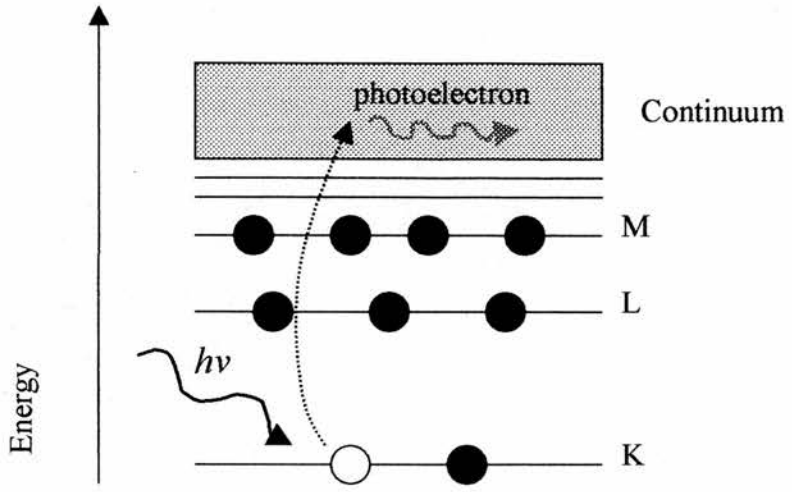

Figure 2.4. The photoelectric effect, in which an X-ray is absorbed and a core electron is promoted out of the atom.

A typical XAFS spectrum is shown in figure 2.5. There is a sharp rise of μ(E) corresponding to the absorption edge and the fine structure (the oscillations) in μ(E) produced as the energy increased. For comparative reasons, the XAFS spectrum of an isolated atom, for example a noble gas, is also shown. For the latter, the spectrum would contain a series of edges corresponding to the binding energies of all electrons present in the atom but no further oscillations with energy, since there is no backscattering present.

The spectrum is usually divided in two portions. The region near edge spectra XANES, till about 30 eV of the main absorption edge contains information about the valence and density of states of the absorber as well as qualitative structural information that is usually interpreted by simulation.The portion over 30 eV corresponds to the extended fine structure region EXAFS, the region that contains the oscillations.

The EXAFS fine structure function, χ(E) is defined as:

$$\chi(E) = \frac{\mu(E) - \mu_0(E)}{\mu_0(E)}$$

where $\mu(E)$ is the measured absorption coefficient, $\mu_0(E)$ is a background function representing the absorption of an isolated atom. This region contains information about the local atomic structure and is usually analysed by curve fitting as described later.

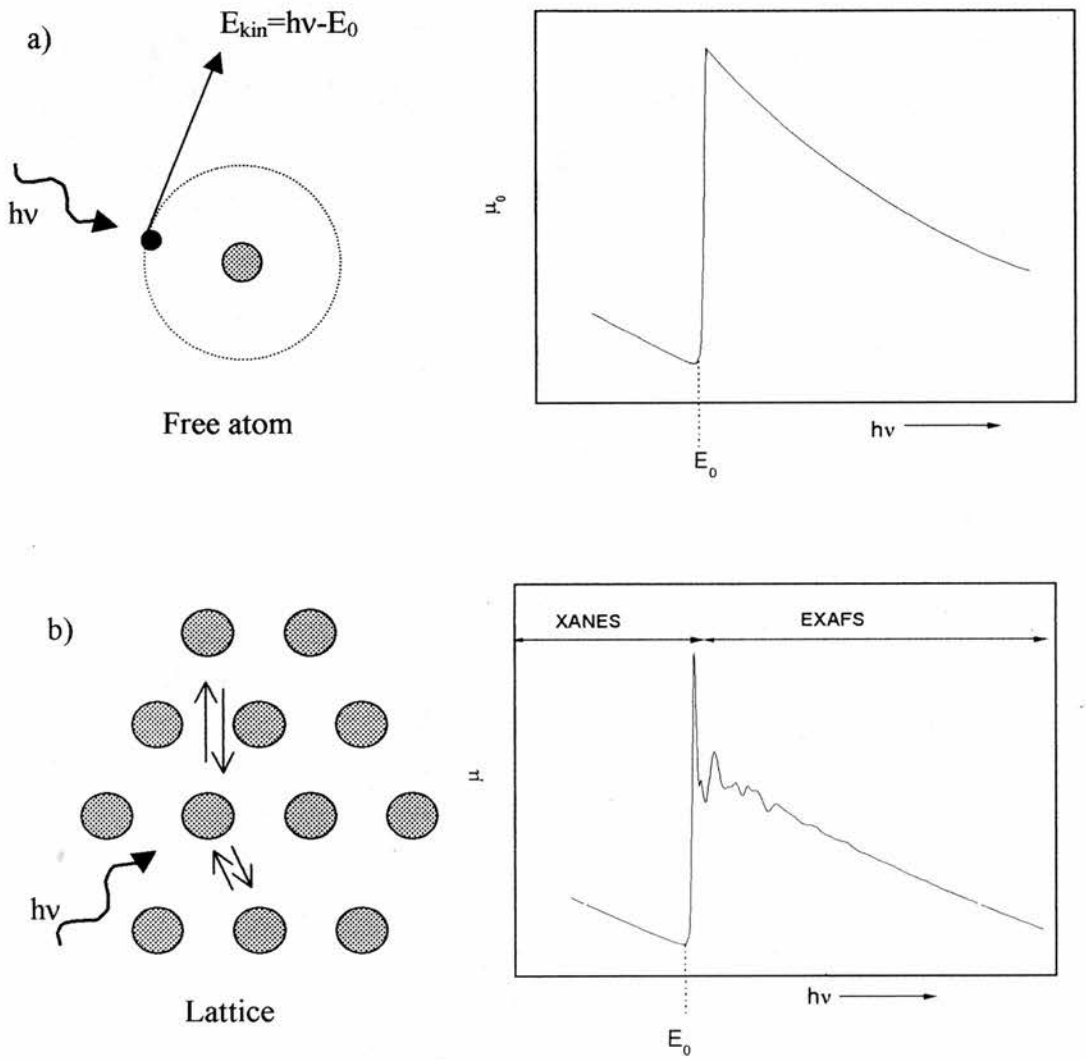

Figure 2.5. Absorption of X-rays as a function of photon energy, for an isolated atom, a) and for an atom in a lattice, b). The fine structure represents the EXAFS function.

2.2.2. Experimental set up

Most of the EXAFS measurements rely on the use of the X-ray radiation produced by synchrotrons. Synchrotron radiation has very interesting properties: is highly intense, highly polarised and highly tuneable with appropriate monochromating devices. This radiation is generated in a storage ring called synchrotron when electrons are accelerated to near the speed of light by a magnetic field. Beamlines are arranged at tangents around the storage ring to collect the radiation produced.

XAFS can be measured in transmission or fluorescence geometries although the use of transmission is more common for elements present at more than 1wt% or so. In a typical transmission experiment the intensity of the X-ray beam is measured before and after a sample and the absorbance μ is calculated using the expression:

$$\mu(E) = \log (I_0/I)$$

A scheme of the set up for the transmission experiment is given in figure 2.6. From the polychromatic X-rays produced in a synchrotron radiation source, a desired energy band (around the absorption edge energy of the element under study) is selected. These energies are well known and tabulated. The X-rays of a particular energy are selected by diffraction from a double crystal monochromator. Only those X-ray photons that are of the correct wavelength to satisfy the Bragg condition $n\lambda=2d\sin\theta$ at the selected angle θ will be reflected from the first crystal; the others are absorbed. The parallel second crystal is used as a mirror to restore the beam to its original direction. The monochromatic X-rays are then allowed to pass through the sample which should absorb approximately 50%-90% of the incident X-rays. The incident and transmitted X-ray fluxes are monitored usually with gas ionisation chambers.

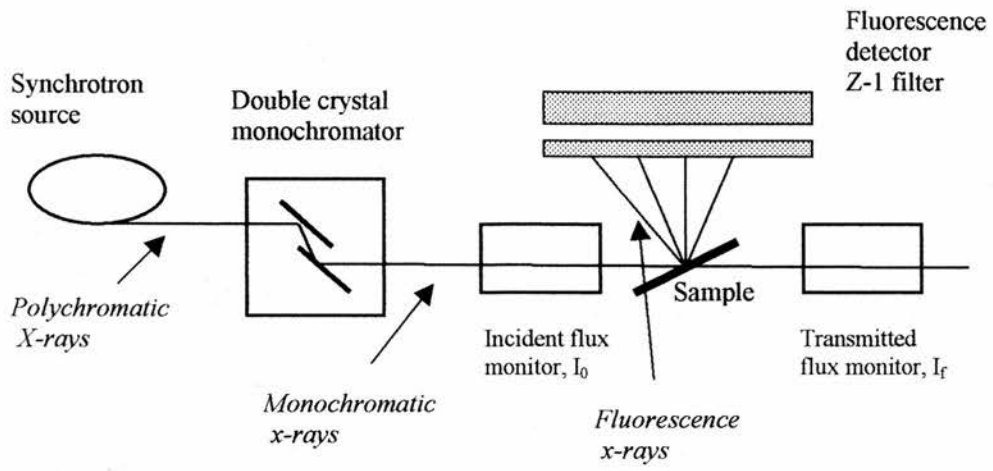

Figure 2.6. Schematic XAFS Transmission experiment.

In a fluorescence experiment the absorbance of the sample is measured by monitoring the intensity of the X-ray fluorescence produced when higher shell electrons drop into the hole left by the photoelectron. The absorption coefficient is given by

$$\mu(E) \propto I_f/I_0$$

where I_f is the monitored intensity of a fluorescence line associated with the absorption process.

2.2.3. Data modelling[11]

Analysis of the fine structure of the EXAFS region is performed by curve fitting. The EXAFS region can be described as a function, $\chi(k)$ expressed in terms of the wave behaviour of the photoelectron created in the absorption process. Hence, $\chi(k)$ is a function of the wave number (k) of the emitted photoelectron defined as:

$$k = \frac{2\pi}{h}\sqrt{2m_e E_k} = \frac{2\pi}{h}\sqrt{2m_e(h\nu - E_0)}$$

where m_e is the mass of an electron, E_k is the kinetic energy of the photoelectron, ν is the X-ray frequency and E_0 is the binding energy of the photoemitted electron.

The EXAFS function is the sum of the scattering contributions of all atoms in neighbouring coordination shells:

$$\chi(k) = \sum_j A_j(k) \sin(2kr_j + \phi_j(k))$$

in which j is the coordination shell around the electron emitting atom, $A_j(k)$ is the amplitude, the scattered intensity due to the *jth* coordination shell, r_j is the distance between the central atom and atoms in the *jth* coordination shell, $\phi(k)$ is the total phase shift, equal to the phase shift of the backscattering. The EXAFS function, $\chi(k)$, is an oscillatory function where the oscillations correspond to different near neighbouring coordination shells that can be described and modelled according to the above equation. The argument of each sine contribution depends on k (the wavenumber) which is known; r, which is to be determined and the phaseshift $\phi(k)$. This phase shift is a characteristic property of the scattering atom in a certain environment and is usually derived from the EXAFS spectrum of a reference compound or calculated from available data. The amplitude $A_j(k)$ of each scattering contribution contains the number of neighbours in a coordination shell and is given by the following expression:

$$A_j(k) = N_j \frac{e^{-2r_j/\lambda(k)}}{kr_j^2} S_0^2(k) F_j(k) e^{-2k^2\sigma_j^2}$$

In the above expression for the amplitude of the EXAFS function, N_j is the number of neighbours in the *jth* coordination shell; the second term expresses that scattering contributions to the EXAFS signal are dominated by nearest neighbours, while contributions from distant shells are weak. The dependence of this term on $1/r^2$ reflects that the outgoing electron is a spherical wave which intensity decreases with the distance squared; The $S_0^2(k)$ term is a correction for relaxation effects in

the emitting atom and is related to the fact that not all absorbed X-ray photon quanta of energy $h\nu$ are converted to photoelectrons of kinetic energy $h\nu$-E_0 (E_0 being the binding energy of the photoemitted electron) but to electrons with lower kinetic energy as well. $F_j(k)$ represents the scattering performance of neighbouring atoms in the *jth* shell. The dependence of this backscattering factor on energy is characteristic for an element. Finally, the term $\exp(-2k^2\sigma^2)$ represents the static disorder on the solid arising from atoms in the same coordination shell that have slightly different distances to the central atom.

The Fourier transform of the EXAFS function, $\theta_n(r)$, is a radial distribution function given by the expression:

$$\theta_n(r) = \frac{1}{\sqrt{2\pi}} \int_{k_{min}}^{k_{max}} k^n \chi(k) e^{2ikr} dk$$

where n is an integer usually chosen as 1,2 or 3. A series of peaks, each of one corresponding to a shell of neighbours around the absorber at a distance r are obtained. Hence, the function $\theta_n(r)$ represents the probability to find an atom at a distance r. Since the amplitude of the EXAFS function $\chi(k)$ decreases with the distance, the intensity of the Fourier Transform also decays for distant shells. Hence, the Transform or the EXAFS function has to be weighted with either k or k^3 to emphasize the oscillations. In principle, the Fourier Transform becomes more accurate when the k-interval is larger but, in practice, the signal noise ratio of the spectrum sets the limit for k.

The straightforward Fourier Transform of the EXAFS signal does not yield the true radial distribution function. Some corrections have to be made from reference samples or from theoretical calculations.

2.2.4. Analysis of the EXAFS data

Analysis of the EXAFS spectrum involves several steps that can be summarised as follows:

1. Convert measured intensities to $\mu(E)$, correcting measurement errors.
2. Pre-edge subtraction and normalisation: a smooth pre-edge function (or simple polynomial) is fitted to the spectrum, $\mu(E)$, below the edge to remove any instrumental background and absorption from others edges. The jump in the edge is approximated and the spectrum is normalised by this value.
3. Identify the threshold energy E_0, typically as the energy of the maximum derivative of $\mu(E)$.
4. Remove a smooth post-edge background function to approximate $\mu_0(E)$, where $\mu_0(E)$ represents the absorption of one isolated atom without neighbours and hence, no backscattering.
5. Evaluate the XAFS $\chi(k)$ from measured data to obtain the oscillations, k-weight this function and Fourier Transform into r-space.
6. Data modelling is performed simulating of the signal of each shell using the formula for $\chi(k)$ and the atomic parameters and phases calculated or extracted from a model system. These structural parameters are typically shell distances (r), occupancy numbers for each shell (N) and Debye-Waller factors (σ) that take into account the disorder on each shell. The expected precision is ± 0.02Å for the distances and between 10 and 20% for the number of neighbours. The fitting has to be carefully done due to correlation between the different parameters.

This procedure of analysis and fitting is performed with computational aid. The EXAFS shown in this work have been treated with the software available at the Synchrotron Radiation Source at Daresbury Laboratory[12]. The EXCALIB program to obtained the $\mu(E)$ vs energy plot (step 1), EXPLINE[13] and EXBROOK programs for doing the background substraction and obtaining the Fourier Transform of the EXAFS signal (steps from 2 to 5). Curve fitting (step 6) was performed with EXCURV98[14] program.

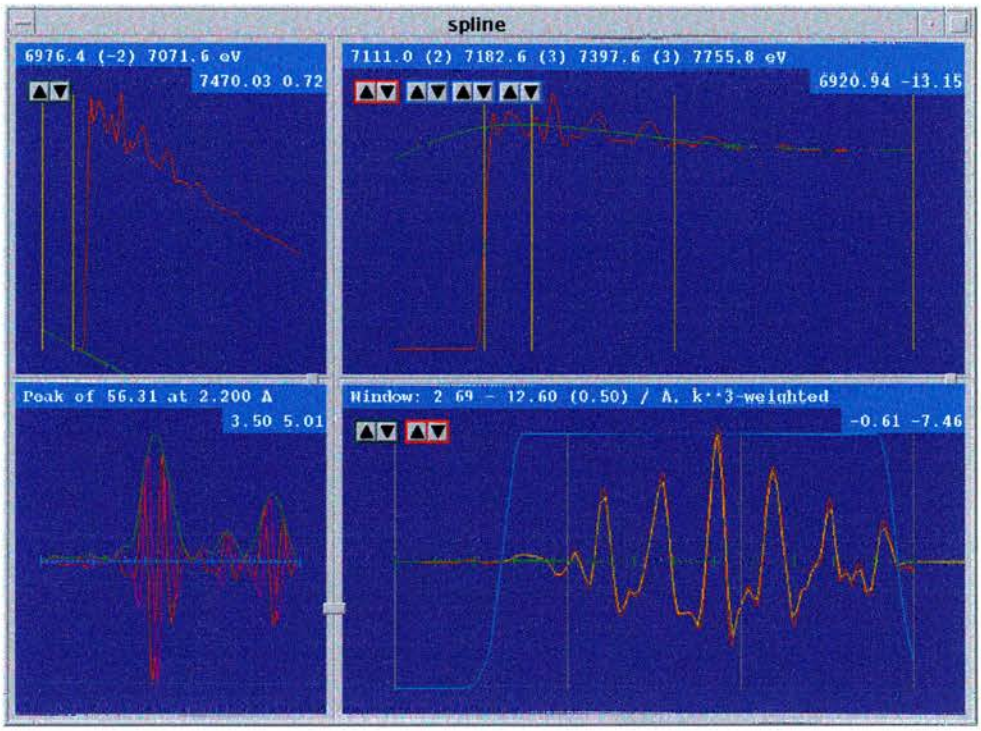

Figure 2.7. Typical window from the Exspline program showing the pre-edge subtraction window (top left), the post-edge subtraction window (top right), the k^3-weighted and normalised EXAFS experimental curve after substracting the pre-edge and post-edge part of the spectrum (bottom right) and the Fourier Transform of the EXAFS function obtained (bottom left).

2.3 OTHER TECHNIQUES

In addition to the techniques described above, several other techniques have been employed to characterise the materials obtained in this work. A brief description of the fundamental of these techniques is given in the following pages.

2.3.1. Solid State NMR[2]

A nucleus with spin quantum number I may take 2I+1 different orientations, relative to an arbitrary axis, which are distinguish by a quantum number m_i. In the absence of an external magnetic field, these orientations are degenerate but in the presence of a magnetic field the 2I+1 orientations have different energies. The NMR spectrum is produced by transitions between these levels caused by a radiation of frequency ν, and associated energy $E=h\nu$, which match the energy gap of the levels. Only those nucleus with a spin quantum moment different than zero will be active in NMR. The transition frequency ν is called 'resonance frequency' and is affected by the chemical environment of the atom. Therefore this technique is employed for the characterisation of the local environment surrounding the atom.

In solid state chemistry, magic angle spinning nuclear magnetic resonance (MAS-NMR) is employed to obtain high-resolution spectra. The fundamental of this technique is that most of the terms producing broad lines in the NMR spectra of a solid involve geometric factors of the type $(3\cos^2\theta-1)$. The last expression is zero when θ is 54° 44' (the 'magic angle'), θ being the angle formed between the magnetic field and the sample spinning axis.

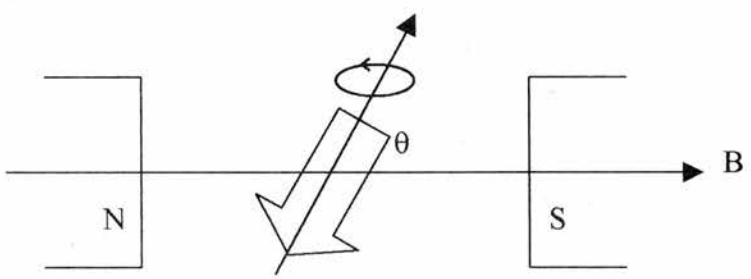

Figure 2.8. Schematic representation of the experimental arrangement for sample spinning in a MAS NMR experiment. The sample is spun around an axis at a θ angle of 54.44° to the applied magnetic field, B.

The technique allows well-resolved high-resolution spectra to be obtained with a chemical shift characteristic for the local environment of the framework element under study. The shifts are always referred to an external sample that takes the zero value. For silicon shifts (see table 2.1), tetramethylsilane (TMS) is currently chosen as reference. Generally, these are noted as Si (nAl, (4-n) Si), indicating that each silicon atom is linked, via oxygen bridges, to *n* aluminium and *4-n* silicon neighbours. Similar shifts are found in SAPO's, as silicon is surrounding by aluminium and in aluminosilicate islands.

Si environment	**Chemical shift(ppm)**
Si(4Al)	-83 to -87
Si(3Al 1Si)	-88 to -94
Si(2Al 2Si)	-93 to - 99
Si(1Al 3Si)	-97 to -107
Si(4Si)	-103 to -114

Table 2.1. Chemical shift ranges vs. TMS for 4-coordinated Si environments

The ^{31}P NMR MAS spectra of the aluminophosphates exhibit chemical shifts ranging from -19 to -30 ppm (relative to external H_3PO_4), which is the range typically observed for tetrahedral phosphorus oxide (PO_4). However, the ^{31}P signal is sensitive to the structural and the chemical environment and substitution of other elements into the AlPO lattice has a pronounced effect on the chemical shifts. Some authors[15] follow the procedure of Barrie and Klinowski[16] in assigning the signals in ^{31}P spectra of some MAPO's. In this approach, the substitution of Al in the AlPO lattice is assumed to increase the chemical shift of an adjacent P, and this effect will increase with the number of adjacent Al atoms substituted. The most negative chemical shift is thus attributed to P (4Al), the next to P (3Al, 1Me) and so on.

The aluminium chemical shifts in the ^{27}Al NMR spectrum depends primarily on the coordination of aluminium with respect to oxygen. In aluminophosphates, the chemical shifts for tetrahedral aluminium are found between 30-50 ppm while octahedral aluminium appears at 0 to 22 ppm[17].

Solid state ^{13}C NMR gives information about the molecule that has acted as a template. It is commonly used to confirm that the template remains intact within the structure[18].

2.3.2. Scanning Electron Microscopy (SEM) and Energy dispersive X-ray Analysis (EDX)

Throughout this work, SEM and EDX have been extensively employed to identify the morphology of the crystalline materials prepared as well as for the determination of their composition. In the scanning electron technique, a fine beam of electrons is scanned over the surface of the sample using a system of deflection coils. The various signals produced by the interaction of the electron with the surface, such as secondary electrons, back-scattered electrons, or emitted X-rays can be used to form an image. The spectrum of emitted X-rays is characteristic of the elements present as the vacancies in core electron levels are filled from higher levels, emitting x-rays of characteristic energy. Measuring the energy of the characteristic X-ray radiation with special detectors a selected area analysis can be performed (EDX). This technique is known as energy dispersive X-ray analysis.

2.3.3. Thermal Analysis[19]

Thermal analysis describes a group of methods whereby the dependence of the parameters of any physical property of a substance on temperature is measured.

The two techniques measuring the change of heat and the change of weight are the methods used preferably for the characterisation of zeolite-like material properties of microporous solids.

These methods are called differential thermal analysis (DTA) and thermogravimetric analysis (TGA). In both methods, the sample and possibly a reference sample are heated or cooled at a controlled rate temperature. In the TGA analysis, the change in weight of the sample is recorded as a function of the temperature.

In the DTA technique, the difference in temperature between a substance and a reference material against either time or temperature is recorded. If any exothermic or heat endothermic process takes place in the sample, the temperature of the sample increases or remains behind the temperature of the reference. When the process is finished, the temperatures of both specimens become equal again.

2.3.4. UV-Visible Diffuse Reflectance[20]

This technique has been used in order to give an insight to the metal coordination in the solids.

UV-Visible spectroscopy provides information about transitions between the electronic energy levels of the metal. These levels will be different depending on the coordination geometry of the metal. There are two types of transitions for a d-metal complex:

- d-d transitions: which are transitions between the metal d-orbital levels. They are usually very low intensity because they are 'forbidden' by Laporte's rule.
- Charge-transfer transitions: correspond to electronic transitions between the ligand orbital to the d-orbital of the metal, or vice versa. They are usually observed at higher energy (lower wavelength) and with higher intensity than the d-d transitions.

2.3.5. Magnetic Susceptibility

A magnetic field (H) can induce a magnetic moment in a substance that is called Magnetization (M) and is given by the expression:

$$M=\chi H$$

Where χ is the magnetic susceptibility of the substance.

The magnetic flux density (B) is related to the applied field strength and the magnetization by

$$B=\mu_0 (H+M)= \mu_0 (1+\chi)H$$

Where is the vacuum permeability: $\mu_0= 4\pi x10^{-7}JC^{-2}m^{-1}s^2$

The magnetic flux density is increased if M adds to H and this happen when the substance is paramagnetic ($\chi> 0$), but the density is decreased if M opposes H (when $\chi< 0$) as is the case with diamagnetic substances. This because if the substance is paramagnetic, the unpaired electrons will add their induced field to the external one, while if the substance is diamagnetic the electron pairs will be repelled by the external field and they will subtract their own field to the external one.

2.3.6. Electron Spin Resonance Spectroscopy[21]

This technique is used in the investigation of transition metal complexes and specially, to study transition metals in zeolites. For example, Kevan has extensively studied the incorporation of transition metal in framework and extraframework positions by this technique[22]. The requirement is that the species to be observed possesses unpaired electrons. Examples include organic radicals and transition metal cations such as Cu^{2+}, Ni^{+}, etc.

The g-tensor and the hyperfine coupling tensor mainly determine the shape of an electron spin resonance spectrum (ESR). The g-tensor measures the deviation of the g value from the g_e value of the free electron caused by a spin-orbit coupling which is dependent on the direction of the crystal. The hyperfine splitting is caused by an interaction with the nuclear spins in the neighbourhood of the electronic spin. In the usual practice, the parameters of the g tensor and the hyperfine splitting are taken approximately from the measured spectrum and then a computer fit is made to find the exact values, and to decide whether additional interactions have to be taken into account. Generally from the symmetry of the g-tensor conclusions on the symmetry of the crystal field at the site of the cation or of the sorption complex can be drawn, which can be refined by the use of the data from the hyperfine interaction.

2.3.7. Elemental Analysis

Microanalysis has been used in order to know the organic moiety of the materials synthesised in this work. The technique can measure the relative percentages of carbon, nitrogen and hydrogen atoms in a sample. In zeolitic materials it can provide information about the integrity of the organic occluded within the structure.

2.4. REFERENCES

1. W. Clegg, *Crystal structure determination*, Oxford Chemistry Primers, Oxford University Press, 1998

2 A. K. Cheetham, P. Day, *Solid State Chemistry Techniques*, Oxford University Press, 1987

3. C. Giacovazzo, *Fundamentals of Crystallography*, OUP, Oxford, 1992.

4. L. B. McCusker, C. Baerlocher, R. Grosse-Kunstleve, S. Brenner, T. Wessels, *Chimia*, 2001, **55**, 497

5. R. A.Young, *The Rietveld Method*, ed. R.A. Young, Oxford University Press, Oxford, 1-38

6. L. B. McCusker, R. B. Von Dreele, D. E. Cox, D. Louër, P. Scardi, *J.Appl.Cryst.*, 1999, **32**, 36.

7. N. Masciocchi, *The Rigaku Journal*, 1997, **14**, 9.

8. a) C. J. Howard, *J.Appl. Cryst.*, 1982, **15**, 615; b) P. T. Thompson, D. E. Cox, J. B. Hastings, *J.Appl. Cryst.*, 1987, **20**, 79

9. M. Gautier-Soyer, *J.Europ.Ceram., Soc.*, 1998, **18**, 2253

10. M. Newville, *Fundamentals of XAFS*, Consortium for advanced Radiation Sources, University of Chicago. available at http://cars9.uchicago.edu/xafs/xas_fun/

11. J. W. Niemantsverdriet, *spectroscopy in Catalysis*, VCH Publishers, 1993

12. http://srs.dl.ac.uk/xrs/index.html

13. M. Newville, P. Livins, Y. Yacoby, E. A. Stern, J. J. Rehr, *Phys. Rev.*, 1993, **47**, 14126

14. N. Binsted, EXCURV98: CCLRC Daresbury Laboratory computer program, 1998

15. D. B. Akolekar and R. F. Howe, *J.Chem. Soc., Faraday Trans.*, 1997, **93**(17), 3263.

16. P. J. Barrie, J. Klinowski, *J. Phys. Chem.*, 1989, **93**, 5972

17. G. Engelhardt, D. Mitchel, *High-Resolution Solid-State NMR of Silicates and Zeolites*, Wiley, New York, 1987

18. M. Kovalakova, B. H. Wouters, P. J. Grobert, 1999, *12th International Zeolite Conference*, Materials Research Society, p.p. 2325.

19. A. R. West, *Basic Solid State Chemistry*, John Wiley & Sons, 1991.

20. P. W. Atkins, *The Elements of Physical Chemistry*, Oxford University Press, 1992.

21. J. E. Harriman, *Theoretical Foundations of Electron Spin Resonance*, Academic Press, London, 1978

22. M. Hartmann, L. Kevan, *Chem. Reviews*, 1999, **99**, 635

3. METALLATED AZAMACROCYCLES AS STRUCTURE DIRECTING AGENTS FOR THE SYNTHESIS OF ALUMINOPHOSPHATE-BASED MOLECULAR SIEVES

3.1 INTRODUCTION

The effect of the addition of nickel to the preparations of STA-6 and STA-7, prepared in the presence of the macrocycle tetramethylcyclam is reported in this chapter. The preparation of these materials in the presence of a reduced amount of macrocycle and additional bases or with cyclam instead of tetramethylcyclam was also explored, and the work was extended to investigate the incorporation of other metals using their azamacrocycle complexes as structure directing agents.

3.1.1. Introduction to macrocyclic ligands[1,2,3]

Macrocyclic molecules make up a special class of polydentate ligands. Molecules that contain several donor atoms can coordinate a metal cation or several metal cations to form metal complexes. Such ligands are called chelating agents. They can be open as in a linear polyamine or closed as in the case of a macrocycle. The "chelate effect" describes the observation that complexes with multidentate ligands are more stable than those with an equivalent number of monodentate ligands.

The differences in the complex formation constants between a multidentate ligand and an equivalent complex with monodentate ligands are shown for a simple example in Scheme 3.1. This enhancement of the complexation constant is generally observed.

(1) $[Ni(H_2O)_6]^{2+} + 6\ NH_3 \leftrightarrow [Ni(NH_3)_6]^{2+} + 6\ H_2O$ log K=8.61

(2) $[Ni(H_2O)_6]^{2+} + 3\ en \leftrightarrow [Ni(en)_3]^{2+} + 6\ H_2O$ log K=18.28

Scheme 3.1. Difference in the equilibrium constants between chelating agents and an equivalent complex with monodentate agent. "en" refers to the ethylenediamine ligand, $H_2NCH_2CH_2NH_2$.

The thermodynamic basis for the chelate effect may be considered in a simplified manner[4]. The complexation constant, K, is related to the standard energy of formation of the complex, ΔG^0,

$$\ln K = -\frac{\Delta G^0}{RT} \quad (1)$$

ΔG^0 is a function of the standard enthalpy of formation of the complex, ΔH^0, and the standard entropy of formation of the complex, ΔS^0, by

$$\Delta G^0 = \Delta H^0 - T\Delta S^0$$

The constant of complex formation (K) increases as ΔG^0 becomes more negative. This can result from a more negative ΔH^0 (enthalpic effect) or a more positive ΔS^0 (entropic effect).

The enthalpic factor is usually small and is related to the energy needed to form the complex. When two monodentate ligands occupy adjacent positions within a complex there are electrostatic repulsions between them and so, there is an initial energetic barrier to this process. In a chelate ligand this barrier is smaller since the two centres are bonded together, making this process more favourable.

The entropic factor has two main contributions. One is related to the different entropy changes associated with complex formation between a complex with monodentate ligands and a similar complex with multidentate ligands. When considering the equilibria in scheme 3.1, the number of molecules on both sides of the equation (1) is seven. For the reactants: 1 nickel aquo-complex and 6 molecules

of ammonia, and for the products: 1 hexaamine complex and six water molecules. However, in equilibrium 2, there are four reactant molecules (1 hexaaquocomplex and 3 molecules of ligand) and seven molecules of products. The increase of the number of molecules randomly distributed in solution in equilibrium (2) for the multidentate ligand represents a more positive entropy change compared to that of equilibrium (1), with a monodentate ligand.

A second contribution to the entropy appears when considering the concentration of the second donor atom in the proximity of the metal cation. The concentration will be higher for the polydentate ligand since the monodentate ligand will be randomly distributed in solution and with a lower probability to bind the metal centre. In other words, the concentration of the second Lewis base on the vicinity of the metallic cation is effectively higher when the second donor atom is attached to the first one by a relatively short carbon chain.

The entropic factor is the more important thermodynamic feature in producing the chelate effect.

Macrocycles are a special class of polydentate ligand. They possess three or more donor atoms and can complex a central cation forming a closed ring. They are usually classified depending on the donor atom; when this atom is nitrogen, they are called azamacrocycles.

Macrocycle complexes are usually more stable than the complexes with related non-cyclic polydentate ligands. This additional stability is called the "macrocyclic effect" and is mainly due to the enthalpic factor. The entropic contribution is smaller since there are the same number of particles before and after the complex formation in both cases, the extra carbon bridge in the macrocycle being the only difference.

Initial approaches to explain the macrocyclic effect were based on the good fit between the macrocyclic cavity and the size of central cation. However, the metal cation is not always situated in the middle of the cavity and the macrocycle can adopt a non-planar configuration to complex it. In general, everything reducing the flexibility of the macrocycle is observed to increase its selectivity and stability with respect to the corresponding cations.

A further consideration on the macrocyclic effect is based on the following factors:

1. The high degree of pre-organisation of the ligand, which is related to the favoured spatial conformation of the macrocycle ligand to co-ordinate the central cation compared to that of the open chain analogue. A good example of the lack of pre-organisation of the open chain ligand is given in figure 3.1. In the free ligand, the piperidine side ring would be in the chair form while it is in the boat form in the macrocycle. So, the open chain ligand would require some extra energy to convert to the boat form in metal complex formation. This explains the difference in the stability constants for these two ligands with copper[5].

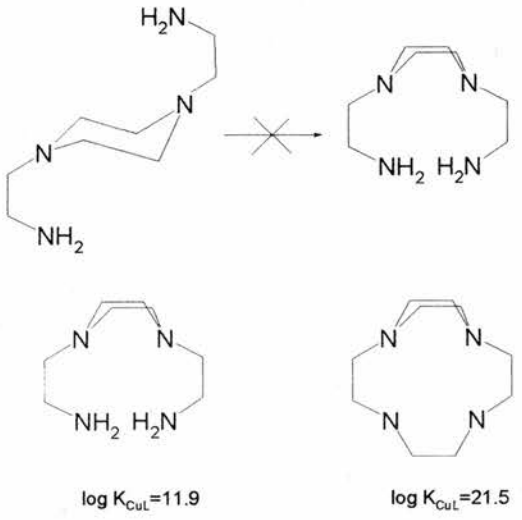

Figure 3.1. Example of pre-organisation of two similar ligands.

2. *Increase on the basicity of the macrocycles* compared to their open chain analogs, due to the inductive electron released by the additional methylene groups that link the donor atoms. Notably, additional basicity is not achieved by alkylation of the donor atoms, as seen by comparing stability constants of tetramethylcyclam with those for cyclam (table 3.1). This is due to the steric repulsions between the methyl groups and the carbon atoms of the macrocycle.

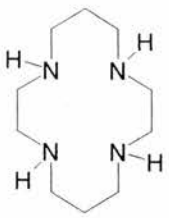

Cyclam

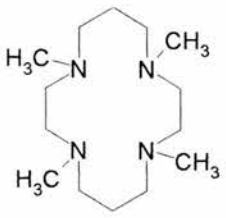

TMC

	Cyclam	TMC	Δ log K	Ionic radius (Å)
log K_1[Cu(II)]	27.2	18.3	8.9	0.65
log K_1[Ni(II)]	22.2	8.6	13.6	0.69
log K_1[Co(II)]	12.7	7.6	5.1	0.72
log K_1[Zn(II)]	15.5	10.4	5.1	0.74
log K_1[Cd(II)]	11.7	9.0	2.7	0.97
log K_1[Pb(II)]	11.3	(~7.5)	(~3.8)	1.21

Table 3.1. N-alkylation decreases the stability constants for cyclam complexes.

3. Finally, the *repulsion between the electron pairs* of the donor atoms in the macrocycle is reduced upon complexation with a metal centre.

3.1.2. Macrocycles as structure directing agents

Macrocycles are therefore expected to have very interesting behaviour in the synthesis of microporous materials due to their complexing properties, since they ensure the solubilization of metal cations. They also offer tremendous potential as structure directing agents since their unique size and shape can lead to new framework materials. Some of the macrocycles that have been employed in zeolite syntheses are shown in figure 3.2

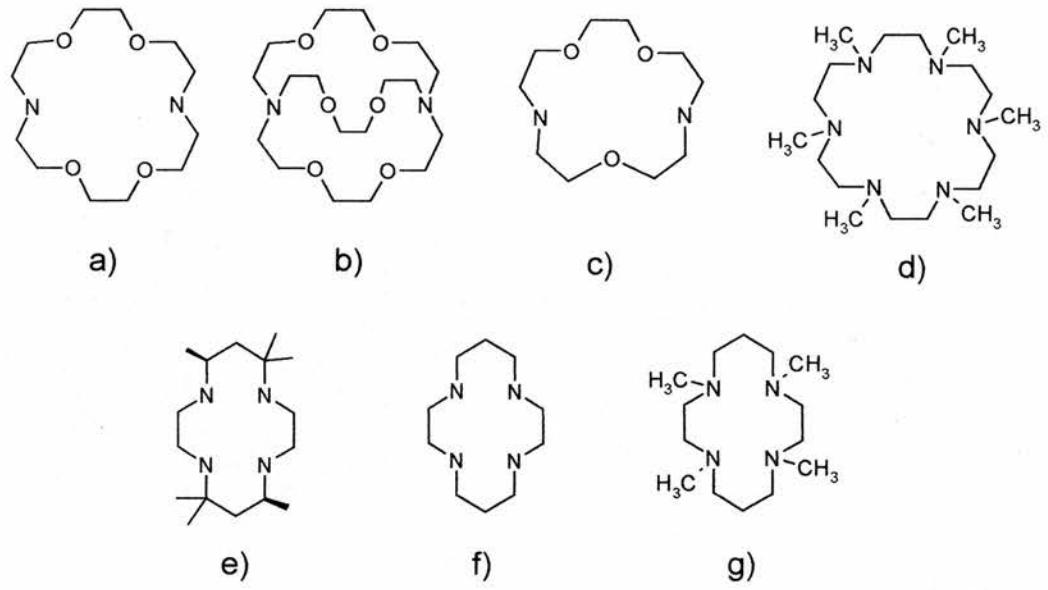

Figure 3.2. Macrocycles that have been employed as structure directing agents in the synthesis of microporous materials: Kryptofix22 a), Kryptofix222 b), Kryptofix21 c), 1,4,7,10,13,16-hexamethyl-1,4,7,10,13,16-hexaazacyclooctadecane (hmhaco) d), meso-5,77,12,14,14-hexamethyl-1,4,8,11-tetraazacyclotetradecane (Tet-A) e), 1,4,8,11-tetraazacyclotetradecane (cyclam) f), 1,4,8,11-tetramethyl-1,4,8,11-tetraazacyclotetradecane (TMC) g).

Azacrown ethers like kryptofix21, kryptofix 22 and kryptofix 222, lead to the formation of several AlPO structures. In fluoroaluminophosphate preparations, the larger K222 acts to template the LTA structure type, being occluded in the larger cage of the structure[6]. In the same preparations, the two other smaller K22 and K21 led, respectively, to a new microporous $AlPO_4$ named Mu-13[7] or did not promote any crystallisation. When the azacrown K222 was employed in metal-substituted aluminophosphate preparations[8], it directed the formation of MAPO-42 (M=Mg, Mn, Fe, Co) together with MAPO-5. When the metal employed in the synthesis was Zn, MAPO-42 was obtained as a pure phase. The refinement of the structure shows the template to be disordered within the α-cages of the structure. No zinc resides within the cryptand in the structure but is rather found to substitute for Al in framework cation sites.

The tetraazamacrocycle cyclam has also been explored as a structure directing agent in the synthesis of aluminophosphate-based materials. A family of such materials has been prepared, the members of which consist of inorganic layers or chains linked together by the octahedral complex formed by the metallated-macrocycle and two apical oxygen atoms of the aluminophosphate. For instance when employed in the synthesis of gallium phosphates[9], cyclam produces an structure that consists of layers of double four rings of gallium and phosphorus tetrahedra connected in such a way that ten member-ring "windows" are formed. The layers are linked together through the six-coordinated complex formed between gallium, cyclam and two of the oxygen atoms from the phosphorus tetrahedra of the double four member-rings units in adjacent layers (figure 3.3). It has also been possible to substitute the gallium in the macrocycle by other metals, such as copper and manganese, during the synthesis of this material[10].

In metalloaluminophosphate syntheses, in particular in the presence of nickel and cobalt cations, cyclam also templates materials in which the cations are bound within the macrocycle and the nitrogens are hydrogen-bonded to phosphate oxygens of aluminophosphate chains[8]. The closely similar macrocycle, Tet-A, has also been shown[11] to direct the synthesis of two new layered aluminophosphate materials in fluoride medium. One of these materials consists of layers of phosphate and aluminate tetrahedra with the macrocycle between these layers, hydrogen-bonded to the oxygens in the framework and also to the fluoride in the framework. The second phase consists of chains of double four member-rings of PO_4 and AlO_4 tetrahedra linked together by the complex formed between the macrocycle and the cobalt in a similar way to the solids described above. However in this structure, the uncoordinated template is also found to reside in the space between the layers.

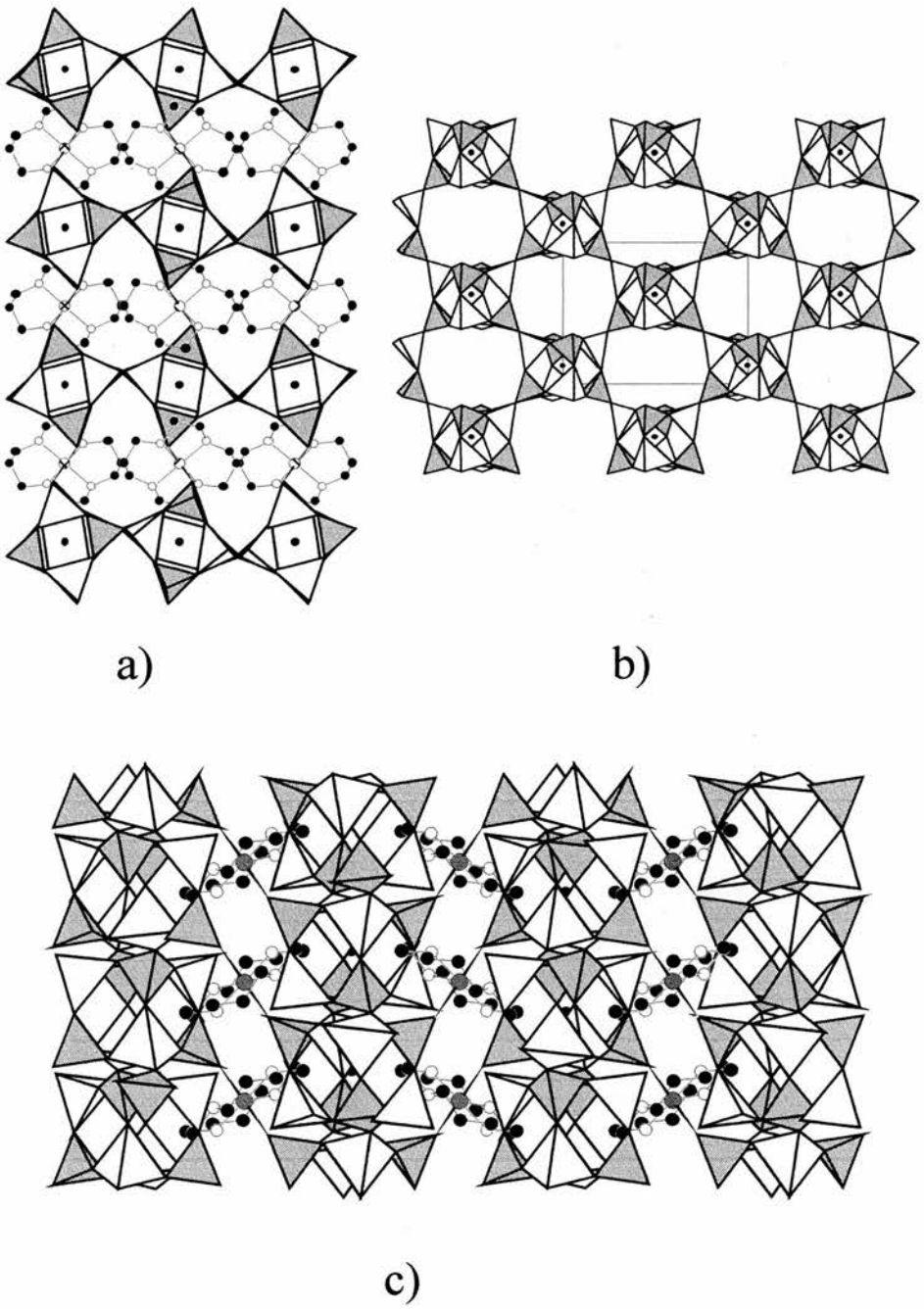

Figure 3.3 . Structure of Cyclam-GaPO. a) Looking down the b axis; b) Stacking of the D4R units along the c axis showing the fluorine atom in the middle of the cage; c) the structure down the a axis. The D4R units are linked through the Ga-cyclam complex.(Key:GaO_4 tetrahedra, grey; PO_4 tetrahedra, white; Ga, white hatched; N, white; C, black; F, black smaller).

In contrast to these layered phases, all of which lose their crystalline structure upon removal of the organic species, the methylated versions of cyclam, 1,4,8,11-tetramethyl-1,4,8,11-tetraazacyclotetradecane (tmtact) and of hexacyclen, 1,4,7,10,13,16-hexamethyl-1,4,7,10,13,16-hexaazacyclooctadecane (hmhaco) have been found to direct the synthesis of the novel divalent metal-substituted framework structures STA-6 and STA-7[12]. Both STA-6 and STA-7 are small pore materials whose frameworks might be considered as made up by the stacking of cavities along the *c* crystallographic axis of the structure.

STA-6 (SAS structure type) is constructed from chains of face-sharing double 6-rings where each one is rotated 90° in relation to the previous one with respect to the direction of the chain (Figure 3.3.1.b). Each chain is linked to four others through Al-O-P bonds which results in the formation of cages as the one shown in figure 3.3.1.c. The cages are connected in the *c* direction through 8-member ring openings but in the *a-b* plane through 6-member ring openings resulting, therefore, in the formation of a monodimensional channel system parallel to the *c* axis.

The framework of STA-7 (SAV structure type) possesses two three-dimensional channel systems A and B accessible through 8-ring openings. The A channels are composed of big cages (figure 3.3.2.b) stacked along the *c*-axis through planar 8-rings. The cages also possess four elliptical 8-ring openings to the B channel system that is made up of smaller interconnecting spaces as the one shown in figure 3.3.2 c. The structure can also be described as constructed from chains of double 6-rings linked along the *c* axis by 4-rings and to each other by Al-O-P bonds (figure 3.3.2.d).

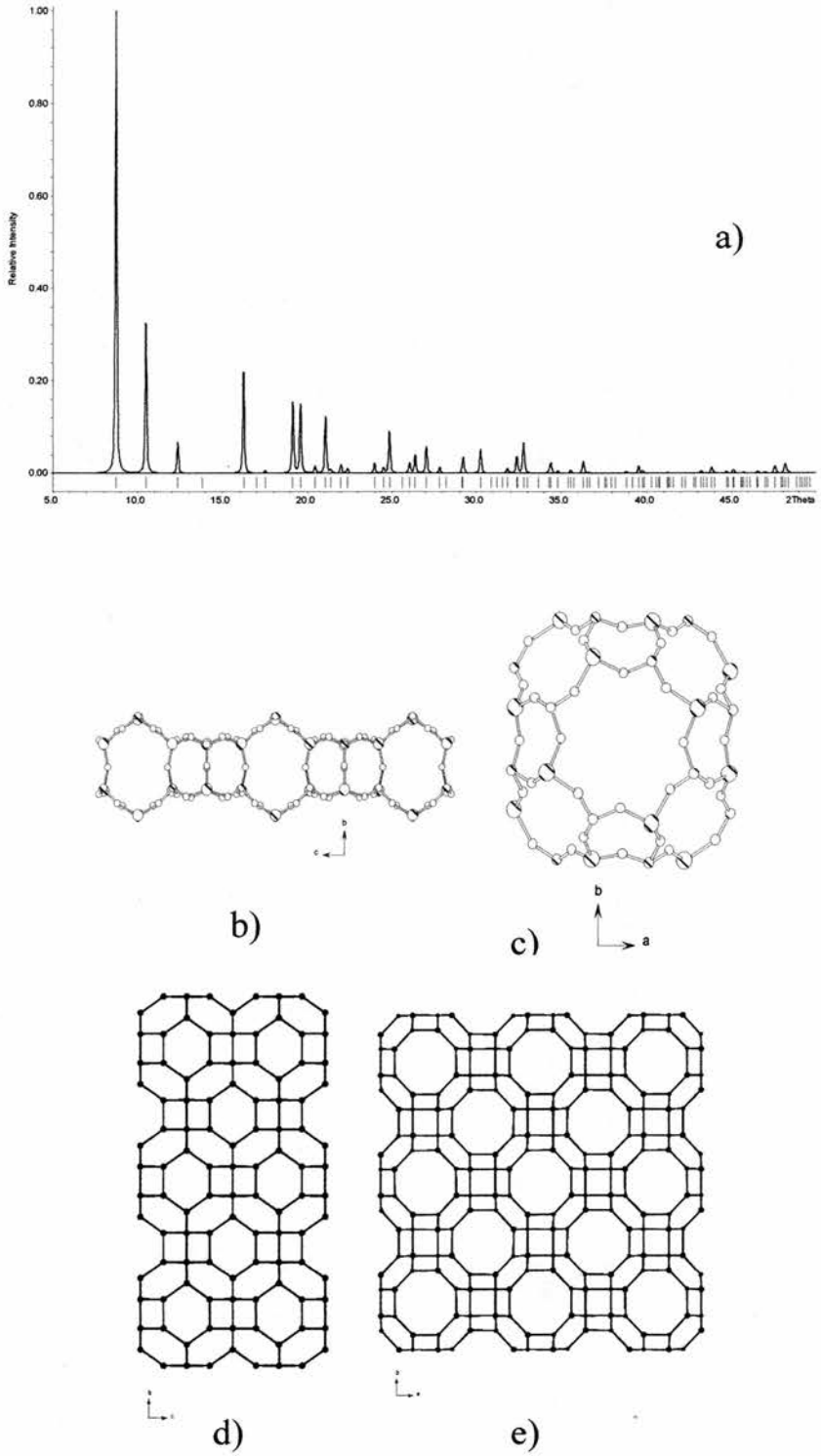

Figure 33.1. a) Simulated XRD powder pattern for STA-6 (SAS structure type); b) The chains of double 6-rings that run parallel to the c direction; c) Cavity found in the STA-6 structure; d) Projection of the structure down the a-axis and e) Projection of the structure down the c-axis. The oxygen atoms are omitted for clarity.

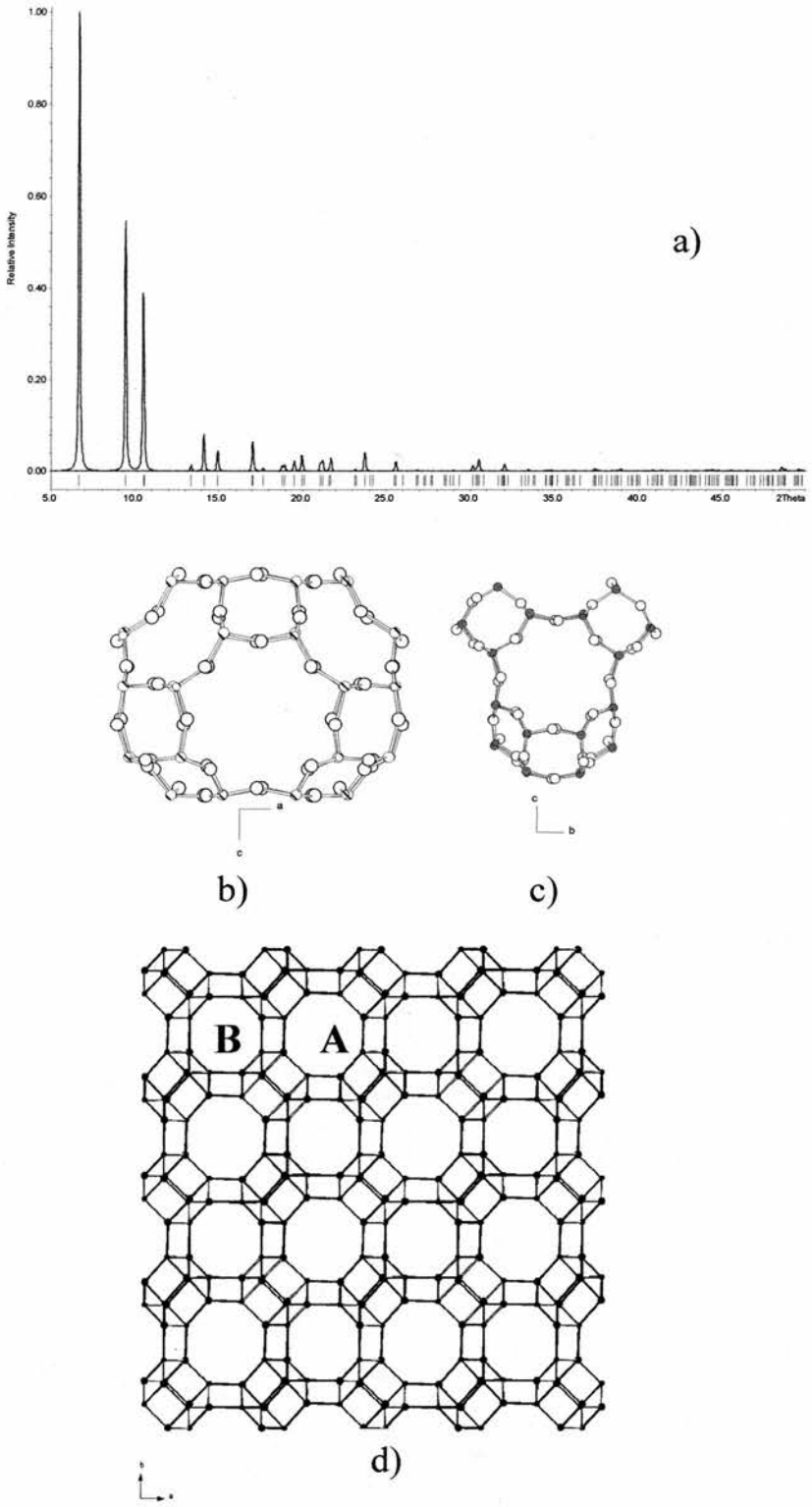

Figure 3.3.2. a) Simulated XRD powder pattern for STA-7 (SAV structure type); b) View of the bigger cavities that made up the A channel system of the STA-7 structure; c) The B channel system is made up of smaller interconnecting spaces; d) Projection of the structure down the c-axis showing both channel systems (A and B). The oxygen atoms are omitted for clarity.

1,4,7,10,13,16-hexamethyl-1,4,7,10,13,16-hexaazacyclooctadecane (hmhaco) templates the synthesis of STA-7 in the presence of Co and Mg. In the case of tetramethylcyclam, the type of divalent cation determines which of the two framework structures is formed. The addition of Mg, Mn or Fe to the gel with tmtact, results in the formation of STA-6, whilst Co or Zn produces STA-7. In these materials, the metals do not remain complexed in the macrocycle and instead end up in a framework cation site. In the absence of these substituting metals in the synthesis, the less open aluminophosphate AlPO-21 is produced.

Different behaviour was observed in preliminary studies performed by Maple, Patinec and Philp[13]. It was observed that when nickel was added to the aluminophosphate gel in the presence of tetramethylcyclam, the crystalline product was orange in colour suggesting the mode of incorporation of the nickel to be different from octahedral or tetrahedral. In separate studies[14] published during the course of this work, it has been shown that copper remains complexed to cyclam within aluminophosphate fluoride microporous materials.

This interesting behaviour offers the possibility of preparing materials incorporating transition metals in both framework and extra framework positions. Hence, syntheses of STA-6 and STA-7 were attempted incorporating metal cations that are not expected to adopt tetrahedral coordination. In the studies documented here, the work built on the previous preliminary results with nickel and on the fact that there are just a few examples of materials where the nickel is believed to be incorporated in the framework of aluminophosphates[15,16] or silico-aluminophosphates[17], and in these cases the environment of the nickel is often poorly defined.

Initially, the effect of the addition of nickel to the tetramethylcyclam-containing preparations of STA-6 and STA-7 was studied. The preparation of these materials in the presence of additional bases and with a lower macrocycle content was also investigated as a way of (1) reducing the amount of expensive macrocycle used to a minimum and (2) exploring the possibility of stabilising new structures or composition variants of known structures. Syntheses using complexes with the unmethylated cyclam macrocycle were also explored and the work was extended to

investigate the incorporation of other metals using their azamacrocycle complexes as structure directing agents.

3.2 EXPERIMENTAL

A description of the different strategies employed to synthesise the materials and the characterisation techniques employed through this work is given in this section. As explained in the introduction to the Chapter, the synthesis of the STA-6 and -7 materials was attempted employing two added metals in the aluminophosphate synthesis gel. One of these metals was chosen as being able to adopt tetrahedral co-ordination in the metalloaluminophosphate framework – typically Zn, Co, Si and Mg. These have different valence to the ions for which they substitute, so that their inclusion imparts a negative charge to the framework. The other metal was chosen so that it does not favour tetrahedral co-ordination, but rather would be expected to remain co-ordinated to the macrocycle, the resultant charged complex compensating the framework charge thereby. Most of the work performed was carried out employing nickel as the extra-cation following the earlier studies[18] done on this subject. However, the inclusion of another metals was also attempted, as is described in the Results and Discussion sections.

In a first approach, the only effect studied was the addition of nickel to the syntheses of MAPOs and SAPOs that in its absence yielded the STA-6 and STA-7 materials. A high concentration of the tetramethylcyclam macrocycle used in these preparations was employed to keep the pH of the synthesis gel close to 7. Since this is an expensive macrocycle, the possibility of preparing the samples with a lower concentration of the macrocycle and in the presence of another amines was attempted. Finally, the use of cyclam instead of tetramethylcyclam was also attempted to compare the effect of changing the macrocycle in metalloaluminophosphate preparations of this kind.

The characterisation techniques comprise those that analyse the microporous materials as well as those that give an insight into the mode of incorporation of metal cations within the solids in either framework or complex.

3.2.1. Synthesis

Metalloaluminophosphates (MAPOs) and silicoaluminophosphates (SAPOs) were prepared hydrothermally by combining aluminium hydroxide, distilled water, orthophosphoric acid, the organic molecules and the cation sources. Further details of the reactants sources are given in table 3.2.

In a typical preparation, phosphoric acid (85%) was added to a mixture of aluminium hydroxide hydrated with water. The macrocycle, the co-base (e.g. TEAOH or ethylenediamine) when stated, the two metal sources and finally the silicon in the SAPO preparations were added to this mixture, while stirring, to form a gel. The final pH of the gel was usually between 5-7. After one hour's stirring, the homogeneous gel was loaded into a Teflon-lined stainless steel autoclave and heated for 2 days at 190 °C. Products were removed from the autoclave and washed with a mixture of distilled water and ethanol. The crystalline fraction was sonicated to allow separation of crystals from the unreacted gel and subsequently left to dry at room temperature.

Removal of the templates by calcination empties the inorganic framework voids and lead to a material with high microporosity and a high void volume. Calcination of the materials was performed by heating to the chosen temperature (550 °C unless otherwise stated) at 10 °C/minute in flowing dry oxygen and kept at that temperature for 10 hours before being allowed to cool to room temperature.

Reagent	Purity (%)	Supplier
Magnesium(II) acetate tetrahydrate	99	Fluka
Cobalt (II) acetate tetrahydrate	98	Aldrich
Zinc (II) acetate dihydrate	98.5	BDH
Nickel acetate tetrahydrate	98	Aldrich
Copper nitrate	95	Fisons
Rhodium (III) chloride hydrate	98	Aldrich
Silica, fumed	97	Fluka
Aluminium hydroxide hydrate	-	Aldrich
Aqueous orthophosphoric acid	85	Prolabo
1,4,8,11-tetraazacyclotetradecane, cyclam	98	Avocado
1,4,8,11-tetramethyl-1,4,8,11-tetraazacyclotetradecane	98	Aldrich
Tetraethylammonium hydroxide	40	Fluka
Tetramethylammonium hydroxide	25%	Aldrich
Ethylenediamine	99	Avocado

Table 3.2. Reagents used in this work, purity and supplier. Materials were employed without further purification.

3.2.2. Crystallography

All crystalline products were examined by X-ray powder diffraction on a Stoe STADIP diffractometer operating in transmission (or Debye-Scherrer mode) using monochromatic Cu $K_{\alpha 1}$ radiation. Samples containing cobalt were analysed on a Phillips X'Pert System diffractometer, also operating with a Cu K_{α} radiation, but in reflectance mode (Bragg-Bentano geometry) and fitted with a secondary (rather than primary) monochromator. This helps to reduce noise from X-ray fluorescence from the cobalt.

For structural analysis, powder diffraction data were collected on the Stoe STADIP diffractometer in a Debye-Scherrer geometry. Samples were loaded in 0.7

mm silica glass capillaries and data were collected over 12 hours. Structure refinement was performed by a Rietveld method employing the GSAS suite of programmes[19].

Selected single crystals were examined by single crystal diffractometry on a Bruker SMART diffractometer operating on Mo K_α radiation with a FAST CCD area detector. The crystal structure was solved and refined using SHELXS and SHELXL[20]. Collection of the data, resolution and refinement of the structure were performed by Dr A.M.Z. Slawin of St. Andrews University.

3.2.3. EXAFS

Room temperature X-ray absorption data were collected at the nickel, rhodium and copper K-edges using stations 7.1, 8.1 and 9.2, at the Daresbury Synchrotron Radiation Source (energy 2GeV, current typically 200 mA) operating in a transmission mode. Wavelength selection was accomplished using a double crystal Si(111) monochromator set at 50% harmonic rejection. Data were collected out to around 15 $Å^{-1}$ over two or more scans and were processed with the suite of programs available at Daresbury: EXCALIB for raw data processing, EXBROOK or EXBACK for the background subtraction and EXCURV98 for the comparison and fitting between theoretical and experimental EXAFS.

3.2.4. Chemical Analysis

Carbon, hydrogen and nitrogen (C,H,N) analysis of the samples was determined by microanalysis by Mrs S.Williamsom on a Carlo Erba Intruments EA1110 analyser in St. Andrews.

The inorganic compositions of the samples were determined in most cases by energy dispersive analysis of emitted X-rays (EDX) on a JEOL 2010 TEM with a Link analyser. Selected samples were examined using ICP-AES (inductively coupled plasma-atomic emission spectroscopy) on samples dissolved in nitric acid.

3.2.5. Other techniques

UV-Visible spectrometry was performed in diffuse reflectance mode on a Perkin Elmer Lambda 35 spectrometer fitted with an integrating sphere. The measurements were typically taken in the range 290 nm to 1200 nm.

Magnetic Susceptibility measurements were performed on a Johnson Matthey balance operating according to a modified Gouy method.

Scanning electron microscopy images were obtained from a JEOL JSM-5600 scanning electron microscope at St. Andrews.

MAS NMR spectroscopy of the Ni-SAPO-STA-6 orthorhombic was performed using a Varian 300 MHz spectrometer at the EPSRC solid state NMR facility in Durham. ^{13}C CP MAS NMR spectra were obtained under the following conditions: contact time 1ms, acquisition time 20 ms, recycle delay 1 s, spinning speed 4.1 kHz. ^{31}P and ^{27}Al MAS NMR were performed using a spinning rate of 12 kHz ans acquisition times and relaxation delays of 20 ms, 300 s and 5 ms, 0.2 s, respectively. Chemical shifts were referenced to a 85 wt% solution of H_3PO_4 and to $[Al(H_2O)_6]^{3+}$. ^{29}Si MAS NMR were collected using cross polarisation from protons, contact time 3 ms, acquisition time 20 ms, relaxation delay 1 s. TMS was used as the reference for ^{13}C and ^{29}Si.

Selected samples were examined by thermogravimetric analysis using a TA Instruments SDT 2960 simulaneous DTA-TGA thermogravimetric analyser. Samples were heated at a rate of 10°C in flowing oxygen up to 1000°C.

ESR spectra were collected on a Bruker EMX 10/12 spectrometer operating at 9.5 GHz with a 100 kHz modulation, with a sweep width of 200 G, field modulation amplitude 5 G_{pp} and power 10 mW. Samples were in powder form and within a 4 mm o.d. quartz tube in the resonance cavity.

3.3 RESULTS AND DISCUSSION

3.3.1. Ni-TMC as a structure directing agent

Results of the experiments performed in the presence of 1,4,8,11-tetramethyl-1,4,8,11-tetraazacyclotetradecane (tetramethylcyclam) as the only base and in the presence of nickel are given in table 3.3. Compositions of the aluminophosphate-base gels were similar to those that in the absence of nickel and in the presence of 1,4,8,11-tetramethyl-1,4,8,11-tetraazacyclotetradecane as the structure directing agent yielded STA-6 when magnesium, manganese or silicon were added and the STA-7 structure when Co or Zn were added[12b)]

MATERIAL	*Cation ratio in gel*	TMC	PRODUCT
	0.20 Mg: 0.8 Al: 1 P: 0.10 Ni	0.4	STA-6(orth)
Ni-MgAlPO	0.20 Mg: 0.8 Al: 1 P: 0.05 Ni	0.4	STA-6(orth)
	0.20 Mg: 0.8 Al: 1 P: 0.025 Ni	0.4	STA-6(tet)
Ni-MnAlPO	0.20Mn: 0.8 Al: 1 P: 0.10 Ni	0.4	STA-6 (orth)
Ni-ZnAlPO	0.125 Zn: 0.75 Al: 1 P: 0.125 Ni	0.4	STA-6(orth)
Ni-CoAlPO	0.125 Co: 0.75 Al: 1 P: 0.125 Ni	0.4	STA6/STA7.
Ni-SAPO	0.25 Si: 1Al: 0.75 P: 0.125 Ni	0.4	STA-6 (orth)

Table 3.3 Gel compositions and crystalline products of hydrothermal syntheses using 1, 4, 8, 11-tetramethyl-1, 4, 8, 11-tetraazacyclotetradecane (tmtact) in the synthesis gel. All gels were heated at 190°C for two days. In all the samples the molar ratio of water to phosphoric acid was 400:1. STA-6 samples prepared in the presence of nickel show an orthorhombic distortion (orth).

Addition of nickel to these preparations produced orange solids for the MgAPO, MnAPO, ZnAlPO and SAPO preparations whilst the CoAlPO preparation yielded dark-blue crystals. X-ray powder diffraction patterns of these preparations were similar to that reported previously for STA-6 although they are characterised by a series of peak splittings - the most obvious being the splitting of the peak at 2θ ~16-17°- when compared with the diffraction pattern of the STA-6 material

prepared in the absence of nickel. These results suggested the products of the MgAlPO, MnAlPO, ZnAlPO and SAPO syntheses were a crystallographic variant of the STA-6 structure. The CoAlPO preparation yielded a mixture of this phase with an appreciable amount of the STA-7 material, clearly visible under the optical microscope. Removal of the template from the STA-6-related samples by calcination removed the distortion and the diffraction patterns of the calcined samples become similar to those of STA-6 prepared in the absence of nickel and subsequently calcined (figure 3.4).

Decreasing the amount of nickel added to the starting gel for the MgAlPO preparation was also shown to reduce the distortion and to give lighter orange crystals of the tetragonal STA-6 phase (figure 3.5). EDX confirmed that the amount of nickel incorporated within the materials decreased as the amount of nickel was reduced in the synthesis gel (table 3.4).

These results suggest that the incorporation of the nickel-macrocycle complex within MgAPO and SAPO preparation are the cause of a crystallographic distortion of the STA-6 phase. In addition, the Ni tetramethylcyclam complex directs the formation of ZnAlPO and CoAlPO compositions to (distorted) STA-6 instead of STA-7. This was the first time STA-6 had been reported in these compositions with the methylated macrocycle.

Although microcrystals of Ni-MgAPO-STA-6 of sufficient size for single crystal diffraction were obtained, they were found by single crystal diffraction to have a complex domain structure and hence, its structure could not be solved. However, the space group of this material was thought to be Pnnm on the basis of systematic absences, which may be derived from the usual space group of STA-6 (P4/mnc) by losing the four-fold axis from P4/mnc.

Input of this space group and the unit cell parameters of the MgAPO-STA-6 tetragonal version as initial parameters, the powder diffraction profile of the Ni-MgAPO-STA-6 distorted and Ni-SAPO-STA-6 distorted could be matched employing the Le Bail routine within the GSAS suite of programs[21]. The program permits the refinement of the unit cell, peak shape, parameters and intensities of individual reflections permitted by the given space group while assigning intensities of the reflections in a 'structureless' refinement.

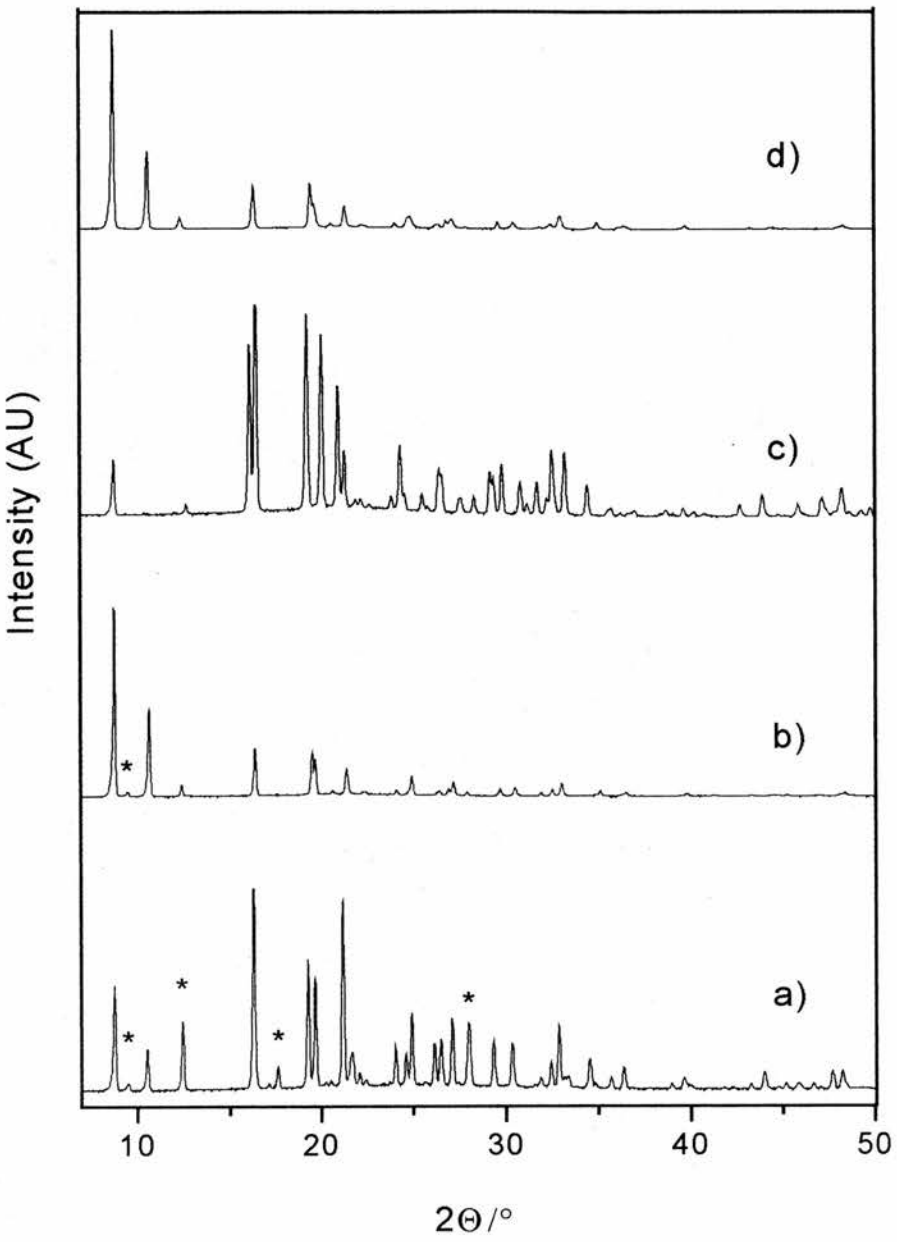

Figure 3.4. X-ray powder diffraction patterns of (a) as-prepared SAPO-STA-6 (SAPO-43 impurity reflections asterisked), (b) calcined SAPO-STA-6, (c) as-prepared Ni-SAPO-STA-6 (orthorhombic) and (d) calcined Ni-SAPO-STA-6.

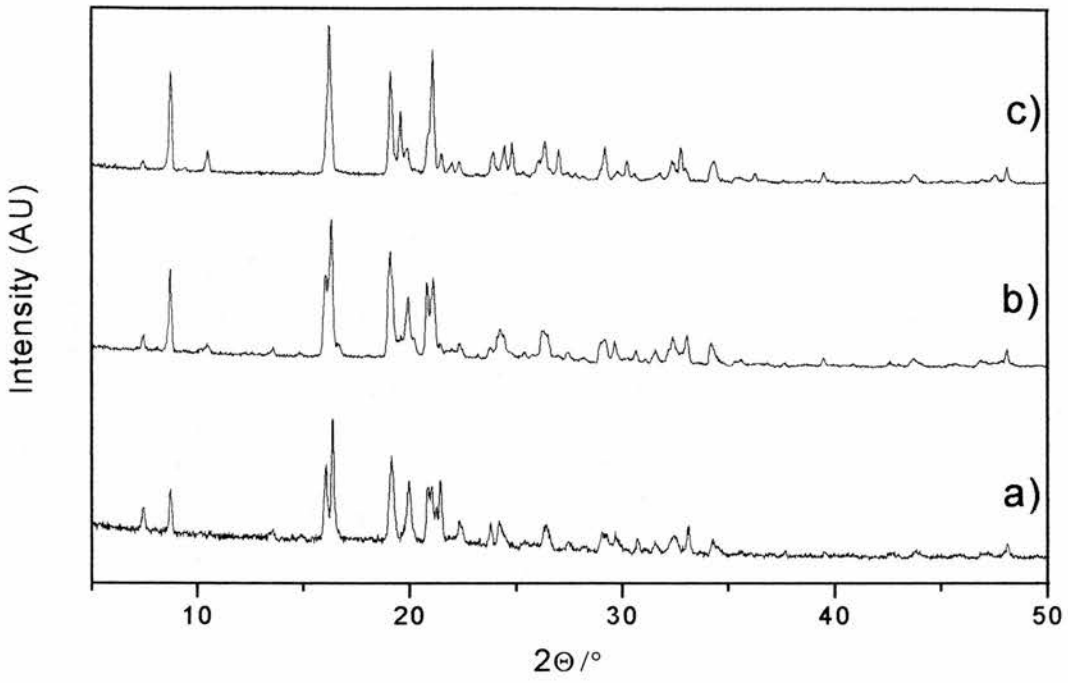

Figure 3.5. XRD of samples synthesised by varying the nickel content of the gel. a) 0.1 Ni; b) 0.05 Ni: c) 0.025

	Ni/P (synthesis gel)	Ni/P EDX	Material (by XRD)
Ni-MgAPO-STA-6	0.10	0.07	STA-6 orth
	0.05	0.03	STA-6 orth
	0.025	0.016	STA-6 tetragonal

Table 3.4. Variation of the nickel content incorporated on the materials as the nickel content on the synthesis gel was reduced.

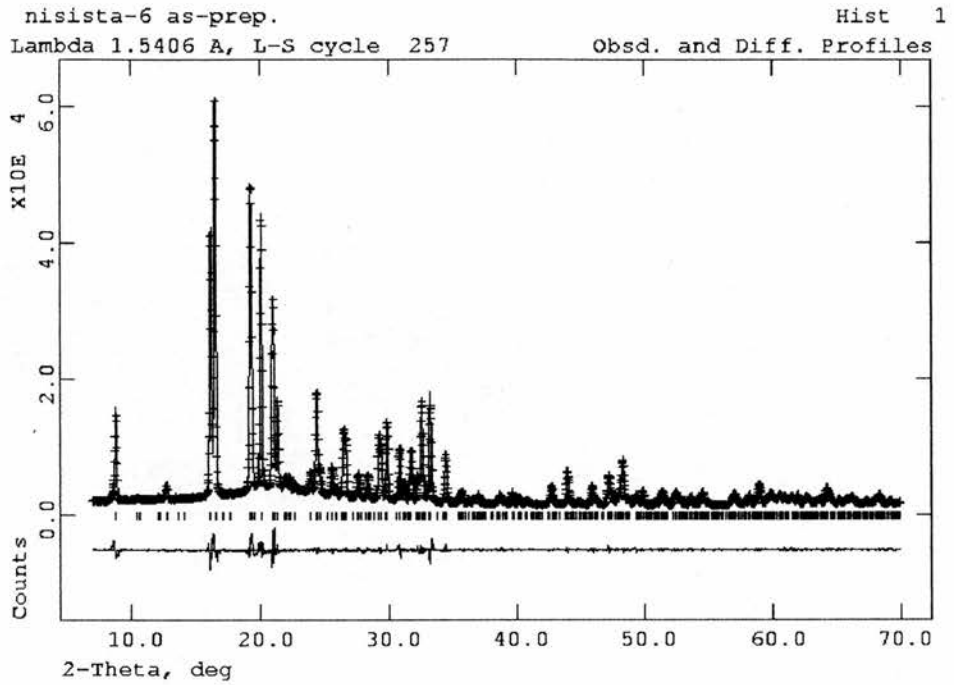

Figure 3.6. Le Bail refinement of X-ray powder diffraction profile of as-prepared Ni-tetramethylcyclam-SAPO-STA-6 (orthorhombic). Details of the refinement given in table 3.5.

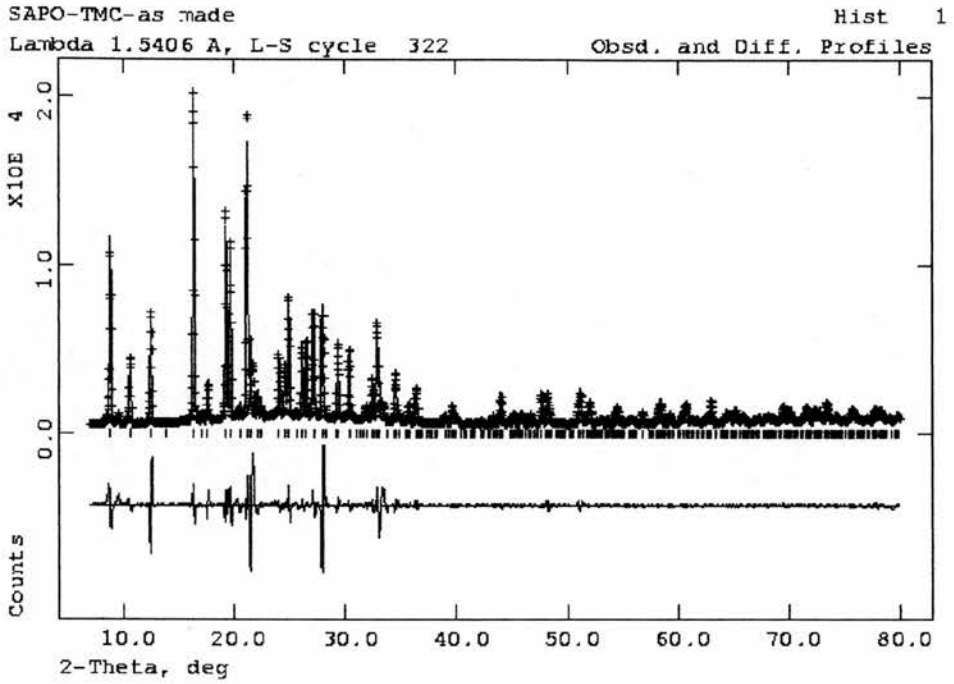

Figure 3.7. Le Bail refinement of X-ray powder diffraction profile of as-prepared tetramethylcyclam-SAPO-STA-6 (tetragonal). Details of the refinement given in table 3.5.

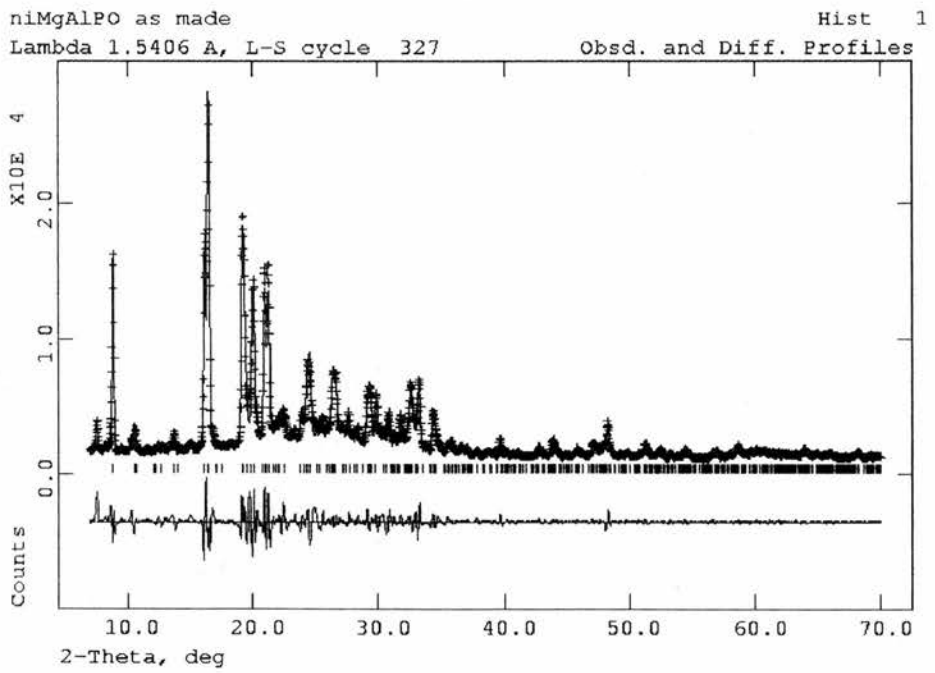

Figure 3.8. Le Bail Refinement of X-ray powder diffraction profile of as-prepared Ni-tetramethylcyclam-MgAPO-STA-6 (orthorhombic). Details of the refinement given in table 3.5.

Refined unit cell parameters for the orthorhombic Ni-MgAPO-STA-6 (table 3.5) were significantly different to those of the tetragonal version of the same material for the MgAPO (tetr). The *a* and *b* axes are no longer equivalent and there is a reduction of the unit cell along the *a* axis (1.97 %) but an enlargement along the *b* axis (2.30%). There are only small changes in the unit-cell volume in the samples with the nickel-complex occluded and those just with the macrocycle, indicating that the framework structure has not changed and the only variation is a distortion in the symmetry.

A range of characterisation techniques was employed to elucidate whether the structure-directing agent (the macrocycle) was intact in the as-prepared materials and also to confirm the presence and state of the nickel in the as-prepared samples.

Material	**Sym**	**Unit cell parameters/ Å**	**wRp**	**Rp**	**Volume/ Å^3**
MgAlPO	T	a=14.339(1) c=10.443(1)	0.1281	-	2147(1)
Ni-MgAlPO	O	a=14.057(9) b=14.669(7) c=10.463(4)	0.1097	0.0754	2157(8)
SAPO	T	a=b=14.321(8) c=10.402(7)	0.2085	0.1048	2133(7)
Ni-SAPO	O	a=13.968(1) b=14.646(9) c=10.412(6)	0.0534	0.0367	2130(3)

Table 3.5. Unit cell parameters for the as-prepared STA-6 materials obtained by Le Bail refinement within the GSAS suite of programs. Orthorhombic symmetry is indicated with O and Tetragonal symmetry with T. Values for the MgAlPO sample were taken from reference 12b).

Chemical analysis performed on the Ni-SAPO, Ni-ZnAlPO and Ni-MgAPO solids (table 3.6) shows a C/N relation in good agreement with the theoretical value of 3.5 expected for the organic molecule. This is an indication that the complex does not undergo decomposition during crystallisation of the inorganic host (this is confirmed by ^{13}C MAS-NMR, below).

Sample	%C exp.	%H exp.	%N exp.	C/N exp
Ni-SAPO	10.41	2.64	3.88	3.13
Ni-ZnAlPO	11.20	2.49	3.91	3.34
NiMgAlPO	11.39	2.70	3.95	3.36

Table 3.6. Results of microanalysis given in wt%. The theoretical value for the C/N molar ratio for the unprotonated macrocycle is 3.5

A sample of as-prepared Ni-SAPO-STA-6 was characterised by MAS NMR, giving good quality carbon, phosphorus, silicon and aluminium spectra without pronounced sidebands. This suggests that the nickel is diamagnetic and not paramagnetic which would have resulted in broad lines. The ^{31}P MASNMR spectrum consists of one symmetric resonance (δ -30ppm) corresponding to phosphorus tetrahedrally coordinated to aluminium through oxygen. ^{27}Al MASNMR of the same sample shows a resonance (δ 31ppm) typical of AlO_4 tetrahedra in aluminophosphate materials plus another signal (δ 6ppm) characteristic of octahedral aluminium. This resonance is usually assigned to framework aluminium atoms coordinated to two extra water molecules[22]. The ^{29}Si MASNMR of this sample presents a simple signal (δ -93ppm) attributed to Si (4Al), i.e. silicon atoms with four aluminium atoms in the second coordination shell. The appearance of this signal indicates the silicon was incorporated by straightforward substitution for phosphorus. If aluminosilicate islands had been present (as in the case, for example, for SAPO-18[23]) other resonances corresponding to the silicon surrounded

by different numbers of aluminiums within second shells would have been observed.

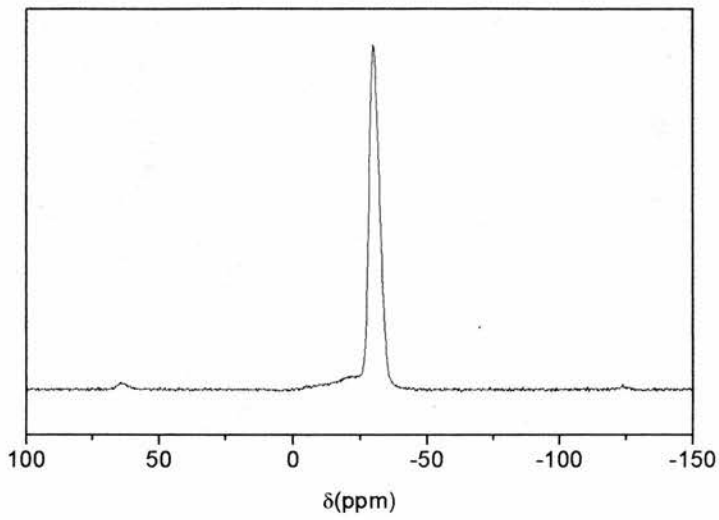

Figure 3.9. ^{31}P NMR spectra of Ni-SAPO-STA-6.

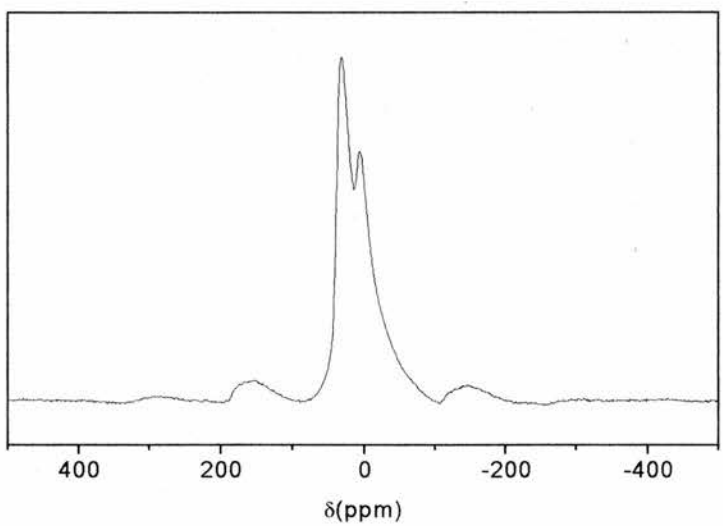

Figure 3.10. ^{27}Al NMR spectra of Ni-SAPO-STA-6.

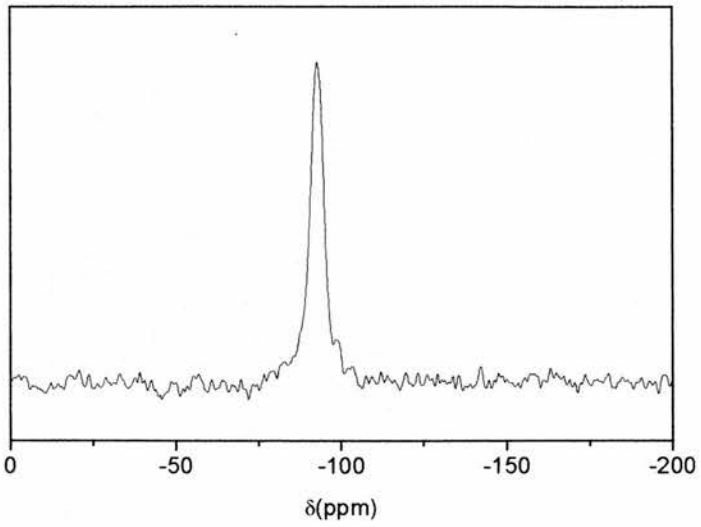

Figure 3.11. ^{29}Si NMR spectra of Ni-SAPO-STA-6

^{13}C MAS-NMR spectra shows four signals at δ ~ 62.624, 47.470, 45.478, 23.329 ppm, which values are slightly different to those given in the literature* for the trans-I and trans-III conformational isomers of the tetramethylcyclam (table 3.7).

Isomer	**δ(ppm)**
trans-I	56.41; 53.61; 39.74;20.54
trans-III	59.82; 58.26; 45.91; 22.12

Table 3.7. ^{13}C NMR Chemical shifts for $Ni(tmc)^{2+}$ isomers (relative to internal dioxane, δ=67.3 ppm) taken from reference 24.

* More information the conformations of the macrocycle given in section 3.3.1.3. "*Single crystal structure of CoAlPO-STA-7*", page 80, and in references 29 a) and b).

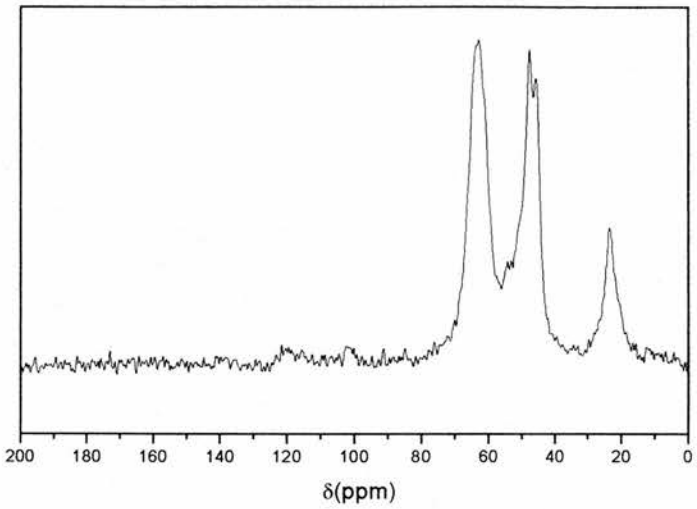

Figure 15. ^{13}C NMR spectra of Ni-SAPO-STA-6.

To determine the inorganic cation content, i.e. the framework composition, EDX (energy dispersive analysis of emitted X-rays) or ICP-AES (inductive coupled plasma-atomic emission spectroscopy) were performed on the samples. EDX analysis was performed in samples of Ni-SAPO and Ni-MgAlPO while ICP analysis was employed with Ni-SAPO and Ni-ZnAlPO samples. It is possible to arrive at a unit cell composition combining this result with the percentage of organic occluded in the structure found by elemental analysis and by taking the water content from the TGA (loss of weight up to ~200°C). The unit cell compositions are given in table 3.8. These results show that the complex occupies most of the cages in these materials (two cages are present in each unit cell).

Material	%Organic	% H_2O	UNIT CELL COMPOSITION	Occupation of cages by nickel complex (%)
Ni-SAPO	16.51	2.72	$Ni_{1.8}Si_{4.8}P_{11.2}Al_{16}O_{64}$. 1.6R. $4H_2O$	85
Ni-ZnAlPO	17.34	1.88	$Ni_{1.5}Zn_3Al_{13}P_{16}O_{64}$. 1.6R. $4H_2O$	78
Ni-MgAlPO	17.59	2.15	$Ni_{1.5}Mg_{1.9}Al_{15.5}P_{16}O_{64}$. 1.8R. $3H_2O$	83

Table 3.8. Unit cell compositions for the different STA-6 (orth) materials. % of organic and water contents are given as g/100g of solid and the % of cage occupancy by the nickel complex was calculated for STA-6 considering that in the structure there are 2 cages per unit cell. The framework compositions of Ni-ZnAlPO and Ni-SAPO were obtained by ICP-AES analysis (the Si content of Ni-SAPO was taken from EDX) and the composition of Ni-MgAlPO was determined by EDX

TGA and DTA for the Ni-SAPO-STA-6 sample are shown in figure 3.13. There is a low temperature weight loss around 175°C associated to an endothermic peak that can be attributed to the loss of water. There is also an exothermic weight loss at high temperature range 200-600°C when the organic template is removed. This proceeds in the Ni-SAPO-STA-6 (orth) sample in multiple stages, with a total weight loss of about 15%. TGA of MAPOs (M=Mg, Zn, ...) containing the nickel complex are similar to this.

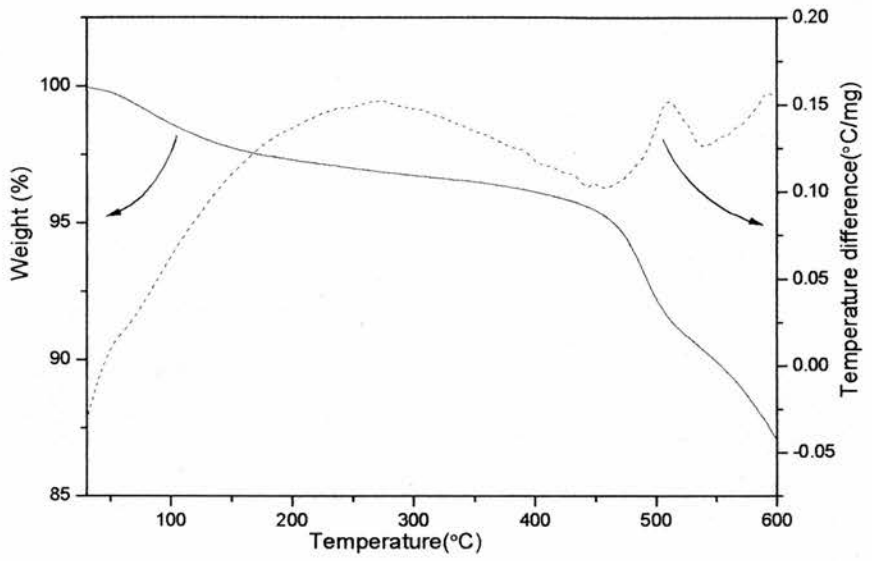

Figure 3.13. TGA of Ni-SAPO-STA-6 in flowing oxygen.

The above results indicate that nickel is present in the materials and the macrocycle is intact after the crystallisation of the inorganic host.

3.3.1.1. Characterising the Ni^{2+} environment in the as-prepared samples

UV-Visible diffuse reflectance spectroscopy of some of the products was performed to get an insight into the Ni(II) coordination geometry. Ni-SAPO-STA-6 (figure 3.14) and Ni-MgAlPO-STA-6 spectra shows one band at ~480 nm typical of nickel in square planar coordination[25]. The value for this d-d transition in the isolated complex (as a perchlorate salt) is 520 nm[26] . The Ni-CoAlPO spectra is shown in figure 3.14. It shows three absorption peaks (~ 650 nm; 610 nm; 560 nm) that are ascribed to d-d absorption bands of cobalt (II) in tetrahedral coordination (CoO_4 units in the framework)[25]. In addition it is possible to distinguish the transition at ~ 480nm, typical of square planar nickel, in the spectra from Ni-MgAlPO-STA-6 and Ni-SAPO-STA-6.

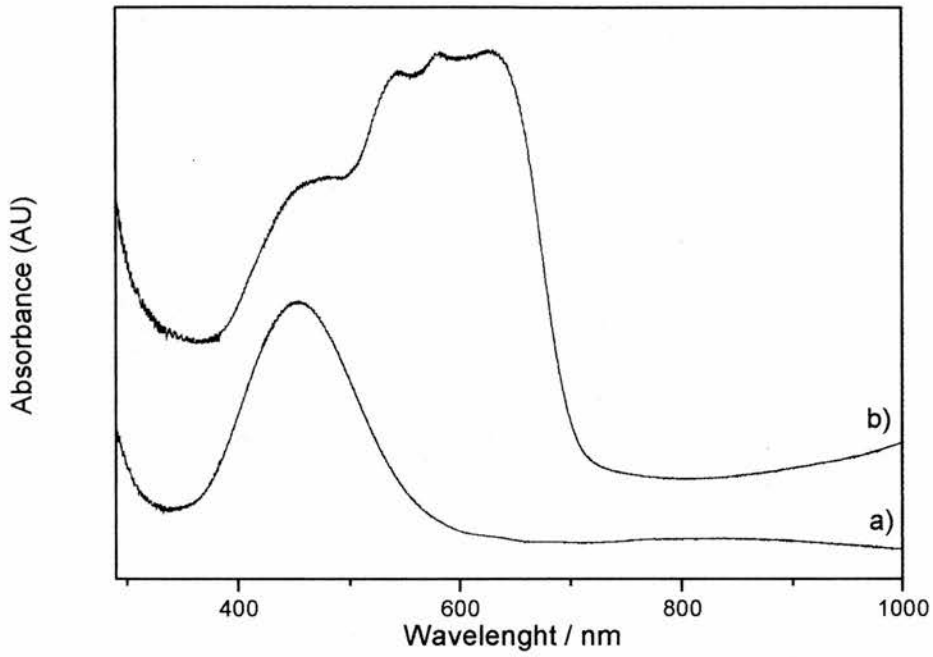

Figure 3.14. UV-visible spectra of Ni-MgAlPO-STA-6 a) and Ni-CoAlPO-STA-6/7 b)

Magnetic susceptibility measurements were performed on the Ni-SAPO sample and the results are also consistent with the square planar coordination for the nickel. A d^8 configuration in octahedral, tetrahedral or tetragonal distorted environment gives unpaired electrons resulting in paramagnetic solids. However, in square planar configuration diamagnetic solids are expected. Magnetic susceptibility for the Ni-SAPO-STA-6 preparation is -3.10^{-7} cgs in the as-made material, showing the nickel is diamagnetic.

3.3.1.2. Calcination of Ni-SAPO-STA-6

After calcination, the diffraction pattern of the orthorhombic variant of the STA-6 becomes similar to those of STA-6 samples prepared without nickel, suggesting that the structures of as-prepared samples have similar framework topology to that of STA-6 prepared without the addition of nickel. The solids become paramagnetic (χ=28.10^{-7} cgs for Ni-SAPO-STA-6) showing the nickel is no longer in square planar coordination. Instead, the nickel is thought to remain as charge-balancing cations coordinated to framework oxygen and adsorbed water.

To preserve its crystallinity and the absorbance of moisture, a sample of Ni-SAPO-STA-6 was calcined in oxygen, saturated with n-hexane vapour and degassed under vacuum. The X-ray powder diffraction pattern of this sample was then measured and a Rietveld refinement of the powder diffraction data was carried out, where the space group (P4/mnc) and coordinates of the as-prepared MgAPO-STA-6 tetragonal variant were employed as a starting model. The lattice parameters and atomic positions were allowed to refine with constraints applied to the atomic coordinates. Difference Fourier maps suggested residual electron density close to the 6-rings that make up the cages of the structure. Hence, Ni was entered in this position and its occupancy and coordinates were refined till final R factor values of $R_{\omega p}$=16.02% and R_p=11.56% with chemical reasonable average bond lengths Al-O= 1.7653(1) and (Si,P)= 1.5135(4). The refined lattice parameters a = 14.3038(9) Å, *c* = 10.2481(5) Å are very similar to those of the calcined MgAPO-STA-6 (*a*=14.282(1) Å and *c*=10.249(1) Å taken from reference12a) although the *a* axis is slightly longer. The final framework structure is that of STA-6 with the nickel atom is located in the 6-rings closer to two oxygen atoms of the framework. The distances Ni-O of 1.9 Å are typical of nickel in a low spin state.

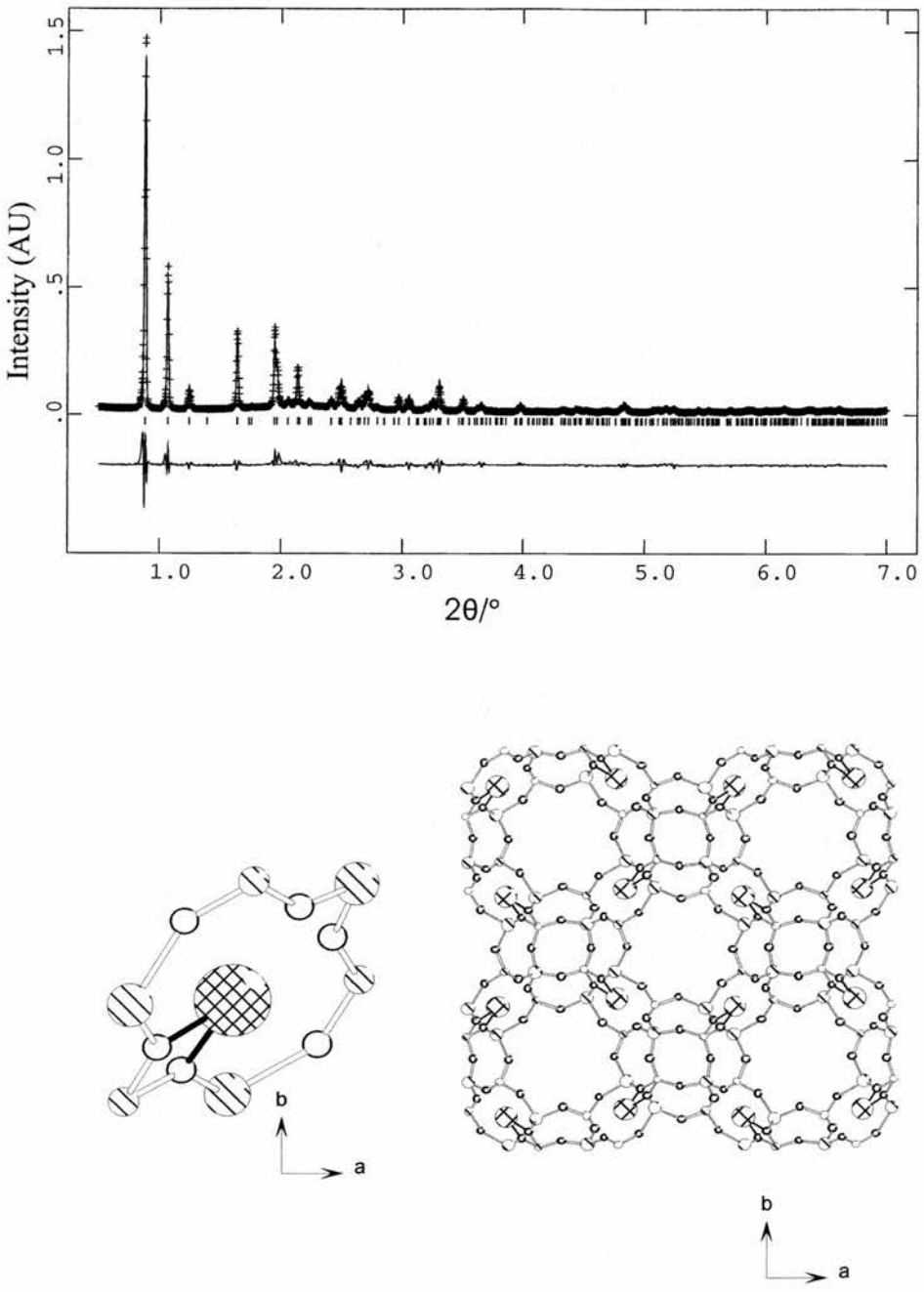

Figure 3.15. (Top figure) Observed, fitted and difference X-ray powder diffraction profiles of Ni-SAPO-STA-6 calcined material fitted using the as-prepared MgAPO-STA-6 tetragonal variant as a starting model and including the position of Nickel suggested by Difference Fourier Analysis. Constrained Rietveld refinement of the whole profile was performed to final fit parameters of R_{wp}=0.16 and R_p=0.12 (Bottom) Diagram of the refined structure of Ni-SAPO-STA-6 calcined material showing the nickel (big hatched sphere) bonded to two of the oxygens (white spheres) of the framework. Al and P appear as medium and small hatched spheres respectively.

The reductive behaviour of divalent nickel present as extra framework or framework species within aluminophosphate-based solids has been studied extensively by electron spin resonance[17,27]. These studies have shown that the divalent nickel can be reduced to Ni(I) by suitable reduction treatments. In this way, a sample of Ni-MgAlPO-STA-6 was exposed to hydrogen in order to reduced Ni(II) to Ni(I) species, which are active in ESR. The main signal g=2.09 may be attributed to Ni(I) species according with the work of Kevan[27]. Continued heating in hydrogen at 573 K results in the reduction to nickel metal.

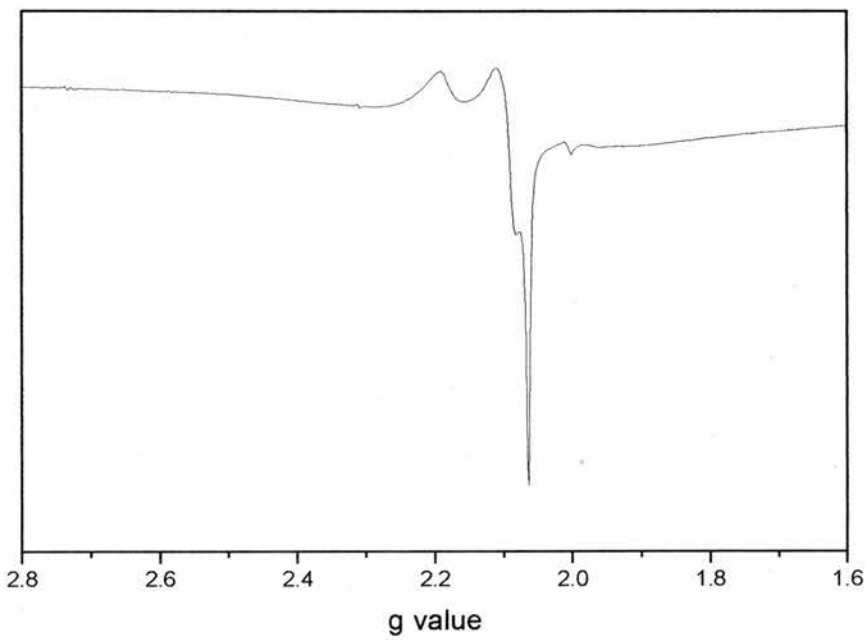

Figure 3.16. ESR of Ni-MgAPO-STA-6, calcined, then reduced under hydrogen at 520 K for 1 hour. The ESR was run in hydrogen at 150 K.

3.3.1.3. Single crystal structure of CoAlPO-STA-7

During this work, it has been shown that the addition of nickel to preparations of metal-aluminophosphates and silicoaluminophosphates tends to favour the crystallisation of the orthorhombic variant of the STA-6 material. However, co-crystallisation of the STA-7 material is observed for the Ni-CoAlPO preparation. A tetragonal crystal of Ni-CoAlPO-STA-7 was found to be suitable for single crystal analysis[†]. This determined the space group to be P4/n, analogous to that of the material prepared in the absence of nickel cation. The structure of the inorganic framework was determined unambiguously and Co, Al and P are found to be strictly ordered on tetrahedral sites with average bond lengths (Co,Al)-O 1.75 (2)Å, P-O 1.51(1) Å and the position of Ni within the bigger cages of the structure. The position of the nickel was successfully refined with a full occupancy indicating that nickel-macrocycle complexes occupy most of the cages. However, lattice parameters (a=18.684(1) Å, c=9.408(1) Å) are slightly smaller than those of the CoAlPO-STA-7 structure synthesised in the absence of nickel cations (a=18.740(5) Å, c= 9.439(7) Å).

Single crystal analysis also locates the nitrogens that are square planar-coordinated to the nickel. The Ni-N distances observed for this structure are 1.98(1) Å, typical for nickel complexes of this kind[28] (figures 3.17) show the location of the NiN_4 core of the complex within the supercage of STA-7.

Additional electron density around the Ni-N_4 core was refined as carbon atoms of the macrocycle. However, it was not possible to determine the position of the carbons unambiguously since they are generated with static disorder because the framework has higher symmetry than the complex. Hence, the single crystal analysis shows more carbon atom positions than the organic possesses. In order to suggest possible orientation, the single crystal data was used as a starting point for molecular modelling, which was performed by Dr. P. A. Cox, of Portsmouth University.

[†] Ni-CoAlPO-STA-7. ($Ni_{2.4}$) [$Co_{4.8}Al_{19.2}P_{24}O_{96}$], M=3221.17 g/mol, Tetragonal, 0.1×0.03×0.01, a=18.684(1) Å, c=9.408 (0)Å, V=3284(4) $Å^3$, T=293 K, space group P 4/n (no. 85), Z=8, μ(Mo-K_α) =1.32 mm^{-1}, 2355 unique reflections, 1316 were observed. The final R(obs) was 0.0781 with ωR(F)=0.1917.

There are five conformations energetically possible for the nickel-tetramethylcyclam complex, depending on the disposition of each of the four methyl groups above or below the coordination plane[29a,b]. Two of them are the most favoured energetically: Trans-I with all four methyl groups disposed on the same side of the ligand and Trans-III with just two methyl groups on the same side of the ligand. Trans-I configuration is obtained by reaction of tetramethylcyclam with nickel in aqueous ethanolic solution and the Trans-III by n-methylation of the nickel-cyclam complex[30]. It is thought that the Trans-III structure was the thermodynamically more stable configuration and the Trans-I structure was the more kinetically stable product. However, interconversion between both structures is possible in coordinating solvents. Theoretical studies have also suggested that when four-coordinated complexes occur, the Trans-I is the most stable isomer while when six-coordinated complexes occur, the Trans-III configuration should predominate[29 b)].

From the crystallographic data is not possible to determinate the complex geometry. It is possible to interpolate the Trans-I configuration incorporating most - but not all- the carbon atoms located in the diffraction experiment, as it would be expected from the four-coordination of the complex (figure 3.17). However, the vigorous conditions of the aluminophosphate synthesis (high temperature and pressure) may affect the proportion of both conformations in solution and the location of observed positions of methyl groups above and below the ring supports the disordered presence of the Trans-III isomer. So the complex may exist in both conformations. Figure 3.18 presents the modelled geometries of both conformations in the STA-7 cage, calculated by P. A. Cox. Further studies are required in order to confirm the conformation of the included complex.

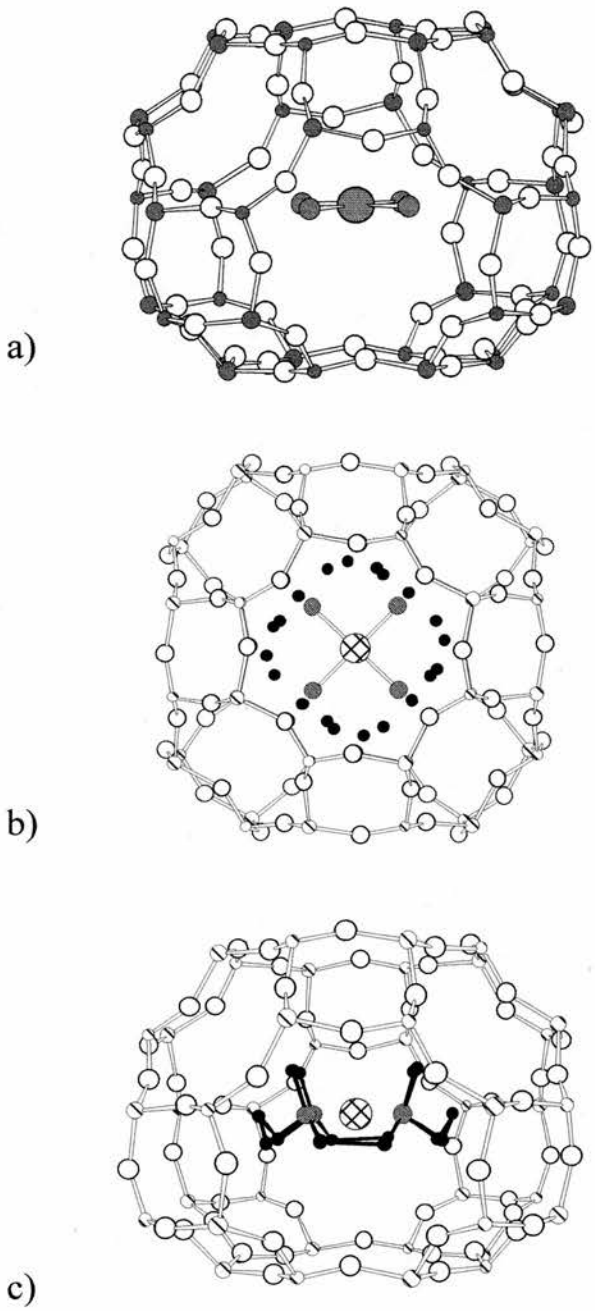

Figure 3.17. Different views of the Ni-CoAlPO-STA-7, obtained by single crystal data, showing NiN_4 core (a), with the ambiguous position of the carbon atoms (b), the interpolated conformation of the complex, Trans-I (c).

a)

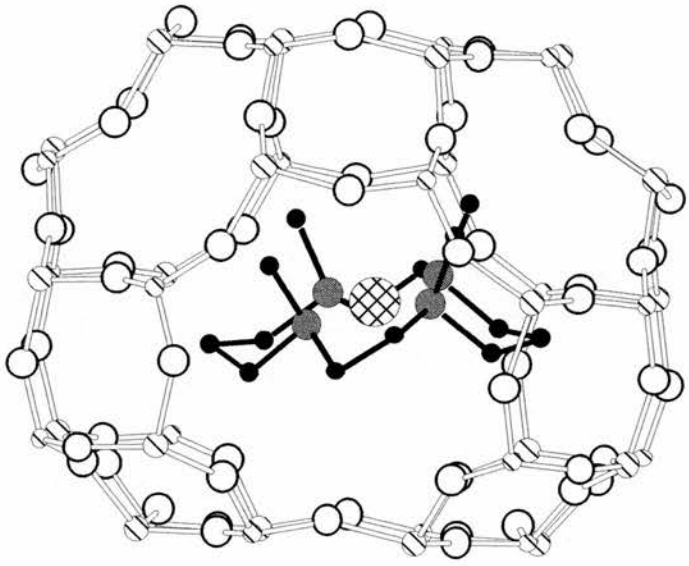

b)

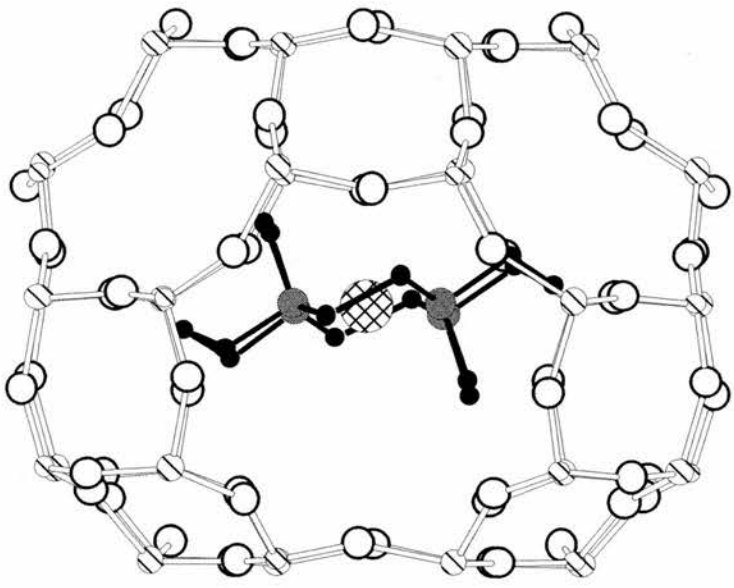

Figure 3.18. Energy minimised locations of (a) the trans-I and (b) the trans-III configurations of the Ni(tmtact)$^{2+}$ complexes within the supercages of STA-7.

3.3.2. Ni-TMC and additional amines as co-bases

Syntheses of the MAPO and SAPO materials with extra-bases as additives were also perfomed. The main objective was to explore the possibility of preparing the phases from gels with a lower content of the expensive macrocycle. It was also thought that other phases might be produced in this way as had been observed previously. In particular, Zones et al.[31] were able to stabilise a new zeolite structure SSZ-47 as a result of adding extra amines to the syntheses of known framework structures. It has also been shown by Wheatley and Morris[14] that the addition of trimethylamine in a Cu-Cyclam preparation leads to the crystallisation of an aluminophosphate related to AlPO-42 (LTA topology) whilst without the presence of trimethylamine and by changing the relative amount of the macrocycle and fluoride, the fluoride-AlPO-34 structure (UT-6) crystallises.

Within the nickel tetramethylcyclam system, one key objective was to obtain pure STA-7. This structure contains two systems of channels. Stacking the larger cages along the *c* axis forms one of them. The second channel system is formed by smaller interconnecting spaces between these channels. In typical preparations of the ZnAlPO and CoAlPO-STA-7 material, the macrocycle has been shown to reside in the bigger cages while the additional pore space was more likely to be filled with products of the decomposition of the structure-directing agent under the synthesis conditions. The approach of employing extra-amines as additives in the syntheses together with the macrocycle and nickel was taken in order to check whether it was possible to stabilise the STA-7 structure in these preparations or at least to control the proportion of the nickel-containing STA-6/STA-7 materials.

Synthesis gels were prepared, decreasing the amount of macrocycle added to the gel. Only a stoichiometric amount of macrocycle expected to remain complexed to the nickel was added to these preparations. The extra bases were added to keep the pH of the synthesis between 5-7, a typical pH range for the crystallisation of microporous aluminophosphates.

3.3.2.1. SAPO preparations

SAPO preparations were performed with tetramethylammonium hydroxide, tetraethylammonium hydroxide and ethylenediamine as additives. Control experiments were performed employing the similar gel compositions and time, but without the addition of nickel. The results of these preparations are given in table 3.9 :

Material addedbase-framework	**Cation ratio in gel** Ni: Al: P: Si: H_2O: tmtact: Co-base	**PRODUCT**
Ni-TMAOH-SAPO	0.125 : 1 : 0.75 : 0.25: 400: 0.125: 0.51	STA-6 (orth)
Ni-TEAOH-SAPO	0.125 : 1 : 0.75 : 0.25 : 400 : 0.125 : 0.51	STA-6 (orth)/STA-7
Ni-en-SAPO	0.125 : 1 : 0.75 : 0.25 : 400 : 0.125 : 0.5	Amorphous
TMAOH-SAPO	0 : 1 : 0.8 : 0.20 : 400 : 0.125 : 0.50	SAPO-20
TEAOH-SAPO	0 : 1 : 0.8 : 0.20 : 400 : 0.125 : 0.50	SAPO-39

Table 3.9. Gel compositions and crystalline products of hydrothermal synthesis of silicoaluminophosphates using tmtact in the presence of another amines to control pH. The nickel containing gels were heated at 190°C for 2 days. Gels without the addition of nickel were heated at 190°C for 7 days.

When nickel was present in the synthesis gel, the only crystalline phases to form were orange crystals of STA-6 or of a mixture of STA-6 and STA-7 upon addition of TMAOH or TEAOH, respectively. When ethylenediamine was employed in these conditions, only amorphous unreacted gel was obtained showing the products of synthesis to depend on the co-base. Repeating the synthesis in the absence of nickel in the same conditions that yielded the SAPO version of the STA-6 material[32] (seven days at 190°C), gave SAPO-39 when the added base was TEAOH and SAPO-20 when the added base was TMAOH. These results show the

nickel complex to be a better directing agent not only than TMAOH and TEAOH but also than the uncomplexed macrocycle. The method permits the synthesis of STA-6 with more efficient use of the tmtact macrocycle (38% in the final crystalline product cf. 17%).

3.3.2.2. The role of TEAOH as a co-base in favouring the crystallisation of STA-7

Interestingly, TEAOH was found to give a mixture of crystals of SAPO-STA-6 with crystals of STA-7, not previously observed with a SAPO framework. Because this is of considerable catalytic interest (SAPOs are usually more stable to template removal and posses stronger acidity than Mg or Co aluminophosphates), a series of syntheses were performed to investigate this further, with the aim of obtaining this material pure (table 3.10).

MATERIAL	x	y	PRODUCT
Ni-SAPO-1	0.51	0.125	STA-6/STA-7
Ni-SAPO-2	0.25	0.125	STA-6/STA-7
Ni-SAPO-3	0.25	0.062	STA-6/STA-7
Ni-SAPO-4	0.25	0.031	Amorphous
Ni-SAPO-5*	0.25	0.017	AlPO-5
SAPO-6	0.25	-	STA-7

Table 3.10. Products of syntheses of SAPO preparations in the presence of TEAOH and nickel. Gel compositions are given by 1 Al:0.75 P: 0.25 Si: 400 H_2O: 0.125 TMC: x TEAOH: y Ni. All gels heated at 190°C for two days but Ni-SAPO-5 was heated at 190°C for seven days.*

Decreasing the amount of TEAOH was shown to slightly favour the formation of the STA-7 material. When the preparation was performed without addition of nickel, a pure sample of SAPO-STA-7 was obtained. Progressively reducing the nickel content in the starting gel as a way of getting the nickel-containing SAPO-STA-7 pure was unsuccessful, since crystallisation of both phases

was always observed (see figure 3.19). Microanalysis of TMC-TEAOH-SAPO-STA-7 gave an organic content of 9.28%C, 1.95 %H, 3.24%N, which gives a C/N ratio of 3.34 and a H/C ratio of 2.52. The theoretical ratios for the macrocycle are C/N=3.5 and H/C=2.28. The TGA of the sample is given in figure 3.20. There is a first loss of weight (~ 2.92%) till 250°C attributed to adsorbed water. There is a second slope till 700°C corresponding to the burning of the organic species occluded within the material. The lost of weight in this region is 16.78% (slightly higher than the organic content determined by the microanalysis 14.47 %).

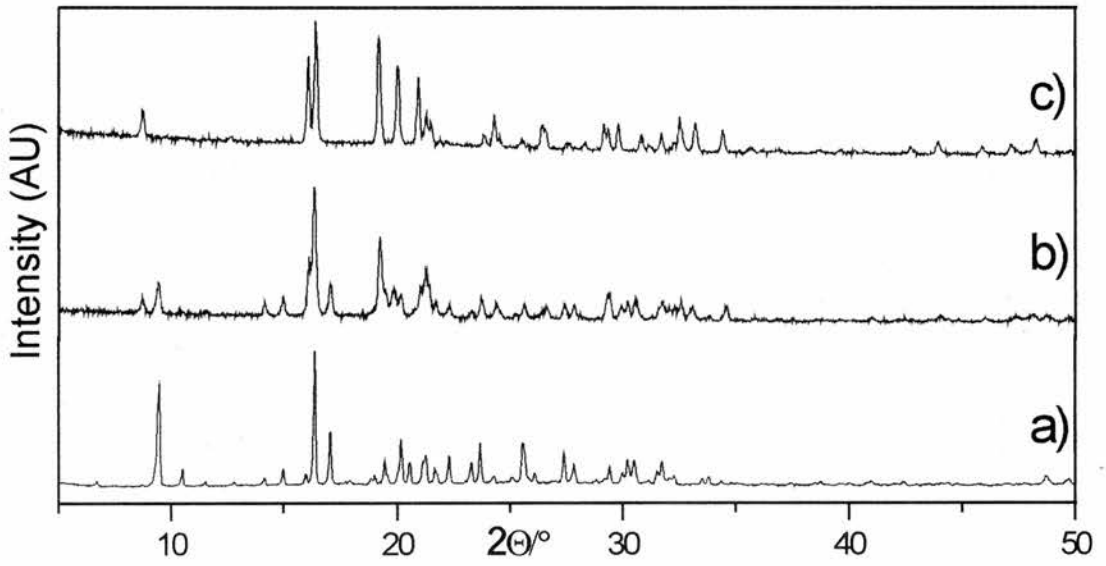

Figure 3.19. XRD powder diffraction pattern of: a) SAPO-STA-7 synthesised with tetramethylcyclam and tetraethylammonium and without adding nickel to the gel; b) Mixture of Ni-SAPO-STA-6 and STA-7 synthesised with tetramethylcyclam and tetraethylammonium; c) Ni-SAPO-STA-6 synthesised with tetramethyl cyclam.

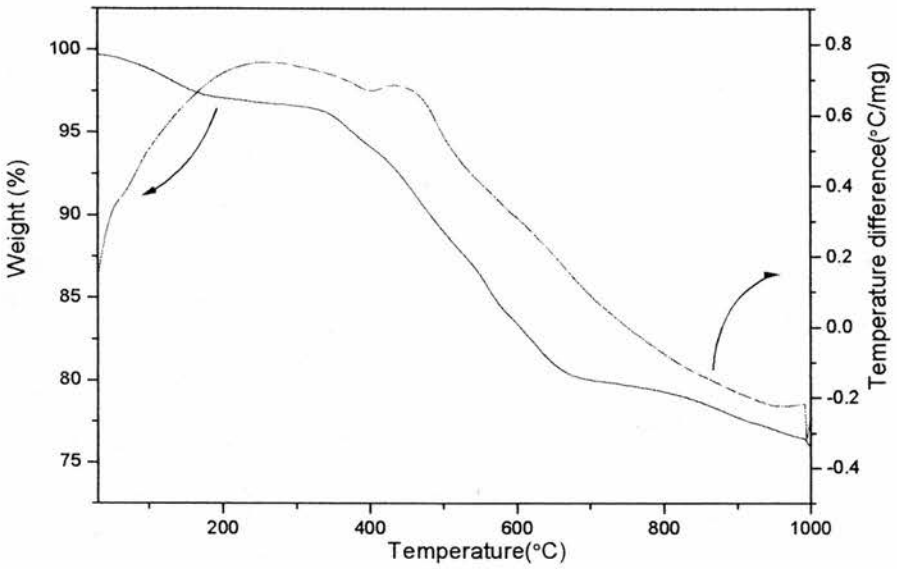

Figure 3.20.TGA and DTA in air of the SAPO- STA-7 prepared with TMC and TEAOH as additive.

3.3.2.3. Role of co-bases in the synthesis of metalloaluminophosphates

Metalloaluminophosphate preparations were also performed with the presence of TEAOH and ethylenediamine as extra-bases (table 3.11).

MATERIAL	Experiments with added TEAOH		Experiments with added ethylendiamine	
	TEAOH/1P	PRODUCT	en/1P	PRODUCT
Ni-MgAPO	0.25	STA-6 (orth)	0.18	STA6 (orth)
MgAPO	0.25	STA-7	-	-
Ni-ZnAlPO	0.25	STA-7	0.18	STA-6/7
Ni-CoAlPO	0.25	STA-7/AFI	0.28	STA6 (orth)

Table 3.11. Products of syntheses of MAPO materials performed in the presence of TMC and Tetraethylammonium hydroxide (TEAOH) or ethylenediamine (en) as extra-bases. Cation ratio in gels were 0.2 Metal: 0.8 Al: 1P: 60 H_2O: 0.125 TMC: 0.125 Ni(when stated). The amount of extra base added to the gel given in the table. All gels heated for two days at 190°C.

Syntheses performed in the presence of nickel and TEAOH yielded the STA-7 structure for the ZnAlPO and the CoAlPO compositions confirming the increased tendency of TEAOH to direct the formation of STA-7. For the MgAPO preparation the orthorhombic version of the STA-6 material was still obtained. When no nickel was employed in these preparations, the STA-7 structure was produced for the MgAPO as well as the SAPO preparation (figure 3.21). The tetraethylammonium ion clearly has an important role to play in preparing STA-7. Co and ZnAlPO preparations with nickel can crystallise as STA-7 in its presence and it directs the crystallisation of the pure MgAlPO and SAPO versions of this material (for the first time with this macrocycle). SEM micrographs of the MgAPO-STA-7 show the sample is made up of tetragonal blocks (figure3.22).

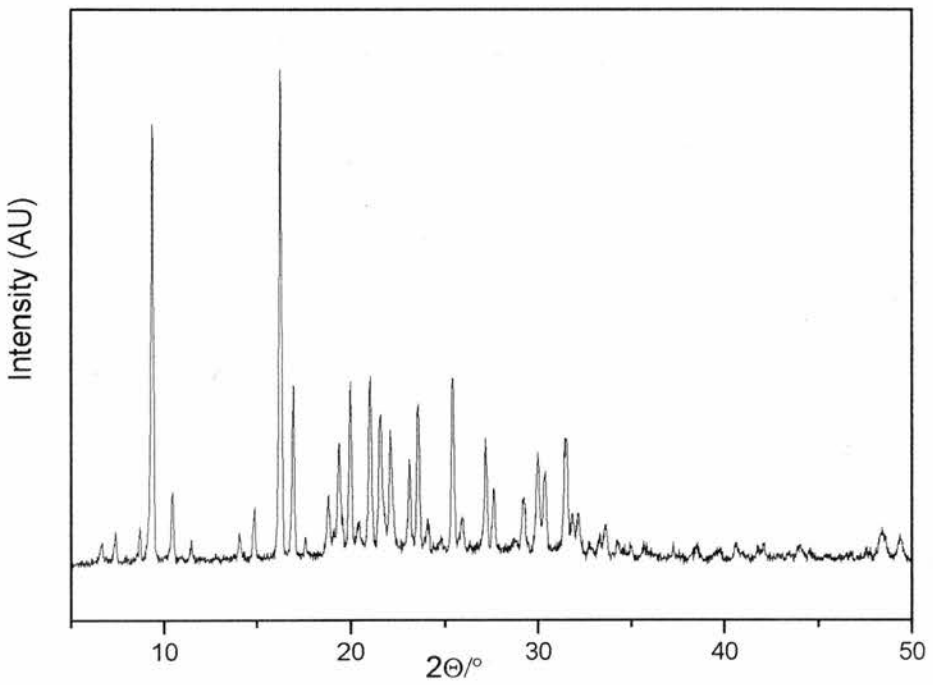

Figure 3.21. X-Ray powder diffraction pattern of MgAPO-STA-7 prepared with tetramethylcyclam and tetraethylammonium.

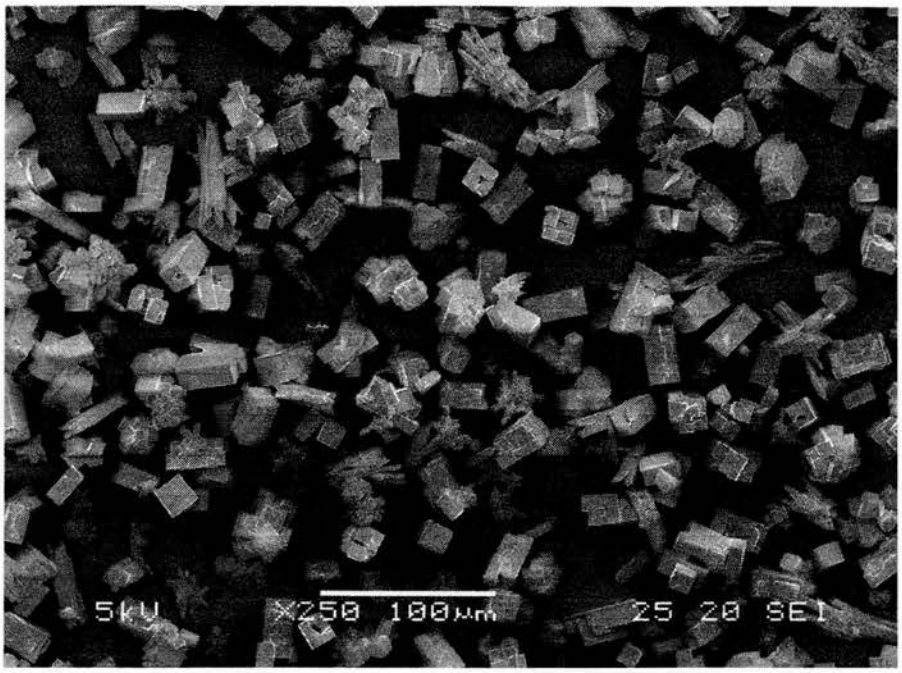

Figure 3.22. SEM micrographs of MgAPO-STA-7 synthesised with tetramethylcyclam and tetraethylammonium.

The framework composition of MgAPO-STA-7 was found by EDX to be Mg:Al:P/0.3:0.9:1, indicative of the substitution of Mg for Al. For the Ni-ZnAlPO, this relation was Ni:Zn:Al:P/0.04:0.25:0.86:1, confirming the presence of nickel in this material.

Microanalysis was performed on the samples to check whether it was possible to determine the presence of extra-amines in the materials. Thermogravimetric analysis performed in the samples is summarised in table 3.12. The loss of weight of the materials is divided in three regions depending on the temperature. The first weight loss (W1) is mainly attributed to the loss of the water occluded in the structure. The second loss of weight (W2) at higher temperature corresponds mainly to the loss of the organic material occluded in the structure. The third region, it is usually assigned to mass loss associated with collapse of the structure at higher temperature and/or the possible recrystallisation to denser phases.

Sample	Elemental analysis					TGA		
	%C exp.	%H exp.	%N exp.	C/N exp[a]	% Total organic[b]	W1[c]	W2[d]	W3[f]
Ni-MgAPO-STA-6 orth	11.11	1.15	3.48	3.72	15.74	2.54	12.74	6.29
MgAPO-STA-7	10.42	1.92	3.03	4.01	15.37	3.37	18.11	0.23
Ni-ZnAlPO-STA-7	11.31	1.43	2.95	4.47	15.69	2.71	14.38	2.00

Table 3.12. Results of the elemental analysis of the samples given in wt% and the loss of weight by TGA. a: molar C/N experimental ratio; b: Total % of organic content determined by elemental analysis; W1: weight loss between 25-250ºC; W2: weight loss between 250-700ºC; W3: weight loss between 700-1000ºC

The microanalysis show that in the three samples the C/N ratio is higher than that of the macrocycle (C/N=3.5). This is significantly higher in the case of the STA-7 and suggests the presence of another organic material besides the macrocycle within this structure. Assuming a TEAOH:TMC ratio of 1:1, would give a C/N ratios of 4.4. The TGA curve has a different shape in the case of the STA-6 and STA-7 materials (figure 3.23). In the former, there is a progressive loss of weight with the increasing of the temperature, so that it is very difficult to determine at what temperature the organic has been burned completely and this can be the reason of the high W3 values. The STA-7 materials have a sharper loss of weight between 400-600°C where most of the organics are removed, presumably due to the better three dimensional pore connectivity possessed by these solids.

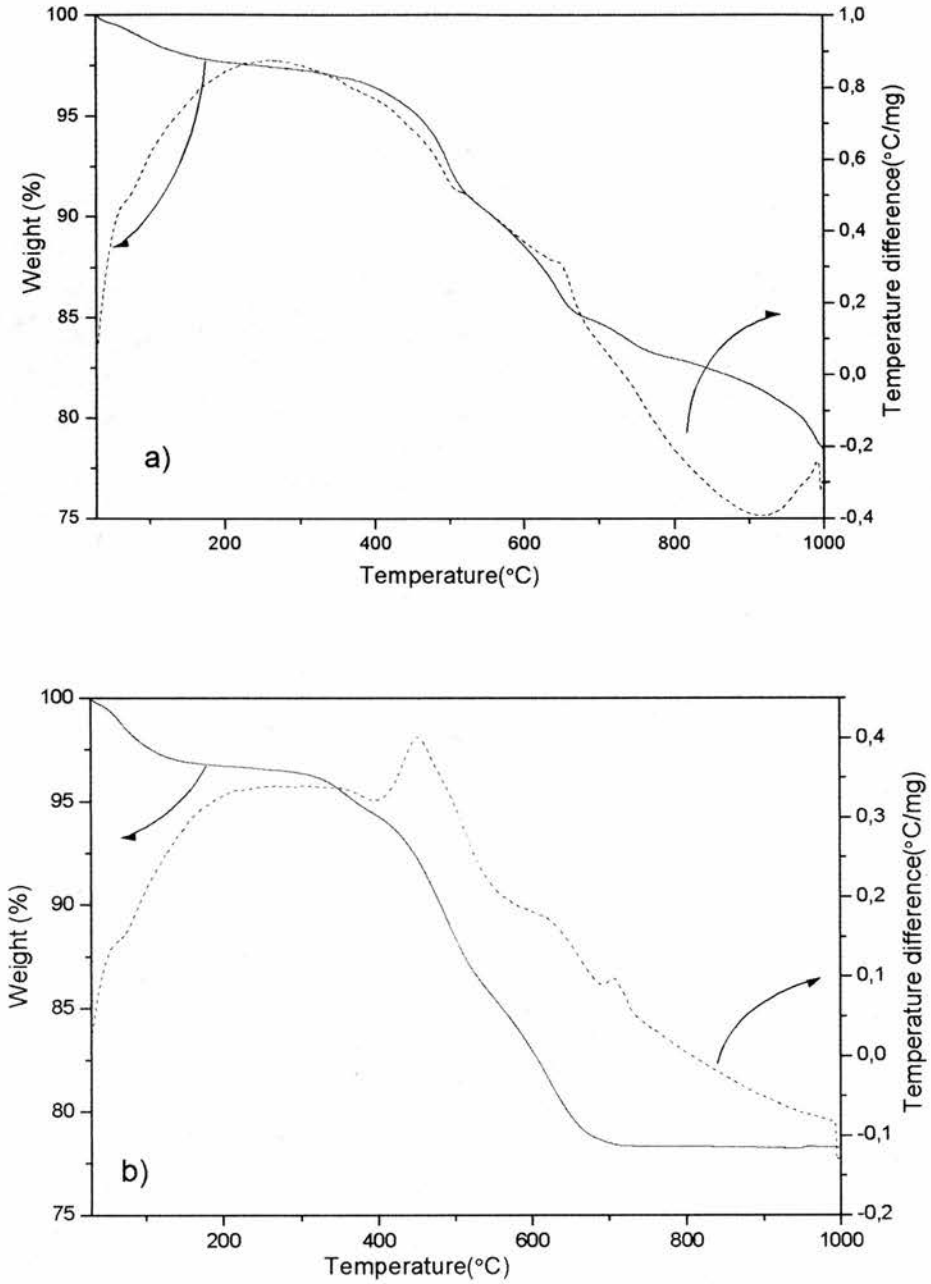

Figure 3.23. (Top) TGA in flowing oxygen of Ni-MgAPO-STA-6 orth prepared with TMC and TEAOH and (Bottom) MgAPO-STA-7 prepared with TMC and TEAOH.

Single crystal analysis was carried out on crystals from the Ni-CoAlPO and Ni-SAPO preparations[‡].

For both samples, the tetrahedrally-connected SAV framework topology was observed. In the case of the SAPO framework all 'phosphorus' sites were refined only as P, because the scattering of Si is so similar giving final average bond length distances of (Si, P)-O 1.546 (3) Å, Al-O 1.729 (3) Å. For the 'Al' sites of the Ni(TMC)–CoAPO material, initial refinements as Al gave residual electron density because of substitution of the heavier cobalt in these sites. Consideration of differences in (Co,Al)–O bond lengths for the three crystallographic 'Al' sites indicated preferential siting of Co. Therefore the fractional occupancies of Co and Al were adjusted so that all sites gave similar thermal parameters and, when summed, gave a reasonable total cobalt concentration (Co/P = 0.2). The average (Co,Al)–O bond lengths of the tetrahedral cation positions were 1.739 Å, 1.744 Å and 1.785 Å, indicating that cobalt is preferentially sited in 'Al3'. This cation site is that in the planar 8-MR that makes the opening to the large cages of STA-7 along the *c* axis. The average bond length for the P-O site was 1.5248 Å.

In both cases, nickel was found to reside in the larger cages of the STA-7 structure complexed within the four nitrogens of the macrocycle (figure 3.24). Electron density in the second channel system of the structure could be refined successfully as nitrogen and carbon atoms coming from the tetraethylammonium cation that was thought to remain in this channel system. Hence, the final structure contains the nickel macrocycle complex located within the bigger cages that form one of the three-dimensional channel systems whilst the tetraethylammonium molecule is located in the cages forming the second channel system. For this last cation, the nitrogen was found to reside on a special position, whereas two

---

[‡] Ni-CoAlPO-STA-7. $(Ni_2N_{10}C_{44}H_{108})[Co_6Al_{18}P_{24}O_{98}]$, M=505.67, Tetragonal, 0.080×0.060×0.040, a=18.7576(1) Å, c=9.4139(1) Å, V=3312.3(4) Å^3, T=103(2) K, space group P 4/n (no. 85), Z=8, μ(Mo-K$_\alpha$) =1.32 mm^{-1}. The final R(obs) was 0.0568 with ωR(F)=0.1452.

Ni-SAPO-STA-7. $(Ni_2N_{10}C_{44}H_{108})$ $[Si_6Al_{24}P_{18}O_{98}]$, M=479.54, Tetragonal, 0.034×0.034×0.010, a=18.726(2) Å, c=9.4487(1) Å, V=3313.1(4) Å^3, T=153(2) K, space group P 4/n (no. 85), Z=8, μ(Mo-K$_\alpha$) =1.32 mm^{-1}. The final R(obs) was 0.0668 with ωR(F)=0.1719.

configurations were found for each ethyl group, presumably statically disordered. This is probably the reason that this additive is stabilising this structure, by being included in the second channel system of the STA-7 structure.

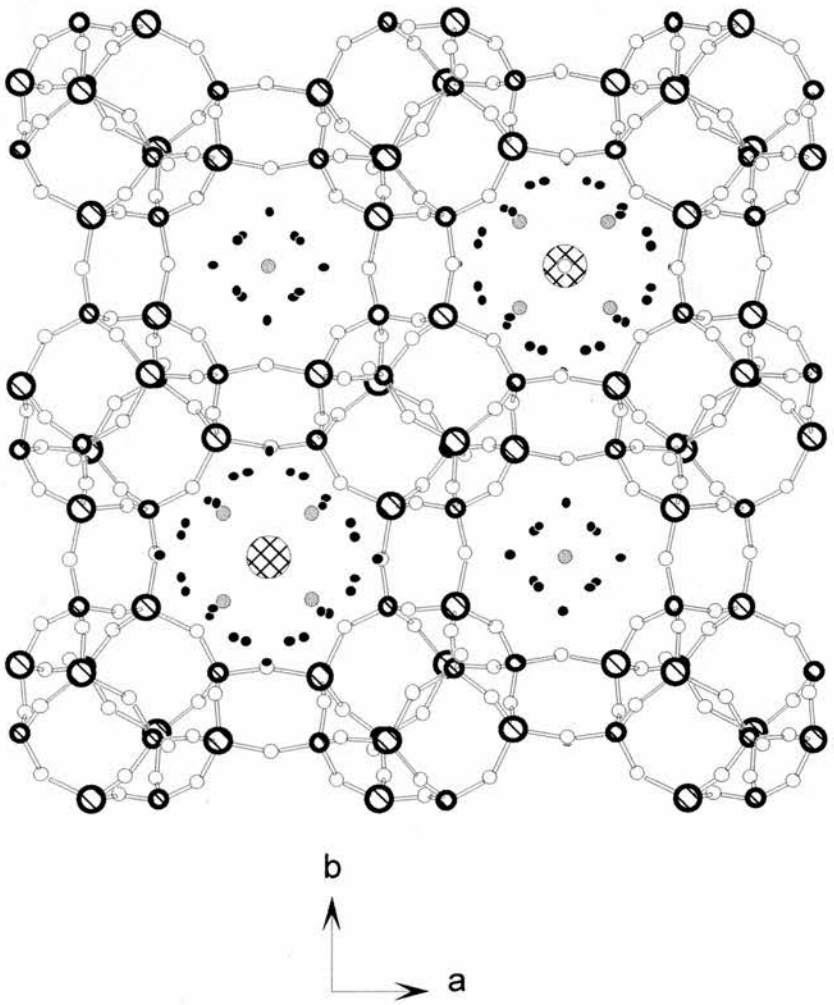

Figure 3.24. Crystal structure of CoAlPO-STA-7 synthesised employing TEAOH and TMC. The Ni-TMC complex occupied the bigger cages in the structure while TEA^+ resides within the smaller interconnecting spaces of the structure.(Key: Al medium hatched; P,small hatched; O,small white; Ni, large cross hatched; N,small light grey; C, small black)

Syntheses employing ethylenediamine as the additional base were shown to be less effective than those performed only in the presence of nickel and tetramethylcyclam as structure directing agents (table 3.11). Only in two cases were the STA-6 orthorhombic materials obtained as pure phases, for the Ni-MgAPO and Ni-CoAlPO preparations. The Ni-MgAPO preparation yielded a pure sample of orange crystals of the orthorhombic STA-6 material. The cation ratio found in the material by EDX was Ni:Mg:Al:P/0.085:0.25:0.80:1. The Ni-CoAlPO preparation yielded a phase of blue needles of the STA-6 (orth) material. The cation ratio composition for this material found by EDX was Ni:Co:Al:P/0.06: 0.25: 0.87: 1. Table 3.13 shows the results of the microanalyses and the loss of weight determined by TGA.

Sample	Elemental analysis					TGA		
	%C exp.	%H exp.	%N exp.	C/N exp[a]	% Total organic[b]	W1[c]	W2[d]	W3[f]
Ni-MgAPO-STA-6 orth	6.93	1.07	3.19	2.53	11.19	-	-	-
Ni-CoAlPO-STA-6 orth	6.03	1.16	1.90	3.70	9.09	1.79	8.32	3.23

Table 3.13. Results of the elemental analysis of the samples given in wt% and the loss of weight by TGA. a: molar C/N experimental ratio; b: Total % of organic content determined by elemental analysis; W1: weight loss between 25-250°C; W2: weight loss between 250-700°C; W3: weight loss between 700-1000°C

The UV-Visible of the Ni-MgAlPO-STA-6 (orth) shows a maximum at ~457 nm, typical for square planar complexes of this type. The Ni-CoAlPO-STA-6 (orth) has a similar UV-Visible spectrum to the one synthesised in the presence of the macrocycle as the only template. As in that case, it shows three absorption peaks typical of cobalt in tetrahedral coordination (~544nm; ~583nm; ~629nm) and also, a fourth transition at ~475 nm, attributed to the nickel macrocycle complex.

3.3.3. Synthesis employing Ni-cyclam as structure directing agent

In a separate series of experiments, preparations similar to those described above were repeated using cyclam rather than tetramethylcyclam. The main objective was to check whether it was possible to obtain the same materials and to what extend the differences in behaviour between the macrocycles affect the products of synthesis. Previously[33] the product of crystallisation of a MgAPO gel with cyclam but in the absence of nickel yielded a pure sample of MgAPO-18, whereas CoAPO gels gave the chain compound Co(cyclam)AlP_2O_8H[8]. Here the results of syntheses using two additional sources of metal cations are given. Compositions and products of syntheses performed in this way are given in table 3.14.

Material	Cation ratio in gel	Cyclam	Product
Ni-MgAlPO	0.20 Mg: 0.8 Al: 1 P: 0.10 Ni	0.4	Ni-MgAPO-5/ Ni-MgAPO-18
Ni-ZnAlPO	0.125 Zn: 0.75 Al: 1 P: 0.125 Ni	0.4	Amorphous
Ni-CoAlPO	0.125 Co: 0.75 Al: 1 P: 0.125 Ni	0.4	NiAPO-cyclam-1
Ni-SAPO	0.25 Si: 1Al: 0.75 P: 0.125 Ni	0.4	Ni-STA-6 (tetrag)

Table 3.14. Gel compositions and crystalline products of hydrothermal syntheses using 1, 4, 8, 11-tetraazacyclotetradecane (Cyclam) in the synthesis gel. All gels were heated at 190°C for two days. In all the samples the water content was 400.

The Ni-MgAPO preparation yielded a mixture of yellow needles and tetragonal plates. Both phases were stable after calcination in nitrogen at 600 degrees. It was not easy to recognise the products on the basis of analysis of the powder pattern of the mixture of phases (figure 3.25). The crystals were also too small for single crystal analysis that could have provided the unit cell parameters to compare with the literature.

The morphology and the powder pattern of the mixture of products obtained in the presence of nickel suggest it is mainly a mixture of MgAPO-5 (the needles)

and MgAPO-18 (tetragonal plates), although some impurities might be present. EDX was performed in the scanning electron microscope for both types of crystals that are easily differentiated on the basis of their shape (figure 3.26). This analysis showed that both materials have incorporated nickel (Ni/P ratio 0.04). The ZnAlPO preparation did not produce any crystalline product whilst the Ni-CoAlPO preparation yielded red crystals of the layered aluminophosphate Co(cyclam)AlP_2O_8H commented above.

However, the NiSAPO preparation yielded yellow crystals of the tetragonal variant of the SAPO STA-6 material confirming that nickel cyclam could be used as an effective template for the STA-6 material. EDX performed in the sample gave a cation ratio of ca. Ni: Si: P: Al/ 0.05: 0.17: 0.62: 1.

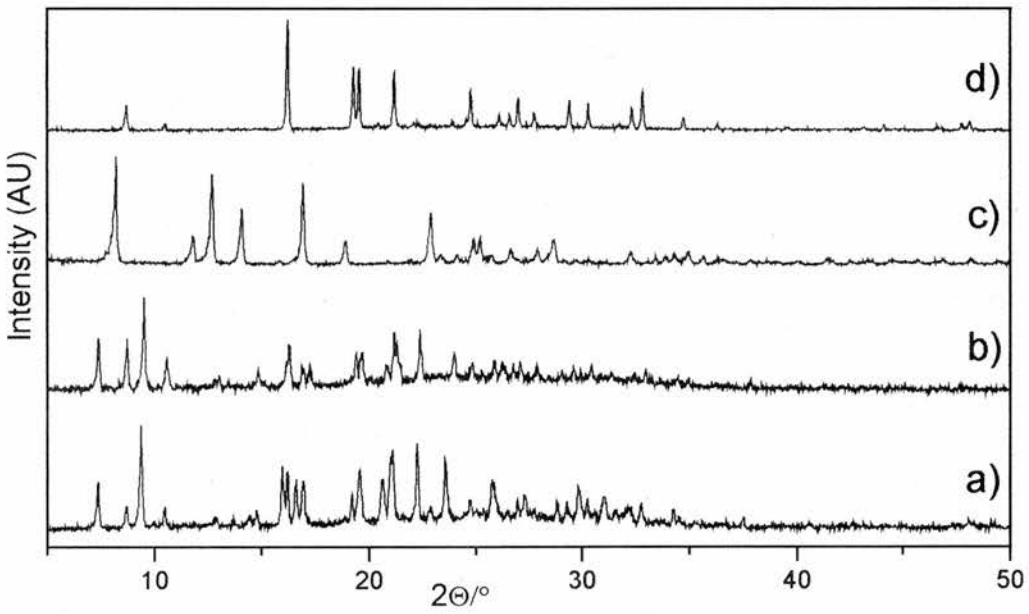

Figure 3.25. X-Ray diffraction pattern of the phases obtained employing cyclam and nickel as structure directing agent (table 3.14): a) mixture of Ni-MgAPO-5 (AFI), Ni-MgAPO-18 and impurities 'as-prepared', b) the above mixture calcined at 600 ℃, c) the chain phase NiAPO-cyclam-1 and d) Ni-SAPO-STA-6 tetragonal.

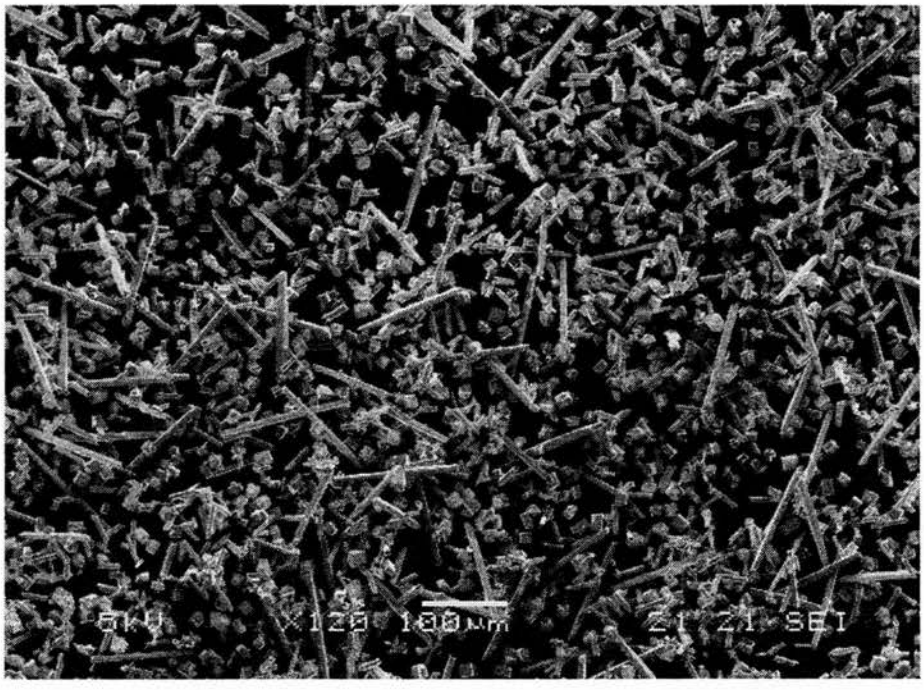

Figure 3.26. SEM micrographs of the mixture of MgAPO-5 (needles) and MAPO-18 (blocks) showing there are mainly two different crystal morphologies.

3.3.4. Ni-cyclam and extra-bases as additives

Following the comparison with the Ni-TMC system, syntheses with the co-bases tetraethylammonium hydroxide and ethylenediamine were performed with cyclam instead of tetramethylcyclam in MAPO and SAPO compositions. Gel compositions and products obtained in the preparations are given in table 3.15.

In general, syntheses performed with cyclam and added TEAOH were successful in producing STA-6 and STA-7 materials, although the syntheses performed with ethylenediamine were less successful. As found for the TMC system, crystallisation of the STA-7 structure is favoured in preparations with added TEAOH. In particular, it was possible to prepare the nickel-containing version of the MgAPO-STA-7 structure when tetraethylammonium was added to the synthesis gel, although it was necessary to reduce the amount of extra-base to avoid the co-crystallisation of AlPO-5.

MATERIAL	Experiments with added TEAOH		Experiments with added ethylendiamine	
	TEAOH/1P	PRODUCT	en/1P	PRODUCT
Ni-MgAPO	0.10	STA-7	0.18	Ni-STA6 (tetr)
Ni-ZnAlPO	0.25	STA-7	0.18	unknown mixture
Ni-CoAlPO	0.25	STA-7/AFI	0.18	Dense phase
Ni-SAPO[a]	0.25	STA-6 (tetr)	0.18	Ni-cyclam-1
SAPO[a]	0.25	STA-7	-	-

Table 3.15. Products of syntheses of MAPO materials performed in the presence of TMC and Tetraethylammonium (TEAOH) or ethylendiamine (en) as extra-bases. Cation ratio in MAPO gels were 0.2 Metal: 0.8 Al: 1P: 60 H_2O: 0.125 Cyclam: 0.125 Ni(when stated). Composition for the SAPO preps was as follows: 1 Al: 0.25 Si: 0.75 P: 400 H_2O: 0.125 cyclam: 0.125 Ni (when indicated). All gels heated for two days at 190°C.

Ni-ZnAlPO and Ni-CoAlPO gels containing TEAOH crystallised as STA-7 and a mixture of STA-7 and AlPO-5 respectively, the AlPO-5 probably being templated by tetraethylammonium ions. The Ni-SAPO composition gave a poor yield of yellow needles of the tetragonal STA-6 structure (by XRD). As in the case of the TMC, when no nickel was added to the SAPO preparation, a pure sample of the STA-7 material was obtained. As discussed previously, this is of interest because it provides a route to SAPO-STA-7 material.

EDX analysis performed in these samples showed a cation ratio of Ni: Mg: Al: P/ 0.06: 0.26: 0.77: 1 for the Ni-MgAPO-STA-7 ; Ni: Zn: Al: P/ 0.093: 0.27: 0.85: 1 and Si:P:Al/ 0.23: 0.56: 1 for the SAPO. UV-Visible spectroscopy on the Ni-MgAPO-STA-7 and Ni-ZnAlPO-STA-7 shows a similar transition to those observed with Ni-TMC indicating the nickel is in square planar co-ordination.

The SAPO-STA-7 was characterised further by solid state MAS NMR. The ^{31}P MASNMR spectrum consists of one resonance (δ ~-30ppm) corresponding to

phosphorus tetrahedrally coordinated to aluminium through oxygen. ^{27}Al MASNMR of the same sample shows very sharp and intense resonance at 41 ppm, from tetrahedrally-coordinated species, with much smaller peaks from species with higher coordination. ^{31}P MASNMR gives a single signal centred at -31 ppm, consistent with phosphorus surrounded by four -OAl- linkages.^{29}Si MASNMR gives a single resonance at -87.6 ppm, which indicates that the silicon substitutes directly for phosphorus. ^{13}C MASNMR performed on the SAPO STA-7 material prepared in the presence of cyclam and tetraethylammonium ions gave a poorly defined spectrum, with a sharp peak at 8 ppm and broader resonances from 20 to 25 ppm and 30 to 55 ppm). The resonance at 8 ppm is assigned to $-CH_3$ of the included tetraethylammonium ions.

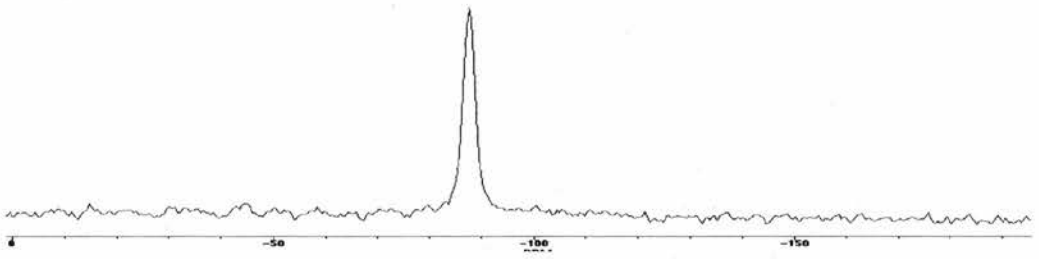

Figure 3.27. ^{29}Si MASNMR spectrum of SAPO-STA-7 prepared with Cyclam and TEAOH indicates that silicon substitutes for phosphorus in the framework.

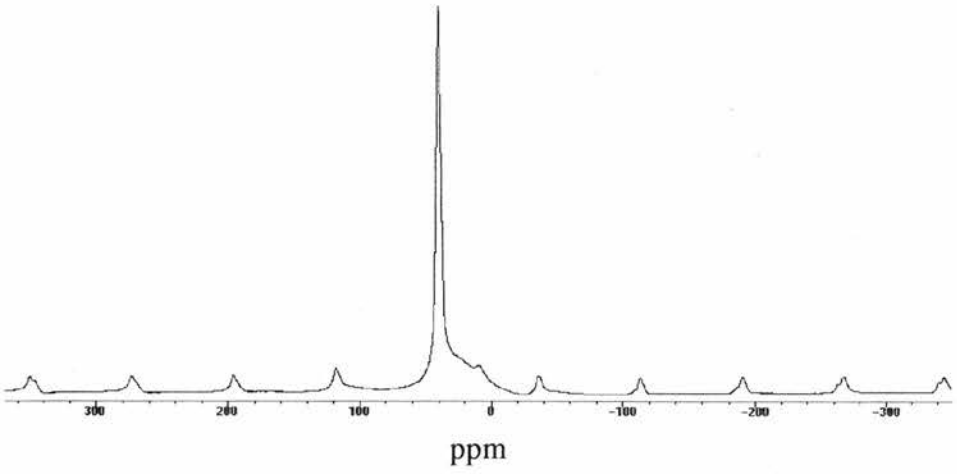

Figure 3.28. ^{27}Al MASNMR spectrum of SAPO-STA-7 prepared with Cyclam and TEAOH, corresponding mainly to tetrahedral aluminium species.

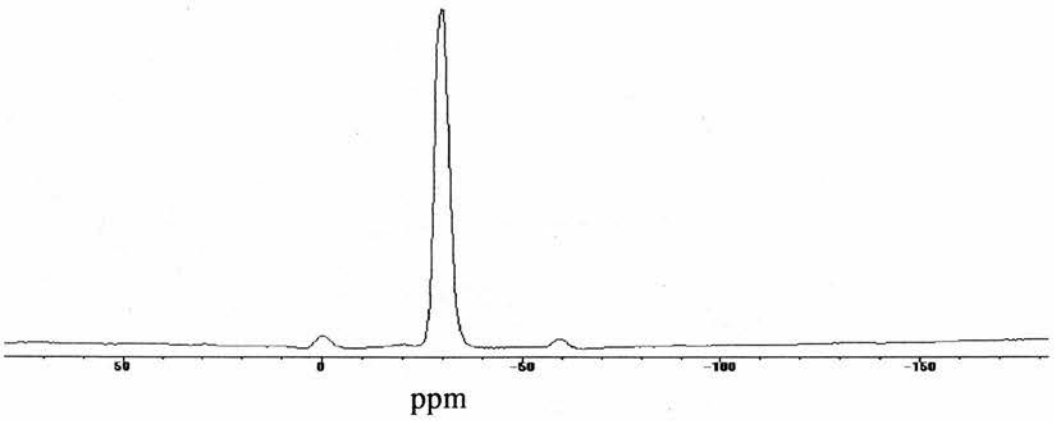

Figure 3.29. ^{32}P MASNMR spectrum of SAPO-STA-7 prepared with Cyclam and TEAOH.

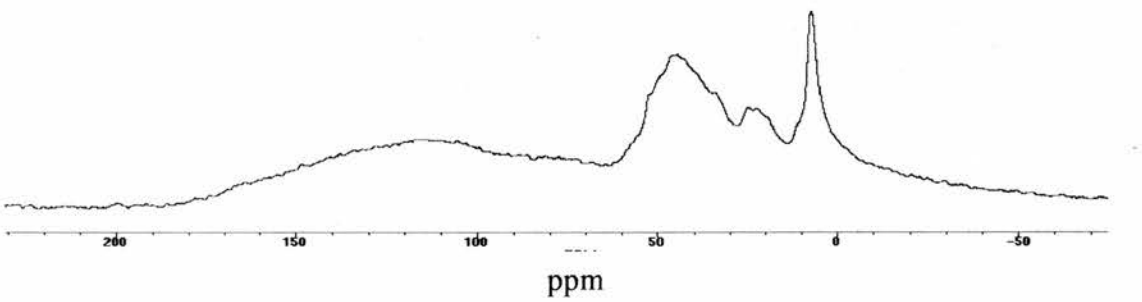

Figure 3.30 ^{13}C MASNMR spectrum of SAPO-STA-7 prepared with Cyclam and TEAOH. Despite the poor low quality, the signal at 8 ppm can be attributed to the methyl groups from the tetraethylammonium cations within the framework.

The nitrogen adsorption isotherm performed in a calcined sample of this material (figure 3.31) revealed that it adsorbs 18.5 wt% of nitrogen resulting in an internal micropore volume of 0.21 cm^3/g, comparable to that of the similar material SAPO-34, typically 0.25 cm^3/g[34].

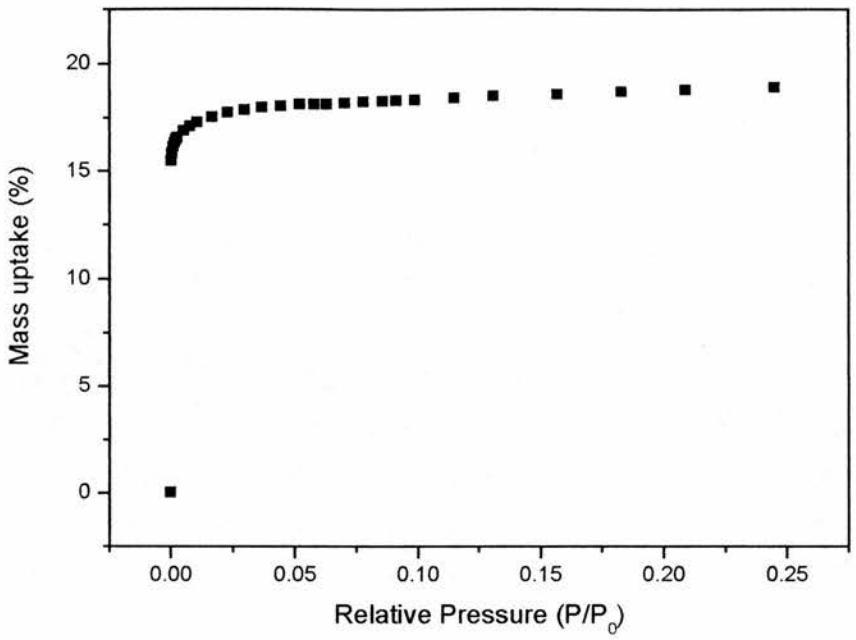

Figure 3.31. Nitrogen adsorption isotherm of calcined SAPO-STA-7 synthesised with cyclam-TEAOH.

Results of elemental analysis and TGA are shown in table 3.16. In particular the C/N ratio of SAPO-STA-7 is higher than expected for cyclam (2.5) and is at least for SAPO-STA-7, closer to that expected for a 1:1 ratio of cyclam and TEAOH (3.6).

Sample	Elemental analysis					TGA		
	%C exp.	%H exp.	%N exp.	C/N exp[a]	% Total organic[b]	W1[c]	W2[d]	W3[f]
Ni-MgAPO-STA-7	8.34	2.16	3.48	2.79	13.98	3.18	14.68	0.05
Ni-ZnAPO-STA-7	10.27	2.33	4.54	2.64	17.14	3.18	14.21	0.87
SAPO-STA-7	7.26	2.59	2.59	3.27	12.44	6.66	14.88	0.04

Table 3.16. Results of the elemental analysis of the samples given in wt% and the loss of weight by TGA. a: molar C/N experimental ratio; b: Total % of organic content determined by elemental analysis; W1: weight loss between 25-250°C; W2: weight loss between 250-700°C; W3: weight loss between 700-1000°C

3.3.4.1. Characterisation of the tetragonal form of Ni(cyclam)-MgAPO-STA-6

Syntheses performed with cyclam and ethylenediamine were not as effective for the preparation of STA-6 and 7 as those performed with tetramethylcyclam. However the Ni-MgAPO preparation with ethylenediamine produced a pure sample of yellow needles of the tetragonal STA-6 (figure 3.32). EDX performed in the Scanning electron microscope show the crystals to have a cation composition of Ni:Mg:Al:P/0.06:0.28:0.71:1. UV-Visible spectroscopy shows the nickel to be in square planar co-ordination with a transitition at ~444 nm. Microanalysis performed on the sample show the added amine is not incorporated within the final solid, the measured molar ratio C/N of 2.3 being similar that of cyclam (2.5).

Figure 3.32. SEM picture of Cyclam-en-MgAPO-STA-6 tetragonal.

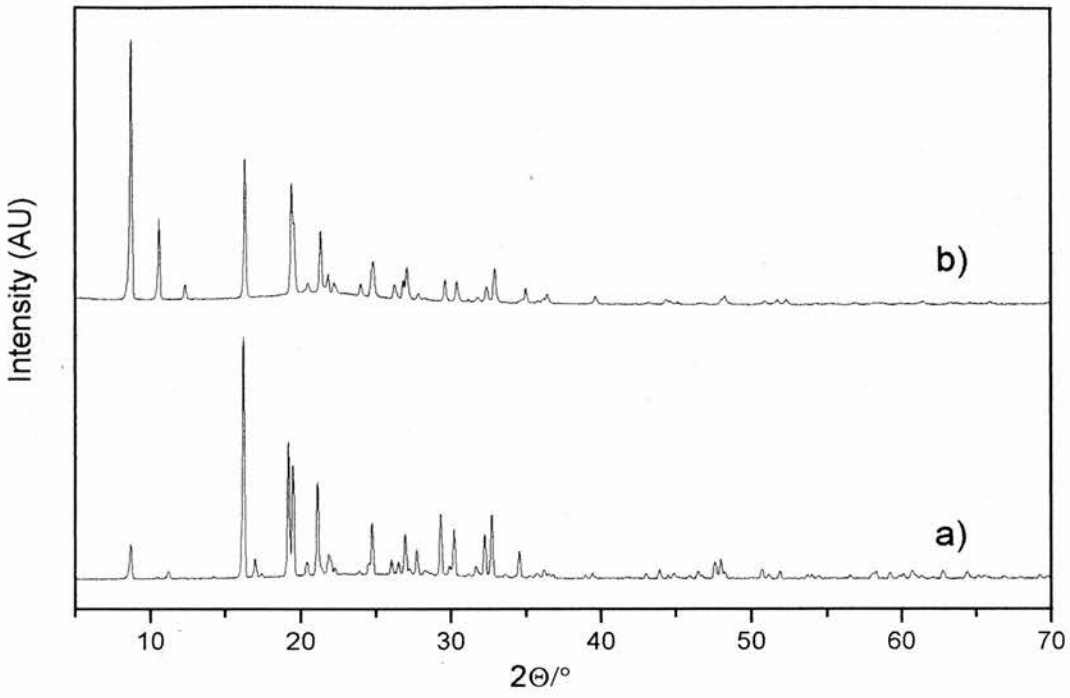

Figure 3.33. Powder XRD of the Ni-MgAPO-STA-6 structure prepared with cyclam and ethylenediamine a) as made material; b) calcined at 550°C for 700 minutes in oxygen.

3.3.5. Ni K-edge EXAFS Studies of as-prepared STA-6 and STA-7 materials containing nickel-azamacrocycle complexes.

Quantitative information on the local environment of the metal cation within the as-prepared materials can be obtained from X-ray absorption studies by analysis of the Extended X-Ray Absorption Fine Structure (EXAFS). The XRA spectra at the Ni K-edge were collected for three of the as-prepared materials: Ni-CoAlPO-STA-6 with minor STA-7 synthesised with TMC as the only base, Ni-MgAPO-STA-6 prepared with cyclam and ethylenediamine and finally, the Ni-cyclam AlPO layered phase prepared in the experiments with a Ni-SAPO gel composition, cyclam and ethylenediamine as the co-base (the final material has an AlPO composition) that is expected to have an analogous structure to $CoAlP_2O_8H$[8]. The state of nickel after calcination was also studied by EXAFS performed in the calcined Ni-MgAPO-STA-6 material.

On the as-prepared materials, the initial model proposed for the EXAFS fitting was in each case based on previous work[35] where a similar study was performed on a copper cyclam complex includded within layered silicate materials. The refinement was performed with the same number of coordination shells used in these works, assuming the M-C initial distances would be similar for both cyclam and tetramethylcyclam complexes. The four methyl carbon atoms of tetramethyl cyclam were included in the first M-C shell. The main differences were expected to be in the first coordination shell parameters. During the refinement distances and the Debye-Waller factors were allow to vary until a good fit to the experimental data was obtained maintaining reasonable atom-atom distances.

3.3.5.1. As-prepared Ni-CoAlPO-STA-6 (orthorhombic) with minor STA-7 impurity

The Ni K edge EXAFS spectrum of the as-prepared sample could be fitted by square planar N_4 model for the complex (fig 3.34, table 3.17). Ni-N distances of 1.9 Å are typical of low spin complexes of Ni(II)[28] and the refined M-C distances remained close to those of the proposed model. The four extra carbons atoms of tetramethyl cyclam compared to cyclam were introduced in the first Ni-C shell.

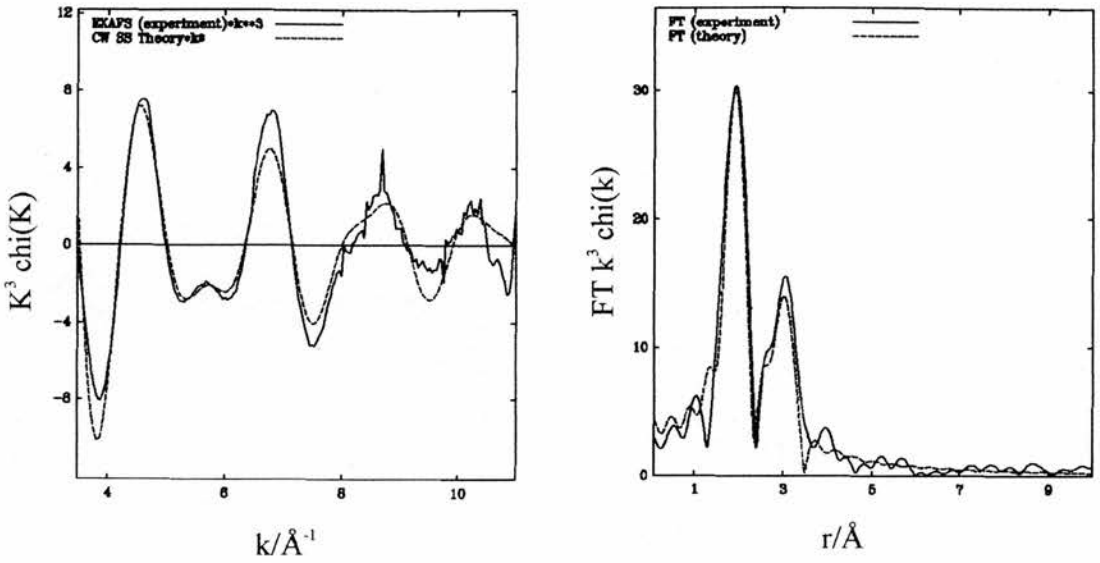

Figure 3.34. Experimental (solid line) and theoretical (dashed line) Ni K-edge EXAFS (left) and its Fourier Transform (right) for Ni-TMC-CoAlPO-STA-6/STA-7.

Atom type	Coordination number N	Distance R(Å)	Debye-Waller factor σ^2((Å)
N	4	1.978	0.012
C	8	2.815	0.029
C	4	2.958	0.012
C	2	3.346	0.003

R=29.63 %,FI=0.00069

Table 3.17. Fit Parameters for the EXAFS data of Ni-TMC-CoAlPO-STA-6/STA-7.

3.3.5.2. As-prepared Ni-MgAPO-STA-6 (tetragonal)

The EXAFS curve was fitted well by a model of nickel coordinated to the cyclam. Ni-N and Ni-C distances are similar to those found for the material prepared with tetramethylcyclam. The Ni-cyclam complex is therefore expected to possess Ni^{2+} in square planar coordination to the four nitrogens of the macrocycle.

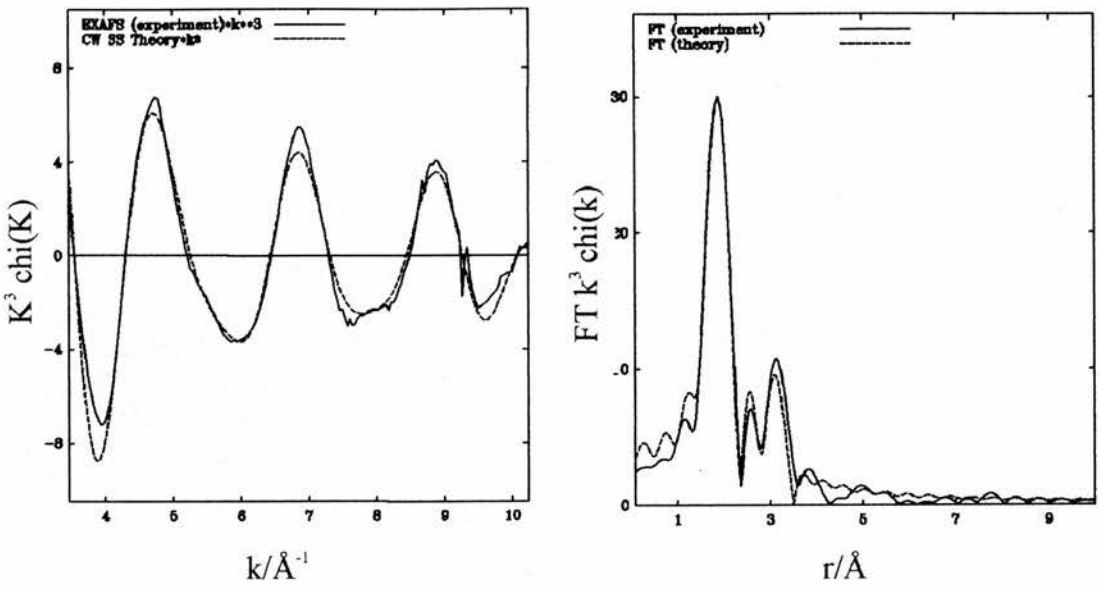

Figure 3.35. Experimental (solid line) and theoretical (dashed line) Ni K-edge EXAFS (left) and its Fourier Transform (right) for Ni-cyclam-MgAPO-STA-6 tetragonal.

Atom type	Coordination number N	Distance R(Å)	Debye-Waller factor σ^2((Å)
N	4	1.932	0.012
C	4	2.734	0.016
C	4	2.953	0.010
C	2	3.330	0.007

R=16.69 %, FI=0.00028

Table 3.18. Fit Parameters for the EXAFS data of Ni-cyclam-MgAlPO-STA-6 tetragonal.

3.3.5.3. Calcined Ni-MgAPO-STA-6 (tetragonal)

To get an insight into the state of the nickel after the calcination treatment, a sample of Ni-MgAPO-STA-6 tetr. was calcined and its EXAFS spectrum measured. Two shells are clearly observed in the Fourier Transform. The first shell could only be fitted by a four oxygen atoms at 2.04 Å. The second shell is at a longer distance and may be due to framework atoms. Hence, this shell was fitted by two phosphorus atoms coming from the framework.

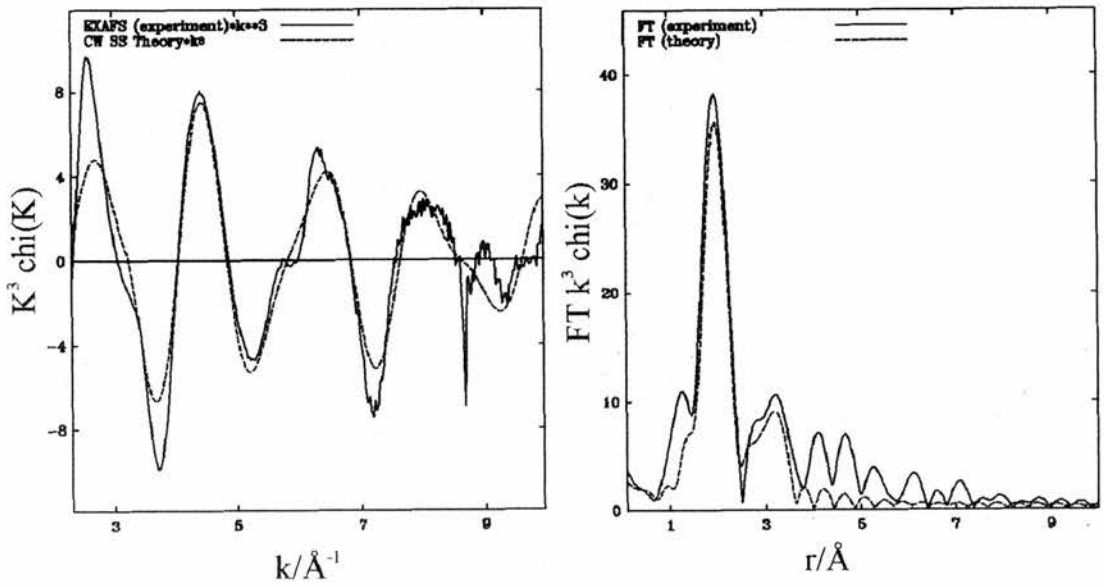

Figure 3.36. Experimental (solid line) and theoretical (dashed line) Ni K-edge EXAFS (left) and its Fourier Transform (right) for the calcined sample of Ni-cyclam-MgAPO-STA-6 tetragonal.

Atom type	Coordination number N	Distance R(Å)	Debye-Waller factor σ^2((Å)
O	4	2.037	0.012
P	2	3.149	0.012

R=34.75 %, FI=0.00083

Table 3.19. Fit Parameters for the EXAFS data of the calcined sample of Ni-cyclam-MgAlPO-STA-6 tetragonal.

3.3.5.4. As prepared Ni-cyclam-AlPO

A slightly different model was employed for this material since it is known that in the analogous cobalt-containing phase, the cobalt atom possesses a distorted octahedral coordination[8]. Hence two extra oxygen atoms were introduced in the model at typical distances found for similar complexes of this type. The Ni-N distance was also set to be 2.1 Å, typical of high spin nickel complexes[3]. After the refinement, the distances remain similar to those found for octahedral complexes of this type(figure 3.37, table 3.20).

The EXAFS analysis of these three as-prepared materials confirms that the nickel complexes are incorporated intact into the as-prepared materials, and are consistent with a square planar coordination for the complexes included into the cavities of STA-6 (and STA-7). On the calcined material, the different shape of the EXAFS curve confirms the change of coordination and even though it is more difficult to interpret, it suggest the nickel could be hexacoordinated by oxygens atoms.

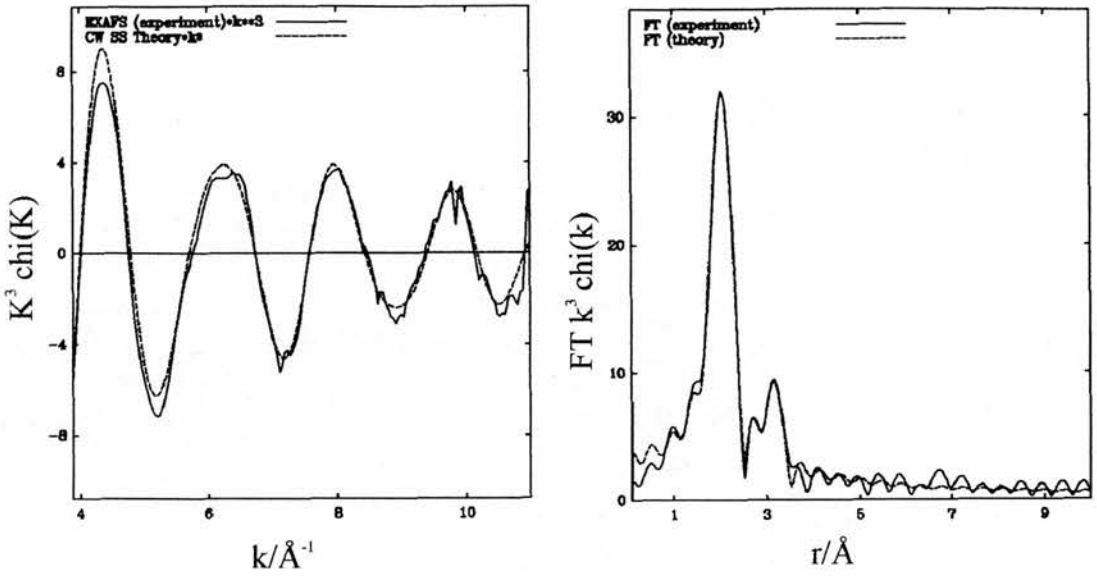

Figure 3.37. Experimental (solid line) and theoretical (dashed line) Ni K-edge EXAFS (left) and its Fourier Transform (right) for the as-prepared sample of Ni-cyclam-AlPO.

Atom type	Coordination number N	Distance R(Å)	Debye-Waller factor σ^2((Å)
N	4	2.063	0.012
O	2	2.122	0.008
C	4	2.854	0.013
C	4	3.035	0.007
C	2	3.339	0.012

R=17.85 %, FI=0.00027

Table 3.20. Fit Parameters for the EXAFS data of the as-prepared sample of Ni-cyclam-AlPO.

3.3.6 Incorporation of other metals

Incorporation of metals others than nickel was also attempted to investigate to what extent the method could be generalised. From what is observed for nickel, the other metals were chosen firstly on the basis of their ability to form complexes with cyclam-type ligands and secondly on their likely preference for coordination within amine complexes compared to inclusion within tetrahedral MO_4 framework sites.

3.3.6.1. Copper

Example of syntheses performed with copper and using extra amines as additives are shown in table 3.21. In these experiments, dark purple crystals of STA-6 and STA-7 were obtained.

Material **Cu-framework-co-base**	**Composition** **Cu:Mg: Si: Al: P: madrocycle: co-base: H_2O**	**Product**
Cu-cyclam-MgAPO-en	0.125 : 0.2 : 0 : 0.8 : 1 : 0.125 : 0.18: 60	STA-6 (orth) major
Cu-cyclam-MgAPO-TEAOH	0.125 : 0.2 : 0 : 0.8 : 1: 0.125 : 0.25: 60	STA-7 major
Cu-cyclam-SAPO	0.125 : 0 : 0.25 : 1 : 0.75 : 0.4 : 0: 200	Amorphous
Cu-TMC-SAPO-TEAOH	0.125 : 0 : 0.25 : 1 : 0.75 : 0.125 : 0.54: 200	STA7

Table 3.21. Results of syntheses performed employing copper and co-bases as additives. Gels heated at 190°C for two days.

The formation of the copper-containing magnesioaluminophosphates resulted in the successful crystallisation of STA-6 and STA-7.

Purple acicular crystals of Cu-MgAPO-STA-6 were obtained in a preparation with cyclam and added ethylenediamine. X-ray powder diffraction (figure 3.38) showed the material to be the orthorhombic variant of STA-6. This is different from the nickel preparations, where this crystallographic variant was

obtained only when using tetramethylcyclam. EDX analysis shows a cation ratio Cu:Mg:Al:P/0.1: 0.29:0.92:1 for the purple acicular crystals (Figure 3.39), confirming that copper was incorporated in the final solid. UV-Vis spectroscopy (figure 3.40) reinforced the presence of the complex within the structure showing a transition at 507.9 nm typical of Cu in square planar geometry Cu-N_4[36]. After calcination at 600 °C in oxygen, the material becomes green in colour but remains crystalline.

When tetraethylammonium was chosen as the extra base in the MgAPO preparation, dark purple tetragonal crystals of Cu-MgAPO-STA-7 were obtained (figure 3.41). Composition by EDX was found to be Cu:Mg:Al:P/ 0.07:0.33:0.89:1. Unlike the Cu-MgAPO-STA-6, after calcination at 600 °C the material recrystallised to a denser phase.

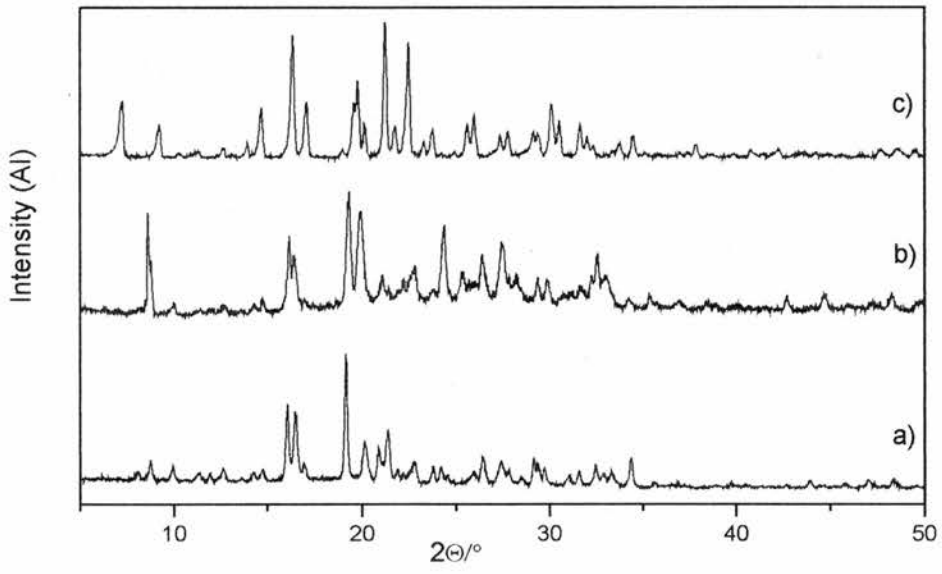

Figure 3.38. X-ray powder diffraction patterns of a) Cu-cyclam-MgAPO-STA-6 as prepared; b) Cu-cyclam-MgAPO-STA-6 after calcination in oxygen at 600 ℃ and c) Cu-cyclam-MgAPO-STA-7 as prepared.

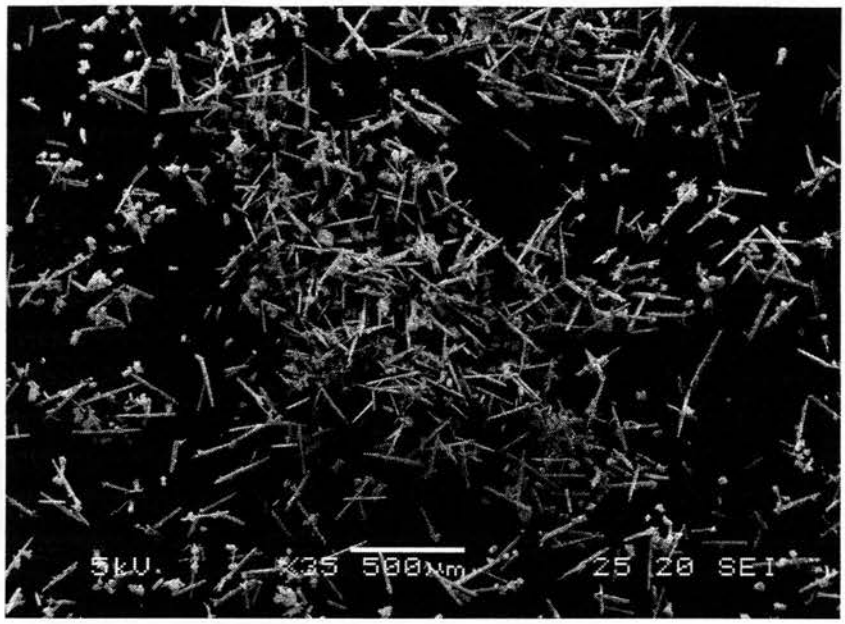

Figure 3.39. SEM picture of the Cu-MgAPO-STA-6 orth showing the needle-like crystals typical of the STA-6 materials.

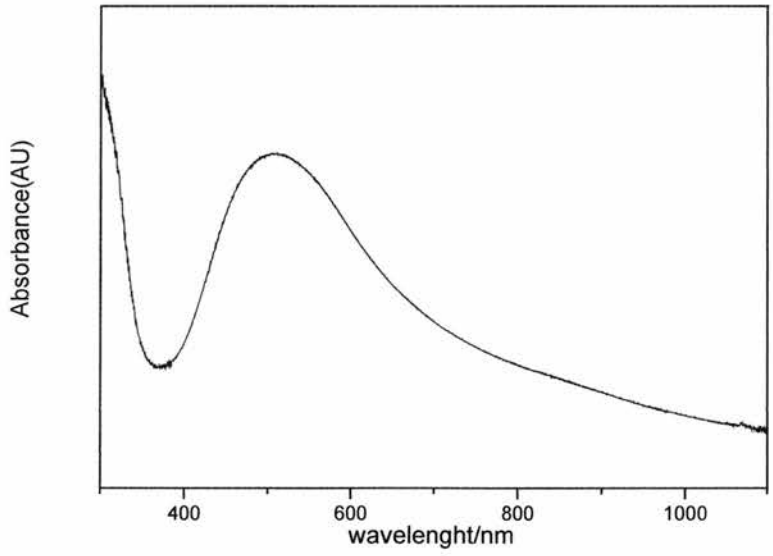

Figure 3.40. UV-visible spectrum of Cu-cyclam-MgAPO-STA-6, showing the d-d transition at 507 nm.

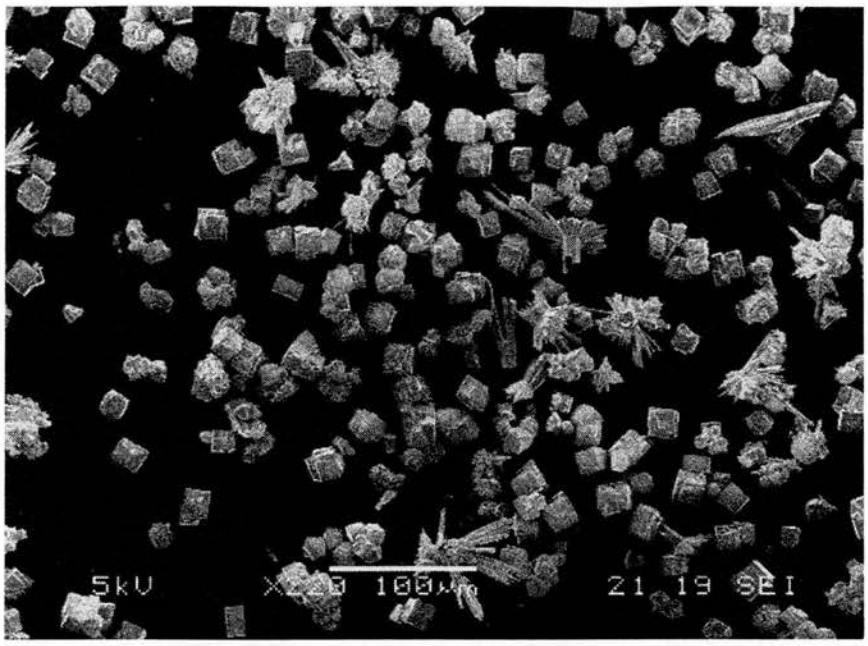

Figure 3.41. SEM picture of Cu-cyclam-MgAPO-STA-7 showing the typical cubic shape of the crystals although some impurities can also be seen.

Silicoaluminophosphate variants crystallised less readily. The SAPO-STA-6 did not crystallise in a similar preparation (Cu-cyclam-SAPO) that gave the material when nickel was used as extra-cation. However, when tetramethylammonium and tetramethylcyclam were employed with a similar gel composition that gave mixtures of STA-6 and 7 for nickel, the copper containing STA-7 material was obtained. The XRD of the sample (figure 3.42) is typical for the STA-7 structure although SEM (figure 4.43) shows the presence of amorphous material and the crystals have a different morphology to the typical tetragonal blocks showed for STA-7. Unlike the Cu-MgAPO-STA-7 described above, the SAPO variant remained crystalline after calcining in flowing oxygen at 700°C.

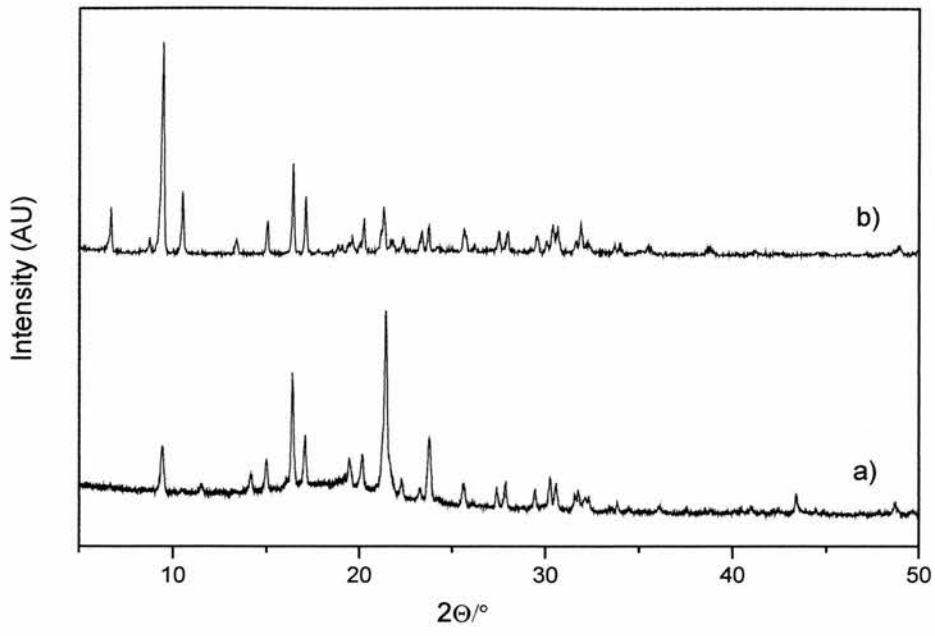

Figure3.3.42. X-ray powder diffraction pattern of Cu-SAPO-STA-7. a) as prepared material; b) calcined in O_2 at 700°C.

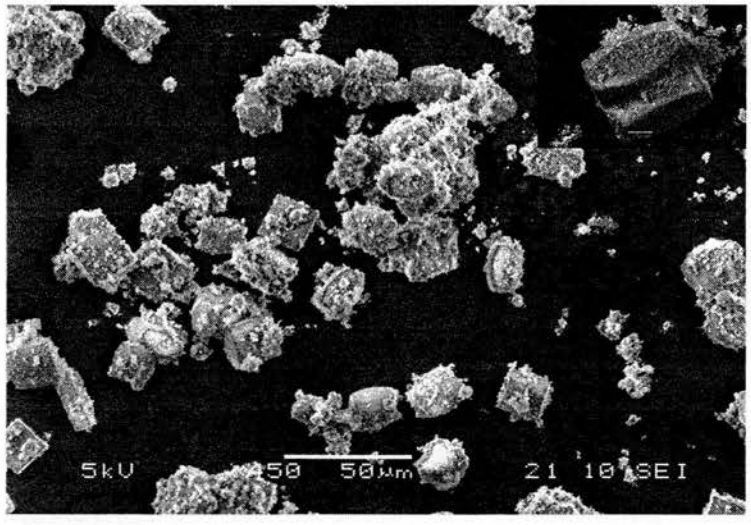

Figure 3.43. SEM showing the crystals of Cu-SAPO-STA-7. Detail of the morphology of some of the crystals on the sample.

3.3.6.2. Rhodium

Incorporation of Rh (III) was also investigated. When Rh was used in MgAPO preparations with tetramethylcyclam, well-defined crystals of STA-6 that exhibit a distortion similar to that observed for Ni-MgAPO-STA-6 (orth) were obtained. Therefore it was concluded that Rh could be incorporated in a similar way to nickel[37]. In this work, incorporation of Rh was attempted in ZnAlPO preparations (table 3.22). In all preparations light grey crystals were separated from a dark suspension of particles of metal or metal oxide precipitate.

Material	Composition	TMC	Material
Rh-TMC-ZnAlPO	0.25 Zn: 0.75 Al: 1 P: 0.1 Rh	0.5	STA-7
	0.25 Zn: 0.75 Al: 1 P: 0.05 Rh	0.5	STA-7

Table 3.22. Composition of the syntheses experiments performed with Rh and TMC.

Notably, for the Rh-ZnAlPO preparations, STA-7 was obtained instead of the distorted STA-6 structure, and the peak intensities are different from the ZnAlPO-STA-7 prepared in the absence of Rh. The crystals were of sufficient quality for single crystal diffraction analysis[§], which showed that complexed rhodium is located at partial occupancy in the STA-7 supercages (occupancy 0.5). A comparison of the observed powder diffraction data and the simulated pattern from the single crystal experiment is shown in figure 3.45. It was therefore concluded that Rh was incorporated within the ZnAlPO-STA-7, the crystallisation of STA-7 favoured by the low amount of Rh-complex incorporated within the structure.

[§] Rh-ZnAlPO-STA-7. $(Rh_1N_4C_{14}H_{40.8})$ $[Zn_{4.8}Al_{19.2}P_{24}O_{98}]$, M=438.91, Tetragonal, 0.1×0.01×0.01, a=18.7461(4) Å, c=9.4215(4) Å, V=3310.9(2) Å^3, T=293(2) K, space group P 4/n (no. 85), Z=8, μ(Mo-K_α) =1.32 mm^{-1}. The final R(obs) was 0.0934 with ωR(F)=0.1870.

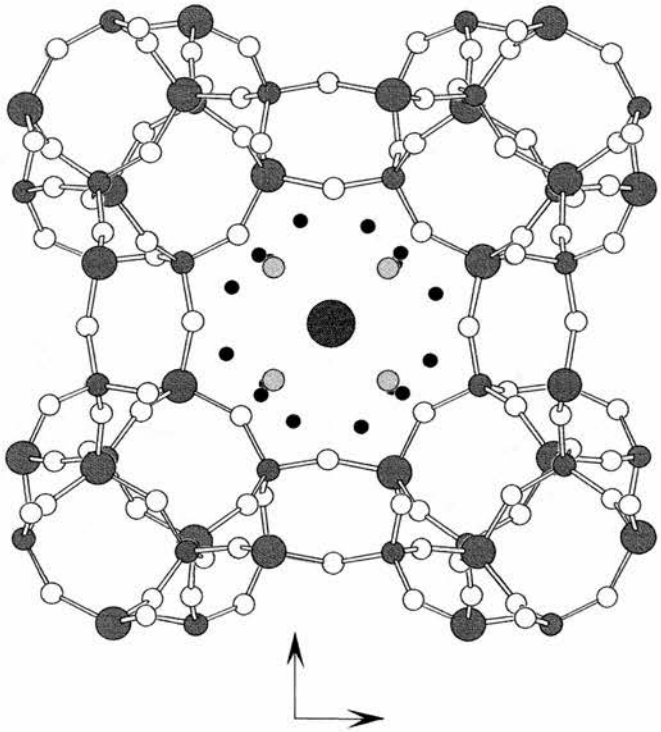

Figure 3.44. Crystal structure of Rh-ZnAlPO-STA-7 showing the location of Rh within the STA-7 cage. Rh was refined with a 0.5 occupancy by single crystal X-ray Diffraction analysis. (Key: Al medium hatched; P,small hatched; O,small white;Rh, large cross grey hatched; N,smal light grey; C, small black)

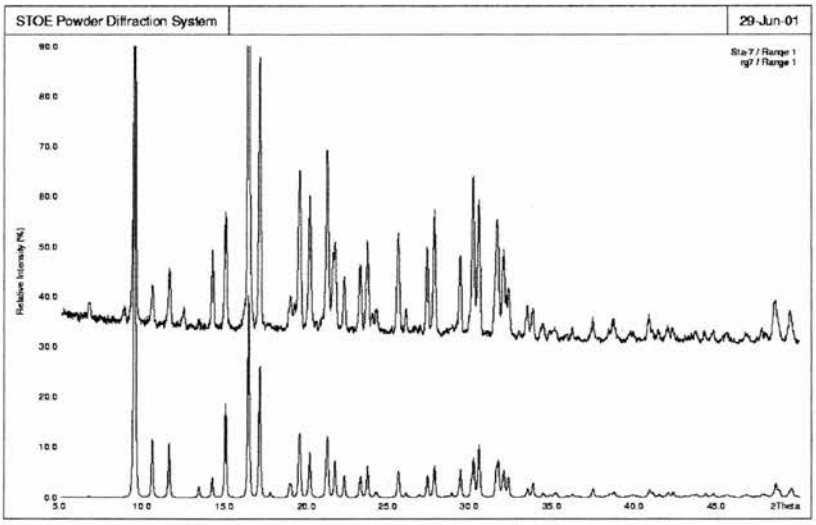

Figure 3.45. Comparison between the observed (top) and simulated (bottom) X-ray powder diffraction patterns of Rh-ZnAlPO-STA-7.

Rh K-edge EXFAS was performed on the Rh-ZnAlPO material to confirm it is included within a complex rather than as a metallic or oxide particles. The analysis shows the Rh complexed to four nitrogens. The fit and the shape of the EXAFS curve is very similar to that of the Ni-CoAlPO-STA-6/7 material, supporting a square planar coordination model for the Rh.

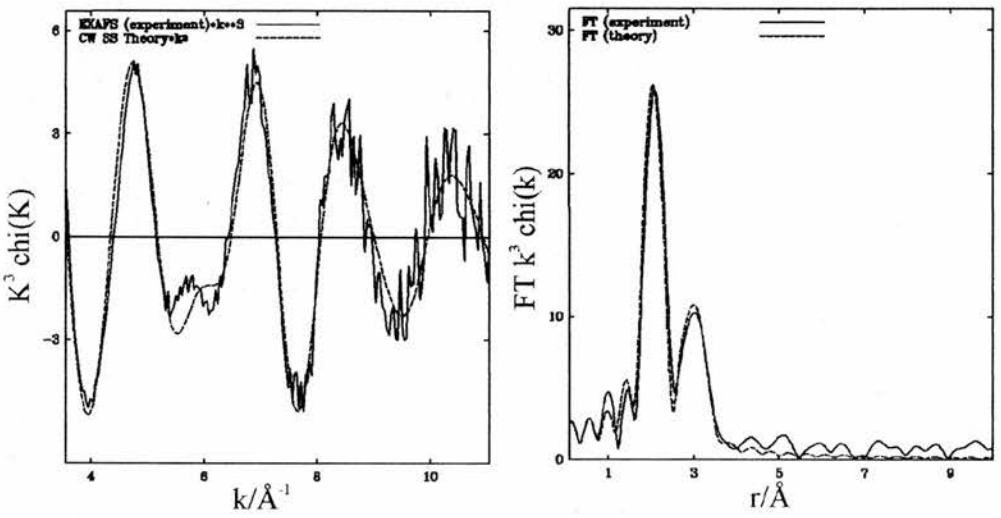

Figure 3.46. Experimental (solid line) and theoretical (dashed line) Rh K-edge EXAFS (left) and its Fourier Transform (right) of Rh-TMC-ZnAlPO-STA-7.

Atom type	Coordination number N	Distance R(Å)	Debye-Waller factor σ^2((Å)
N	4	2.080	0.007
C	8	2.540	0.017
C	4	2.913	0.017
C	2	3.391	0.008

R=29.05 %,FI=0.00061

Table 3.23. Fit Parameters for the EXAFS data of the calcined sample of Rh-TMC-ZnAlPO-STA-7

3.4 SUMMARY AND CONCLUSIONS

Synthesis using Ni-macrocycle complexes

In this work we have found that nickel complexed to cyclam or tetramethylcyclam can be incorporated within MAPO-STA-6 and STA-7 structures and SAPO-STA-6 frameworks producing materials in which the nickel remains complexed to the macrocycle, the charge of the complex being balanced by the negative charge of the framework. The nickel remains in the materials in square planar geometry as shown by UV-visible spectroscopy, magnetic measurements and EXAFS spectroscopy. EXAFS performed on samples containing the nickel complexed to the tetramethylcyclam and on samples containing nickel complexed to cyclam, has confirmed the square planar co-ordination of the nickel.

Extra bases can be used together with the macrocycle to produce these materials with a more efficient use of the macrocycle. Remarkably, TEAOH has been shown to favour the formation of the STA-7 structure acting as a co-template. This will be discussed in more detail below.

STA-6 can be prepared with nickel (II) azamacrocycle complexes with both tetragonal and orthorhombic symmetry. The orthorhombic distortion is only observed for the materials prepared in the presence of nickel and tetramethylcyclam as a template whilst those prepared with nickel and cyclam show tetragonal symmetry. Reducing the amount of nickel in the starting gel in preparations containing tetramethylcyclam as template removes the distortion and gives tetragonal STA-6. In order to investigate this further, energy minimisation studies of the effect on the structure of the STA-6 upon inclusion of the protonated TMC and the Ni(TMC) complex were performed by P.A.Cox(Portsmouth). First the framework structure was modelled without symmetry constraints and for the full unit cell. The framework adopted tetragonal symmetry (a=b=14.04Å). Upon adding the protonated TMC within the STA-6 cage (in a geometry previously optimised within a tetragonal unit cell) and permitting the refinement of the framework and template in alternate cycles without symmetry constraints, the unit cell remained

close to tetragonal (a=14.25 Å, b=14.29 Å). Inputting into the STA-6 cage the Ni(TMC) complex in the trans-III configuration, again the geometry of which had been previously optimised, the degree of orthorhombicity increased markedly (a=14.01 Å, b=14.44 Å). These preliminary results suggest the incorporation of the nickel within the methylated macrocycle to be the reason producing the distortion of the framework since the STA-6 materials produced in the absence of nickel do not present this distortion. The materials prepared with nickel and cyclam instead of tetramethylcyclam do not present this distortion for similar nickel loadings.

After calcination in oxygen, the nickel macrocycle complex is degraded. The nickel remains in the frameworks probably complexed to the framework oxygen and water molecules, balancing the negative charge of the framework. The Ni(II) is accessible to hydrogen and can be reduced by heating in a hydrogen atmosphere producing Ni(I) species that can be characterised by ESR spectroscopy.

Tetraethylammonium as a co-template

As shown in the *Results and Discussion* section, the presence of tetraethylammonium in the synthesis gels tend to produce the STA-7 structure even in the presence of nickel either for the cyclam or tetramethylcyclam preparations. Different characterisation techniques have shown that in the final STA-7 structures the tetraethylammonium remains incorporated in the secondary cages in this structure. Final confirmation and location of the presence of this molecule on the STA-7 structure was given by the single crystal structure analysis of the CoAlPO-STA-7 and Ni-SAPO-STA-7 that shows the TEAOH resides in the secondary channel system of this material.

Ni-SAPO-STA-7 has not be obtained pure even though the SAPO-STA-7 composition can be prepared without the presence of nickel for both TMC and cyclam. In the case of tetramethylcyclam, the reason seems to be the stabilisation of the STA-6 (orth) structure when nickel is added to the gel, since even the Ni-MgAPO preparation in the presence of TEAOH yielded this structure and STA-7 was only obtained for the Ni-CoAlPO and Ni-ZnAlPO preparations.

Therefore, this work has broadened the compositional spectrum in which the STA-6 and STA-7 materials can be prepared. A summary of the preparations and the products obtained in this work is given in table 3.24.

Other metals such as Cu or Rh (although the latter only in small quantities) can be incorporated in extraframework positions. Copper can be incorporated within the macrocycle in the MgAPO-STA-6 and –7 structures and within the SAPO-STA-7. These materials could potentially be active catalysts in the decomposition of NO.

No additives

	Macrocycle	
	TMC	Cyclam
Ni-MgAPO	STA6 orth	AFI/AEI
Ni-ZnAlPO	STA-6 orth	Amorphous
Ni-CoAlPO	STA-6 orth/STA-7	CoAPO-cyclam-1
Ni-SAPO	STA-6 oth	STA-6 tetrag.

TEAOH Preparations

	Macrocycle	
	TMC	Cyclam
Ni-MgAPO	STA6 orth	STA7+AFI minor
MgAPO	STA-7	MgAPO-STA7+AFI
Ni-ZnAlPO	STA-7	STA-7
Ni-CoAlPO	STA7+AFI	AFI
Ni-SAPO	STA6/7	STA-6
SAPO	STA-7	SAPO-STA7

Ethylenediamine Preparations

	Macrocycle	
	TMC	Cyclam
Ni-MgAPO	STA6 orth	STA-6 tet
Ni-ZnAlPO	STA6 orth/7 and AFI	Mixture crystalline phases
Ni-CoAlPO	STA-6 orth	Dense phase
Ni-SAPO	Mostly amorphous	NiAPO-cyclam-1

Table 3.24. Summary of the different composition and products (by XRD) prepared in this work.

3.5. REFERENCES

1. A. E. Martell, R. D. Hndcock, R. J. Motekaitis, *Coord. Chem. Rev.*, 1994, **133**, 39.

2. J. Rivas-Gisbert, *Química de Coordinación*, Edicions Universitat de Barcelona, 2000.

3. E. C. Constable, *Coordination Chemistry of Macrocyclic Compounds*, Oxford Chemistry Primers, Oxford University Press, 1999.

4. A. Bianchi, M. Micheloni, P. Paleotti, *Coord. Chem. Rev.*, 1991, **110**, 17

5. a) R. D. Hancock, S. M. Dobson, A. Evers, P. W. Wade, M. P. Ngwenya, J. C. A. Boeynes, K. P. Wainright, *J. Am.Chem. Soc.*, 1988, **110**, 2788; b) R. D. Hancock, A. Evers, M. P. Ngwenya, P. W. Wade, *J. Chem. Soc. Chem. Commun.*, 1987, 1129

6. a) L. Schreyeck, D'agosto, J. Stumbe, P. Caullet, J.C. Mougenel, *Chem. Commun.*, 1997, 1241.; b) L. Schreyeck, P. Caullet, J. C. Mougenel, B. Marler, 1999, *12th International Zeolite Conference*, Materials Research Society, p.p. 1731; c) L. Schreyeck, J. Stumbe, P. Caullet, J. C. Mougenel, B. Marler, *Micro. Mesoporous Materials*, 1998, **22**, 87.

7. L. Schreyeck, P. Caullet, J. C. Mougenel, B. Marler, *Micro. Mesoporous Materials*, 2001, **42**, 177

8. M. J. Maple, E. F. Philp, A.M.Z. Slawin, P.Lightfoot, P.A. Cox and P.A. Wright, *J. Mater. Chem.*, 2001, **11**, 98.

9. a)D. S. Wragg, G. B. Hix, R. E. Morris, *J. Am. Chem. Soc.*, 1998, **120**, 6822.; b)T. Wessels, L. B. McCusker, C. Baerlocher, P. Reinert, J. Patarin, *Micro. Mesoporous Materials*, 1998, **23**, 373.

10. D. S. Wragg, R. E. Morris, *J. Mater. Chem.*, 2001, **11**, 513

11. P.S.Wheatley, C.J.Love, J.J.Morrison, I.J.Shannon and R.E.Morris, *J. Mater. Chem.*, 2002, **12**, 477.

12. a) V. Patinec, P. A. Wright, P. Lightfoot, R. A. Aitken and P. A. Cox, *J. Chem. Soc. Dalton Trans.*, 1999, 3909 b) P. A. Wright, M. Maple, A. M. Z. Slawin, V. Patinec, R. A. Aitken, S. Welsh and P.A. Cox, *J. Chem. Soc. Dalton Trans.*, 2000, 1243.

13. Personal Communication

14. P. S. Wheatley, R. E. Morris, *J. Solid State Chem.*, 2002, **167**, 267

15. N. Rajic, D. Stojakovic, V. Kaucic, *Zeolites*, 1991, **11**, 612

16 S. P. Elangovan, V. Krishnasamy, V. Murugesan, *Bull.Chem.Soc.Jpn.*, 1995, **68**, 3659

17. M. Hartmann, L. Kevan, *Chem. Rev.*, 1999, **99**, 635

18. E. F. Philp, *Final Year Project*, St Andrews University, 2000.

19. A.C.Larson, R.B.von Dreele, Generalised Crystal Structure Analysis System, Los Alamos National Laboratory, USA, 1994.

20. G.M.Sheldrick, SHELXS, University of Göttingen, 1986; SHELXTL, version 5.3, Program for the solution of crystal structures, University of Göttingen, 1993.

21. (a) Le Bail, *J.Solid State Chem.*, 1989, **83**, 267; (b) A. C. Larson and R.B. von Dreele, Generalized Crystal Structure Analysis System, Los Alamos Laboratory, USA, 1998.

22. Y. Kustanovich, D.Goldfarb, *J.Am.Chem.Soc.*, 1991, **95**, 8818

23. J. Chen, P. A. Wright, J. M. Thomas, S. Natarajan, L. Marchese, S.M. Bradley, G. Sankar, C. R. Catlow, P. L. Gai-Boyes, R. P. Townsend, C. M. Lok, *J. Phys. Chem.*, 1994, **98**, 10216

24. N. Herron, P.Moore, *Inog.Chim. Acta*, 1979, **36**, 89

25. A.B.P.Lever, *Inorganic electronic spectroscopy*, Studies in Physicsl and Theoretical Chemistry, Elsevier, 1984.

26. E.K. Barefield, F. Wagner, *Inorg. Chemistry*, 1973, **12**, 2435

27. a)N. Azuma, M. Hartmann, L. Kevan, *J. Phys. Chem.* 1994, **98**, 1221; b) M. Hartmann, N. Azuma, L. Kevan, *J. Phys. Chem.* 1995, **99**, 10988

28. L. Fabbrizzi, *J. Chem. Soc. Dalton Trans.*, 1979, 1857

29. (a) P.Moore, J.Sachinidis and G.R.Willy, *J. Chem. Soc. Chem. Commun.*, 1983, 522.; (b)T.W. Hambley, *J. Chem. Soc., Dalton Trans.*, 1986, , 565.

30. F. Wagner, M. T. Mocella, M. J. D'Aniello jun., A. H-J. Wang, E. K. Barefield, *J. Am. Chem. Soc.*, 1974, **96**, 2625

31. S. I. Zones, S. –J. Hwang, *Chem. Mater.*, 2002, **14**, 313

32. R. Garcia, E. F. Philp, A. M. Z. Slawin, P. A. Wright, P. A. Cox, *J. Mater. Chem.*, 2001, **11**, 1427.

33. M. J. Maple, *Structure and Catalytic Properties of Microporous Aluminophosphates*, PhD thesis, University of St Andrews, 2003.

34. D. B. Akolekar, S. K. Bhargava, *Appl. Catal. A: General*, 2001, **207**, 355

35. (a) J. –H. Choy, D. –K. Kim, J. –C. Park, S.-N. Choi, Y. –J. Kim, *Inorg. Chem.*, 1997, **36**, 189; (b) J. –H. Choy, J. –B., Yoon, H. Jung, *J. Phys. Chem.B*, 2002, **106**, 11120.

36. A. R. Amundsen, J. Whelan, B. Bosnich, *J. Am. Chem. Soc.*, 1977, **99**, 6730

37. R. García, E. F. Philp, A.M.Z. Slawin, P.A. Wright and Paul A. Cox, *Stud. Surf. Sci. Catal.*, 2001, **135**.

4. COMPLEXES OF LINEAR POLYAMINES WITH NICKEL AS STRUCTURE DIRECTING AGENTS

4.1 INTRODUCTION

The behaviour of complexes of transition metals with linear polyamines as structure-directing agents for the synthesis of microporous materials has not been extensively explored, but they have been shown to direct crystallisation to layered phases and three dimensionally connected framework solids. The ligands have the advantages of being more readily available and less expensive than the azamacrocycles, but their complexes display lower stability than azamacrocycle or metallocene complexes under hydrothermal conditions.

Among the transition metal complexes of linear polyamines that have been studied in the synthesis of microporous materials (table 4.1), cobalt complexes are the most common.

Polyamine	Metal	Framework structure	Ref
Pyridine	Cu(II), Cu(I)	Ferrierite	1, 2
1,2-diaminoethane	Co(III)	GaPO-15	3
Diethylenetriamine	Co(III)	CoAlPO-AlPO-34	4
1,2-diaminoethane	Co(II)	layered AlPO	5
1,2-diaminoethane	Ir(III)	layered AlPO	5
Trans-1,2-diaminoethane	Co(II)	chain AlPO	5
Trans-1,2-diaminoethane	Ir(III)	chain AlPO	5
1,2-diaminoethane	Ni(II)	AlPO-34 triclinic	6
tris(1,2-diaminoethane)amine	Ni(II)	AlPO-5	7
1,2-diaminoethane	Ni(II)	VO framework	8

Table 4.1. Summary of some of the frameworks and metals that have been employed on syntheses of microporous materials with linear polyamines.

Their complexes with linear polyamines are among the most studied on synthesis of microporous materials of different compositions. They have been included in aluminophosphates[9,10], gallophosphates[11], borophosphates[12] and zincophosphates. Many of these materials are layered phases where the complex and water molecules reside in the interlayer space. There is usually a hydrogen-bonding network involving the phosphate oxygens on the layers, the coordinated amine and the water molecules. One example of this layered phases is given in figure 4.1 for the gallophosphate $[Co(en)_3][Ga(H_2PO_4)_6(HPO_4)_3]$[13]. The structure of this material consists of layers containing linked GaO_6 octahedra and PO_4 tetrahedra with the complex located in the interlayer region.

In another preparation, one of the isomers of this complex, d-$Co(en)_3[H_3Ga_2P_4O_{16}]$ was successfully used as a structure directing agent in a gallophosphate preparation, producing a three-dimensionally connected chiral framework[11] with the complex included within the pores. Each gallium is linked to four phosphate groups that bridge between two galliums (figure 4.1 bottom) The metal complex interacts with the framework electrostatically and through hydrogen bonds.

In most of the above examples the complex was pre-formed before using it as a structure directing agent.

A different complex, $Co(deta)_2^{3+}$ complex[14] was successfully incorporated in CoAlPO-34, a cobalt-substituted aluminophosphate with the chabazite framework topology (CHA). The amine and the cobalt(II) were added separately during the preparation of the gel and the complex formed "in situ" during crystallisation of the microporous host. Single crystal analysis of the material shows the $Co(deta)_2^{3+}$ complex together with two water molecules located in the cages of the CHA structure, compensating the negative charge on the framework. The complexing nitrogens were located unambiguously, but the carbon atoms of the amine showed static disorder. It is also remarkable that in this compound, cobalt is present in two oxidation states: Co(II) in framework positions and Co(III) in the complex, so that the final solid contains mixed valence cobalt.

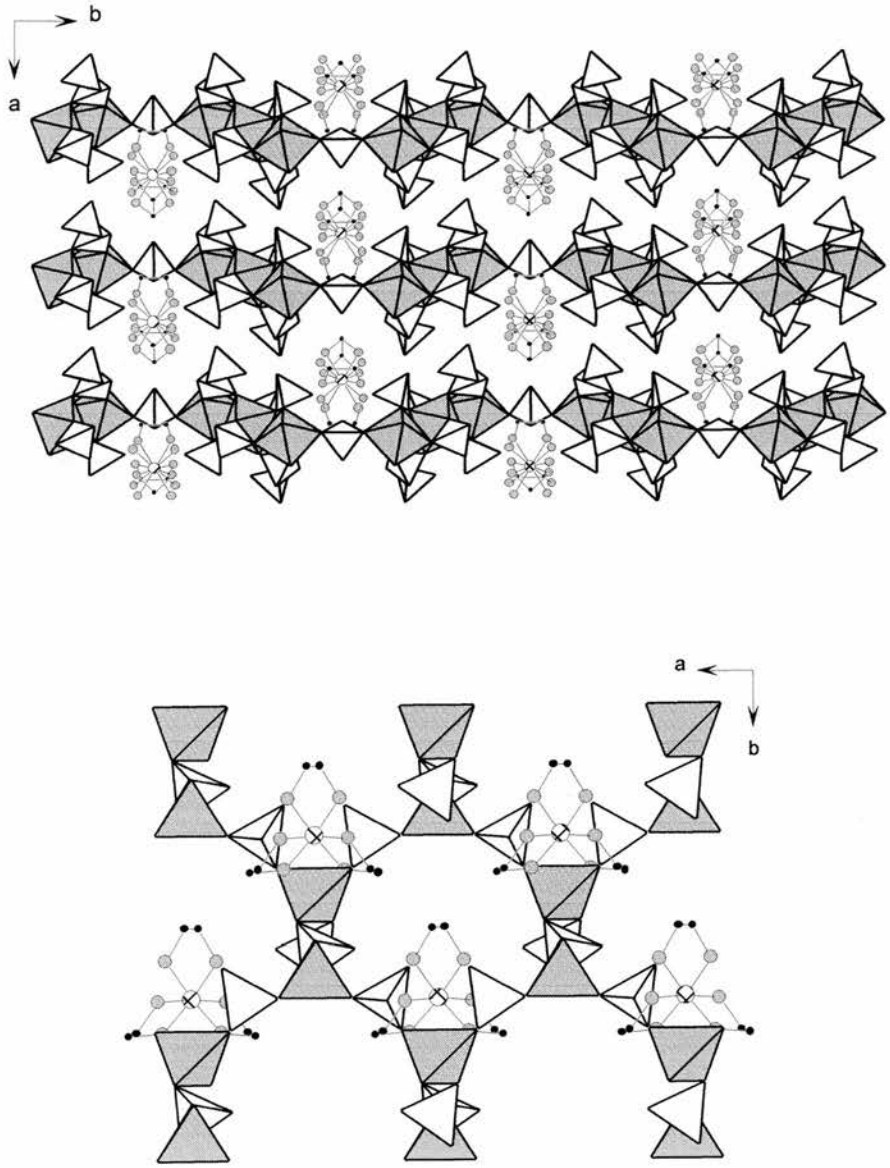

Figure 4.1. <u>*Top*</u>*: View of* $[Co(en)_3][Ga(H_2PO_4)_6(HPO_4)_3]$ *down the c axis, showing the inorganic phosphorous and gallium layers with the cobalt ethylenediamine complex between them. Part of the Carbon and Nitrogen atoms of the* $Co(en)_3^{3+}$ *complex are disordered. (Key:* GaO_6*,, gray octahedra;* PO_4*, white tetrahedra; N: black; C, gray, Co, hatched).*

<u>*Bottom*</u>*: View of* $[d\text{-}Co(en)_3][H_3Ga_2P_4O_{16}]$ *along the c axis showing the threedimensionally connected framework. Unlike the top framework, in this structure the gallium atoms are tetrahedrally coordinated to oxygen atoms.(Key:* GaO_4*, gray tetrahedra;* PO_4*, white tetrahedra; N, black; C, gray, Co, hatched).*

Examples of the use of other metal complexes is rarer still. Apart from the iridium complex mentioned in the general introduction, copper and nickel complexes have been used in the syntheses of vanadium oxide materials[8,15], which have shown remarkable versatility as hosts for these complexes. The diversity of coordination geometries and oxidation states exhibited by vanadium give rise to this structural flexibility. One such structure is that of $[Ni(en)_2][V_6O_{14}]$, which consists of vanadium oxide layers covalently bound to the nickel of the complexes (figure 4.2). Notably the nickel complex was not pre-prepared but rather formed *in situ* during crystallisation of the material.

There are also some examples of the inclusion of nickel-amine complexes during the synthesis of microporous aluminophosphates. In particular, Rajic and co-workers[7] employed the pre-formed bis((2-aminoethyl)amine) nickel (II) complex, $(Ni(tren)_2^{2+}$, Scheme 1 b)), in crystallisation of aluminophosphate (an extra amine was added to raise the pH of synthesis). The product was $AlPO_4$-5 with the complex incorporated in the channels of the structure. The charge of the complex was thought to be balanced by structural defects.

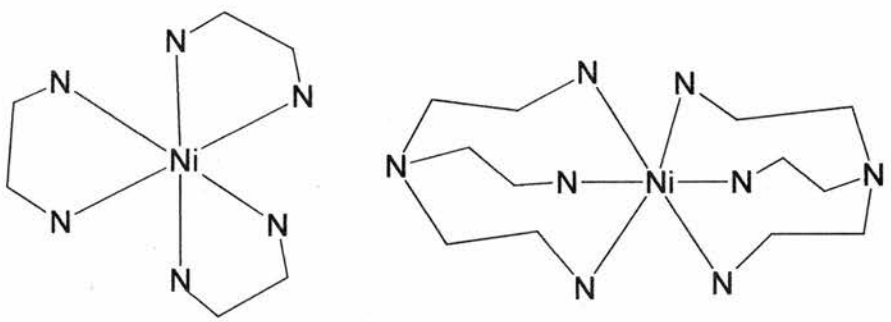

a) b)

Scheme 1. Representation of the nickel complexes a) tris(1,2-ethylenediamine)nickel (II), b) bis((2-aminoethyl)amine) nickel (II).

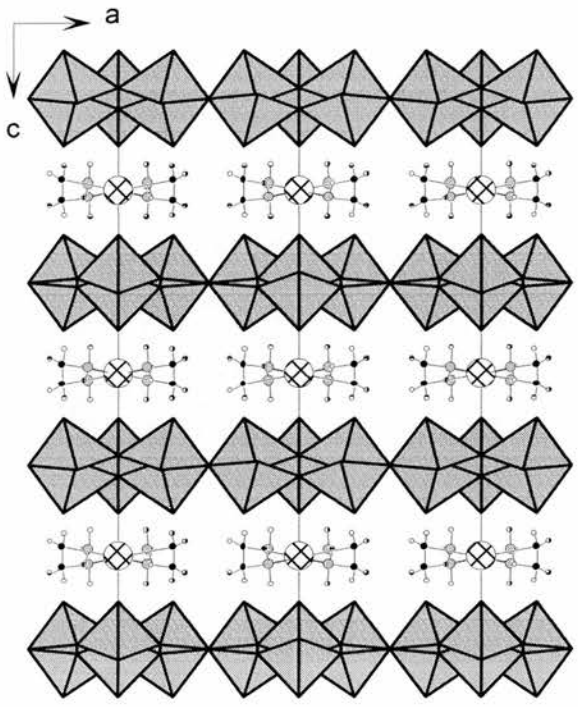

Figure 4.2. Projection of $[Ni(en)_2][V_6O_{14}]$ along the b axis. The vanadium oxide layers, $[V_6O_{14}]^{2-}$, composed of VO_5 square pyramids which are connected by Ni complexes into a three-dimensional framework with monodimensional channels. (Key: gray polyhedra: Vanadium oxide layers; Ni: big, hatched; N : gray; C: black; H: white)

These authors also employed another octahedral complex of Nickel ($Ni(en)_3^{2+}$, Scheme 1) in an aluminophosphate preparation[6]. This time instead of $AlPO_4$-5, the product was a crystallographic variant of AlPO-34[16]. During crystallisation the complex loses one of the three 1,2-diaminoethane ligands, which are replaced by two P-OH groups of the framework, causing a triclinic distortion of the rhombohedral framework. The resulting $[Ni(en)_2O_2]^{2-}$ complex resides within the large cages of the structure. Some of the P-O-Al linkages are broken and the aluminium atoms associated with this disruption become five-coordinated and form double Al-O-Al bridges while the phosphate P-O groups interact strongly with the Ni(II) complex to form an unusual P-O-Ni-O-P bridge across the cage, figure 4.3.

This triclinic distortion disappears upon calcination when the complex is removed and the fully connected chabazite-like framework is formed.

In this chapter the results of investigation of the use of nickel complexes of diethylenetriamine, dipropylenetriamine and tris(1,2-diaminoethane)amine as structure directing agents in the synthesis of aluminophosphates and substituted aluminophosphates are presented. Two synthetic approaches were taken, one employing additional bases within the AlPO, MAPO and SAPO gel crystallisation compositions, the second adopting the fluoride synthetic route[17] to syntheses of aluminophosphate fluorides containing the nickel complexes. Finally the results of these syntheses using analogous copper(II) complexes in place of nickel are described.

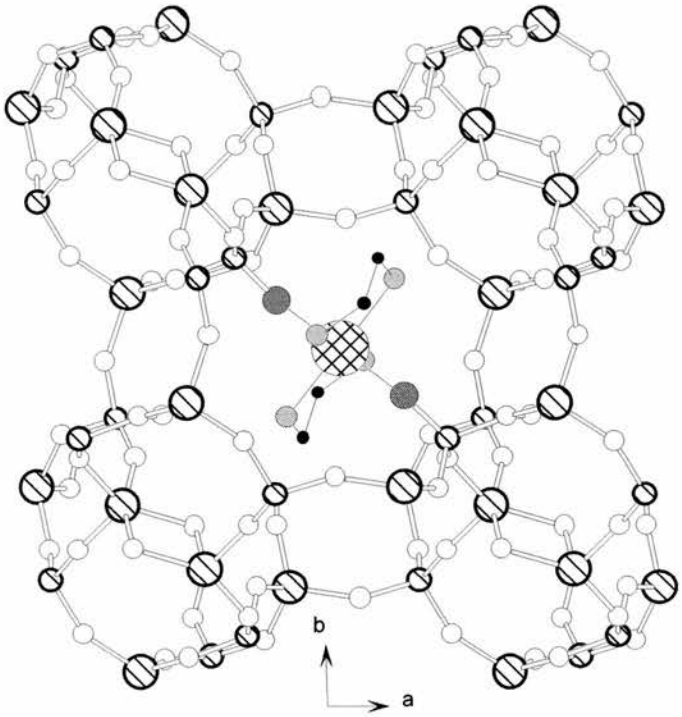

a)

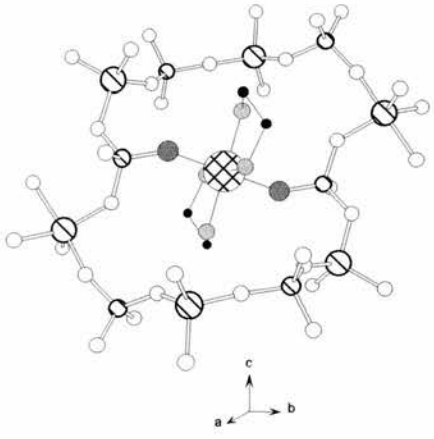

b)

Figure 4.3. Framework of the crystallographic variant of AlPO-34 synthesised with $Ni(en)_3^{2+}$. a) View of the AlPO-34 cage along the c axis; b) Detailed of the unit cell, showing the $[Ni(en)_2O_2]^{2-}$ complex formed by substituting one of the original 1,2-ethylendiamine ligands for two P-OH groups of the framework (the oxygen of this group is represented in dark grey colour for clarity). It can also be appreciated the five coordination of one of the aluminium atoms in the unit cell.(Key:Al medium hatched;P,small hatched;O,small white; Ni, large cross.hatched; N,small light gray; C, small black).

4.2 EXPERIMENTAL

4.2.1. Syntheses of Microporous Materials

A description of the procedure to prepare the complexes and the crystallisation gels is given below. The reactants employed in these preparations are given in table 4.2. Scheme 2, shows the three complexes employed in this work.

Reagent	Purity(%)	Supplier
Magnesium(II) acetate tetrahydrate	99	Fluka
Cobalt (II) acetate tetrahydrate	98	Aldrich
Copper (II) nitrate	95	Fisons
Nickel chloride hexahydrated	98	Avocado
Silica, fumed	97	Fluka
Aluminium hydroxide hydrate	-	Aldrich
Aqueous orthophosphoric acid	85	Prolabo
Diethylenetriamine	98	Avocado
N-(3-aminopropyl)-1,3-propanediamine	98	Aldrich
Tris(2-aminoethyl)amine	98	Aldrich
Di-n-propylamine	99%,	Aldrich
Tetramethylammonium hydroxide	25%	Aldrich
Tri-n-propylamine	98%	Aldrich
Triethylamine	99	BDH reagents
Decamethonium bromide	98	Aldrich
Ethylenediamine	99	Avocado
Ammonium fluoride	98	Aldrich
Silver(I) oxide	-	Johnson-Matthey

Table 4.2 List of reactants with supplier and degree of purity employed in both, preparation of the complexes and aluminophosphate-base gels.

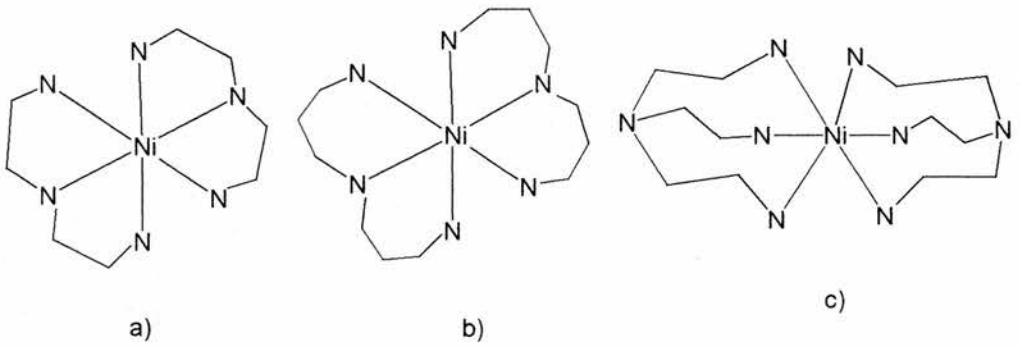

Scheme 2. The three-nickel complexes used as structure directing agents in this work: a) bis (diethylenetriamine) nikel (II); b) bis (triehylenetriamine) nickel (II); c) bis(2-aminoethyl)amine) nickel (II).

4.2.1.1. Synthesis of the complexes

The complexes were prepared following the general procedure given in reference[18] by the addition of an ethanolic solution of the metal source over an ethanolic solution of the amine while stirring in an ice bath. The precipitate formed is filtered under vacuum and left to dry. For example, in a typical preparation for bis(diethylenetriamine) nickel (II), a solution of 24.26g (0.1 mols) of nickel chloride hexahydrate in 31g of ethanol was added to a solution of 21.72g (0.2 mols) of diethylenetriamine. A purple solid precipitates and is recovered trough filtration.

The nickel complexes were all purple in colour whilst the copper one was dark blue. The four solids were characterised by C, H, N analysis and UV-visible spectroscopy, tables 4.3 and 4.4 respectively.

C,H,N contents found for the four complexes match closely those expected for the complex, supporting the complex formation in all cases. This is further confirmed by UV-visible spectroscopy.

Complex	Theoretical					Experimental				
	%C	%H	%N	C/N mol	H/C mol	%C	%H	%N	C/N mol	H/C mol
$Ni(deta)_2Cl_2$	28.6	7.7	25.0	1.33	3.25	27.4	8.3	23.8	1.33	3.63
$Ni(trien)_2Cl_2$	36.8	8.7	21.1	2.0	2.83	35.3	9.2	20.5	2.01	3.10
$Ni(tren)_2Cl_2$	33.8	9.8	26.2	1.50	3.50	29.6	8.3	22.5	1.53	3.38
$Cu(deta)_2(NO_3)_2$	24.4	6.6	28.5	1.00	3.25	24.5	6.8	28.9	0.99	3.32

Table 4.3 Results of the elemental analyses for the complexes employed as structure directing agents in the syntheses performed in this work.

Complex	Wavelength (nm)
$Ni(deta)_2Cl_2$	~349.78; ~543.37; ~861.83
$Ni(trien)_2Cl_2$	~355.06; ~562.57; ~922.83
$Ni(tren)_2Cl_2$	~350.74; ~545.28; ~886.33
$Cu(deta)_2(NO_3)_2$	~571

Table 4.4. Transitions observed in the diffuse reflectance UV-Visible spectra for the complexes used as structure directing agents in this work.

4.2.1.2. Hydrothermal Synthesis from AlPO (or MAPO/SAPO) gels

Two sets of syntheses were performed either with additional amines or with ammonium fluoride as an additive. The preparation of the gels was slightly different in each case. Gels were prepared by combining a solution of the phosphoric acid with an aqueous suspension of the aluminium hydroxide while stirring. The rest of the reactants were added to this mixture in the following order, depending on the type of synthesis: the metal cation source (generally as acetate), the organic, the complex, the silicon source and, the ammonium fluoride. The resulting gel was

stirred for one hour until homogeneous and then heated for the specified time and temperature.

In a typical preparation where additional extra amines were used to control the synthesis pH to ca 5-7, 2.26g of phosphoric acid were mixed with 1.93g of aluminium hydroxide in 8.90g of water. To this, 1g of di-n-propylamine and 0.33g of the $Ni(deta)_2Cl_2$ were finally added. The gel was stirred for one hour and was heated at 190°C for 48 hours in polytetrafluoroethylene-lined autoclaves. The final molar ratios in the gel were:

$$0.05\ Ni(deta)_2Cl_2 : 0.5\ \text{di-n-propylamine} : 1\ Al : 1\ P : 25\ H_2O$$

In a typical preparation from ammonium fluoride-containing gels, 0.54g of phosphoric acid were added over a solution of 0.45g of aluminium hydroxide in 9.77g of water. Addition of 0.38g of $Ni(deta)_2Cl_2$ and 0.0848g of ammonium fluoride to the above solution gave a gel of molar composition

$$0.25\ Ni(deta)_2Cl_2 : 0.5\ NH_4F : 1\ Al : 1\ P : 100\ H_2O$$

After one hour of stirring, the homogeneous gel was placed in autoclaves and heated for one day in the oven at 190°C. Once the thermal treatment was completed the autoclaves were taken out and allowed to cool to room temperature. The resultant crystalline products were washed with distilled water and dried at room temperature.

Previous to its use in syntheses of the microporous materials, the decamethonium bromide was converted to the dihydroxide form by stirring with silver (I) oxide in water.

4.2.2. Characterisation Techniques

4.2.2.1. Crystallography

All crystalline products were examined by X-ray powder diffraction on a Stoe STADIP diffractometer operating on monochromatic Cu $K_{\alpha 1}$ radiation. For structural analysis, powder diffraction data were collected on the Stoe STADIP diffractometer in a Debye-Scherrer geometry. Samples analysed for structural purposes were loaded in 0.7 mm silica glass capillaries and data were collected over 12 hours. Structure refinement was performed by a Rietveld method employing the GSAS suite of programmes[19].

Single crystals were examined by single crystal diffractometry on a Bruker SMART diffractometer running on MoK_{α} radiation with a FAST CCD area detector. The crystal structure was solved and refined using SHELXS and SHELXL[20]. Collection of the data, resolution and refinement of the structure were performed by Dr A.M.Z. Slawin at St Andrews University.

4.2.2.2. EXAFS

Room temperature X-ray absorption data were collected at the nickel K-edge using stations 7.1 and 8.1 at the Daresbury Synchrotron Radiation Source (energy 2 GeV, current typically 200 mA) operating in a transmission mode. Wavelength selection was accomplished using a double crystal Si(111) monochromator set at 50% harmonic rejection. Data were collected out to around 15 $Å^{-1}$ over two or more scans and were processed with the suite of programs available at Daresbury: EXCALIB for raw data processing, EXBROOK or EXBACK for the background subtraction and EXCURV98 for the comparison and fitting between theoretical and experimental EXAFS.

4.2.2.3. Chemical Analysis

Carbon, hydrogen and nitrogen analysis of the samples was determined by microanalysis by Mrs S.Williamsom on a Carlos Erba Intruments EA1110 analyser in St Andrews.

The inorganic composition of the samples were determined in most cases by energy dispersive analysis of emitted X-rays (EDX) on a JEOL 2010 TEM with a Link analyser. Ni(deta)$_2$-UT-6 and Ni(deta)$_2$-AlPO(F)-5 were examined using ICP-AES (inductively coupled plasma-atomic emission spectroscopy).

4.2.2.4. Other Techniques

UV-Visible spectrometry was performed in diffuse reflectance mode on a Perkin Elmer Lambda 35 spectrometer fitted with an integrating sphere. The measurements were typically taken in the range 290 nm to 1200 nm.

^{31}P and ^{27}Al MAS NMR spectra were recorded on a Bruker 500 MHz spectrometer and the chemical shifts related to phosphoric acid and aluminium nitrate at 0 ppm in each case.

Infrared spectra were taken in KBr pressed pellets on a Perkin-Elmer 1710 Infrared Fourier Transform Spectrometer.

Scanning electron microscopy images were obtained from a JEOL JSM-5600 scanning electron microscope at St. Andrews.

4.3. RESULTS AND DISCUSSION

4.3.1. Incorporation of $Ni(deta)_2^{2+}$ within different structures

For the first set of experiments, relatively low amounts of the pre-formed complex $Ni(deta)_2Cl_2.H_2O$ were added to aluminophosphate gels to which amines or alkylammonium hydroxides had been added. These bases were chosen to include those that had a strong templating role (such as decamethonium hydroxide, which templates the magnesioaluminophosphate DAF-1[21] and tripropylamine, which templates MgAPO-36[22]) as well as those whose main function was expected to be the modification of the pH, such as dipropylamine.

The results are given in table 4.5. The table shows that the complex has a strong structure directing role towards AlPO-5, MgAlPO-34 and SAPO-34 rather than being incorporated as other structures form. The presence of the complex tends to result in crystallising one of these phases even in the presence of other templates and from gels that give other products in its absence. Only in the presence of the complex and decamethonium hydroxide does the same phase form as in the preparation without the complex. Presumably the decamethonium ion exerts a stronger templating effect because no complex is included in the colourless crystals of DAF-1 that form. Increasing the amount of complex in preparations where competing phases crystallise usually enabled the complex-templated material to be prepared phase pure.

Samples in which the compound was thought to have been incorporated intact (i.e. those that were purple in colour) were characterised further. SEM was used to examine the crystal morphology and assess the phase purity, in conjunction with the XRD (figure 4.5). Three different complex-containing materials were prepared pure according to this criteria: AlPO-5 (Exp. 1C), MgAPO-34 (Exp. 2C and 4B) and SAPO-34 (exp. 3B). The AlPO-5 sample, which was obtained pure by increasing the complex content of the gel (from 0.05 to 0.1) crystallised as spherical aggregates of hexagonal crystals. The MgAPO-34 displayed typical rhombohedralmorphology, as did the SAPO-34 material, although the latter appeared to be more nearly cubic.

EXP	COMPOSITION	PRODUCT
1A	1Al :1 P : 0.5 DPA : 25H_2O	AlPO Tridymite
1B	1Al :1 P: 0.5 DPA : 25H_2O : 0.05 R1	Ni(deta)$_2$-AlPO-5 + imp
1C	1Al :1 P: 0.5 DPA : 25H_2O : 0.1 R1	Ni(deta)$_2$-AlPO-5
2A	0.15 Mg : 0.85 Al :1.3 DPA : P: 25H_2O *	MgAPO-43
2B	0.15 Mg : 0.85 Al : 1 P: 25 H_2O : 1.3 DPA : 0.05 R1*	Ni(deta)$_2$-MgAPO-34 +imp
2C	0.15 Mg : 0.85 Al : 1 P: 25 H_2O : 1.3 DPA : 0.1 R1*	Ni(deta)$_2$-MgAPO-34
3A	1 Al : 1P:25 H_2O : 0.215 SiO_2 : 1 TPAOH: 0.025 T MAOH	SAPO-20
3B	1Al :1 P : 25 H_2O : 0.215 SiO_2 : 1 TPAOH : 0.025 TMAOH : 0.05 R1	Ni(deta)$_2$-SAPO-34
4A	0.1Mg : 0.9Al : 1 P : 40 H_2O : 0.75 TPA**	MgAlPO-36
4B	0.1 Mg : 0.9 Al : 1 P : 40 H_2O : 0.75 TPA: 0.05 R1**	Ni(deta)$_2$-MgAPO-34 +imp
5A	0.45 Dec(OH)$_2$: 0.2 Mg : 0.8 Al : 1 P : 30 H_2O	DAF-1
5B	0.45 Dec(OH)$_2$: 0.2 Mg : 0.8 Al : 1 P : 30 H_2O : 0.05 R1	DAF-1 +AlPO-5 impurity

Table 4.5 Composition and products of the first set of syntheses. The compositions are expressed as molar ratios of the reactants in the gel. The codes for the organics are DPA (dipropylamine), TMAOH (tetramethylammonium hydroxide), TPAOH (tetrapropylammonium hydroxide), TPA(tripropylamine) and Dec(OH)$_2$ is referred to Decamethonium hydroxide. R1 refers to the Ni(deta)$_2$Cl$_2$.H$_2$O complex. Apart form the asterisked samples, the rest of the gels were heated at 190°C for two days.

** Gel heated at 160°C for x days*

*** Gel heated at 110°C for 2 days and at 150°C for one day*

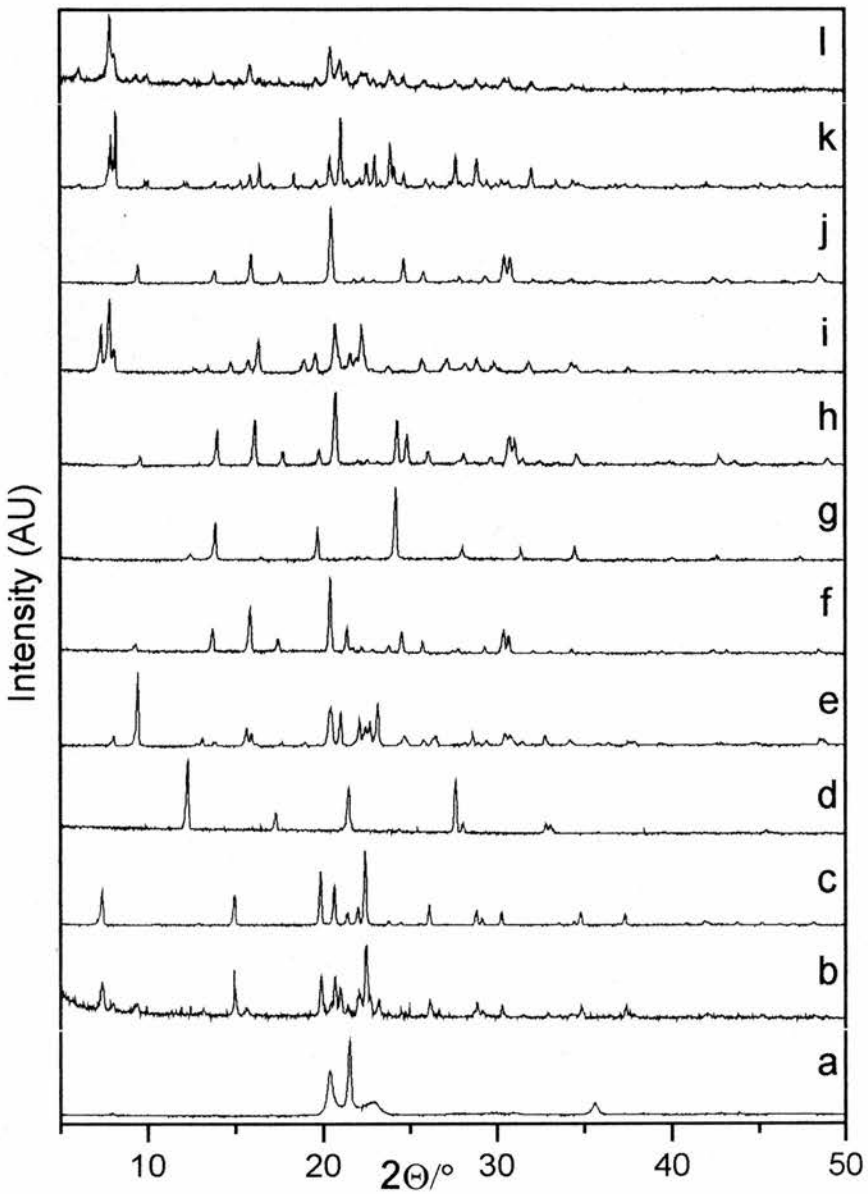

Figure 4.4. XRD patterns of the products obtained from the syntheses summarised in table 4.5. a)$AlPO_4$ "tridymite", b) Ni(deta)$_2$-AlPO-5 with imp, c) Ni(deta)$_2$-AlPO-5, d) MgAPO-43, e) Ni(deta)$_2$-MgAPO-34 with imp, f) Ni(deta)$_2$-MgAPO-34, g) SAPO-20, h) Ni(deta)$_2$-SAPO-34, i) MgAlPO-36, j) Ni(deta)$_2$-MgAPO-34, k) DAF-1, l) DAF-1 with AlPO-5 impurity.

EDX, UV-Visible spectroscopy and elemental analysis were performed in the samples to confirm the incorporation of the complex in these materials. The results are summarised in table 4.6. EDX confirmed the presence of nickel in the samples at an approximate content below 0.1 Ni/ 1P (Ni/Al for the SAPO) and corroborates the incorporation of the heteroatoms on the frameworks. Elemental analysis for the AlPO-5 (experiment 1C) gives C/N and H/C ratios very close to those expected for the complex (C/N=1.33; H/C=3.25). The other materials with the chabazite-like structure gave higher C/N ratios, probably due to other amines or organic fragments occluded within the structure.

Confirmation of the integrity of the complex within the solids was achieved by UV-visible spectroscopy. The spectrum of the solids is similar to the spectrum of the chloride salt and shows the three d-d transitions of a nickel cation in an octahedral environment (figure 4.5).

Exp	Cation ratio (EDX) Ni : Mg : Si :Al : P	Wavelenght (nm)	Elemental analysis				
			%C exp.	%H exp.	%N exp.	C/N exp	H/C exp
1C	0.05 : 0: 0: 1:1	351.25;532.50;901.75	5.30	1.61	4.64	1.33	3.65
2C	0.07: 0.23: 0: 0.73: 1	348.92;525.06;880.37	6.06	1.54	3.19	2.22	3.05
3B	0.07: 0: 0.21: 1: 0.58	346.99;526.49;890.07	7.14	2.30	4.72	1.76	3.86
4B	0.09: 0.28: 0: 0.70: 1	348.44;526.45:884.89	7.38	2.87	6.15	1.40	4.67

Table 4.6. Results of EDX, UV-Visible spectroscopy and elemental analyses of the purest samples of the complex-containing materials. Theoretical ratios expected for the complex are C/N=1.33 and H/C=3.25.

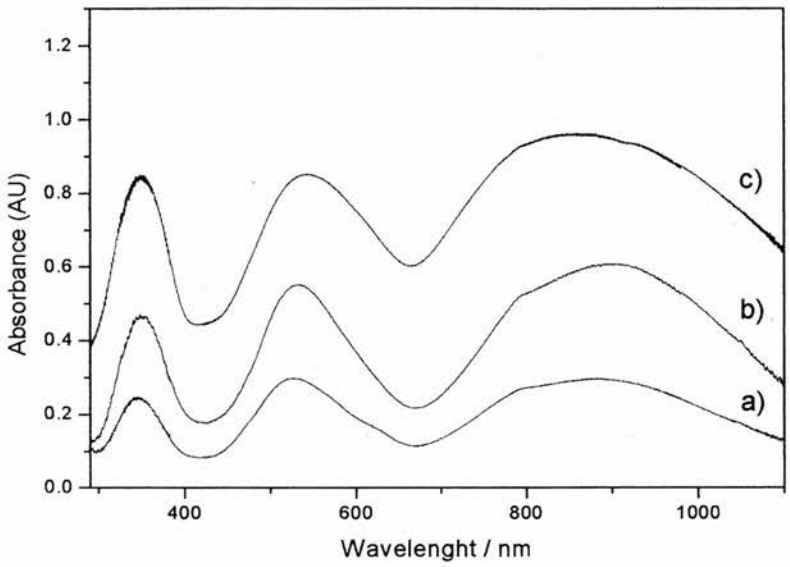

Figure 4.5. UV-Visible spectra of the a) $Ni(deta)_2$- SAPO-34 (sample 3B); b) $Ni(deta)_2$- AlPO-5 (sample 1C) and c) $Ni(deta)_2Cl_2$

4.3.2. Comparison with other Ni complexes

$Ni(tren)_2Cl_2$ and $Ni(trien)_2Cl_2$ complexes with a similar geometry to that of $Ni(deta)_2$ were tried in the aluminophosphate preparations similar to 1B to compare their behaviour as SDAs.

The table 4.7 summarised the results obtained in these syntheses and the X-ray diffraction patterns of the samples are given in figure 4.6.

Under the conditions shown on the table, $Ni(deta)_2^{2+}$ was the only complex that was occluded in the products after crystallisation. The addition of both the $Ni(trien)_2Cl_2$ and $Ni(tren)_2Cl_2$ resulted in the formation of other materials without incorporation of the complexes.

The product from experiment 6, with $Ni(trien)_2^{2+}$, was identified as AlPO-21. The material crystallised as spherical aggregates of small crystals. Under the optical microscope the sample appeared colourless but EDX analysis of the sample revealed that the crystals contained nickel at low concentration Al:P:Ni /1:0.68:0.01.

$Ni(trien)_2^{2+}$ yielded AlPO-5 product. The crystals appear faintly blue under the optical microscope. EDX analysis revealed they contained nickel in a molar cation proportion in the crystals of Al:P:Ni/ 1: 0.69: 0.03.

EXP.	COMPOSITION	PRODUCT
1A	1 Al : 1 P : 0.5 DPA : 25 H_2O	AlPO-Trydimite
1B	1 Al :1P : 0.5 DPA : 25 H_2O :0.05 $Ni(deta)_2Cl_2$	$Ni(deta)_2$-AlPO-5
6	1Al:1P: 0.5 DPA : 25 H_2O : 0.05 $Ni(trien)_2Cl_2$	AlPO-21
7	1Al : 1P: 0.5 DPA : 25 H_2O : 0.05 $Ni(tren)_2Cl_2$	AlPO-5

Table 4.7. Comparison of the different nickel complexes under the same synthesis conditions. All the gels were heated at 190°C for two days. DPA refers to Di-n-propylamine.

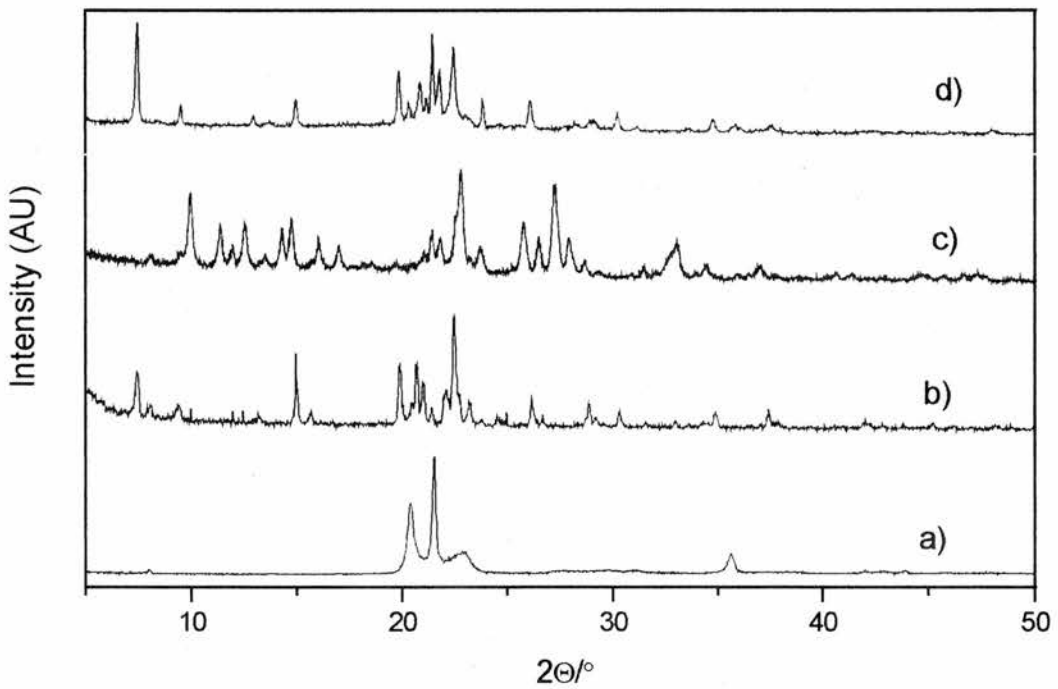

Figure 4.6. Patterns of the samples obtained employing the three different nickel complexes as structure directing agent given in table 4.7: a) AlPO-"Tridymite", b) $Ni(deta)_2$-AlPO-5, c) AlPO-21 and d) AlPO-5.

In summary, then, this first set of experiments shows the $Ni(deta)_2^{2+}$ directs the crystallisation of substituted AlPO-34 and AlPO-5 structures. In pure aluminophosphate preparations, the complex usually directs the formation of AlPO-5 whilst magnesium- or silicon-substituted preparations, the AlPO-34 structure tends to crystallise. This tendency for materials with the chabazite framework topology to form in substituted aluminophosphate frameworks has been reported previously[16,23]. The performance of $Ni(deta)_2^{2+}$ was compared with the similar complexes, $Ni(trien)_2^{2+}$ and $Ni(tren)_2^{2+}$, in an aluminophosphate preparation. Under analogous synthesis conditions, $Ni(deta)_2^{2+}$ was the only complex included in the final product, suggesting that under these conditions it is more stable than the other two octahedral complexes.

4.3.3 Synthesis without extra amines and with Ammonium Fluoride

The $Ni(deta)_2Cl_2$ complex was also used in the preparation of aluminophosphates in fluoride-containing synthesis. In these preparations, NH_4F performed the role of mineralising agent and there is no requirement to add additional bases to give a pH close to 7. A larger amount of complex was added to the synthesis gel together with ammonium fluoride. Ammonium fluoride was used instead of hydrofluoric acid as a source of fluoride, since the latter would destroy most of the pre-formed complex once added to the synthesis gel.

Experiments were performed varying different synthesis parameters in order to study their effect on the products. Hence, the amount of water, ammonium fluoride and complex were varied as indicated in table 4.8.

On the basis of the XRD data, three different complex-containing, purple, phases were obtained in these syntheses, $Ni(deta)_2F_4$-AlPO-5(orth), an orthorhombic crystallographic variant of the AlPO-5 structure (see later); $Ni(deta)_2F_4$-UT-6, a complex-containing version of the fluorinated AlPO-34 structure and the hexagonal AlPO-5 material, $Ni(deta)_2$-AlPO-5(hexag) prepared in the absence of NH_4F or extra bases, as well as two different green phases, NiAlPO-LMU-3 and NiAlPO-CJ2[†]. The XRD of these phases (pure) are shown in figure 4.7.

[†] NiAlPO-CJ2 was obtained pure from a separate set of experiments, see later.

Two of the complex-containing phases were prepared in the presence of ammonium fluoride by varying the water content or reducing the complex concentration of the gel. These two phases were not identified initially but were found (see later) to be fluorinated aluminophosphates with the AlPO-5 (AFI) and AlPO-34 (CHA) framework topology. The fluoride version of the aluminophosphate AlPO-34 is denominated UT-6 as it was first synthesised by Ozin et al[24] with pyridine as the structure directing agent.

Sample	$Ni(deta)_2Cl_2$	H_2O	NH_4F	Products
8	0.5	400	0.5	$Ni(deta)_2$AlPO-5(orth)
9	0.5	100	0.5	$Ni(deta)_2$UT-6 (major) + $Ni(deta)_2$-AlPO-5(orth)
10	0.5	50	0.5	NiAPO-CJ2 (major) + NiAlPO-LMU-3+ AlPO-UT-6
11	0.5	5	0.5	NiAPO-CJ2 (major) + AlPO-UT-6
12	0.5	100	0	$Ni(deta)_2$-AlPO-5(hexag)
14	0.5	100	0.25	$Ni(deta)_2$-UT-6 + $Ni(deta)_2$-AlPO-5(orth)+ NiAlPO-LMU-3
15	0.5	100	0.75	NiAlPO-LMU-3
17	0.25	100	0.5	$Ni(deta)_2$-AlPO-5(orth)

Table 4.8 Experiments performed in the presence of ammonium fluoride changing dilution x NH_4F : y $Ni(deta)_2Cl_2$:1 Al: 1P: z H_2O. All gels were heated at 190° C for two days. Three complex containing phases were produced: $Ni(deta)_2$-AlPO-5(orth), the orthorhombic crystallographic variant of the AlPO-5 structure; $Ni(deta)_2$-UT-6, the complex containing version of the fluorinated AlPO-34 structure and the hexagonal AlPO-5 material, $Ni(deta)_2$-AlPO-5(hexag). NiAlPO-LMU-3. Two nickel aluminophosphate phases crystallised in these preparations: NiAlPO-LMU-3 and NiAlPO-CJ2.

A preparation with the same composition that gives Ni(deta)$_2$-UT-6, but without the addition of ammonium fluoride, yielded complex-containing crystals of hexagonal AlPO-5 similar to those synthesised on the presence of extra amines. Mixtures of two green nickel aluminophosphate phases, NiAlPO-CJ2 and NiAlPO-LMU-3 were also produced. NiAlPO-CJ2 become the main phase to crystallise at lower water contents while NiAlPO-LMU-3 was obtained pure in a preparation with a high ammonium fluoride content.

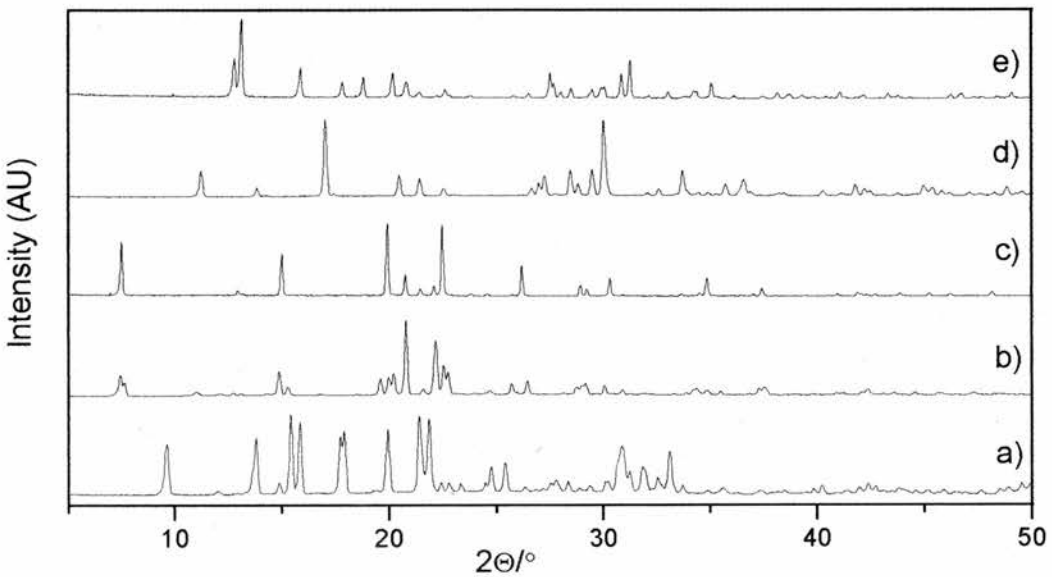

Figure 4.7. X-ray diffraction patterns of the phases obtained in the syntheses performed in the presence of ammonium fluoride and bis(diethylenetriamine) nickel (II). a) Ni(deta)$_2$-UT-6; b) Ni(deta)$_2$-AlPO-5(orth); c) Ni(deta)$_2$-AlPO-5(hexag) and the two nickel aluminophosphate phases,d) NiAlPO-LMU-3 and e) NiAlPO-CJ2.

UV-visible spectroscopy (figure 4.7) and elemental analysis (table 4.9) showed that the complex was intact within the three purple solids, although the observed C/N ratios are slightly smaller than the expected for the complex (C/N theor= 1.33).

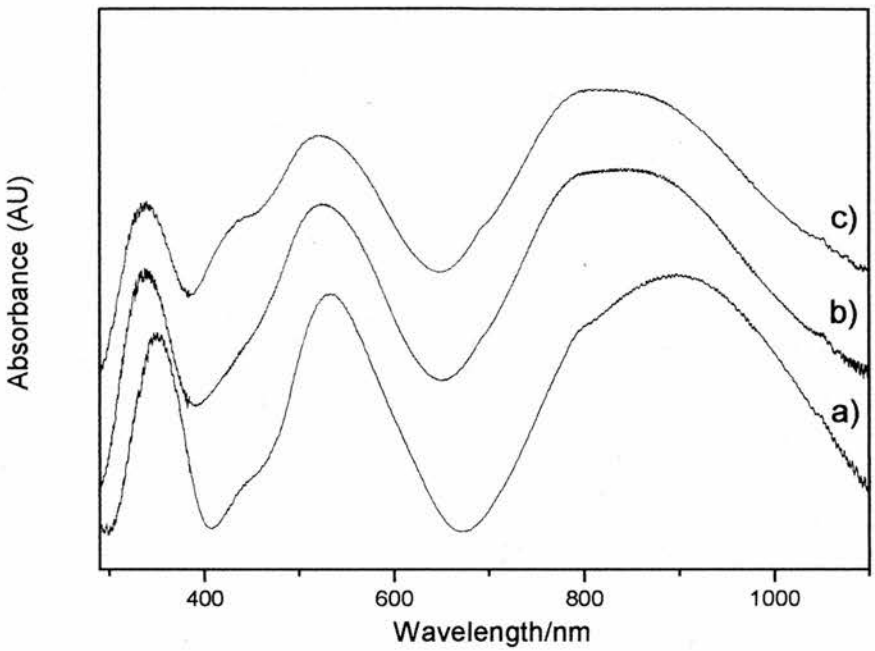

Figure 4.8. UV-visible spectra of a) Ni(deta)$_2$-AlPO-5 hexag; b) Ni(deta)$_2$-AlPO-5(orth); c) Ni(deta)$_2$-UT-6

Material	%C exp.	%H exp.	%N exp.	C/N exp
Ni(deta)$_2$-UT-6	9.21	2.37	8.21	1.31
Ni(deta)$_2$-AlPO-5(orth)	5.67	1.53	5.20	1.27
Ni(deta)$_2$-AlPO-5(hexag)	4.16	1.21	4.29	1.13

Table 4.9. Results of the elemental analysis on the purple materials. The C/N ratio in the complex is 1.33.

C, H, N analysis of the two green nickel aluminophosphates given in table 4.10 shows a very low organic content and indicates that the ammonium cation or amine fragments have became trapped within the solids rather than the complex. Furthermore, their UV-visible spectra is different from the one of the purple materials and exhibits two broad maxima centered at a different wavelength. These results indicate that the nickel is not complexed by the amine in the materials, but is rather included as nickel coordinated octahedrally by oxygens.

Material	Wavelenght (nm)	Elemental analysis				
		%C exp.	%H exp.	%N exp.	C/N mol exp	H/C mol exp
NiAlPO-CJ2	420; 725	0.24	2.31	8.13	-	3.98
NiAlPO-LMU-3	430; 800	-	0.12	2.98	-	0.56

Table 4.10. Results of the elemental analysis and UV-visible spectra of the green nickel aluminophosphates.

A further structural description of the structures identified within this system is given below. Particular attention was paid to those materials including the complex intact.

4.3.3.1. Ni(deta)$_2$-UT-6

The X-ray powder profile of the Ni(deta)$_2$-UT-6 was indexed by Louer's algorithm as triclinic, a = 9.288 Å, b = 9.091 Å, c = 9.355 Å, α = 88.36°, β = 78.91°, γ = 89.20°. The unit cell volume and unit cell parameters suggested a resemblance with the fluoride version of AlPO-34, the material denoted UT-6, that was prepared using pyridine as structure directing agent[24] and with tetraethyleneglycol as solvent (table 4.11). The ^{31}P MAS NMR spectrum of this sample shows three well defined peaks $\delta \sim$ -27 ppm, $\delta \sim$ -40 ppm, $\delta \sim$ -50 ppm in the ratio 1:1:1, consistent with the space group P-1, similar to that of the pyridine-UT-6 material. ^{27}Al MASNMR spectrum shows two peaks, $\delta \sim$ 50 ppm, $\delta \sim$ -10 ppm, corresponding to four and six coordinated aluminium, respectively.

Material	a	b	c	α	β	γ	V	Ref
Pyr-UT-6	9.118(1)	9.161(1)	9.335(1)	85.98(1)	77.45(1)	89.01(1)	759.25(1)	24
AlPO-34	9.383(4)	9.383(4)	9.383(4)	94.08(5)	94.08(5)	94.08(5)	826.19(1)	25
AlPO(F)-34	9.099(3)	9.223(2)	9.392(9)	77.88(1)	87.20(5)	87.77(7)	769.48(6)	26
$Ni(en)_2(OH)_2$ AlPO-34	9.085(4)	9.332(7)	8.936(1)	86.27(6)	101.26(6)	92.72(5)	757.70(4)	16
$Ni(deta)_2$-UT-6	**9.288**	**9.091**	**9.355**	**88.36**	**78.91**	**89.20**	**789.91**	**This work**

Table 4.11. Unit cell parameters of different variants of AlPO-34 structure.

Material	^{27}Al, δ (ppm)	^{31}P, δ (ppm)
Pyr-UT-6	29.5;-17.9	-8.5; -25.2;-31.1
$Ni(deta)_2$-UT-6	50; -10	-27; -40; -50

Table 4.12. Comparison between the ^{31}P and ^{31}Al MAS NMR spectra of Pyridine-AlPO-UT-6 [24] and $Ni(deta)_2$-AlPO-UT-6.

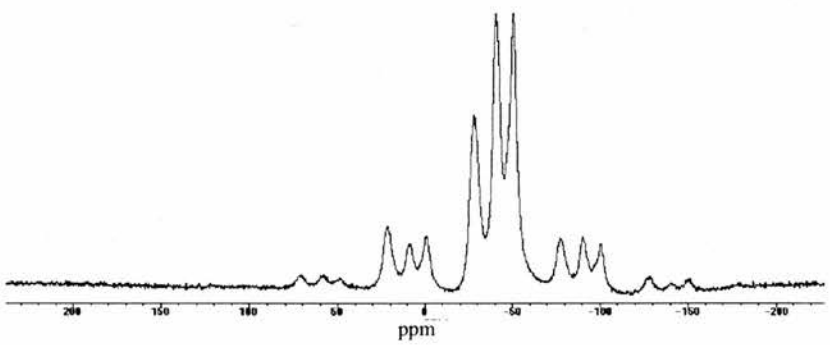

Figure 4.9. ^{31}P MAS NMR of $Ni(deta)_2$-AlPO-UT-6.

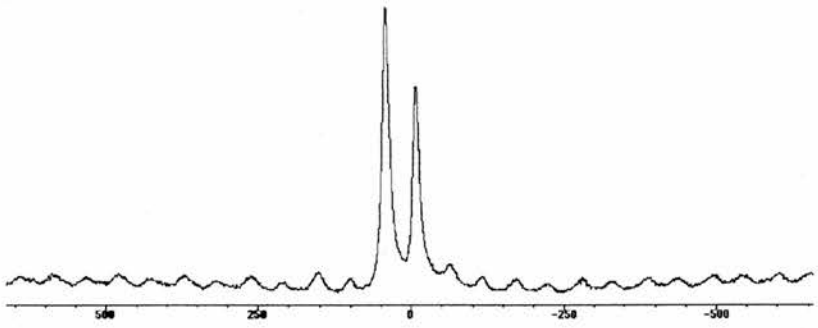

Figure 4.10. ^{27}Al MAS NMR of Ni(deta)$_2$-AlPO-UT-6

A constrained Rietveld refinement of the powder data of the Ni(deta)$_2$-UT-6 was performed employing the framework atomic coordinates of the pyridine-UT-6 material as a starting model and matching the angle most distorted from AlPO-34 (94.07° in the undistorted variant) to β in UT-6. Tetrahedral Al-O distances were constrained to be 1.73 ± 0.05 Å while P-O distances were constrained to be 1.53± 0.05 Å. Tetrahedral geometry of Al(1) and Al(2) and P(1), P(2), P(3) was input by restraining O-O bond distances to 2.87 ± 0.1 Å for AlO_4 tetrahedra and to 2.55 ± 0.1 Å for PO_4 tetrahedra. Al-O, O-O and O-F distances of the AlO_4F_2 octahedra were restrained to be 1.86 ± 0.05 Å, 2.65 ± 0.1 Å and to 1.90± 0.1 Å respectively.

In order to improve the fit of the simulated to the observed X-ray powder pattern it was necessary to include scattering from the nickel complex. It is known that the complex can adopt different conformational isomers. The three possible configurations for an octahedral $[M(deta)_2]^{n+}$ complex (shown in figure 4.11) are the unsymmetrical facial (μ-fac) isomer that is chiral, the symmetrical achiral facial (s-fac) isomer and finally, the meridional (mer) isomer that is chiral for the diethylenetriamine ligand due to the non-planarity of the central nitrogen atom[27] The three isomers are in equilibrium in solution and which isomer crystallises depends on the anion employed to precipitate the complex[28]. When the complex is obtained as the chloride salt, it crystallises as the *mer* isomer. This was confirmed by single crystal analysis on the starting salt of the complex employed in the synthesis gel. It gave similar structure and crystal parameters to the one reported previously[29,30].

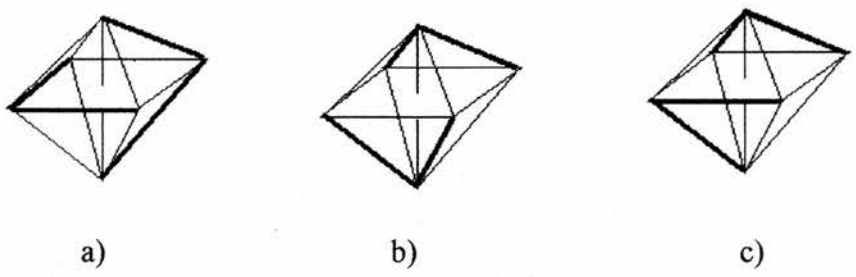

a) b) c)

Figure 4.11. Edge configurations for $[M(deta)_2]^{n+}$ octahedral complexes: a) mer isomer, b) s-fac and c) μ-fac.

To try to determine the isomer present in Ni(deta)$_2$-UT-6, computational simulation was performed to estimate the relative energies of the two more common isomers (the *mer* and *μ-fac* isomers) within the distorted cage of the microporous material. This simulation was performed by P.A. Cox (University of Portsmouth) and the details of the simulation can be found elsewhere[31]. These calculations found the *μ-fac* isomer to be strongly energetically favoured (by 0.99 eV) in the UT-6 framework structure determined in this study. The I.R. spectrum of the Ni(deta)$_2$-UT-6 also revealed a sharp resonance in the mid-I.R. at 788.5-789 cm^{-1}. Such a band is reported to be characteristic of the *fac* isomers[28] recorded at 780 cm^{-1}. This band is not found in the UT-6 structure synthesised with pyridine (figure 4.12) and it is not found in the other materials synthesised with the complex as Ni(deta)$_2$-AlPO-5(orth) or Ni(deta)$_2$-MgAPO-34. These results suggest the complex could be included as the *μ-fac* isomer in UT-6.

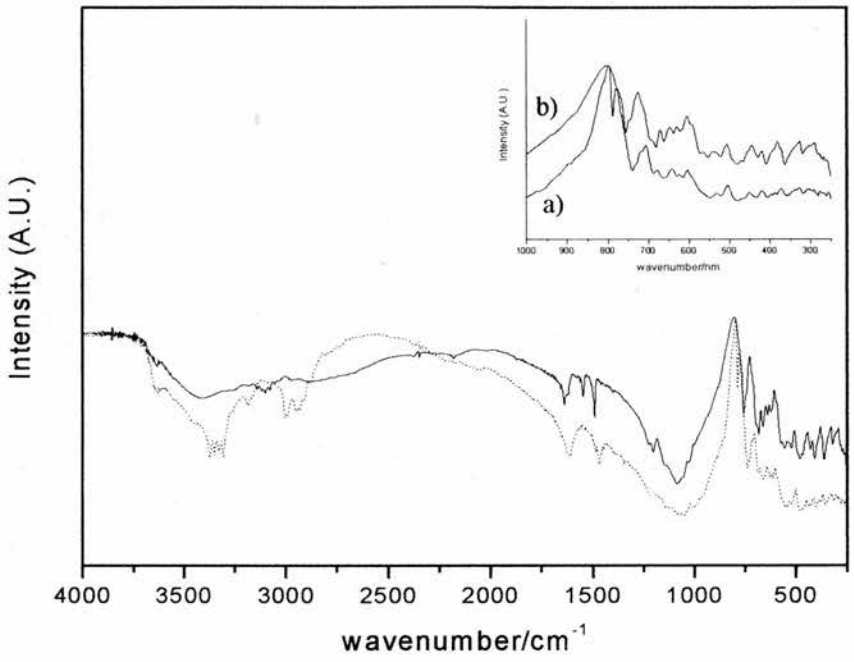

Figure 4.12. I.R. spectra of samples of Ni(deta)$_2$-UT-6 (dashed line) and pyridine-UT-6. Inset: the I.R. spectra in the region 250-1000 nm of both a) Ni(deta)$_2$-UT-6 and b) pyridine-UT-6, that contains the resonance characteristic of the μ-fac isomer at ~780 cm^{-1}. The extra band appears in the Ni(deta)$_2$-UT-6 sample.

Inclusion of the scattering of the complex in its simulated position in this configuration significantly improved the fit to the X-ray powder diffraction data to give a final R_{wp} of 14.7 % with chemically reasonable bond lengths Al-O $_{octahedral}$ 1.90(6) Å, Al-F 1.90(4) Å, Al-O $_{tetrahedral}$ 1.74(6) Å, P-O 1.53(4) Å. The final fit is given in figure 4.13 and the refined coordinates on table 4.13

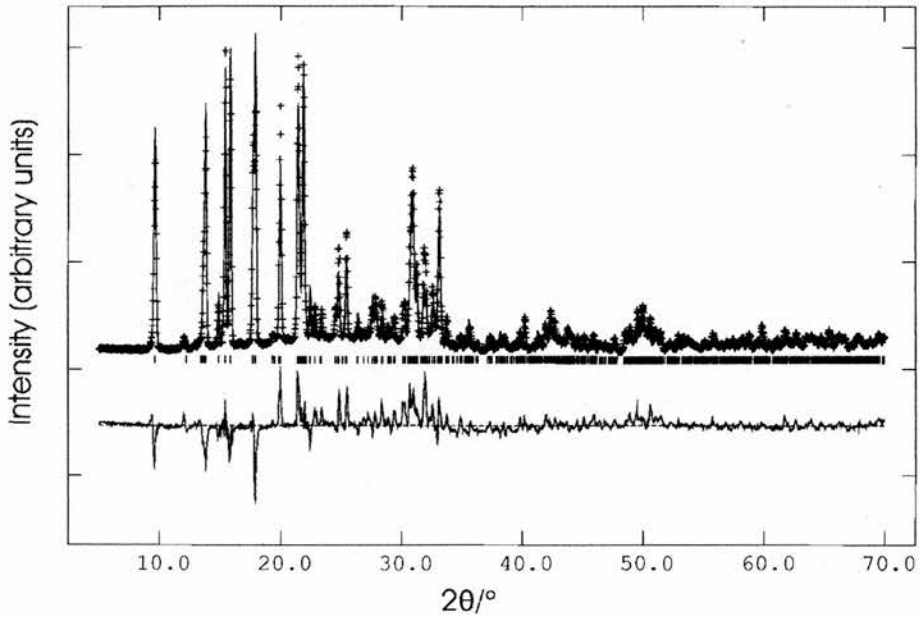

Figure 4.11. Observed, fitted and difference X-ray powder diffraction profiles of Ni(deta)$_2$-UT-6, fitted using the framework of UT-6 as a starting model and including the Ni(deta)$_2$ complex within the cages in the position determined by energy minimisation calculations. Constrained Rietveld refinement of the whole profile was performed to final fit parameters of R_{wp}=0.15 and R_p=0.12. Although far from being a good fit, the model employed in the refinement showed some convergence and seems a reasonable model for the structure.

The structure of the UT-6 material is similar to that of AlPO-34 but each of the double six membered rings of the material contains one octahedral aluminium (AlO_4F_2) that connects to that of another 6MR through two bridging fluoride ions. The complex resides in the cages of the structure probably as the *μ-fac* isomer, balancing the negative charge of the fluoride ions within the framework (figure 4.14). ICP analysis of Ni, Al and P gives a unit cell composition of $Ni_{2.0}Al_{25.6}P_{24}$ assuming 24 P and is consistent with the crystallographic one, obtained by refining the model of the structure, $[Ni(deta)_2]_{0.48}Al_6P_6O_{24}F_2$, so that the occupancy of nickel is one per cage.

Atom	x	y	z	U_{iso}
P(1)	377(2)	200(2)	891(2)	0.025
P(2)	820(2)	333(2)	850(2)	0.025
P(3)	630(2)	376(2)	314 (2)	0.025
Al(1)	633(2)	154(2)	071(2)	0.025
Al(2)	138(2)	446(2)	901(2)	0.025
Al(3)	586(2)	368(2)	661(2)	0.025
O(1)	781(3)	173(3)	919(3)	0.025
O(2)	463(3)	203(4)	014 (3)	0.025
O(3)	347(4)	033(2)	892(4)	0.025
O(4)	480(3)	230(4)	743(3)	0.025
O(5)	233(3)	265(3)	956(3)	0.025
O(6)	775(2)	457(4)	018(4)	0.025
O(7)	761(3)	394(4)	712(3)	0.025
O(8)	988(4)	359(4)	807(4)	0.025
O(9)	766(5)	472(5)	271(3)	0.025
O(10)	649(4)	346(4)	477(3)	0.025
O(11)	624(5)	235(4)	239(4)	0.025
O(12)	500(4)	473(5)	315 (5)	0.025
F(1)	-004(3)	384 (3)	083(3)	0.025
Ni(1)*	009	020	520	0.1

Table 4.13. Fractional atomic coordinates (× 10^3) for Ni(deta)$_2$-UT-6 from the Rietveld Refinement of X-ray powder data; $P\bar{1}$, a=9.283(1) Å, b=9.091(1)Å, c=9.357(1) Å, α=88.35(1)°, β=78.91(1)°, γ=89.21(1)°. Occupancy of Ni(deta)$_2$ complex in energy minimised position= 0.48(2), i.e. ca. 1 per cage.

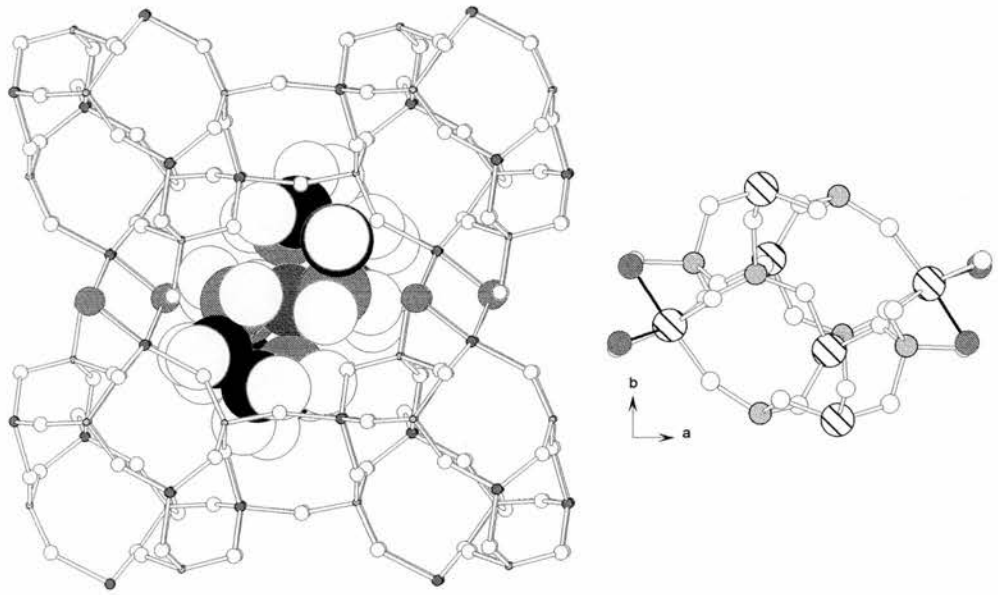

a) b)

Figure 4.14. The refined structure of Ni(deta)$_2$-UT-6, a) view along the c axis showing the energy-minimised position of the complex within the UT-6 cage and b), the octahedral coordination of selected aluminium atoms in the structure. (Key: Al medium hatched; P, small gray; O ,small white; Ni, large cross-hatched; N,large dark gray; C, large black; H, large light gray).

4.3.3.2. Ni(deta)$_2$-AlPO(F)-5

The second phase synthesised in the fluoride-containing preparations was an orthorhombic variant of AlPO-5. A similar orthorhombically-distorted AlPO(F)-5 has been reported from other preparations, using a different structure directing agent, performed within this university[26]. The structure[‡] of Ni(deta)$_2$-AlPO(F)-5 was solved by single crystal X-ray diffraction. It consists of an orthorhombic variant of the AlPO-5 structure in the space group Ccc2, due to the presence of fluoride

[‡] $[Al_6P_6O_{24}F].0.5[Ni(N_3C_4H_{13})$, M=883.26, orthorhombic, 0.14×0.05×0.05, a=13.8603(5) Å, b=23.1285 (5) Å, c=8.5420 (4) Å, V=2738.29 (2) Å^3, T=293 K, space group Ccc2 (no. 37), Z=4, μ(Mo-K$_\alpha$) =1.032 mm^{-1}. The final R(obs) was 0.0681 with ωR(F)=0.1727.

ions coordinated to aluminium atoms in the structure. The fluoride ions bridge two aluminium atoms within 4-member rings in the structure so that one aluminium atom becomes trigonal-bipyramidally-coordinated to four oxygens and fluorine (AlO_4F). The complex is disordered within the channels and it was not possible to locate the ligands unambiguously.

The location of the nickel complex within the channels was simulated as for the Ni(deta)$_2$-UT-6 structure. The *mer* and *fac* isomers were found to have similar total energies within the channels of the structure (within 0.03 eV). Notably, the I.R. spectrum (Figure 4.16) does not present the band at 788-789 cm^{-1} that appears in that of the Ni(deta)$_2$-UT-6 structure, so that the included complex could be in the *mer* configuration, figure 4.15.

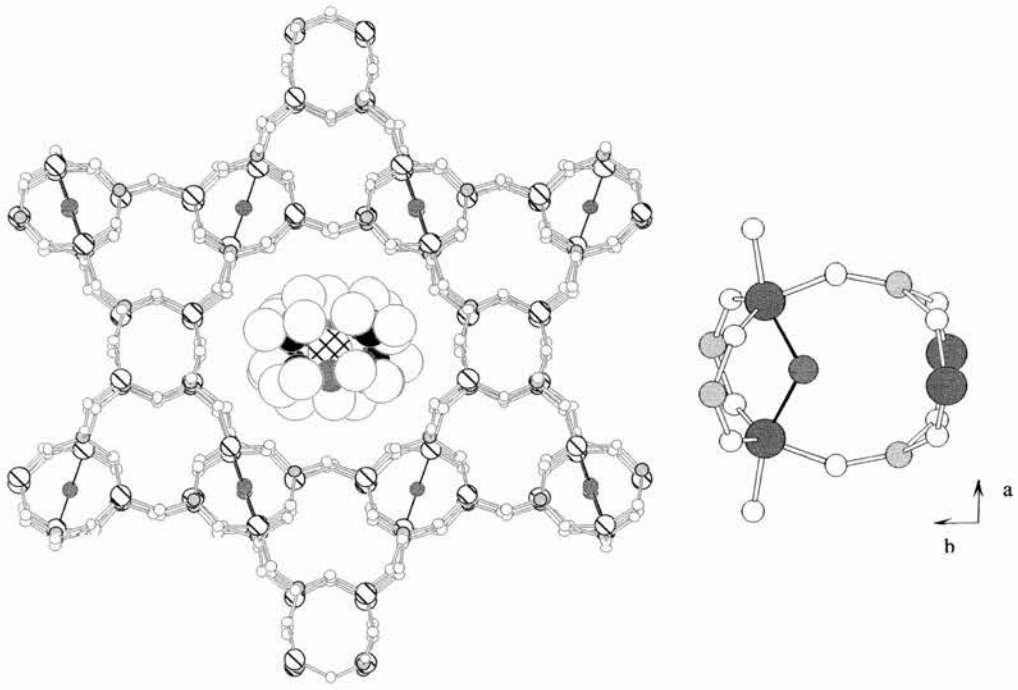

a) b)

Figure 4.15. Crystal structure of Ni(deta)$_2$-AlPO-5 (orth) showing the computer simulated energy minimised position of the template a), and b) a close up part of the framework showing how the fluoride bridges two aluminium ions in the same four-membered ring, so that their coordination becomes trigonal-bipyramidal. (Key: Al medium hatched; P,small gray; O,small white; Ni, large cross-hatched; N,large dark gray; C, large black; H, large light grey).

It can also be noticed that the Ni/AlPO ratio in this Ni(deta)$_2$-AlPO-5 (orth) is half that of the Ni(deta)$_2$-UT-6 material prepared with a higher amount of complex (or a lower water content) on the synthesis gel.

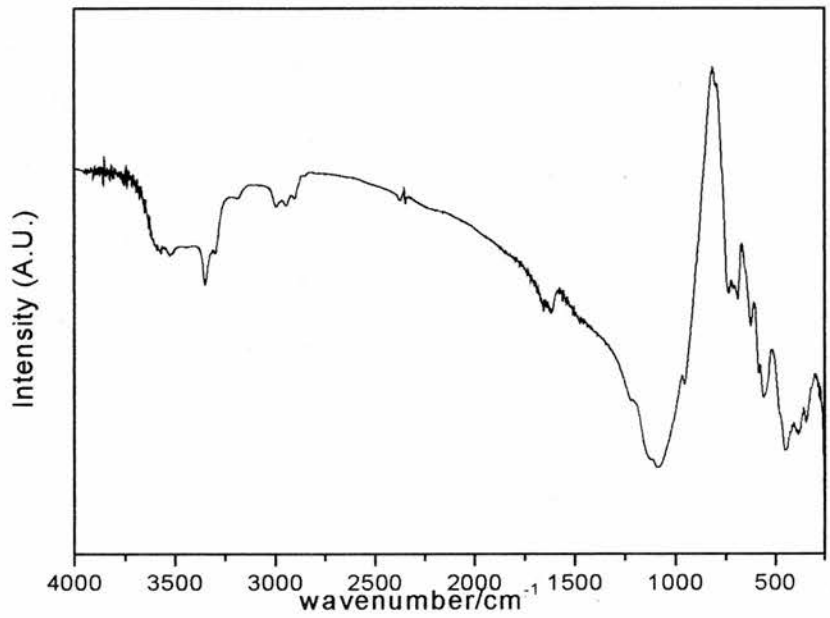

Figure 4.16. I.R. spectrum for Ni(deta)$_2$-AlPO-5 (orth). This spectrum the band does not present the sharp resonance at 789 cm^{-1}

The Ni K-edge EXAFS spectra of the as-prepared Ni(deta)$_2$-AlPO-5 (orth) sample can be fitted by an octahedral model for the complex giving similar parameters to that of the pure complex in the chloride salt, with similar Ni-N and Ni-C distances to those observed experimentally in the X-ray crystal structure, figures 4.17 and table 4.14. The EXAFS of the complex included in the UT-6 material is more difficult to fit with this model, suggesting that a more complicated model could be necessary in this case, possibly due to a change on the conformation of the complex with respect to that of the complex in the chloride salt and when incorporated to the orthorhombic AlPO-5.

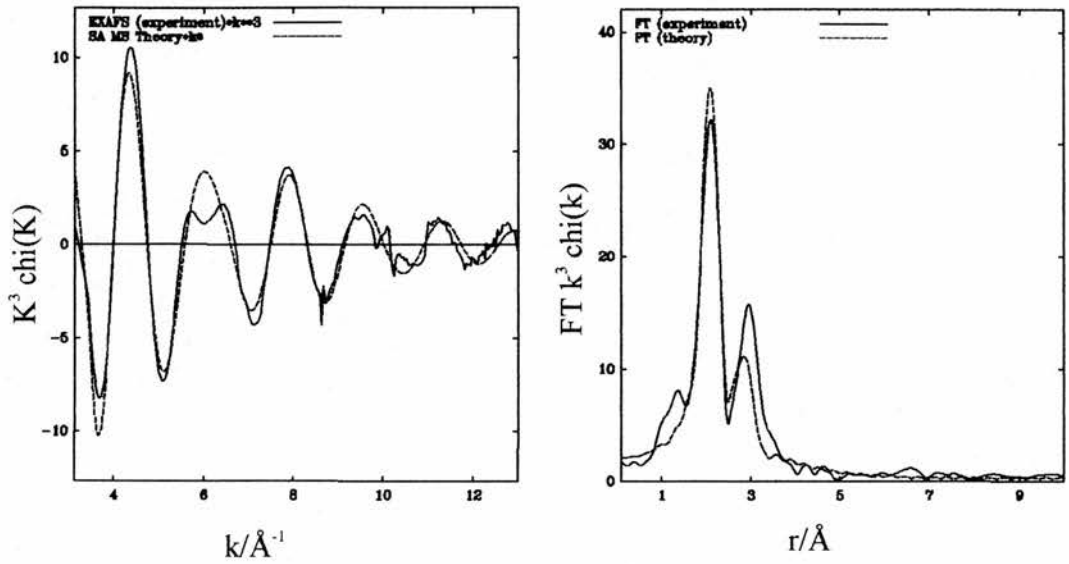

Figure 4.17. Experimental (solid line) and theoretical (dashed line) Ni K-edge EXAFS (left) and its Fourier Transform (right) for $Ni(deta)_2Cl_2$ complex.

Atom type	Coordination number N	Distance R(Å)	Debye-Waller factor σ^2((Å)
N	6	2.128	0.014
C	8	2.909	0.030

R=28.95 %, FI=0.00055

Table 4.14. Fit Parameters for the EXAFS data of $Ni(deta)_2Cl_2$ complex.

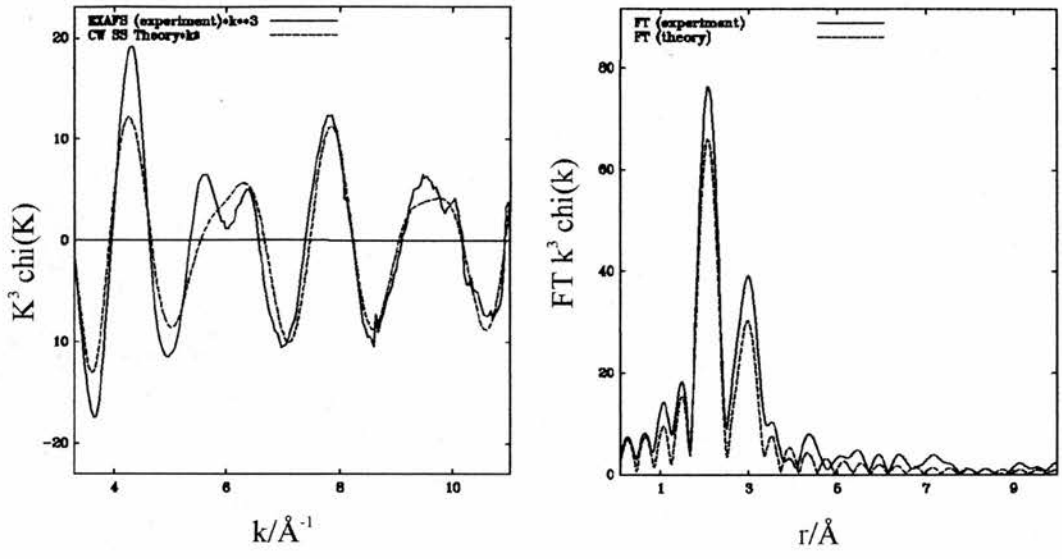

Figure 4.18. Experimental (solid line) and theoretical (dashed line) Ni K-edge EXAFS (left) and its Fourier Transform (right) for Ni(deta)$_2$-UT-6.

Atom type	Coordination number N	Distance R(Å)	Debye-Waller factor σ^2((Å)
N	6	2.120	0.000
C	8	2.969	0.001

R=32.68 %, FI=0.00078

Table 4.15. Fit Parameters for the EXAFS data of Ni(deta)$_2$-UT-6. The fit is different than those of the complex within AlPO-5 (orth) and the Ni(deta)$_2$Cl$_2$ complex.

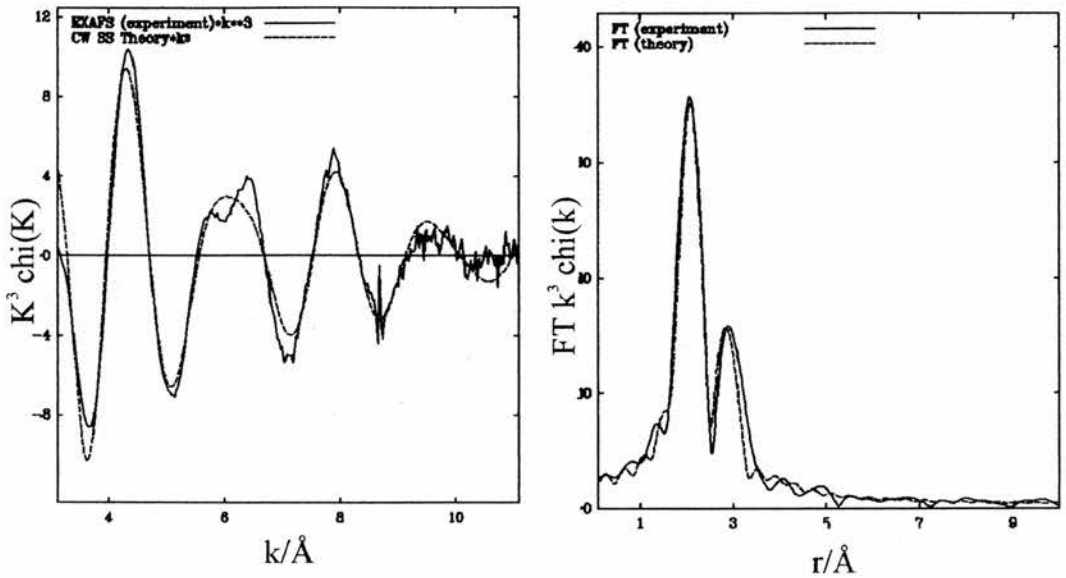

Figure 4.19 Experimental (solid line) and theoretical (dashed line) Ni K-edge EXAFS (left) and its Fourier Transform (right) for Ni(deta)$_2$-AlPO-5 (orth).

Atom type	Coordination number N	Distance R(Å)	Debye-Waller factor σ^2((Å)
N	6	2.120	0.015
C	8	2.927	0.021

R=24.45 %, FI=0.00035

Table 4.16. Fit Parameters for the EXAFS data of Ni(deta)$_2$-AlPO-5 (orth), very similar to those of Ni(deta)$_2$Cl$_2$

4.3.3.3. Ni(deta)$_2$-AlPO-5 and the green aluminophosphate NiAlPO-LMU-3 and NiAlPO-CJ2

The AlPO-5 hexagonal crystallographic variant was prepared from the same gel composition as Ni-(deta)$_2$-UT-6 but in the absence of fluoride ions. Semiquantitative EDX analysis shows a composition (Ni:Al:P/ 0.032:1:0.87) with a lower Ni content than the materials synthesised with fluoride. The charge balance

might, in this case, be achieved by the presence of structural defects rather than by the inclusion of fluoride in the structure.

The green phase NiAlPO-LMU-3[§] synthesised as a pure phase in preparations with a higher content of ammonium fluoride, was identified by unit cell indexing and by searching in the ICSD database[32] by Miss Emily Lear[33]. The material is related to the phases $K[Ni(H_2O)_2Al_2(PO_4)_3]$[34], $NH_4[Co(H_2O)_2Ga_2(PO_4)_3]$[35] and $NH_4[Co(H_2O)_2Al_2(PO_4)_3]$ (denominated LMU-3,) and is expected to be $NH_4[Ni(H_2O)_2Al_2(PO_4)_3]$[36]. NiAlPO-CJ2 become the major phase to crystallise from a gel with very low water content (see table 4.8). It was obtained as a pure phase in experiments whith triethylenetriamine and nickel were added separately to the gel, for a gel composition: 0.5 Ni:1P:1triethylenetriamine:0.5 NH_4F: 100 H_2O after heating at 190°C for two days. The solid[**] has unit cell parameters, symmetry and X-ray diffraction pattern similar to the aluminophosphate CJ2[37], and its gallophosphate[38] and cobalt aluminophosphate[39] analogous. Clearly in both solids, the nickel complex is not retained intact and nickel becomes octahedrally-coordinated with the framework.

4.3.4 Comparison with other complexes

The complexes $[Ni(tren)_2]^{2+}$ and $[Ni(trien)_2]^{2+}$ were also tried in these syntheses with ammonium fluoride in order to asses the structure-directing activity of these complexes under these conditions. As was the case for the syntheses performed with dipropylamine only the $[Ni(deta)_2]^{2+}$ complex succeeded in producing a phase with the complex incorporated intact.

[§] NiAlPO-LMU-3: C2/c, a = 13.055(1) Å, b = 10.168(1) Å, c = 8.738(1) Å, β = 108.54(1) °. More details can be found on reference 33

[**] NiAlPO-CJ2: $P2_12_12_1$, a= 9.406(1) Å, b = 9.572(1) Å, c = 9.916(1) Å, β = 108.54(1) °. More details can be found on reference 33

Exp	Composition	Product
132A	0.5 NH_4F: 0.5 $Ni(deta)_2Cl_2$:1 Al: 1P: 100H_2O	$Ni(deta)_2$-UT-6
136A	0.5 NH_4F: 1 Al: $Ni(trien)_2Cl_2$ 1P: 100H_2O	NiAlPO-CJ2+ NiAlPO-LMU-3
137B	0.5 NH_4F: 0.5 $Ni(tren)_2Cl_2$:1 Al: 1P: 100H_2O	unidentified

Table 4.17. Products of the syntheses performed with ammonium fluoride and with the different nickel complexes. All gels were heated at 190°C for two days.

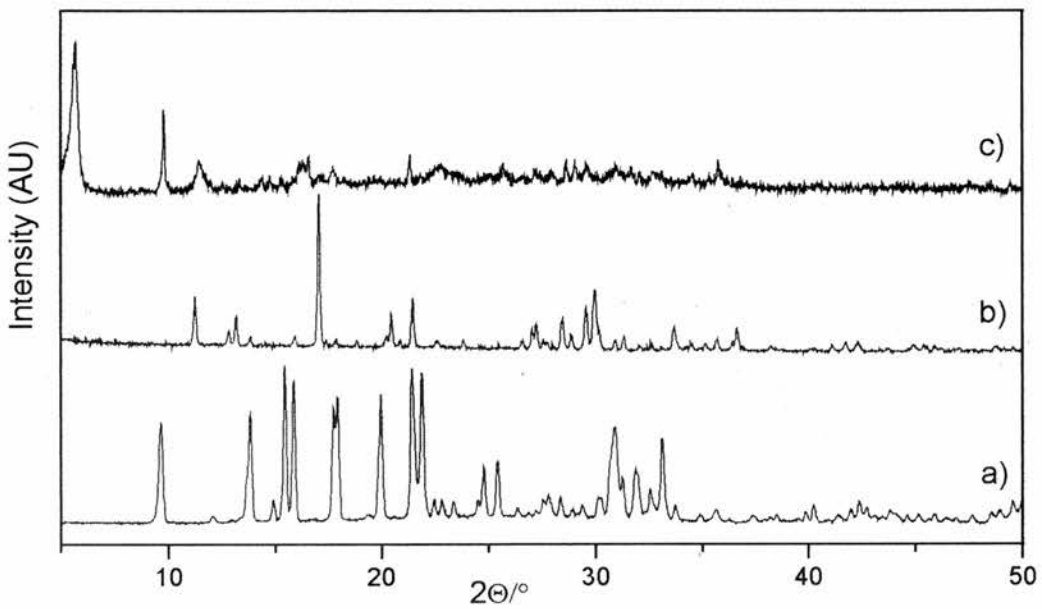

Figure 4.20. XRD patterns of the samples obtained in the ammonium fluoride preparations performed with the three different complexes: a) $Ni(deta)_2$-UT-6; b)Mixture of green phases NiAlPO-CJ2 and NiAlPO-LMU-3 and c) unidentified phase.

The $Ni(trien)_2Cl_2$ complex yielded a mixture of two green phases that were identified as NiAlPO-CJ2 and NiAlPO-LMU3. The complex has been destroyed under the synthesis conditions and the nickel has entered the framework, octahedrally bound. In a similar way, $[Ni(tren)_2]^{2+}$ directs crystallisation to the formation of very small crystals of an unidentified phase that collapsed after calcination at 550°C in flowing oxygen.

Again, this shows that under the synthesis conditions only the $[Ni(deta)_2]^{2+}$ complex directs the crystallisation to a microporous material.

4.3.5. Attempted incorporation of copper

A series of experiments were performed in which the $Cu(deta)_2^{2+}$ complex was used in the syntheses in place of $Ni(deta)_2^{2+}$. In most cases, however, only complex mixtures were obtained and the copper complex was thought to have broken down in many cases. It was possible, however, to incorporate the copper complex intact in a MgAPO preparation with composition 0.05 $Cu(deta)_2(NO_3)_2$: 0.25 Dipropylamine: 0.1 Mg : 0.9 Al : 1 P: 25 H_2O, where dipropylamine was used as an extra base. Reducing the amine content to 0.25 (compared to the nickel equivalent) gave a nearly phase pure sample of blue crystals of AlPO-5.

U.V.-visible spectroscopy confirmed the integrity of the complex within the material and the semiquantitative cation ratio found by EDX (Cu: Mg: Al: P/ 0.07: 0.23: 1.2: 1). The material is stable to calcination at 550°C in flowing oxygen for 700 minutes.

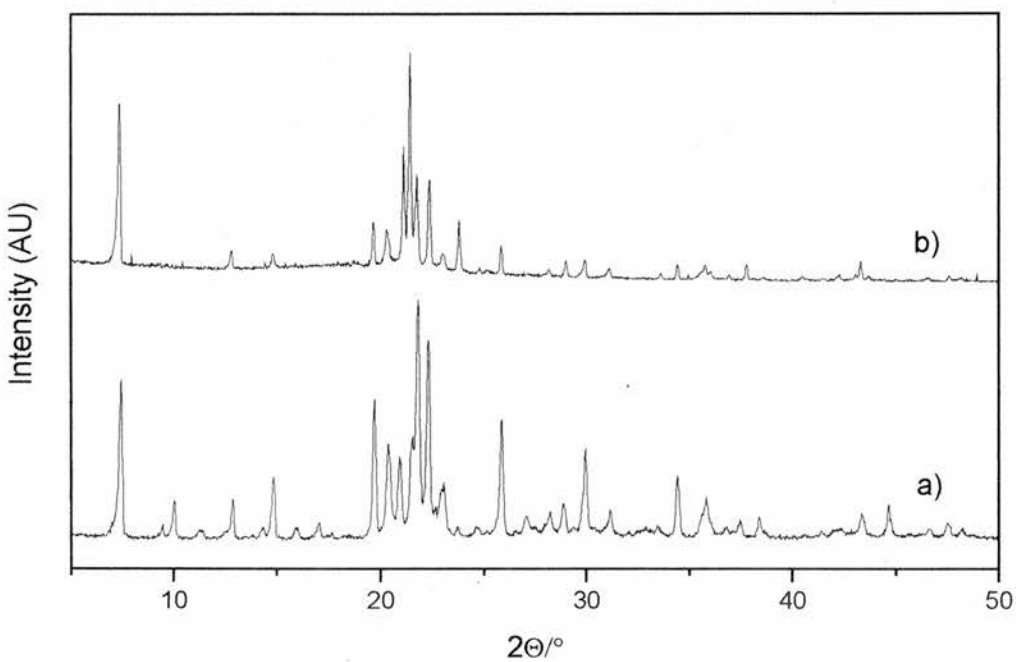

Figure 4.21. XRD pattern of Cu(dien)$_2$-MgAPO-5 as prepared a), and calcined in nitrogen at 600 degrees for 700 minutes, b).

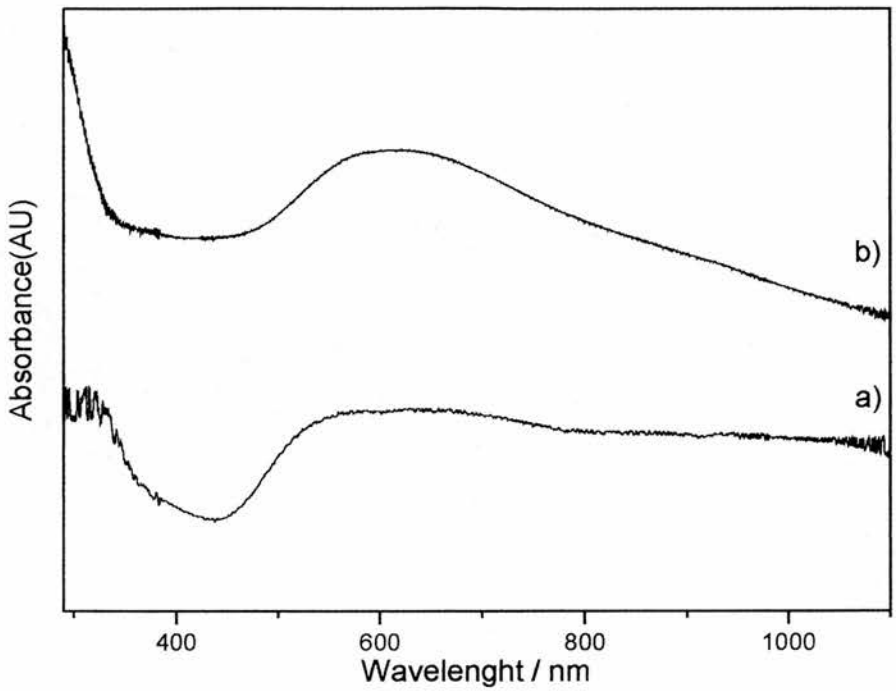

Figure 4.22. UV-visible spectrum of a) $Cu(deta)_2(NO_3)_2$; b) $Cu(deta)_2$-MgAPO-5

4.4. CONCLUSIONS

The nickel complex $[Ni(diethylenetriamine)_2]^{2+}$ acts as an efficient structure directing agent in the synthesis of microporous aluminophosphates, giving frameworks with the AFI and CHA topologies, depending on the synthesis conditions. The octahedral complex remains intact during synthesis and its positive charge is balanced by aliovalent substitution for Al^{3+} or P^{5+} in the framework, or, for aluminophosphate preparations performed in the presence of ammonium fluoride, by F^- ions coordinated to aluminium. These fluoride ions distort the frameworks away from their maximum symmetry, giving triclinic $AlPO_4$-fluoride with the CHA topology (related to UT-6) and orthorhombic $AlPO_4$-fluoride with the AFI topology.

Under similar crystallisation conditions than those employed for $Ni(deta)_2Cl_2$, the two similar complexes $Ni(trien)_2^{2+}$ and $Ni(tren)_2^{2+}$ did not produced any complex-containing material.

The copper complex with diethylenetriamine, $Cu(deta)_2^{2+}$, also showed a different behaviour to that of the nickel one producing mainly mixtures of products. However it could be incorporated within MgAlPO-5 in a preparation that usually yield MgAPO-34 for the nickel variant of the complex. This shows that changing the metal for the same complex can also result in different products under the same synthesis conditions.

4.5. REFERENCES

1. M. P. Attfield, S. J. Weigel, F. Taulelle, A. K. Cheetham, *J.Mater.Chem.*, 2000, **10**, 2109.

2. B. Gomez-Lor, M. Iglesias, C. Cascales, E. Gutierrez-Puebla, M. A. Monge, *Chem. Mater.*, 2001, **13**, 1364.

3. S. M. Stalder, A. P. Wilkinson, *Chem. Mat.*, 1997, **9**, 2168.

4. Y. H. Xu, Z. Yu, X. F. Chen, S. H. Liu, X. Z. You, *J. Solid State Chem..*, 1999, **146**, 157.

5. D. J. Williams, J. S. Kruger, A. F. McLeroy, A. P. Wilkinson and J. C. Hanson, *Chem. Mater.*, 1999, **11**, 2241.

6. N. Rajic, A. Meden, P. Sarv, V. Kaucic, *Micropor.Mesopor Mater,* 1998, **24**, 83.

7. N. Rajic, D. Stojakovic, A. Meden, V. Kaucic, *Proc. 12th Int. Zeolite Conf.*, Eds. M. M. J. Treacy, B. K. Marcus, M.E. Bisher, J.B. Higgins, MRS, Warrendale, Pennsylvania, 1999, 1765.

8. J.R.D. DeBord, Y. Zhagang, R. C. Haushalter, J. Zubieta, C. J. O´Connor, *J.Solid State Chem.*, 1996, **122**, 251

9. D.A. Bruce, A. P. Wilkinson, M.G. White, J.A. Bertrand, *J.Chem.Soc. Chem. Commun.*, 1995, 2059.

10. K.R. Morgan, G.J. Gainsford, N.B. Milestone, *Chem.Commun.*, 1997, 61

11. S.M. Stalder, A.P. Wilson, *Chem.Mater.*, 1997, **9**, 2168

12. G. Yang, S.C. Sevov, *Inorg.Chem.*, 2001, **40**, 2214

13. Y. Wang, J. Yu, Z. Shi, R. Xu, *J.Solid State Chem.*, 2003, **170**, 176.

14. Y.-H Xu, Z. Yu, X.-F Chen, S.-H Liu, X.-Z You, *J. Solid State Chem.*, 1999, **146**, 157

15. B.Z. Lin, S.X. Liu, *Polyhedron*, 2000, **19**, 2527

16.A. Meden, L. McCusker, C. Baerlocher, N. Rajic, V. Kaucic, *Micropor. Mesopor. Mater.*, 2001, **47**, 269

17. M. A. Camblor, M. A. Barret, M. J. Díaz-Cabañas, L. A. Villescusa, *MicroMesoporous Materials*, 2001, **48**, 11.

18. E.G. Rochow (Ed.), Inorganic synthesis, McGraw-Hill, 1960, **200**, 6

19. A.C. Larson, R.B. von Dreele, Generalised Crystal Structure Analysis System, Los Alamos National Laboratory, USA, 1994.

20. G.M.Sheldrick, SHELXS, University of Göttingen, 1986; SHELXTL, version 5.3, Program for the solution of crystal structures, University of Göttingen, 1993.

21. P.A. Wright, R.H. Jones, S. Natarajan, R.G. Bell, J. Chen, M. Hursthouse, J.M. Thomas, *J.Chem.Soc.Chem.Commun.*, 1993, 633

22. P.A. Wright, S. Natarajan, J.M. Thomas, R.G. Bell, P.L .Gai-Boyes, R.H. Jones, J.Chen, *Angew.Chem.Int.Ed.Engl.*, 1992, **31**, 1472

23. N. Rajic, A. Ristic, A. Tuel, V. Kaucic, *Zeolites*, 1997, **18**, 115

24. S. Olivier, A. Kuperman, A.Lough, G.A.Ozin, *J.Mater.Chem.*, 1997, 7, 807

25. J.J. Pluth, J.V. Smith, *J. Phys. Chem.*, 1989, **93**, 6516

26. P.S. Wheatley, PhD thesis, University of Saint Andrews, 2003.

27. V. Rodriguez, J. M. Gutierrez-Zorrilla, P. Vitoria, A. Luque, P. Román, M. Martinez-Ripoll, *Inorg.Chim. Acta*, 1999, **290**, 57.

28. A. K. Mukherjee, S. Koner, A. Ghosh, N. R. Chaudhuri, M. Mukherjee, A. J. Welch, *J.Chem.Soc.Dalton Trans.*, 1994, 2367.

29. P. Paleotti, S. Biagini, M. Cannas, *Chem. Comm.*, 1969, 513.

30. S. Biagini, M. Cannas, *J.Chem.Soc.(A)*, 1970, 2390

31 R. Garcia, I.J. Shannon, A.M.Z. Slawin, W. Zhou, P.A. Cox, P.A. Wright, *MicroMesoporous Mater.*, 2003, **58**, 91.

32. Inorganic Crystal Structure Database (ICSD) service, UK Chemical Database service.

[33] E. Lear, *Final Year Project*, St.Andrews University, 2002.

34. L.M. Meyer, R.C. Haushalter, *Chem.Mater.*, 1994, **6**, 349

35. A.M. Chippindale, A.R. Cowley, R.I. Walton, *J.Mater.Chem.*, 1996, **6**, 611

36. C. Panz, K. Polborn, P. Behrens, *Inorg.Chim.Acta, 1998*, **269**, 73

37. L-Yu, W. Pang, L. Li, *Solid State Chem.*, 1990, **87**, 241

38. G. Férey, T. Louseau, P. Lacorre, F. Taulelle, *J.Solid State Chem.*, 1993, **105**,179

39. N.Z. Logar, L. Golic, V. Kaucic, *Micropor.Mater.*, 1997, **9**, 63

5. CALCINATION OF Ni(DETA)$_2$-UT-6 AND RELATED SOLIDS

5.1. INTRODUCTION

Molecular sieves synthesised hydrothermally commonly include organic structure directing agents within their pores. To permit their application as adsorbents and catalysts, the organics have to be removed from the pores by a post-synthetic treatment. This treatment usually consists of burning off the organic species at elevated temperatures (calcination), leaving free access to the pore space.

Several processes can take place during calcination. First, calcination usually removes certain volatile species from the framework such as the organic template, water, fluoride (as hydrogen fluoride), etc. and leaves purely inorganic species within the framework. Normally, calcination only produces small changes within the framework structure and hence, the calcined material can be employed to refine and confirm the crystal structure. Indeed, it is often preferable for new materials available only as powders, to attempt to solve their structures using diffraction from the calcined form. Although still challenging to solve, the calcined materials are purely inorganic and have fewer atoms to locate (no organics, etc). Furthermore, the calcined materials commonly exhibit higher symmetry, aiding in structure solution.

Férey and co-workers have developed a method, based on energy minimisation studies, to simulate and anticipate the calcined crystal structure of materials whose as-prepared crystal structure is known.[1,2,3]. In this procedure starting from the known crystal structure of the zeolitic material, the atoms and molecules that are thought to be removed during the calcination treatment are eliminated from the original model of the structure. In cases where the structures possess atoms in coordinations other than tetrahedral, this leaves some of the atoms on highly distorted environments. In a final step, the modified structures are minimised allowing both cell parameters and fractional coordinates to relax in the original space group of the as-prepared materials subject to study ($AlPO_4$-14, MIL-34, UT-6 and GaPO-34 triclinic). In this way, the structure of the calcined material

can be predicted and for these systems, the approach has shown encouraging success.

However, calcination of a zeolitic material sometimes involves more complex rearrangements. These may concern structural rearrangements of the framework-forming elements of the structure or chemical changes in the species that are present within the pore space. One such transformation is the recrystallisation of lamellar phases to produce three-dimensional frameworks after calcination. This is the case of the two lamellar precursor phases, MCM-22(P)[4] and PREFER[5], that upon calcination condense to form the fully-connected three-dimensional framework of the zeolites MCM-22 and ferrierite respectively, both thermally stable and with empty voids. These materials are of great interest since the as-prepared lamellar forms can be exfoliated and the organics removed subsequently by calcination to yield the delaminated materials ITQ-2[6] and ITQ-6[7] that have different properties from those of MCM-22 and ferrierite.

This behaviour of a layered material that upon calcination transforms to a solid with three-dimensional connectivity has also been observed in the phosphate-based system. For example, a versatile lamellar phase denominated AlPO-L[8] converts upon calcination into $AlPO_4$-5. This material can also be a precursor for other structural related frameworks under different synthesis conditions. The fluorinated layered phase prepared with the macrocycle Tet-A[9] condenses after calcination to give a material with a similar X-ray pattern to that of $AlPO_4$-41 (AFO), although it exhibits differences in the relative intensities and broader peaks than the typical AFO material. Since this transformation requires the translation of the layers along the *a* and *b* directions and the condensation of the layers along the *c* direction, the differences observed between the patterns of these two materials are attributed to the structural disorder from the condensation reaction.

Three-dimensional frameworks can also be subject to thermally-induced phase transformations. The behaviour of aluminosilicate cation-exchanged zeolites on heating can be summarised as follows. The first stages of the calcination process correspond to a dehydration and rearrangement of the extra framework cations and residual water molecules, and at higher temperatures, irreversible topological changes of the initial framework occur due to breaking of T-O-T bridges. The breaking of the T-O-T bridges most often cause a collapse of the framework structure, with formation of an amorphous intermediate product, formed out of

fragments of the previous zeolite framework that after prolonged heating reorganise into a new framework type (usually denser phase). There are also examples of direct topotactic transformation into a more stable structure where the mechanism of the breaking and re-establishing of the T-O-T bridges are simultaneous and inseparable.

Examples of the first type of transformation are aluminosilicates that have been subject to cation exchange and, depending on the cation introduced into the framework, recrystallised upon calcination at high temperatures to other phases through an amorphous stage. This is the case of the aluminosilicate zeolite A (LTA) that, depending on the type of extraframework cation, can be transformed into cristobalite[10], analcime (ANA)[11] and ABW[12].

Transformations have also been observed in both silicate- and phosphate-based materials where there is a crystallographic relation between the structure that existed before calcination and the structure of the calcined material. Such examples are known as topotactic phase changes. Remarkable examples of such transformations of silicates include the solid state transformation of the sodium-exchanged zeolite E, (EAB-type) and sodium exchanged ZK-14 zeolite, a synthetic chabazite, to sodalite-type phases when heated at temperatures over 360°C and 500°C, respectively[13,14]. The potassium and rubidium-exchanged phases do not undergo this transformation[15]. In the phosphate-based system, examples are the transformation of AlPO-C into AlPO-D[16], the transformation of AlPO-21 to AlPO-25[17] and the reversible transformation of VPI-5 to AlPO-8[18]. For the first two examples mentioned (AlPO-C-to-AlPO-D and AlPO-21-to-AlPO-25) the frameworks before and after calcination present similar layers that are connected by chains consisting of 4-rings containing tetrahedral atoms with specific up and down tetrahedral directivity. The calcination process changes the orientation of some of these tetrahedra on the chains and this produces the change in the structure (see figure 5.1). In the case of the AlPO-21 to AlPO-25, the transformation is more complex because it also involves dehydroxylation of the five-coordinated aluminium atoms that constitute 2/3 of the aluminiums in the AlPO-21 framework.

The transformation of VPI-5 to AlPO-8 is an example of a slightly different type, since it is only produced under specific conditions (removal of water under specific washing and drying steps or calcination under specific conditions) and it is reversible. A scheme of the transformation is given in fig. 5.2.

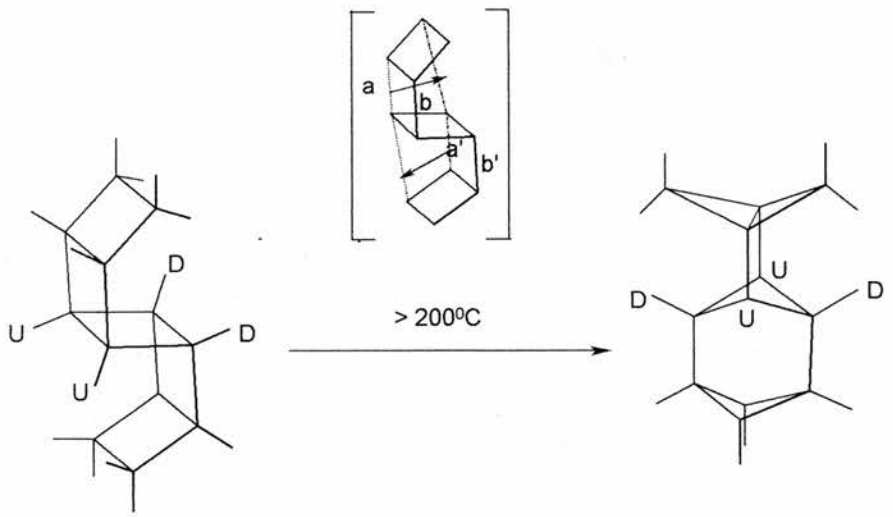

Figure 5.1. Topotactic transformation of AlPO-C to AlPO-D.

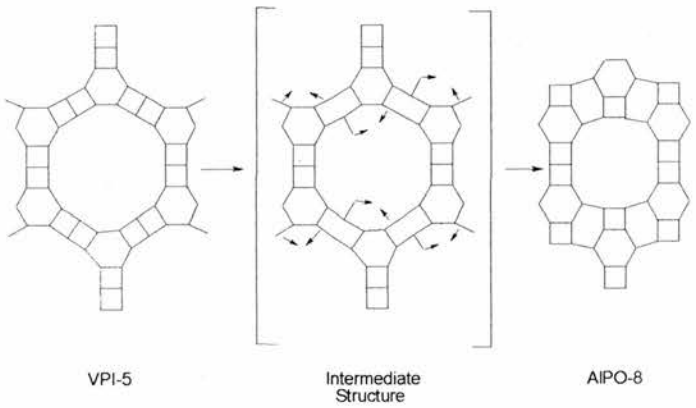

Figure 5.2. Schematic representation of the transformation of VPI-5 into AlPO-8.

Finally, where metal complexes are included within the microporous materials, calcination results in removal of their organic ligands. The state of the metal after calcination depends on the particular material, the nature and the concentration of the metal within the framework. As discussed previously, after calcination of the STA-6 and 7 MAPO structures, Ni^{2+} cations remain balancing the negative charge of the frameworks, coordinated to the framework oxygen and adsorbed water. In the case of UTD-1, a very open aluminosilicate synthesised with

a cobaltocenium complex as a structure directing agent, calcination in nitrogen and air yields a blue solid that contains cobalt oxide occluded in the pores and on the external surface of the crystals[19]. This cobalt oxide can be removed from the pores of the material by acid treatment, yielding complete access to the pores of the material. Cobaltocenium[20] and ferrocene[21] ions have been adsorbed within AlPO-5 by impregnation to give similar complex-containing materials prior to calcination. The iron or cobalt species resulting from calcination were studied by EXAFS spectroscopy which suggest that the metal ions remain within the framework, coordinated to framework oxygens. The charge introduced by the metal cations was thought to be compensated in this case by structural defects on the frameworks.

In this chapter, the effects of calcination on microporous aluminophosphates prepared using the $Ni(deta)_2^{2+}$ complex as a structure directing agent are studied. These include complex-containing MgAPO-34, hexagonal and orthorhombic variants of AlPO-5 and the UT-6, described previously in Chapter 4. They represent examples of frameworks that would be expected either to retain a negative charge or to be neutral after calcination, and the behaviour of the nickel is likely to differ in the two cases. In particular, structural changes of the framework and observation of changes of the state of the nickel are examined in detail.

5.2. EXPERIMENTAL

5.2.1. Calcination conditions

In order to remove the organics from the as-prepared $Ni(deta)_2$-containing solids, a sample of the material was placed in a tube furnace and heated at 10°C/min to the desired temperature (350-700°C) in either flowing oxygen or nitrogen, and kept at that temperature for a further 700 minutes before being allowed to cool.

5.2.2. Powder X-ray diffraction

Powder X-ray diffraction of the calcined materials were collected on a STOE STADIP diffractometer operating on monochromated Cu K_α radiation in Debye-Scherrer geometry. Samples were loaded in 0.7 mm silica glass capillaries.

5.2.3. Extended X-ray Absorption Fine Structure (EXAFS)

To determine the effect of calcination on the state of nickel within the solids, room temperature EXAFS data were collected at the nickel K-edge in station 7.1 of the Daresbury Synchrotron Radiation Source (energy 2GeV, current typically 200 mA) operating in a transmission mode. Wavelength selection was accomplished using a double crystal Si(1 1 1) monochromator set at 50% harmonic rejection. The Ni K-edge position was determined using nickel foil while the samples were mounted as self-supporting wafers. Data were processed with EXCALIB (raw data processing), EXSPLINE or EXBROOK programs to perform the background substraction and EXCURV98 to compare theoretical and experimental EXAFS[22]. Multiple scattering effects were included in the refinement of nickel metal and nickel oxide nanoparticles when these were formed within the neutral frameworks. The multiple scattering on these samples is expected to be strong due to the shadowing effect of co-linear arrangements of neighbouring atoms[23].

5.2.4. Other techniques

HRTEM studies shown in this work were performed by Dr. Zhou (St Andrews University) on a JEOL JEM-200CX electron microscope operating at 200 kV equipped with a CCD Gatan camera.

The organic content of the samples was determined by microanalysis using a Carlo Erba 1106 CHN elemental analyser by Mrs S. Williamson.

Thermogravimetrical analysis (TGA) was performed using a TA Instruments SDT 2960 simultaneous DTA-TGA thermogravimetric analyser. Samples were heated in a crucible at a rate of 10°C/min to a maximum temperature of 1000°C in a flowing atmosphere of oxygen or nitrogen as stated in the text. Recalcined aluminium oxide was employed as the reference material.

The N_2 adsorption isotherms reported in this Chapter were measured at 77 K using an IGA-2 series Intelligent Gravimetric Analyser by Mr Jorge Gonzalez.

5.3. RESULTS

Table 5.1 shows the samples examined in this chapter and the composition of the gels from which they were prepared from.

Calcinations were performed in either oxygen or nitrogen. Nitrogen calcination usually yields frameworks with better crystallinity, whilst calcination under oxygen is more likely to remove all the carbon products within the framework. It was also thought that the type of calcination could affect the nature of the nickel particles formed in each case, as discussed later.

Samples	Gel Composition
Ni(deta)$_2$ -MgAPO-34	0.15 Mg : 0.85 Al : 1 P: 25 H_2O : 1.3 DPA : 0.1 Ni(deta)$_2$Cl$_2$
Ni(deta)$_2$-AlPO-5	0.5 NH_4F : 0.5 Ni(deta)$_2$Cl$_2$:1 Al: 1P: 400 H_2O
Ni(deta)$_2$-UT-6	0.5 NH_4F : 0.5 Ni(deta)$_2$Cl$_2$:1 Al: 1P: 100 H_2O

Table 5.1. Materials studied in this chapter, showing the gel composition for their crystallisation.

5.3.1. Calcination of Ni(deta)$_2$-MgAPO-34.

The material was synthesised as described in chapter 4, with the presence of the complex plus additional amines in the synthesis gel. After calcination at 550°C under flowing oxygen, the solid retained its structure and symmetry although it loses some crystallinity (see figure 5.3).

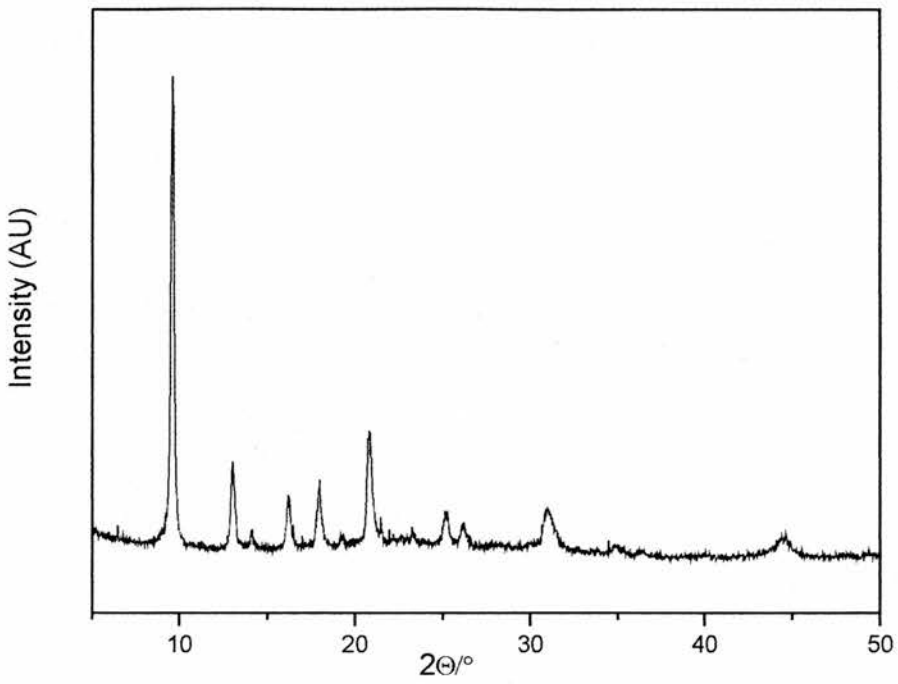

Figure 5.3. X-ray diffraction pattern of Ni(deta)$_2$ -MgAPO-34 calcined in flowing oxygen at 550°C.

EXAFS was employed to get an insight to the nature of the nickel left in the framework after calcination of the microporous hosts. EXAFS spectroscopy at the Ni K-edge was performed on a sample of the calcined MgAPO-34 to analyse the environment of the nickel on this sample. The EXAFS spectrum for the material could be fitted well by a model consistent with six oxygens at 2.04 Å as it corresponds to a high spin complex of nickel. Hence, it is thought after calcination the nickel cation is left isolated as Ni^{2+} in extraframework positions, probably coordinated on an octahedral fashion to water molecules and/or oxygens of the framework. Calcination of these samples only removes the organic species, leaving the nickel cation in extraframework sites.

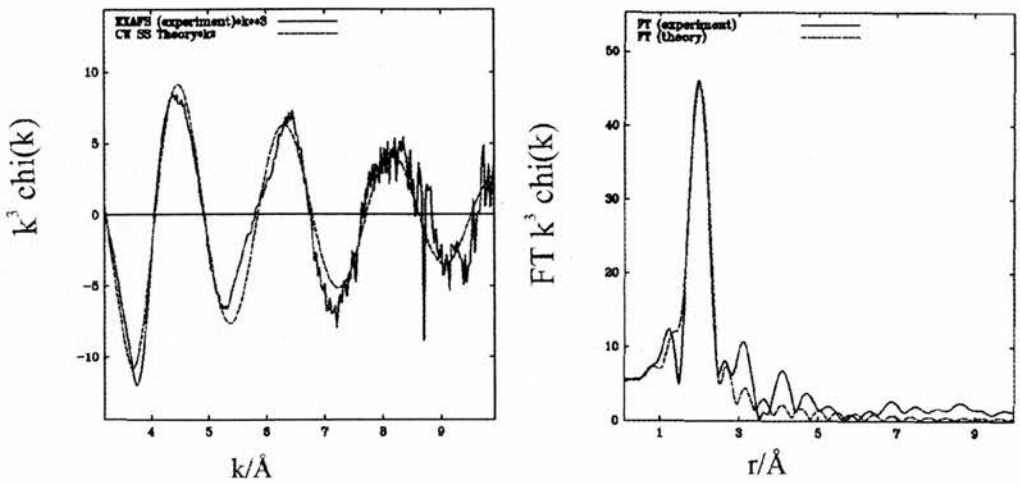

Figure 5.4 Experimental (solid line) and theoretical (dashed line) Ni k-edge EXAFS (left) and its Fourier transform (right) for the calcined Ni(deta)$_2$-MgAPO-34. Parameters for the fit are shown in table 5.2.

Sample	Atom type	Coordination number N	Distance R(Å)	Debye-Waller factor σ^2((Å)
Calcined Ni-MgAPO-34-dpa	O	6	2.041	0.013

R=29.77 %, FI=0.00060

Table 5.2. Results from the fitting of the EXAFS of the MgAPO-34 structure calcined in oxygen at 550 °C.

5.3.2. Calcination of Ni(deta)$_2^{2+}$-UT-6

Calcination of this material showed a more complex behaviour than expected from the observed similar material (UT-6) synthesised with pyridine[24] but without Ni, which becomes AlPO-34 after calcination.

The triclinic Ni(deta)$_2^{2+}$-UT-6 retains its framework structure, which becomes rhombohedral after heating at temperatures of 350-385°C[1], kept at that temperature for 700 minutes, and subsequently heated in oxygen to burn the organics and empty the inorganic framework. The material obtained in this way has the chabazite structure (CHA) as observed for UT-6 and predicted by modelling studies of Férey[2].

When the Ni(deta)$_2^{2+}$-UT-6 is heated directly to temperatures of 500°C or above in oxygen, however, most of the sample converts to AlPO-5 (with some AlPO-34). Heating at 600-700°C in nitrogen first, then switching to oxygen, results in phase-pure AlPO-5. Remarkably, once the AlPO-34 structure is obtained at 350-385°C, subsequent calcination at a higher temperature (700°C), gives no conversion to AlPO-5 (figure 5.5).

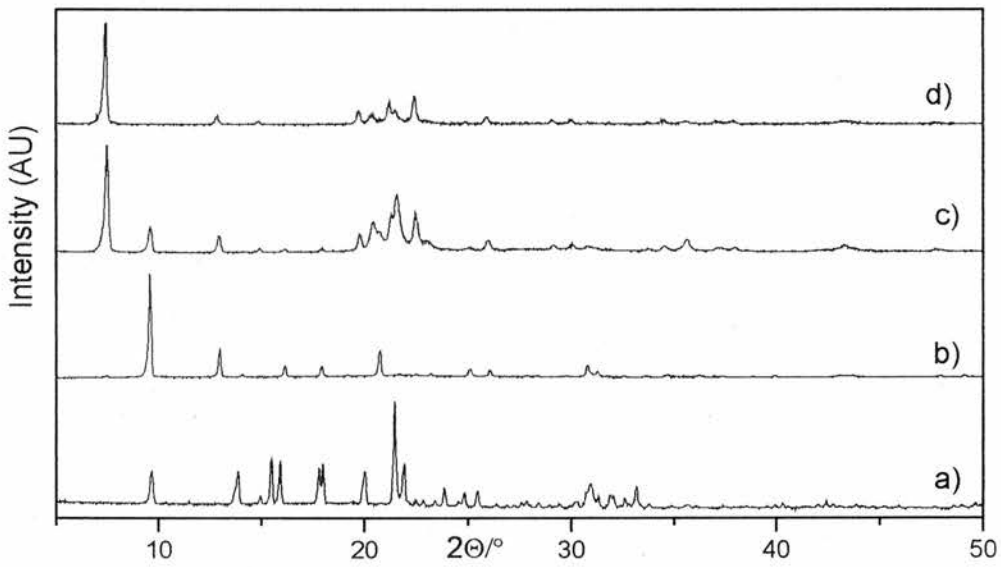

Figure 5.5. X-ray diffraction pattern corresponding to sample of Ni(deta)$_2^{2+}$-UT-6 as prepared a); Calcined in N_2 atmosphere till 350°C and subsequent heated in Oxygen at 700°C, b); Calcined in O_2 at 600°C, c); Calcined in N_2 at 600°C and switching to oxygen then, d).

[1] The temperature depends on the sample, but it is usually within this range.

A series of calcinations were therefore performed in flowing nitrogen over the temperature range (350-700°C), with the aim of getting more information about the transformation process. It can be seen that the sample remains crystalline during the treatment and both phases coexist after heating at some temperatures (see figure 5.6). These patterns show that the material recrystallises as AlPO-5 without losing crystallinity. There is no evidence of formation of an amorphous phase since the background scattering remains low.

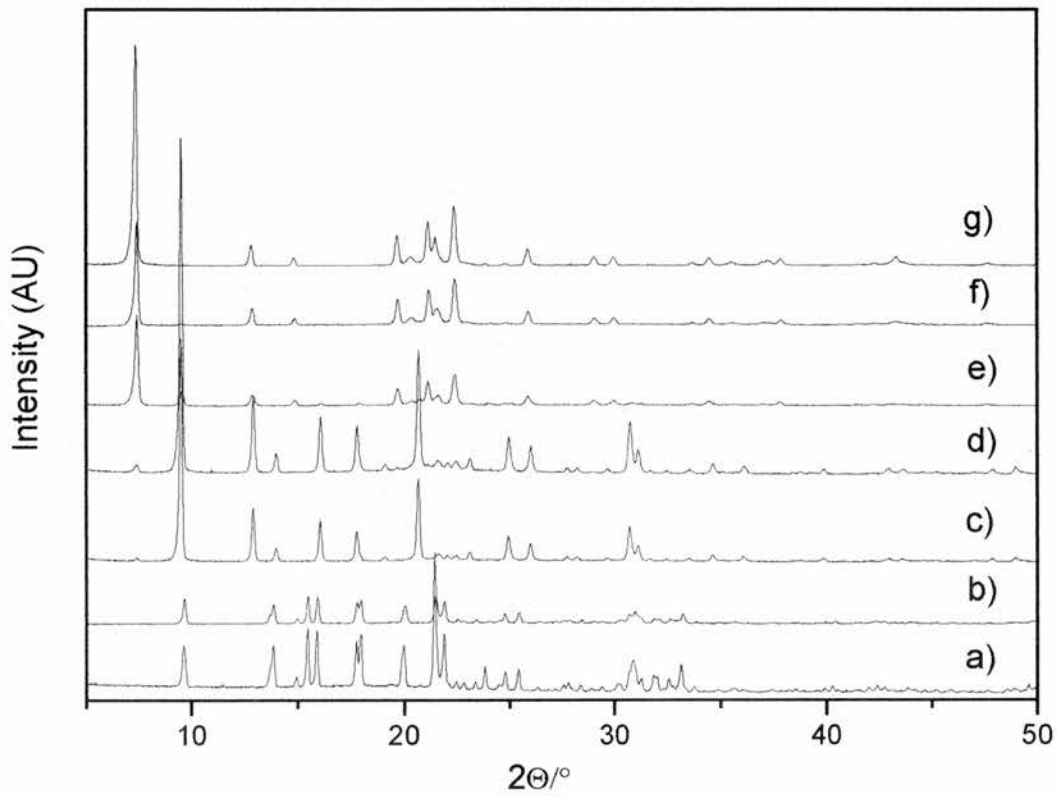

Figure 5.6. X-Ray diffraction patterns ofNi(deta)$_2$-UT-6 calcined in nitrogen at different temperatures. The sample was heated and kept at that temperature for 700 minutes. a) Ni(deta)$_2$-UT-6 as prepared; b) Ni(deta)$_2$-UT-6 calcined at 300°C; c) at 375°C; d) at 385°C; e) at 400°C; f) at 500°C; g) at 600°C.

Thermogravimetric analysis was performed separately for Ni(deta)$_2$-UT-6 in only oxygen and only nitrogen (figure 5.7). The TGA in oxygen shows the material does not lose almost any weight till 300°C, only 1.8%. From 300 till 1000°C it loses 21.83 %. The shape of the TGA in nitrogen is very similar to that in oxygen. The main loss of weight (22.15 %) occurs between 300-1000°C.

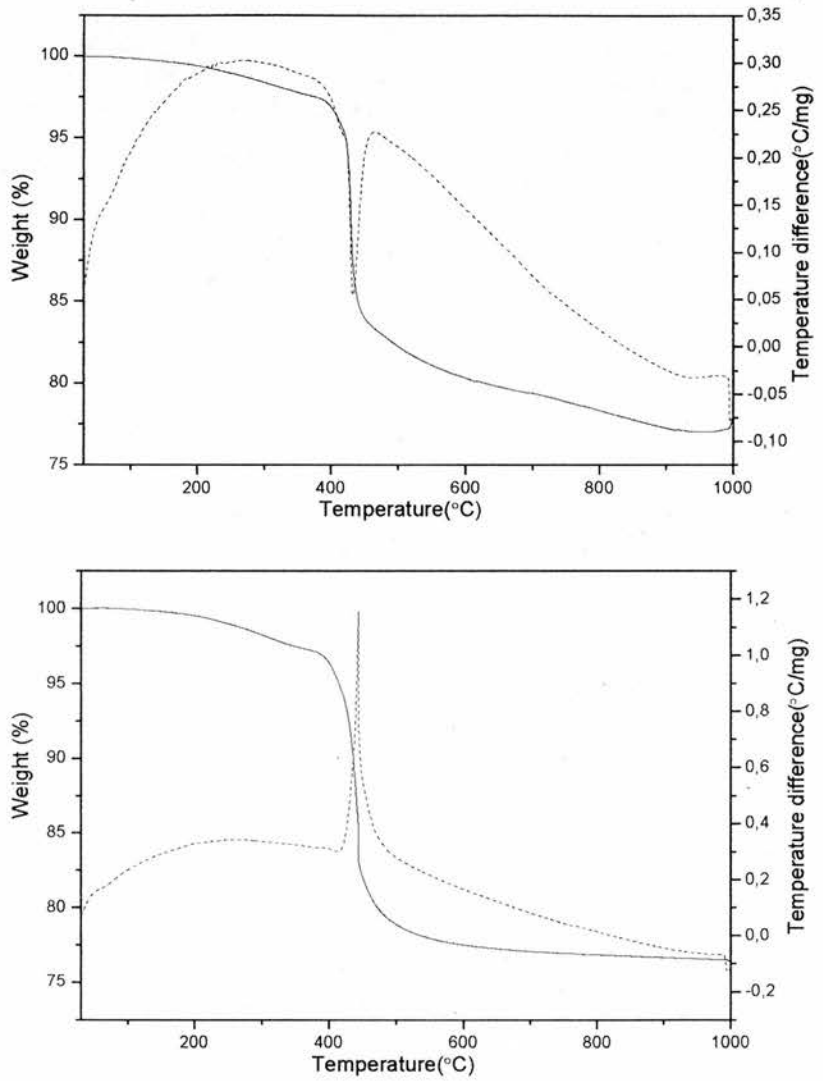

Figure 5.7. TGA analysis for Ni(deta)$_2$-UT-6 in both N_2 atmosphere (top) and in O_2 atmosphere (bottom).

TEM was performed on one of the samples obtained by calcination in nitrogen and then oxygen at 600-700°C that was pure AlPO-5 by XRD (figure 5.8). The sample was very sensitive to the beam and it was not possible to obtain electron diffraction or lattice images. However, low magnification electron microscopy shows that the original crystallites had been replaced by a many small domains, suggesting that the conversion from AlPO-34 to AlPO-5 has not taken place topotactically but rather at a number of nucleation points. EDX elemental mapping on this sample revealed an inhomogeneous distribution of nickel species over the particles, figure 5.10 a).

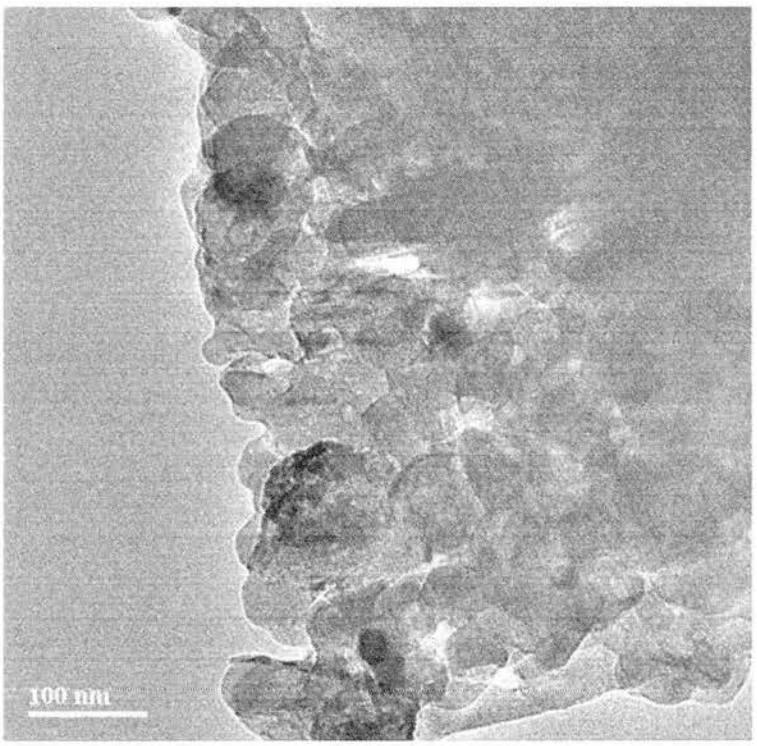

Figure 5.8. TEM low magnification image of a sample of AlPO-5 obtained by calcination of Ni(deta)$_2$-UT-6 in nitrogen and oxygen at 600-700°C. The image shows that the original crystallites have been replaced by many small domains.

A sample calcined in oxygen at 600°C to give a mixture of AlPO-5 with some AlPO-34 by XRD (as observed in figure5.5.c) was also studied by electron microscopy. It was only possible to get images of the AlPO-34 particles at high magnification (figure 5.9) since the AlPO-5 particles were again unstable under the

electron beam. However, this time EDX mapping showed a homogeneous distribution of nickel species across the material (figure 5.10 b)). This shows that the distribution of the nickel particles forming on calcination is dependent on the conditions of calcination.

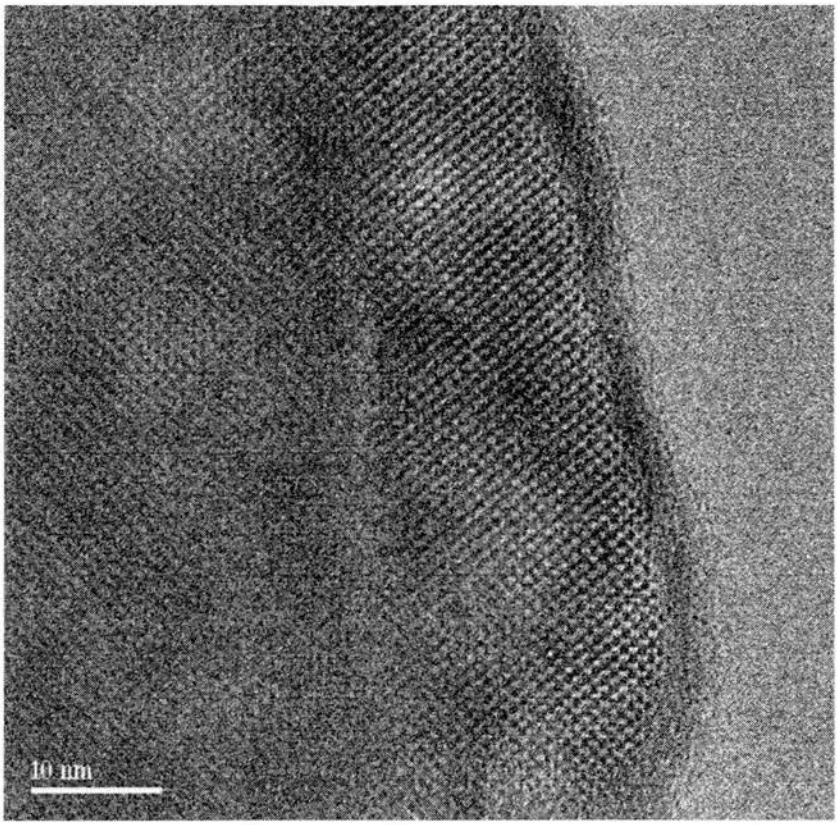

Figure 5.9. High resolution TEM image of Ni(deta)$_2$-AlPO-34 after calcination in oxygen at 600℃, that was found to be a mixture of AlPO-34 and AlPO-5 by XRD.

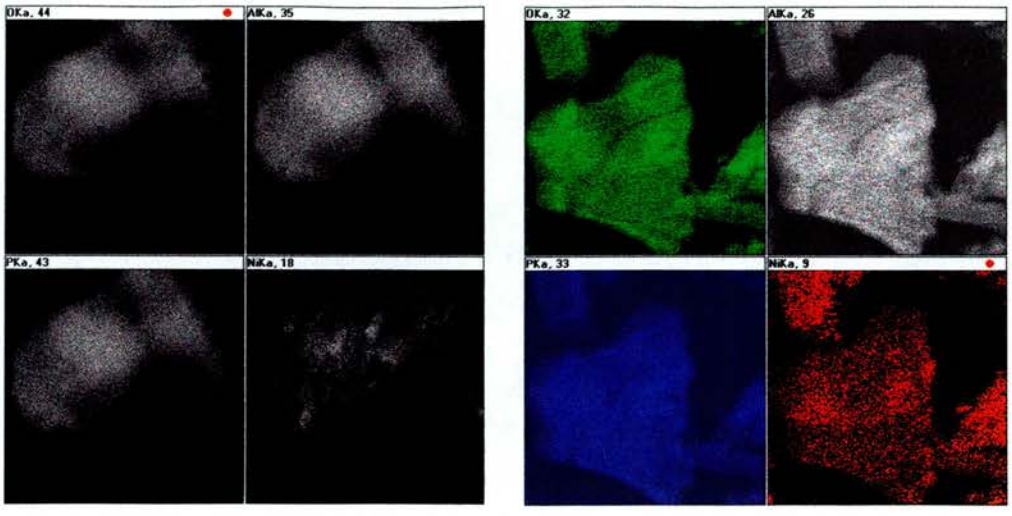

a) b)

Figure 5.10. EDX elemental mapping of two samples of Ni(deta)$_2$-UT-6 calcined under different conditions. a) The sample calcined in N_2 at 600°C shows uneven distribution of nickel species on the solid; b) Sample calcined in oxygen at 600°C showing an homogeneous distribution of nickel species on the particles.

Porosity of the AlPO-34 and AlPO-5 formed after calcination of the original UT-6 structure, was studied by nitrogen adsorption performed on samples calcined under oxygen. For the AlPO-34 structure obtained by calcination at 385°C in nirogen followed by heating in oxygen, the shape of the N_2 isotherm was typical of a microporous solid, with a pore volume of 0.17 cm^3/g on the range of the typical AlPO-34 structure. The AlPO-5 formed by calcination at higher temperature, shows a lower pore volume (0.06 cm^3/g). This is indicative that in the recrystallisation process, some of the organisation disappears and the microporosity is reduced.

EXAFS analysis was performed on a sample of the calcined material that was originally Ni(deta)$_2$-UT-6 with the aim of studying the chemical and structural state the nickel once the organics were removed. In this case, the nickel species have to be different to those of charged frameworks in order to maintain the electroneutrality of the framework. Calcinations were performed either in oxygen or

in nitrogen, since it was clear from TEM that the species formed depend on the calcination conditions.

5.3.2.1. Calcination in oxygen

Formation of nickel oxide particles was postulated since the neutrality of the framework might be kept after calcination. On a first approach, this was observed for a sample calcined in oxygen at 600 °C. When the EXAFS plot and Fourier transform were compared with those corresponding to a sample of bulk nickel oxide, it may be seen that the inner shells of both samples were of approximately the same intensity. However, the outer shells possess lower intensity. This was attributed to the smaller size of the nickel oxide nanoparticles formed during the calcination process. The refinement was then performed changing the number of occupancy, N, of the higher shells. This might give an approximate idea of the size of the nanoclusters formed upon calcination[25].

Samples of the same material were calcined at different temperatures in oxygen and the EXAFS were measured. The multiple scattering analysis procedure was applied to these samples to check how the size of the particles was changing on the basis of the change on the occupancy numbers of the shells (N) on samples calcined at different temperatures. In all cases the samples were analysed by elemental analysis. This confirmed that there was almost no organic left within the different samples table 5.3. XRD also confirmed the stage of the transformation and it is shown in figure 5.12.

Analysis of the EXAFS showed that on the samples heated at temperature of 500°C or over, formation of nickel oxide nanoparticles is observed. The size of these nanoparticles is different depending on the calcination temperature of the sample, but this change in size (observed throught the coordination numbers, N, for every shell) is not very marked from 500, 600 and 700°C. The size of the nanoparticles only slightly increased with the increasing of temperature. This could be as a result of the confinement of the nanoparticles inside the zeolitic host which could be limiting the growth of the nanoparticles.

Temperature (°C)	Organic content		
	% C	% H	% N
Room temperature	9.21	2.37	8.21
350	0.80	2.45	0.55
400	0.32	1.69	0.05
500	0.11	0.61	0.11
600	0.06	0.83	0.07
700	0.06	0.04	0.68

Table 5.3. C,H,N analysis of samples of Ni(deta)$_2$-UT-6 calcined at different temperatures.

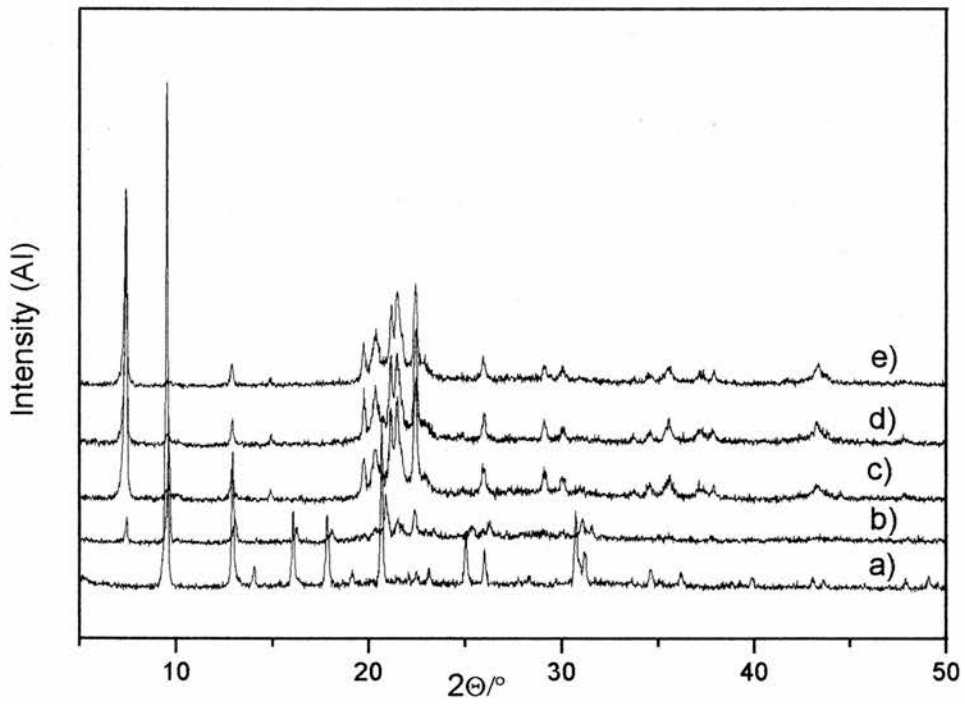

Figure 5.12. X-ray patterns of samples of Ni(deta)$_2$-UT-6 calcined in oxygen at different temperatures. EXAFS studies were performed in these samples: a) calcined at 350 °C, b) 400 °C, c) 500 °C, d) 600 °C and e) 700 °C..

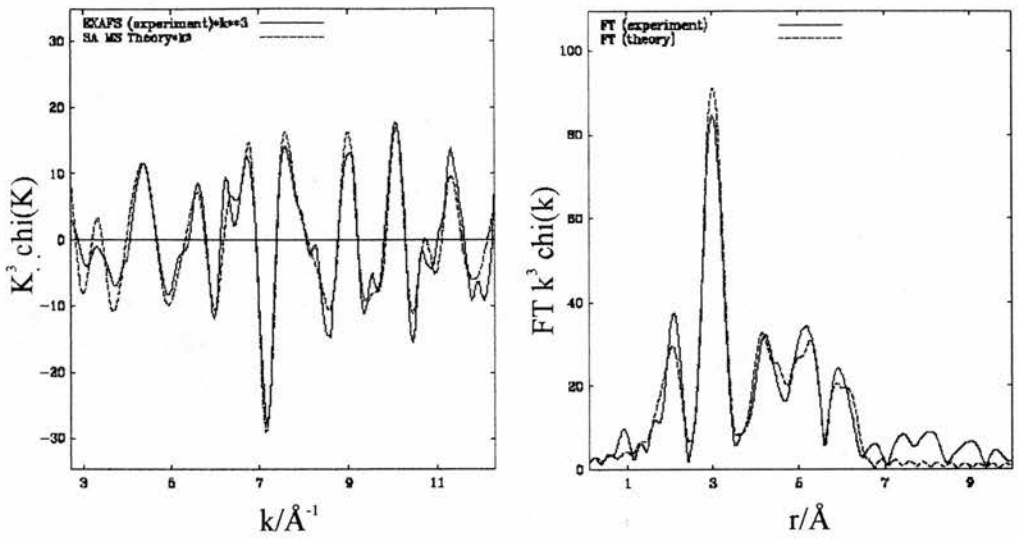

Figure 5.13. Experimental (solid line) and theoretical (dashed line) Ni K-edge EXAFS (left) and its Fourier Transform (right) for NiO standard.

Atom Type	Coordination Number N	Distance R / Å	Debye-Waller factor σ^2 / Å^2
O	6.0	2.09	0.011
Ni	12.0	2.96	0.008
O	8.0	3.51	0.011
Ni	6.0	4.18	0.009
O	24.0	4.61	0.011
Ni	24.0	5.13	0.009
Ni	12.0	5.92	0.009

R=33.83 % , FI=0.00066

Table 5.4. Fit Parameters for the EXAFS data for NiO standard.

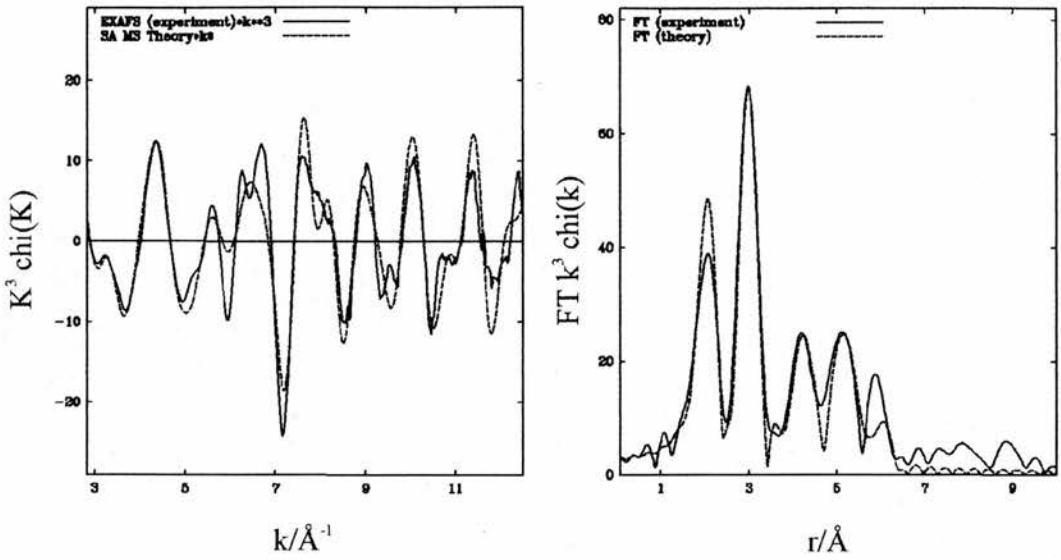

Figure 5.14. Experimental (solid line) and theoretical (dashed line) Ni K-edge EXAFS (left) and its Fourier Transform (right) for Ni(deta)$_2$-UT-6 calcined in oxygen at 500°C.

Atom Type	Coordination Number N	Distance R / Å	Debye-Waller factor σ^2 / Å^2
O	6.0	2.09	0.011
Ni	5.0	2.96	0.008
O	5.8	3.51	0.011
Ni	2.1	4.18	0.009
O	5.7	4.61	0.011
Ni	9.9	5.13	0.009
Ni	5.0	5.92	0.009

R=41.01% , FI=0.00088

Table 5.5. Fit Parameters for the EXAFS data for Ni(deta)$_2$-UT-6 calcined in oxygen at 500°C.

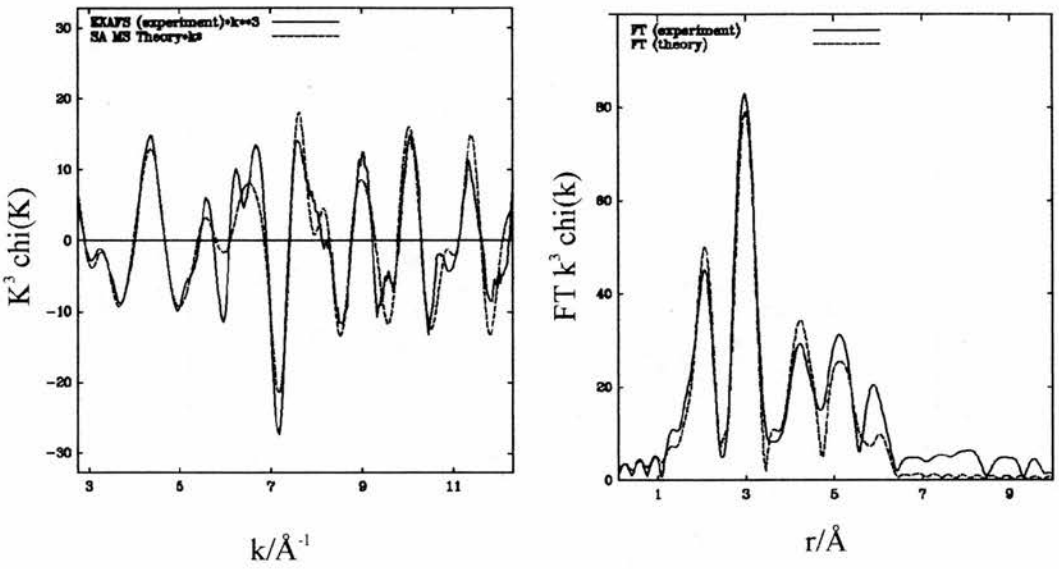

Figure 5.15. Experimental (solid line) and theoretical (dashed line) Ni K-edge EXAFS (left) and its Fourier Transform (right) for Ni(deta)$_2$-UT-6 calcined in oxygen at 600°C.

Atom Type	Coordination Number N	Distance R / Å	Debye-Waller factor σ^2 / Å^2
O	6.0	2.09	0.011
Ni	5.9	2.96	0.008
O	6.5	3.51	0.011
Ni	4.0	4.18	0.009
O	6.4	4.61	0.011
Ni	10.2	5.13	0.009
Ni	5.3	5.92	0.009

R=35.20% ,FI=0.00068

Table 5.6. Fit Parameters for the EXAFS data for Ni(deta)$_2$-UT-6 calcined in oxygen at 600°C.

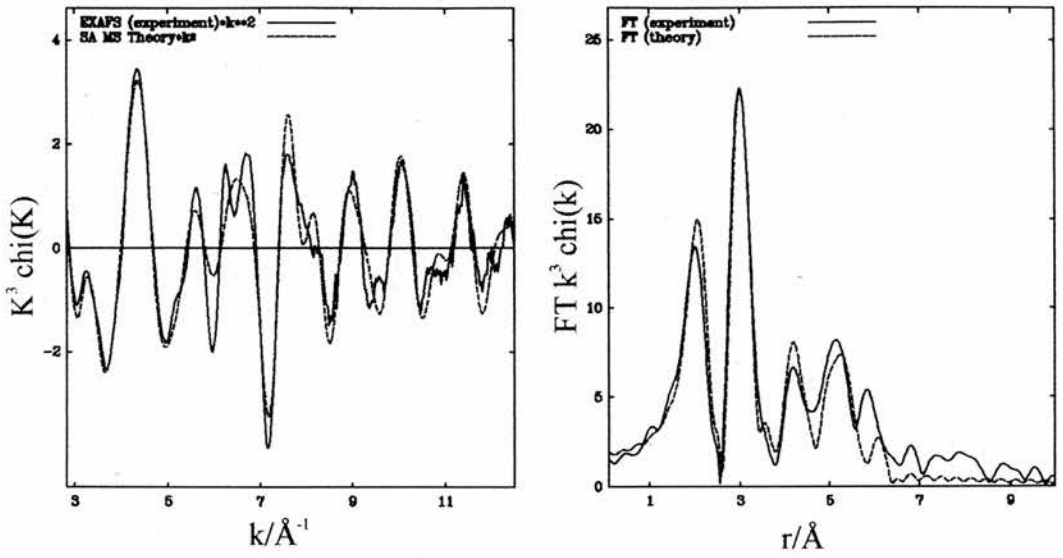

Figure 5.16. Experimental (solid line) and theoretical (dashed line) Ni K-edge EXAFS (left) and its Fourier Transform (right) for Ni(deta)$_2$-UT-6 calcined in oxygen at 700°C.

Atom Type	Coordination Number N	Distance R / Å	Debye-Waller factor σ^2 / Å^2
O	6.0	2.09	0.011
Ni	6.6	2.96	0.008
O	7.5	3.51	0.011
Ni	4.0	4.18	0.009
O	4.0	4.61	0.011
Ni	13.3	5.13	0.009
Ni	5.7	5.92	0.009

R=32.79 %,FI=0.00052

Table 5.7. Fit Parameters for the EXAFS data for Ni(deta)$_2$-UT-6 calcined in oxygen at 700°C.

In contrast to these EXAFS curves, the samples calcined at 350°C and 400°C showed a different spectrum from the NiO-containing solids. On the sample calcined at 350°C, a single major shell can be observed in the Fourier Transform of the EXAFS data. The sample calcined at 400°C also shows a similar EXAFS

spectrum to this one, although some coordination shells at higher K are becoming of higher intensity. However, it was not possible to fit either this curve or that of the sample heated at 350°C with the nickel oxide model. It is difficult to propose a model to fit the EXAFS spectrum for these two samples since the nature of the nickel species remaining within the framework is unknown. They do not correspond to nickel oxide but they have to be neutral to keep the electroneutrality of the framework. The proposed model contains six oxygen atoms in the first shell for the sample calcined at 350°C and six oxygen atoms and some nickel for the sample calcined at 400°C.

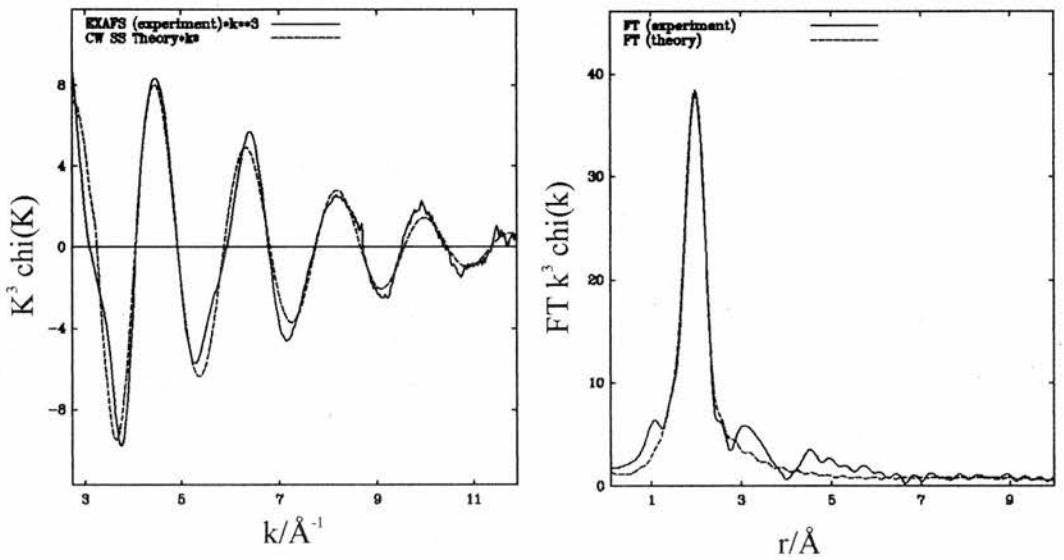

Figure 5.17. Experimental (solid line) and theoretical (dashed line) Ni K-edge EXAFS (left) and its Fourier Transform (right) for Ni(deta)$_2$-UT-6 calcined in oxygen at 350°C.

Atom type	Coordination number N	Distance R(Å)	Debye-Waller factor σ^2((Å)
O	6	2.034	0.019

R=23.21 %, FI=0.00036

Table 5.8. Fit Parameters for the EXAFS data for Ni(deta)$_2$-UT-6 calcined in oxygen at 350°C.

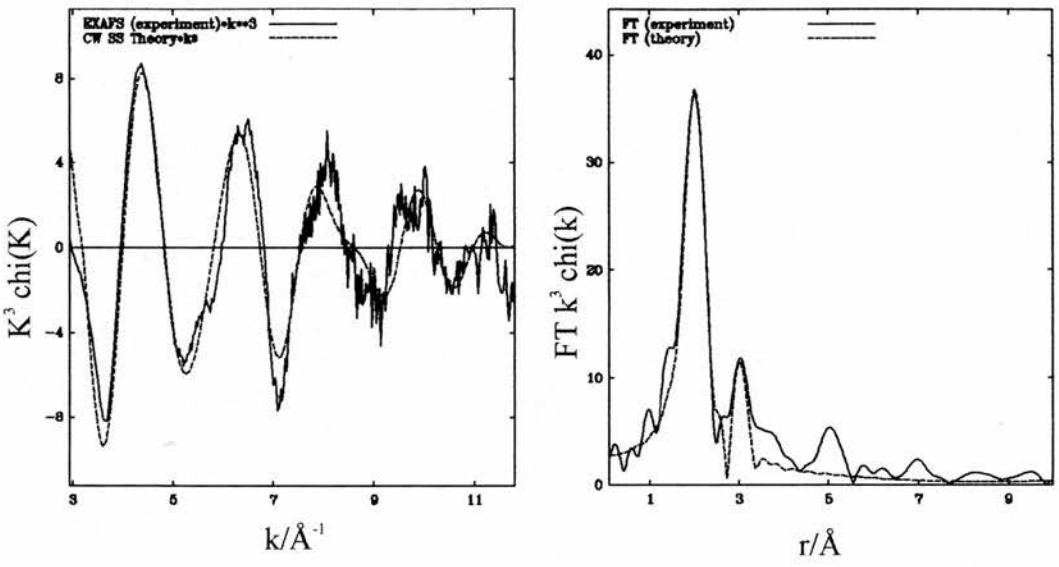

Figure 5.18. Experimental (solid line) and theoretical (dashed line) Ni K-edge EXAFS (left) and its Fourier Transform (right) for Ni(deta)$_2$-UT-6 calcined in oxygen at 400°C.

Atom type	Coordination number N	Distance R(Å)	Debye-Waller factor σ^2((Å)
O	6	2.060	0.018
Ni	0.9	3.005	0.011
R=39.24 %,FI=0.00079			

Table 5.9. Fit Parameters for the EXAFS data for Ni(deta)$_2$-UT-6 calcined in oxygen at 400°C.

5.3.2.2. Calcination in Nitrogen

A sample of the UT-6 material was calcined at 600°C in flowing nitrogen. The nickel is expected to remain in the material as nickel metal.

The refinement of the EXAFS is performed in a similar way as for the Ni(deta)$_2$-UT-6 samples calcined in oxygen but in this case, the inner coordination shell of the material calcined in nitrogen at 600ºC is smaller than that of the Ni metal foil and therefore, it can not be assumed that it remains intact. The EXAFS show that the nickel takes the form of small particles of nickel metal since the coordination number for the different shells are smaller than those corresponding to the Ni foil standard.

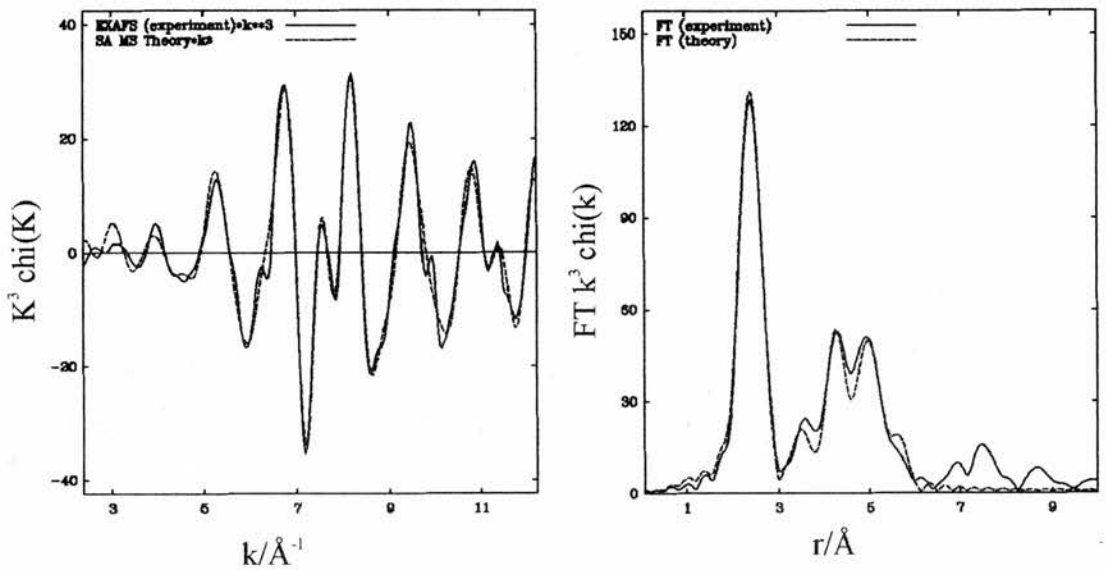

Figure 5.19. Experimental (solid line) and theoretical (dashed line) Ni K-edge EXAFS (left) and its Fourier Transform (right) for Ni metal foil.

Atom Type	Coordination Number N	Distance R / Å	Debye-Waller factor σ^2 / Å^2
Ni	12.0	2.48	0.016
Ni	6.0	3.49	0.023
Ni	24.0	4.32	0.020
Ni	12.0	4.98	0.016
Ni	24.0	5.59	0.025

R=21.37 %, FI=0.00030

Table 5.10. Fit Parameters for the EXAFS data for Ni metal foil.

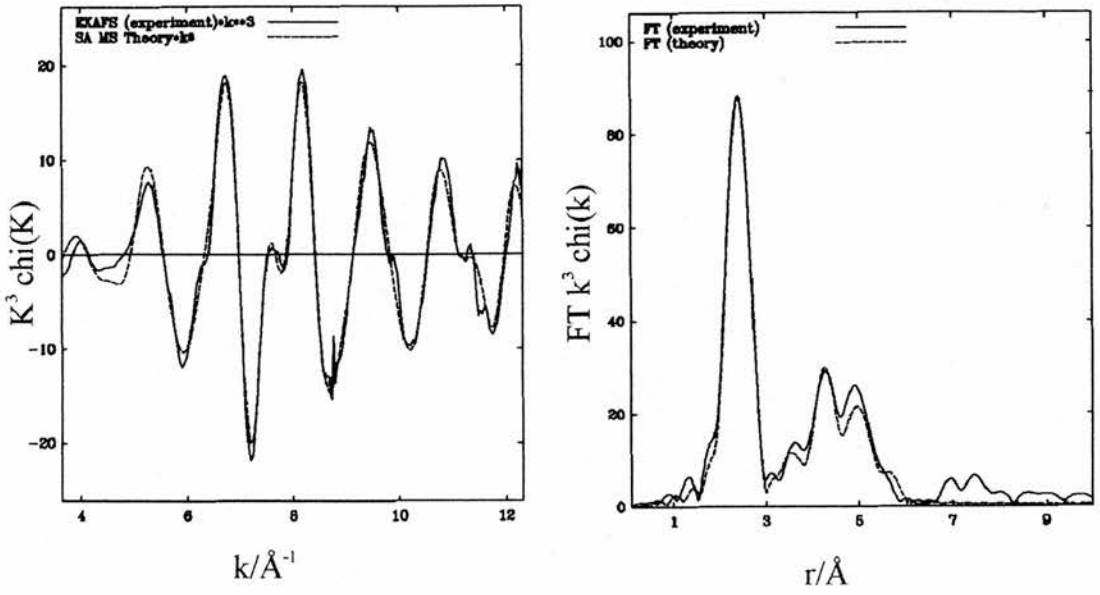

Figure 5.21. Experimental (solid line) and theoretical (dashed line) Ni K-edge EXAFS (left) and its Fourier Transform (right) for Ni(deta)$_2$-UT-6 calcined in nitrogen at 600°C.

Atom Type	Coordination Number N	Distance R / Å	Debye-Waller factor σ^2 / Å^2
Ni	8.0	2.48	0.016
Ni	3.7	3.49	0.023
Ni	14.1	4.32	0.020
Ni	5.0	4.98	0.016
Ni	9.9	5.59	0.025

R=19.06 %, FI=0.00019

Table 5.11. Fit Parameters for the EXAFS data for Ni(deta)$_2$-UT-6 calcined in nitrogen at 600°C.

5.3.3. Calcination of the hexagonal and orthorhombic variants of Ni(deta)$_2$-AlPO-5.

The hexagonal AlPO-5 prepared with extra amines and the one prepared with a similar gel composition to the ammonium fluoride preparation but without the addition of ammonium fluoride, retained the hexagonal symmetry upon calcination. The orthorhombic variant of this material, prepared in the synthesis where ammonium fluoride was added, becomes hexagonal after calcination, probably due to the removal of the fluoride ions that give rise to the distortion of the framework. Some extra peaks that correspond to a dense phase can be seen in the diffraction pattern of the calcined material. Since these diffraction peaks are not seen in the patterns of the as-prepared materials, it is thought that part of the material has recrystallised as a dense phase during calcination.

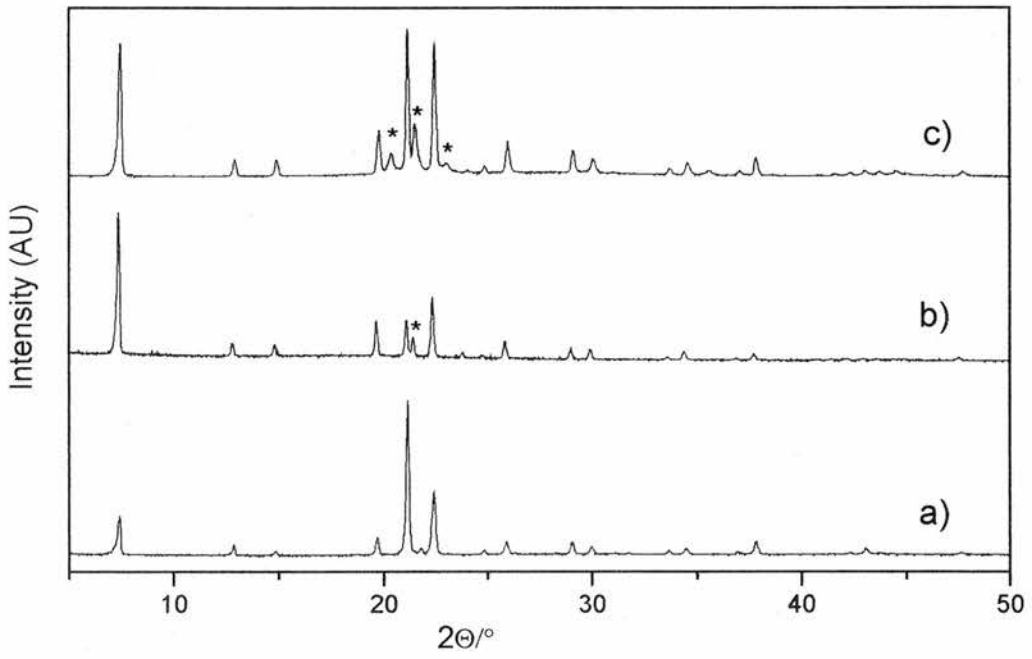

Figure 5.22. Diffraction patterns of the different Ni(deta)$_2^{2+}$-AlPO-5 materials calcined under oxygen at 600 °C for 700 minutes; a) Ni(deta)$_2^{2+}$-AlPO-5 hexagonal prepared without NH_4F and without extra amines; b) Ni(deta)$_2^{2+}$-AlPO-5 hexagonal prepared with dipropylamine as an extrabase; c) Ni(deta)$_2^{2+}$-AlPO-5 orthorhombic prepared in the presence of ammonium fluoride, the asterisk peaks correspond to reflections of a dense phase.

A sample of the orthorhombic AlPO(F)-5 calcined in oxygen was studied by EXAFS. As expected by analogy with the UT-6 material, which also possesses a neutral framework, NiO nanoparticles are also formed on calcination and hence, the EXAFS plot was fitted using the same approach adopted for the UT-6 material (figure 5.23).

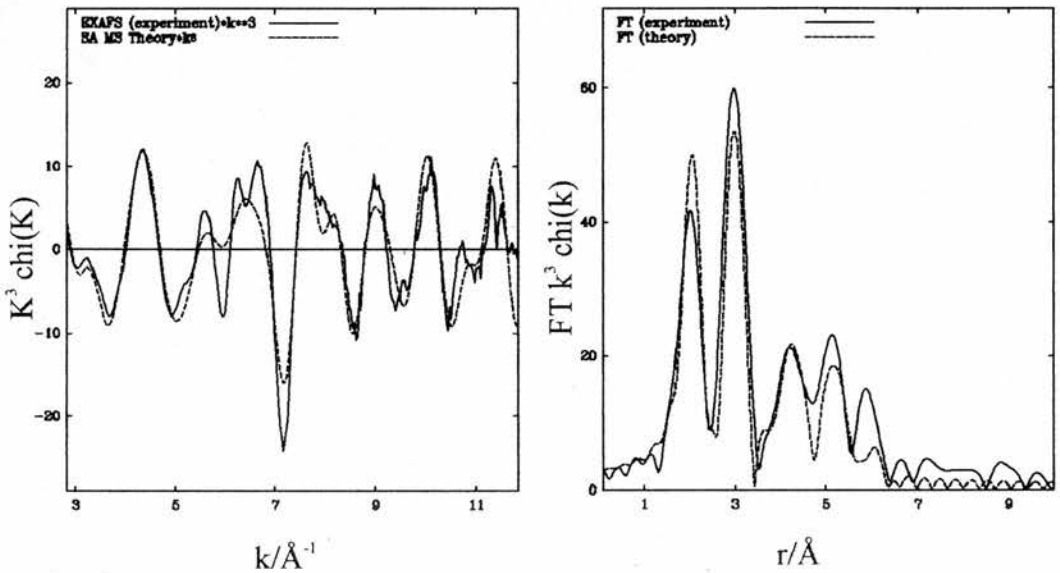

Figure 5.23. Experimental (solid line) and theoretical (dashed line) Ni K-edge EXAFS (left) and its Fourier Transform (right) for Ni(deta)$_2$-AlPO-5 orth calcined in oxygen at 600°C.

Atom Type	Coordination Number N	Distance R / Å	Debye-Waller factor σ^2 / Å^2
O	6.0	2.09	0.011
Ni	4.1	2.96	0.008
O	5.3	3.51	0.011
Ni	2.7	4.18	0.009
O	5.2	4.61	0.011
Ni	7.2	5.13	0.009
Ni	4.1	5.92	0.009

R=44.89 %,FI=0.00116

Table 5.12. Fit Parameters for the EXAFS data for Ni(deta)$_2$-AlPO-5 orth calcined in oxygen at 600°C.

5.4. SUMMARY AND CONCLUSIONS

In this chapter, the process of calcination of materials containing nickel has been studied, focusing on structural changes of the aluminophosphate framework and the nature of the nickel species left after calcination. This has shown that for materials that possess charged frameworks the nickel remains as a charge compensating cation, in a similar way to the samples of STA-6 and STA-7, shown in chapter 3.

However, in a neutral framework, other nickel species have to be formed to keep the neutrality of the bulk solid. The nature and distribution of species are dependent on the calcination conditions. In general, it has been shown that calcination of the materials under oxygen results in the formation of NiO nanoparticles, while calcination under N_2, gives nickel metal nanoparticles. TGA and elemental analysis seem to confirm that in both type of atmospheres most of the carbon is lost. This means that on the calcination under nitrogen not much carbon is left in the material as coke. Hence the proposed mechanism of calcination is:

$$Ni(deta)_2^{2+} \xrightarrow{O_2,\Delta} NiO + \text{volatiles (amines,}CO_2\text{, etc)}$$

$$Ni(deta)_2^{2+} \xrightarrow{N_2,\Delta} Ni\ (metal) + \text{volatiles (amines, etc)}$$

Ni(deta)$_2$-AlPO(F)-5, after calcination in oxygen becomes hexagonal and formation of NiO particles is also observed, although electron microscopy suggest that they leave the pores.

The Ni(deta)$_2$-UT-6 shows more complex behaviour. Calcination at temperatures on the range 350-385 °C, removes the fluoride leaving the AlPO-34 structure, which is porous and shows ordering by electron microscopy. The nature of the nickel species formed at this temperature on calcinations under oxygen is unclear, but it is not NiO nanoparticles, since the EXAFS spectrum is very different. When the material is calcined at temperatures of 500°C or over, the framework structure recrystallises to AlPO-5. This recrystallisation is thought to be happening

at a small number of nucleation points rather than topotactically, since TEM images show small domains on crystals of the converted material. AlPO-34 and AlPO-5 possesses very different structures so a topotactic transformation is very unlikely. Instead, it is thought that on calcination of Ni(deta)$_2$-UT-6 at higher temperatures, the structure becomes amorphous locally at a small number of nucleation points in the crystal and then recrystallises to AlPO-5.

This behaviour is not typical for the aluminophosphate UT-6 prepared with pyridine that becomes the chabazite framework after calcination. It is also different from the MgAPO-34 and SAPO-34 materials prepared with the same complex in this work, which maintain their framework structure upon calcination. It has not been observed in the triclinically-distorted material prepared by Rajic and co-workers with a similar nickel complex but in the absence of ammonium fluoride. This suggest that the transformation is related to both the presence of fluoride within the framework and the formation of the nickel or nickel oxide particles (in a similar way to that of the exchange alkaline cations in the zeolites E and ZK-14). The combination must permit the major amount of bond breaking and making that are required in this reconstructive solid state transformation.

5.5. REFERENCES

1. S. Girard, C. Mellot-Draznieks, J. D. Gale and G. Férey, *Chem. Commun.*, 2000, 1161.

2. S. Girard, A. Tuel, C. Mellot-Draznieks and G. Férey, *Angew. Chem. Int. Ed.*, 2002,**41**, 972.

3. T. Loiseau, C. Mellot-Draznieks, C. Sassoye, S. Girard, N. Guillou, C. Huguenard, F. Taulelle and G. Férey, *J.Am.Chem.Soc.*, 2001, **123**, 9642

4. S.L. Lawton, A.S. Fung, G.J. Kennedy, L.B. Alemany, C.D. Chang, G.H. Hatzicos, D.N. Lissy, M.K. Rubin, H.J.C. Timken, S. Stenernagel, D.E. Woessner, *J.Phys.Chem.*, 1996, **100**, 3788

5. L. Schreyeck, P. Caullet, J.C. Mougenel, J.L. Guth, B. Marler, *Microporous Mater.*, 1995, **6**,259.

6. A. Corma, V. Fornés, J.M. Guil, S. Pergher, Th.L. M.Maesen, J.G. Buglass, *Micro.Mesopoous. Materials.*, 2000, **38**, 301.

7. A. Corma , U. Diaz , M.E. Domine,V. Fornés, *J.Am.Chem.Soc.*, 2000, **122**, 2804

8. N. Venkatathri, S. G.Hegde, V. Ramaswamy, S. Sivasanker, *Micro.Mesoporous. Materials.*, 1998, **23**, 277

9. P.S. Wheatley, C.J. Love, J.J. Morrison, I.J. Shannon, R.E. Morris, *J.Mater.Chem.*, 2002, **12**, 477

10. V. Dondur, R. Dimitrijević, *J.Solid.State Chem.*, 1986, **63**, 46.

11. V. Dondur, R. Dimitrijević, N.Petranović, *J.Solid.State Chem.*, 1991, **95**, 335

12. V. Dondur, R. Dimitrijević, *J.Solid.State Chem.*,1995, **115**, 214.

13. W.M. Meier, M. Groner, *J.Solid.State Chem.*, 1981, **37**, 204

14. S. Cartlidge, W.M. Meier, *Zeolites*, 1984, **4**, 218

15. S. Cartlidge, E.B. Keller, W.M.Meier, *Zeolites*, 1984, **4**, 226

16. E.B. Keller, W.M. Meier, *Sol.St.Ionics*, 1990, **43**, 93.

17. J. Li, J. Yu, K. Wang, G. Zhu, R. Xu, *Inorg.Chem.*, 2001,**40**, 5812

18. L. Maistriau, Z. Gabelica, E.G. Derouane, E.T.C. Vogt, J. van Oene, *Zeolites*, 1991, **11**, 583.

19. R.F. Lobo, M. Tsapatsis, C.C. Freyhardt, S. Khodabandeh, P. Wagner, C.-Y. Chen, K.J. Balkus Jr, S.I. Zones,M.E. Davis, *J.Am.Chem.Soc.*, 1997, **119**, 8474

20. M. Endregard, D.G. Nicholson, M. Stöker, G.M. Lamble, *J.Mater.Chem.*, 1995, **5**, 785.

21. A. Lund, D.G. Nicholson, G.M. Lamble, B. Beagley, *J.Mater.Chem.*, 1994, **4**, 1723

22. N. Binsted, EXCURV98:CCLRC Daresbury Laboratory computer program, 1998.

23. B.K. Teo, *J.Am.Chem.Soc.*, 1981, **103**, 3990.

24. S. Olivier, A. Kuperman, A. Lough, G.A. Ozin, *J.Mater.Chem.*, 1997, **7**, 807

25.R.Garcia, I.J. Shannon, A.M.Z. Slawin, W. Zhou, P.A. Cox, P.A. Wright, *Micro.Mesoporous Mater.*, 2003, **58**, 91.

6. CATALYTIC TEST

6.1. INTRODUCTION

Among the applications of zeolitic materials, their use as heterogeneous catalysts is one of the most thoroughly investigated. Indeed they have been used as catalysts in petrochemical process for 40 years, mainly in the field of oil refining and basic petrochemistry [1]. Examples of zeolitic materials that are employed in industrial catalytic process include zeolite Y, ZSM-5, Mordenite and SAPO-11 among others[2]. Table 5.1 shows a summary of industrial processes involving acid catalysts:

Industrial proccess	Catalyst	Conditions	Product Importance
Etherification of methanol and alkenes	Acidic ion-exchange resin	30-100°C, liquid phase	Synthesis of oxygenate octane enhancers such as MTBE
Alkylation of monoaromatics with ethene, propene, etc.	H-ZSM-5	300-400°C, 20 bar	Ethylbenzene, ethyltoluene precursors for styrenes used for polymers, isopropylbenzene precursor for phenol
Synthesis of methylamines from methanol and ammonia	H-Rho, modified H-Mordenite	350-500°C, 15-30 bar	Important intermediates for solvents, insecticides, herbicides, pharmaceuticals and detergents
Reforming gasoline to increase alkane branching	Pt, Re on Al_2O_3, zeolites	450-550°C, 15-70 bar	Improved octane number fuels
Isomerization of xylenes	H-ZSM-5	300-400°C, 20 bar	*Para*-xylene precursor for terephthalic acid, etc.
Skeletal isomerization of n-butenes, n-pentenes	H-Ferrierite	400-500°C, ~ 1 bar	Isobutenes, isopentenes for synthesis of octane enhancers
Hydrocarbon cracking	Y-zeolites, silica-aluminas	400-500°C, ~ 1 bar	More valuable lower molecular weight fractions
Hydrocracking of heavy fractions of petroleum	Pt/H-zeolites	270-450°C, 80-200 bar H_2	Useful fractions from heavy residue

Table 6.1 Commercial catalytic uses of molecular sieves (refining and petrochemistry), adapted from reference 3.

Aluminosilicate zeolites find their major use in acid-catalysed reactions, where the main aim of research is the replacement of traditional liquid acids such as sulphuric and hydrofluoric acid by these solid acids allowing the preparation of environmentally-friendly and shape selective catalysts[4]. The family of aluminophosphate-based materials is particularly interesting since they can present acid properties when modified by the inclusion of divalent cations (MAPO's) or silicon into framework positions, and so they can also be employed as selective and active solid acid catalysts. For example, SAPO-34 is one of the most investigated materials for the conversion of methanol to light olefins[5] such as ethylene, propene and butene, which are important in the production of synthetic fibers, plastics and petrochemicals.

Furthermore, since aluminophosphate-based materials readily accommodate transition metal cations within their structures such as cobalt, manganese and iron, they also find potential applications in oxidation catalysis. Some of these oxidation reactions are important industrially as for example, the oxidation of cyclohexane to oxygenated products (as cyclohexanone or adipic acid, etc) generating key precursors in the polymer industry[6] and different metalloaluminophosphate materials such as Co- or Mn-AlPO-36[7], Fe- or Mn-AlPO-5[8] and Fe-AlPO-5[9], have been shown to be active catalysts in this oxidation reaction. The performance of aluminophosphate-based materials as catalysts has recently been reviewed[10,11].

The acidity of microporous materials can be characterised by several methods[12]: titration, adsorption and temperature programmed desorption of bases for example pyridine or ammonia, infra-red spectroscopy or catalytic probe reactions. The catalytic cracking of light alkanes is one of the most commonly employed methods to characterised the Bronsted acid sites of molecular sieves. The process is complex and it will only be briefly outlined here. The primary step is thought to be the protonation of the alkane over the acid site producing a carbonium cation (pentacoordinated carbocation) that rearranges to give hydrogen or methane and carbenium ions (tricoordinated carbocation). When there are no strong acid sites present in the solid, the reaction will stop at this point yielding mainly hydrogen, methane and propene and butenes (Scheme 5.1). When stronger acid sites are present in the solid, the carbenium ion would be more strongly adsorbed over the acid site and hence, there will be more probability of colliding with other molecules

from the gas flow and, hence, to undergo secondary reactions yielding a more complex product distribution[13].

$R'\text{-}CH_2\text{-}CH_2\text{-}R + H^+ \longrightarrow R'\text{-}CH_3^+\text{-}CH_2\text{-}R \longrightarrow H_2 + R'\text{-}CH^+\text{-}CH_2\text{-}R$ *or* $R'\text{-}CH_3 + CH_2^+\text{-}R$

Scheme 5.1. Mechanism of alkene cracking over a weak acid site.

The catalytic activity of some of the materials synthesised in this work was tested on the n-butane cracking reaction, which also allows for the characterisation of the acidity of the materials. They were selected on the basis of possessing three-dimensional frameworks and prepared with and without nickel complexes to check the role of nickel (II) and nickel oxide on their catalytic behaviour. Therefore, a series of experiments were performed to (1) examine the acidity of novel solid acids MgAPO- and SAPO-STA-7 (prepared by method described in Chapter 3) compared to that of SAPO-34 which has a similar three dimensional framework with medium pore openings and cage-like structure, and (2) examine the effect of including nickel into the molecular sieves where it can be Ni^{2+} or NiO and when possible, to compare with the behaviour of the material without nickel.

6.2. EXPERIMENTAL

The materials selected for this study were SAPO-34, Ni-SAPO-34, $Ni(deta)_2$-AlPO-UT-6, MgAPO-STA-7, Ni-MgAPO-STA-7, SAPO-STA-7. In addition and for comparative reasons, a sample of $Ni(deta)_2$-AlPO-UT-6 was calcined *in situ* in the reactor at 350^0C to give NiO-AlPO-34 and this was also tested. The samples were prepared as described in this work except for SAPO-34, which was prepared according to reference 14. The purity of all the materials under study was checked by means of powder XRD. Powder X-ray diffraction was performed on the samples after the catalytic test to determine crystallinity in a similar way to that described in previous chapters. Chemical composition of the materials was determined by EDX analysis.

Material	Gel composition	Framework composition (by EDX)
SAPO-34	1 Al: 0.27 P: 0.137 Si: 0.26 Mor: 8.7 H_2O	$Si_{0.40}Al_1P_{0.75}O_4$
SAPO-STA-7	1Al: 0.76 P: 0.24 Si: 192 H_2O: 0.27 TEAOH: 0.15 Cyclam	$Si_{0.23}Al_1P_{0.56}O_4$
MgAPO-STA-7	0.2 Mg: 0.8 Al: 1 P: 60 H_2O: 0.10 TEAOH: 0.125 TMC	$Mg_{0.30}Al_{0.9}P_1O_4$
Ni(deta)$_2$AlPO-UT-6	0.5 Ni(deta)$_2Cl_2$: 1 Al: 1 P: 0.5 NH_4F: 100 H_2O	$Ni_{0.08}Al_{1.07}P_1O_4$ (*)
Ni-SAPO-34	0.1 Ni(deta)$_2Cl_2$: 1 Al: 0.8 P: 0.2 Si: 25 H_2O: 2.60 DPA	$Ni_{0.05}Si_{0.28}Al_1P_{0.77}O_4$
Ni-MgAPO-STA-7	0.125 Ni: 0.2 Mg: 0.8 Al: 1 P: 60 H_2O: 0.10 TEAOH: 0.125 Cyclam	$Ni_{0.06}Mg_{0.26}Al_{0.77}P_1O_4$

Table 6.2. Materials, gel compositions and framework compositionsof the materials under study.(Key: Mor, Morpholine; TEAOH, Tetraethylammonium; TMC tetramethylcyclam; DPA, dipropylamine). The (*) composition correspond to ICP analysis.

Cracking reactions were performed in a continuous flow fixed Cambridge Reactor Design (CRD) model 5000 with a stream of 10% of n-butane (BOC, 99.7%) in helium. The reactant (n-butane, 2 cm^3 min^{-1}) and carrier (helium, 28 cm^3 min^{-1}) gases were metered separately through Brooks mass flow controllers. Catalyst samples were loaded into a quartz glass tube (i.d.95mm) mounted vertically in a water cooled tubular furnace. In each experiment, the gas mixture passed through the solid and the temperature was raised in steps of 25 °C from 350 to 550 °C, and was kept constant at each temperature for 40 min. The product distibution was monitored by on-line gas chromatography (G.C.) on a CE Instruments 8000 TOP Series GC fitted with a 25 m PLOT (Porous Lined Open Tubular) capillary column with a KCl-stabilised Al_2O_3 stationary phase and an flame ionisation FID detector. The GC traces were recorded on a Fisons Instruments DP700 Data Processor (integrator).

Calcined samples of selected materials chosen on the basis of possessing three dimensional pore connectivity were tested for their catalytic activity in the transformation of n-butane. Samples (0.2 g) of as-prepared solids, pelletised and sieved to sizes between 40 and 100 mesh were loaded in a fully automated plug flow reactor. Samples of SAPO-STA-7, SAPO-34, Ni-SAPO-34, MgAPO-STA-7 and Ni-MgAPO-STA-7 were calcined *in situ* in flowing oxygen to remove organic molecules from the pores before being flushed in helium. All samples were calcined at 550°C except Ni(deta)$_2$-AlPO-UT-6, which was heated to 350 °C to ensure that AlPO-34 was obtained.

6.3. RESULTS AND DISCUSSION

The materials under this study are all small pore materials possessing three-dimensionally connected pore networks. Post-catalysis XRD indicates that Ni(deta)$_2$-AlPO-UT-6, SAPO-34, Ni-SAPO-34 and SAPO-STA-7 samples remained fully crystalline during catalysis but the MgAPO-STA-7 and Ni-MgAPO-STA-7 samples lose most of their crystallinity giving broadened diffraction peaks. Nevertheless, all the samples are active for the conversion of n-butane. Catalysis results are given in tables 6.3 till 6.8, showing the overall conversions and selectivities for each material at each temperature.

6.3.1. Solid acidity of SAPO-STA-7 and MgAPO-STA-7 compared to SAPO-34

Results of the n-butane cracking for SAPO-STA-34, SAPO-STA-7 and MgAPO-STA-7 are shown in tables 6.3, 6.4, 6.5 and figure 6.2.

The catalytic activity of SAPO-34 is characteristic of hydrocarbon cracking over a reasonably strong acid. The product distribution includes all C1-C4 alkanes and alkenes with the predominance of propane at lower temperatures. The activity markedly increases with temperature and this also results in the increase of the production of methane at higher temperatures. SAPO-STA-7 shows a lower activity although with a different product distribution richer in propene than SAPO-34 at all temperatures. This indicates the material possesses weaker acid sites than those present in SAPO-34. MgAPO-STA-7, which a similar

framework structure but different composition to that of SAPO-STA-7, shows unusual behaviour when compared with that of the above samples giving high conversions at low temperatures. This might be due to defect structure. The material possesses strong acid sites, as demonstrated by a predominance of propane in the product distribution although the activity dramatically decreases at higher temperatures (525 °C) which is attributed to a loss of crystallinity (fig. 6.1).

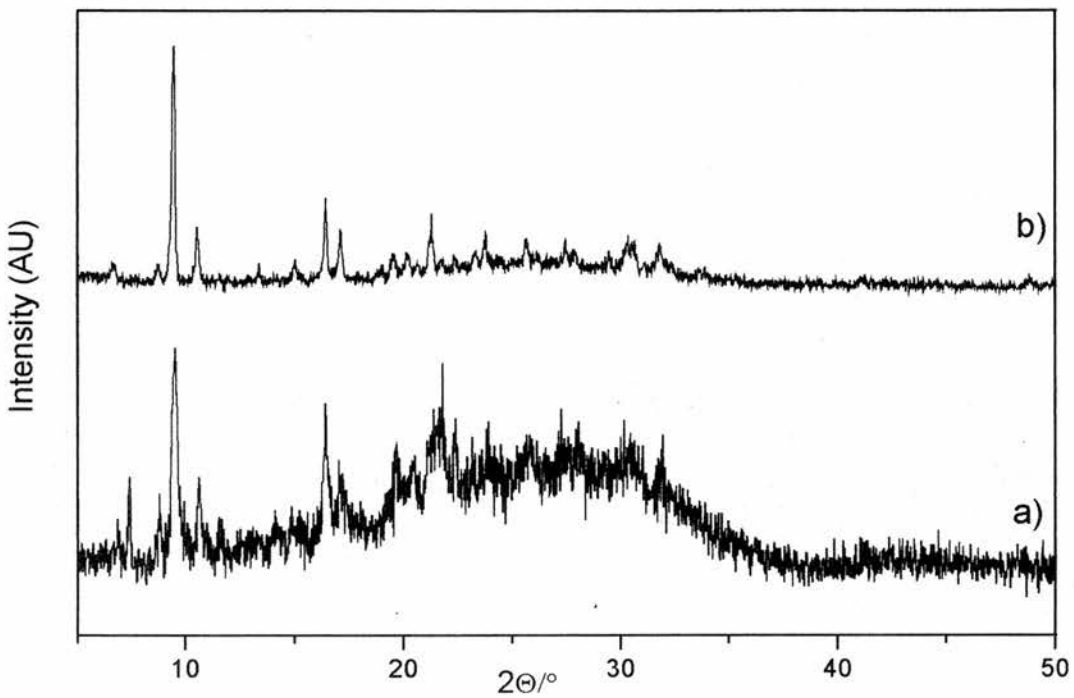

Figure 6.1. X-ray Diffraction patterns of a) MgAPO-STA-7 and b) SAPO-STA-7 after the catalysis test, showing the loss of crystallinity suffered by the MgAPO- when compared with the SAPO-STA-7.

T (°C)	Conv nC4	Total % of volatile products (by mass)	Molar distribution of products (%)					
			%C1	%C2	%C2=	%C3	%C3=	%C4+
350	0.05	100	15.6	0.0	22.5	33.9	11.5	16.5
375	3.1	100	3.3	1.4	6.3	68.2	6.9	13.8
400	4.6	100	3.8	1.6	8.1	66.5	7.5	12.5
425	6.5	100	5.1	2.2	10.4	63.5	8.3	10.4
450	8.8	100	7.4	3.3	12.6	58.8	9.2	8.7
475	9.1	100	12.2	5.4	13.7	51.4	10.0	7.3
500	10.5	100	21.0	8.9	13.0	41.2	10.0	5.9
525	16.6	100	24.8	10.6	15.1	33.2	11.3	5.1
550	30.8	88.2	30.5	12.5	16.5	23.9	12.0	4.6
575	40.0	78.2	42.8	16.0	14.1	12.5	11.1	3.6

Table 6.3. Conversion and product distribution data for n-butane cracking by SAPO-34.

T (°C)	Conv nC4	Total % of volatile products (by mass)	Molar distribution of products (%)					
			%C1	%C2	%C2=	%C3	%C3=	%C4+
350	0.2	100	0.0	0.0	16.0	56.6	13.5	13.9
375	0.4	100	0.0	0.0	12.7	55.0	14.7	17.6
400	0.5	100	8.2	0.0	11.1	41.5	14.9	24.3
425	0.9	100	11.9	3.4	11.3	37.5	14.4	21.4
450	1.6	100	14.3	4.7	12.7	36.8	14.3	17.3
475	2.5	100	16.9	6.3	14.0	34.8	14.3	13.7
500	3.6	100	20.3	7.8	15.6	30.0	15.4	10.9
525	7.4	100	22.0	8.9	17.2	27.7	15.7	8.5
550	10.9	100	25.1	10.3	18.4	23.4	16.2	6.7
575	21.2	100	30.3	12.3	18.9	17.8	15.8	4.9

Table 6.4. Conversion and product distribution data for n-butane cracking by SAPO-STA-7.

T (°C)	Conv nC4	Total % of volatile products (by mass)	Molar distribution of products (%)					
			%C1	%C2	%C2=	%C3	%C3=	%C4+
350	2.1	100	6.7	2.5	3.2	75.8	1.2	10.6
375	23.8	100	1.5	0.9	1.6	89.1	1.6	5.3
400	32.3	100	2.6	1.5	2.2	87.6	1.9	4.2
425	33.2	100	4.7	2.7	3.4	82.9	2.5	3.8
450	37.9	100	8.6	4.5	4.9	75.6	3.2	3.3
475	34.0	100	13.7	6.6	7.2	64.5	4.6	3.5
500	37.1	100	20.7	9.1	9.1	51.9	5.8	3.4
525	22.6	100	25.6	10.2	12.4	37.9	9.0	4.9
550	20.5	100	32.8	12.2	13.1	24.9	11.1	5.8
575	18.7	100	41.3	13.6	12.3	13.1	13.0	6.6

Table 6.5. Conversion and product distribution data for n-butane cracking by MgAPO-STA-7.

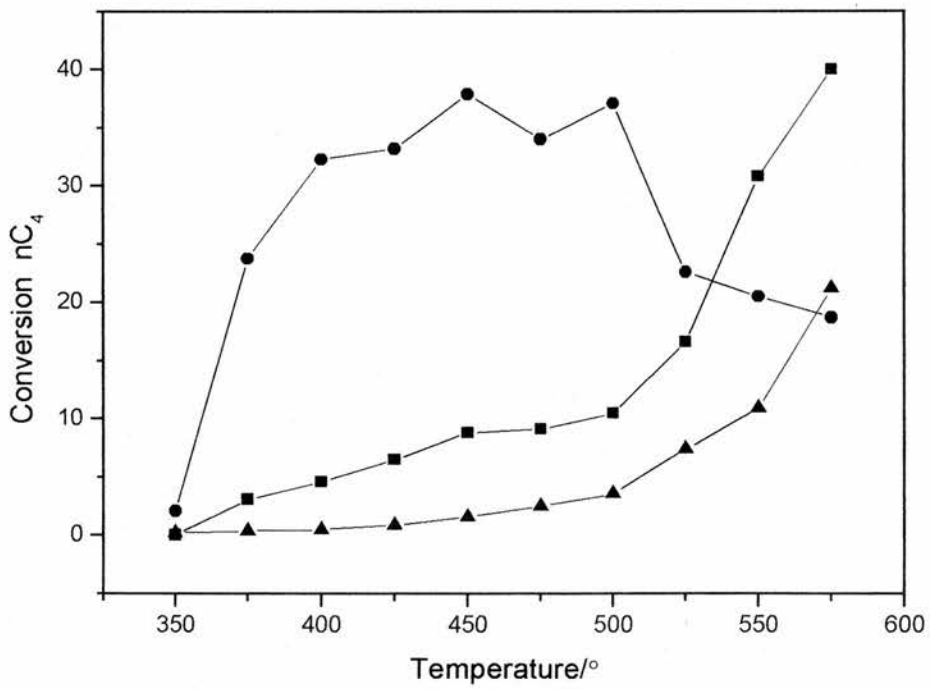

Figure 6.2. Plot of conversion of n-butane vs temperature for SAPO-34, SAPO-STA-7 , MgAPO-STA-7. Key: ■ SAPO-34, ▲ SAPO-STA-7 and ● MgAPO-STA-7.

6.3.2. Nickel-containing materials

The *in situ* calcined sample of Ni(deta)$_2$-AlPO-UT-6 shows few products of acid catalysts (< 1%) at temperatures below 475°C, as expected for being a neutral framework and therefore, without the presence of acid sites. At higher temperatures the catalyst become very active (> 90% conversion) in the conversion of n-butane to methane.

Ni-SAPO-34 and Ni-SAPO-STA-7 both contain acid sites due to the charge on their frameworks and hence they show a different behaviour at lower temperatures than UT-6. At lower temperatures, the complete range of hydrocarbons is observed indicating a contribution of acid catalysis on this range of temperatures. However there is in each case a sharp increase in conversion and a change in product distribution to pure methane at around 500°C. Ni-SAPO-34 shows higher activity to that of Ni-MgAPO-STA-7 the product distribution being richer in methane. Ni-MgAPO-STA-7 shows variable conversions with temperature which is attributed to the loss of crystallinity. Ultimately, the only product of reaction is methane.

This change in the product distribution of the nickel containing materials is attributed to the onset of the formation of nanoparticulate nickel since nickel metal is known to be a selective methanation catalyst[15] making and breaking C-H bonds. Nanoparticles of nickel are expected to be formed by the reduction of extra-framework Ni(II) species in the presence of hydrocarbons at high temperatures. The formation of nickel metal on the nickel containning samples was confirmed by TEM performed on the Ni-SAPO-34 sample after catalysis, which shows nanoparticles of nickel 5-20 nm in diameter (figure 6.4).

T (°C)	Conv nC4	Total % of volatile products (by mass)	Molar % of products					
			%C1	%C2	%C2=	%C3	%C3=	%C4+
350	0.1	100	22.1	4.3	16.4	10.7	2.1	44.4
375	0.3	100	46.7	6.7	27.3	4.9	3.1	11.4
400	0.4	100	15.2	3.5	49.5	10.4	8.8	12.6
425	0.8	100	30.4	6.4	34.7	4.9	12.5	11.2
450	0.3	100	37.6	6.3	10.3	10.1	13.0	22.7
475	66.1	56.3	99.6	0.0	0.0	0.2	0.0	0.2
500	67.2	51.9	94.5	4.7	0.0	0.7	0.1	0.0
525	37.5	67.1	90.7	6.3	0.9	1.2	0.8	0.0
550	58.1	48.8	93.0	4.9	0.6	1.0	0.4	0.0
575	75.9	35.5	99.3	0.0	0.1	0.4	0.2	0.0

Table 6.6. Conversion and product distribution data for n-butane cracking by Ni-AlPO-UT-6.

T (°C)	Conv nC4	Total % of volatile products (by mass)	Molar % of products					
			%C1	%C2	%C2=	%C3	%C3=	%C4+
350	36.5	100	40.8	40.8	0.0	17.1	0.4	1.0
375	13.9	100	42.1	29.5	1.6	20.9	2.3	3.5
400	13.7	100	44.4	25.6	2.2	20.3	3.4	4.1
425	15.3	100	49.8	23.1	2.6	16.6	3.8	4.1
450	16.6	100	59.3	20.9	2.1	11.6	2.7	3.4
475	37.4	80.9	78.5	14.2	0.8	4.1	0.7	1.6
500	69.7	60.0	92.2	6.4	0.2	0.6	0.1	0.5
525	92.0	50.6	99.8	0.0	0.0	0.0	0.0	0.2
550	96.5	49.2	100.0	0.0	0.0	0.0	0.0	0.0
575	97.4	45.1	100.0	0.0	0.0	0.0	0.0	0.0

Table 6.7. Conversion and product distribution data for n-butane cracking by Ni-SAPO-34

T (°C)	Conv nC4	Total % of volatile products (by mass)	Molar % of products					
			%C1	%C2	%C2=	%C3	%C3=	%C4+
350	27.1	100	33.2	32.6	0.0	32.3	0.4	1.5
375	22.3	100	34.8	29.6	0.8	32.2	0.7	1.9
400	18.4	100	43.7	29.6	1.1	22.5	1.1	2.0
425	11.0	100	49.7	28.1	1.6	14.7	2.2	3.8
450	6.80	100	53.7	25.5	1.9	7.8	3.6	7.4
475	2.23	100	51.7	16.9	2.4	4.0	6.5	18.5
500	2.28	100	55.3	16.5	2.1	2.4	5.6	18.0
525	28.1	100	83.5	13.7	0.5	1.0	0.3	1.1
550	73.1	100	99.8	0.0	0.0	0.0	0.0	0.2
575	87.0	100	99.9	0.0	0.0	0.0	0.0	0.1

Table 6.8. Conversion and product distribution data for n-butane cracking by Ni-MgAPO-STA-7

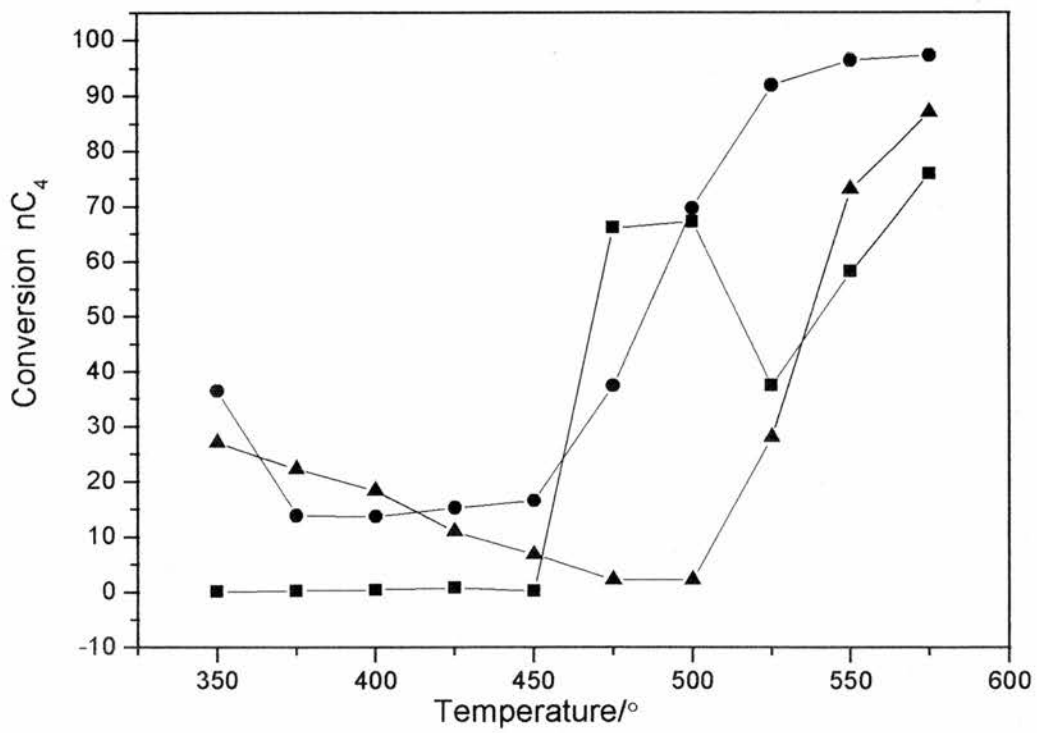

Figure 6.3. Plot of conversion of n-butane cracking vs temperature for Ni-UT-6, Ni-MgAPO-STA-7 and Ni-SAPO-34. Key: ■ Ni-UT-6, ▲ Ni-MgAPO-STA-7 and ● Ni-SAPO-34.

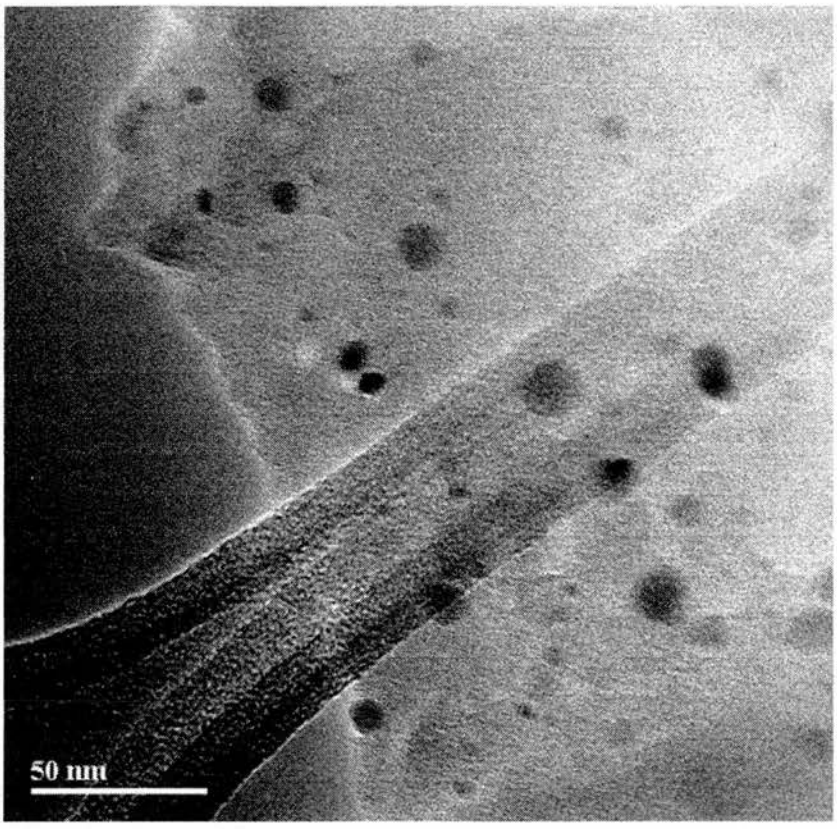

Figure 6.4. Transmission electron micrograph of the Ni-SAPO-34 sample after the n-butane cracking reaction, showing the formation of nickel particles.

6.4. CONCLUSIONS

The performance of the novel acids SAPO-STA-7 and MgAPO-STA-7 as catalysts has been tested by employing a probe reaction, the cracking of n-butane and their performance has been compared to that of SAPO-34, a known acid catalysts with a similar small pore cage-like struture.

SAPO-STA-7 and MgAPO-STA-7 have shown to be active for this reaction but with weaker acid sites than those of their polytype SAPO-34. SAPO-STA-7 shows less activity than SAPO-34 and MgAPO-STA-7 lose the unusual activity that its observed at low temperature as the temperature is increased, probably due to the collapse of the structure. Nevertheless, SAPO-STA-7 is an interesting material with a similar structure to that of SAPO-34 and SAPO-18 and by carefully changing

variables such as composition, some improvement in its acid performance could be gained.

The nickel containing materials have shown a characteristic pattern on activity for this reaction. At low temperatures, the product distribution is governed by the acid sites of the catalysts. As the temperature increases, the materials behave as supported metal catalysts due to the reduction of the nickel to nickel metal particles that sinter and leave the pores.

6.5. REFERENCES

1. J. Weitkamp, *Solid State Ionics*, 2001, **131**, 175

2. J. A. Rabo, M. W. Schoonover, *Applied Cat. A: General*, 2001, **222**, 261

3. P.A. Wright, *Encyclopedia of Materials: Science and Tecnology*, Elsevier Science Ltd., 2001, pp. 1-6.

4. K. Wilson, J. H. Clark, *Pure Appl. Chem.*, 2000, **72**, 1313.

5. M. Stöcker, *Micro. Mesoporous Materials*, 1999, **29**, 3

6. J.M. Thomas, R. Raja, G. Sankar, B.F.G. Johnson, D.G. Lewis, *Chem.Eur.J.*, 2001, **7**

7. G. Sankar, R. Raja, J.M. Thomas, *Cat.Letters*, 1998, **55**, 15

8. R. Raja, G. Sankar, J.M. Thomas, *J.Am.Chem.Soc.*, 1999, **121**, 11926

9. M. Dugal, G. Sankar, R. Raja, J.M. Thomas, *Angew.Chem.Int.Ed.*, 2000, **39**, 2310

10. J.M. Thomas, R. Raja, *Chemm.Commun.*, 2001, 657

11. J.M. Thomas, *Angew.Chem.Int.Ed.*,1999, **38**, 3588

12. W.E. Farneth, R.J. Gorte, *Chem.Rev.*, 1995, **95**, 615

13. P.A. Wright, C. Sayag, F. Rey, D.W. Lewis, J.D. Gale, S. Natarajan, J.M. Thomas, *J.Chem.Soc.Faraday T.*, 1995, **91(19)**, 3537

14. "Verified Syntheses of Zeolitic Materials", 2nd Edition, H. Robson, K.P. Lillerud, Amsterdam, 2001.

15. C.W. Hu, J. Yao, H.Q. Yang, Y. Chen, A.M. Tian, *J.Catal.*, 1997, **166(1)**, 1

7. GENERAL CONCLUSIONS

This work has shown that metal complexes of both azamacrocycles and linear amines can be incorporated in several structures of microporous materials. In the case of azamacrocycles, because of their better complexing properties compared to those of linear amines, metal cations such as Ni^{2+}, Cu^{2+} or even rhodium (at low loadings) can be incorporated on the STA-6 and STA-7 materials. Linear amine complexes of nickel are also incorporated within aluminophosphate microporous hosts, mainly those with CHA and AFI framework topologies. Incorporation of other metals such as copper has been found to be more difficult employing this type of complex.

The metal-complexes act as structure directing agents during the syntheses of the materials rather than being passively incorporated during crystallisation of the microporous hosts. This is shown by the formation of the crystallographically distorted variant of STA-6 for preparations that in the absence of nickel yielded STA-7 as CoAlPO and ZnAlPO with tetramethylcyclam, and in the preparation of chabazite and AlPO-5 with the $Ni(deta)_2^{+2}$ complex.

The use of additives together with a main template in the syntheses of microporous hosts is of interest, specially when two structure types crystallise under similar synthesis condition as STA-6 and STA-7. Tetraethylammonium ions for example, favour the crystallisation of STA-7 over STA-6 and their use permits the compositional range of the STA-7 materials that can be prepared to be broadened (with and without nickel).

EXAFS studies performed on the materials synthesised in this work show that upon calcination of nickel complex-containing solids, nickel remains as a charge compensating cation when incorporated within charged frameworks. However, when incorporated in a framework that is neutral after calcination, it forms nickel metal or nickel oxide clusters depending on the calcination conditions (heating under nitrogen or oxygen, respectively).

The catalytic performance of the nickel-containing materials synthesised in this work for the n-butane cracking reaction shows a different behaviour characterised for two different regions. At low temperatures, the nickel-containing materials behaved as acid catalysts catalysing the cracking of butane. However as the temperature increases, the nickel is probably reduced to nickel metal catalysing the formation of methane which becomes the main product at higher temperatures.

8. APPENDIX

Suplementary information is tabulated for all crystal structures, selected bond lengths and angles, anisotropic displacement parameters and fractional occupancies. The framework structures were solved by single crystal X-ray diffraction by Dr A. M. Z. Slawin. The data for the materials where a Rietveld refinement was performed is also included in this appendix.

8.1. NiTMC-CoSTA-7

Atom	x	y	z	U_{eq}	Occ.
Al(1)	0.16453(6)	0.04424(6)	0.15671(11)	0.0212(5)	0.84
Al(2)	-0.06542(7)	0.16586(6)	-0.08060(12)	0.0327(6)	0.83
Al(3)	-0.05063(6)	0.06639(7)	0.33547(12)	0.0315(6)	0.83
Co(1)	0.16453(6)	0.04424(6)	0.15671(11)	0.0212(5)	0.16
Co(2)	-0.06542(7)	0.16586(6)	-0.08060(12)	0.0327(6)	0.17
Co(3)	-0.05063(6)	0.06639(7)	0.33547(12)	0.0217(11)	0.17
P(1)	0.06421(7)	-0.05660(7)	0.33485(13)	0.0297(4)	1
P(3)	0.05057(7)	0.16669(7)	0.16026(14)	0.0337(4)	1
P(5)	-0.16652(7)	0.06778(7)	0.09574(13)	0.0290(4)	1
O(1)	0.0734(2)	-0.0812(2)	0.4871(3)	0.0546(13)	1
O(2)	0.0584(2)	-0.1232(2)	0.2423(3)	0.0486(12)	1
O(3)	0.1286(2)	-0.0112(2)	0.2933(4)	0.0529(13)	1
O(4)	-0.0049(2)	-0.0151(2)	0.3217(4)	0.0518(13)	1
O(5)	0.1553(2)	-0.0007(2)	-0.0114(4)	0.0535(13)	1
O(6)	0.2560(2)	0.0629(2)	0.1917(4)	0.0592(13)	1
O(7)	0.1217(2)	0.1267(2)	0.1555(4)	0.0531(13)	1
O(8)	0.0140(2)	0.1578(2)	0.0173(4)	0.0466(12)	1
O(9)	0.0048(2)	0.1362(2)	0.2781(3)	0.0445(12)	1
O(10)	-0.1376(2)	0.1335(2)	0.0173(4)	0.0521(13)	1
O(11)	-0.0806(2)	0.2554(2)	-0.1228(4)	0.0564(13)	1
O(12)	-0.1297(2)	0.0601(2)	0.2395(4)	0.0492(12)	1
O(20)	0.1210(12)	-0.2502(13)	0.4968(24)	0.114(8)	0.25

O(30)	0.2176(19)	0.2715(29)	1.0020(36)	0.134(17)	0.15
O(40)	0.2393(37)	0.2481(208)	1.2806(31)	0.106(12)	0.10
Ni(1)	0.2500	0.2500	0.6431(2)	0.0517(5)	1
N(1)	0.3249(4)	0.1754(4)	0.6432(8)	0.109(2)	1
N(51)	0.2500	-0.2500	0.6325(55)	0.124(18)	0.20
C(1)	0.3441(9)	0.1519(9)	0.7846(17)	0.153(6)	0.75
C(2)	0.3004(10)	0.1021(9)	0.5602(18)	0.185(7)	0.75
C(3)	0.2900(15)	0.1076(15)	0.6928(28)	0.184(11)	0.50
C(4)	0.2030(10)	0.1091(10)	0.5519(21)	0.124(7)	0.50
C(5)	0.2376(17)	0.0946(15)	0.6396(29)	0.193(11)	0.50
C(6)	0.3432(15)	0.1518(15)	0.4809(32)	0.196(11)	0.50
C(50)	0.2500	-0.2500	0.5000	0.176(24)	0.40
C(52)	0.1869(27)	-0.2487(29)	0.7019(52)	0.133(18)	0.20

Table 8.1. Atomic coordinates and thermal parameters for Ni-CoAlPO-STA-7 synthesised with TMC from single crystal X-ray data refined in space group P4/n, with lattice parameters a = 18.6842(12) Å, c =9.4080(8) Å.

Atom-Atom	**Distance, Å**
Al(1)-O(7)	1.736(4)
Al(1)-O(6)	1.775(4)
Al(1)-O(5)	1.799(4)
Al(1)-O(3)	1.782(4)
Al(2)-O(2)	1.722(3)
Al(2)-O(8)	1.753(4)
Al(2)-O(10)	1.741(4)
Al(2)-O(11)	1.743(4)
Al(3)-O(9)	1.751(4)
Al(3)-O(4)	1.751(4)
Al(3)-O(1)	1.745(3)
Al(3)-O(12)	1.735(4)
P(1)-O(4)	1.512(4)
P(1)-O(3)	1.523(4)

P(1)-O(2)	1.523(4)
P(1)-O(1)	1.514(4)
P(3)-O(8)	1.518(4)
P(3)-O(9)	1.512(4)
P(3)-O(6)	1.492(4)
P(3)-O(7)	1.525(4)
P(5)-O(12)	1.525(4)
P(5)-O(5)	1.498(4)
P(5)-O(10)	1.531(4)
P(5)-O(11)	1.500(4)

Table 8.2. Selected bond distances for Ni-CoAlPO-STA-7 synthesised with TMC.

Atom- Atom- Atom-	**Angle, °**
O(7)-Al(1)-O(6)	105.7(2)
O(7)-Al(1)-O(3)	110.3(2)
O(6)-Al(1)-O(3)	110.0(2)
O(7)-Al(1)-O(5)	111.4(2)
O(6)-Al(1)-O(5)	110.3(2)
O(3)-Al(1)-O(5)	109.1(2)
O(4)-P(1)-O(2)	108.1(2)
O(4)-P(1)-O(3)	111.7(2)
O(1)-P(1)-O(2)	107.5(2)
O(4)-P(1)-O(1)	109.3(2)
O(3)-P(1)-O(1)	108.8(2)
O(3)-P(1)-O(2)	111.4(2)
O(2)-Al(2)-O(11)	104.8(2)
O(10)-Al(2)-O(11)	109.1(2)
O(8)-Al(2)-O(2)	111.1(2)
O(10)-Al(2)-O(8)	110.4(2)
O(8)-Al(2)-O(11)	109.9(2)
O(2)-Al(2)-O(10)	111.4(2)

O(6)-P(3)-O(9)	107.9(2)
O(8)-P(3)-O(6)	110.6(2)
O(9)-P(3)-O(8)	110.8(2)
O(6)-P(3)-O(7)	110.2(2)
O(9)-P(3)-O(7)	109.2(2)
O(8)-P(3)-O(7)	108.2(2)
O(1)-Al(3)-O(12)	107.5(2)
O(1)-Al(3)-O(4)	109.1(2)
O(12)-Al(3)-O(9)	113.2(2)
O(9)-Al(3)-O(12)	108.5(2)
O(1)-Al(3)-O(9)	108.8(2)
O(9)-Al(3)-O(4)	109.7(2)
O(10)-P(5)-O(12)	110.1(2)
O(5)-P(5)-O(12)	109.1(2)
O(5)-P(5)-O(10)	111.5(2)
O(5)-P(5)-O(11)	111.1(2)
O(10)-P(5)-O(11)	107.3(2)
O(12)-P(5)-O(11)	107.7(2)

Table 8.3. Selected bond angles for Ni-CoAlPO-STA-7 synthesised with TMC.

8.2. Ni-CoAlPO-TMC-TEAOH

Atom	x	y	z	U_{eq}	Occ.
Al(1)	0.9351(1)	0.3334(1)	0.4190(1)	0.021(1)	0.75
Al(3)	0.8358(1)	0.5453(1)	0.3432(1)	0.016(1)	0.75
Al(5)	1.0516(1)	0.5651(1)	0.1639(1)	0.021(1)	0.75
Co(1)	0.9351(1)	0.3334(1)	0.4190(1)	0.021(1)	0.25
Co(2)	0.8358(1)	0.5453(1)	0.3432(1)	0.016(1)	0.25
Co(3)	1.0516(1)	0.5651(1)	0.1639(1)	0.021(1)	0.25
P(2)	0.8336(1)	0.4327(1)	0.5958(1)	0.017(1)	1
P(4)	0.9495(1)	0.6671(1)	0.3396(1)	0.019(1)	1
P(6)	0.9373(1)	0.4426(1)	0.1648(1)	0.018(1)	1

O(1)	0.8649(2)	0.3687(2)	0. 5160(4)	0.034(1)	1
O(2)	0.9427(2)	0.3759(2)	0.2559(4)	0.034(1)	1
O(3)	0.9173(3)	0.2451(2)	0.3780(5)	0.039(1)	1
O(4)	0.8434(2)	0.5015(2)	0.5143(4)	0.035(1)	1
O(5)	0.8696(2)	0.4392(2)	0.7409(4)	0.034(1)	1
O(6)	0.8753(2)	0.4894(2)	0.2098(5)	0.036(1)	1
O(7)	0.8772(2)	0.6295(3)	0.3467(5)	0.044(1)	1
O(8)	0.7452(2)	0.5612(3)	0.3025(5)	0.048(1)	1
O(9)	0.9956(2)	0.6330(2)	0.2240(5)	0.035(1)	1
O(10)	0.9852(2)	0.6595(2)	0.4848(4)	0.035(1)	1
O(11)	1.0085(2)	0.4822(2)	0.1754(4)	0.032(1)	1
O(12)	0.9253(2)	0.4181(2)	0.0123(4)	0.037(1)	1
Ni(1)	1.2500(1)	0.2500(0)	0.1419(2)	0.034(1)	1
N(1A)	1.1759(4)	0.1756(4)	0.1393(8)	0.056(2)	0.50
C(1A)	1.1115(14)	0.1911(14)	0.0460(30)	0.097(7)	0.50
C(2A)	1.0684(15)	0.2527(15)	0.0620(30)	0.101(8)	0.50
C(3A)	1.1110(12)	0.3090(12)	0.0530(30)	0.080(6)	0.50
C(4A)	1.1525(11)	0.1490(10)	0.2820(20)	0.070(5)	0.50
N(1B)	1.1759(4)	0.1756(4)	0.1393(8)	0.056(2)	0.50
C(1B)	1.1040(30)	0.2160(30)	0.1560(50)	0.174(17)	0.50
C(2B)	1.1040(20)	0.2870(20)	0.1690(40)	0.149(13)	0.50
C(4B)	1.1576(18)	0.1625(18)	-0.0100(40)	0.123(10)	0.50
N(21)	0.7500(1)	0.2500(1)	1.0000(1)	0.033(2)	1
C(21A)	0.8013(9)	0.2066(10)	0.9054(19)	0.064(5)	0.50
C(21B)	8.028(10)	0.2920(11)	0.9100(20)	0.071(5)	0.50
C(22)	8.430(6)	0.2480(5)	0.8019(11)	0.077(3)	1
O(31)	0.7500	0.2500	-0.2700(150)	0.110(40)	0.10
O(32)	1.2500	0.2500	-0.2030(30)	0.107(9)	0.60
O(33)	1.2500	0.2500	-0.4840(140)	0.150(40)	0.20

Table 8.4. Atomic coordinates and thermal parameters for Ni-CoAlPO-STA-7 synthesised with TMC and TEAOH from single crystal X-ray data refined in space group P4/n, with lattice parameters a = 18.7576(10) Å, c = 9.4139(8) Å.

Atom-Atom	Distance, Å
(Co,Al)(1)-O(2)	1.735(4)
(Co,Al)(1)-O(3)	1.735(4)
(Co,Al)(1)-O(1)	1.733(4)
(Co,Al)(1)-O(10)	1.753(4)
(Co,Al)(3)-O(7)	1.762(5)
(Co,Al)(3)-O(8)	1.767(4)
(Co,Al)(3)-O(6)	1.796(4)
(Co,Al)(3)-O(4)	1.813(4)
(Co,Al)(5)-O(5)	1.731(4)
(Co,Al)(5)-O(12)	1.743(4)
(Co,Al)(5)-O(11)	1.755(4)
(Co,Al)(5)-O(9)	1.746(4)
P(2)-O(4)	1.512(4)
P(2)-O(3)	1.524(4)
P(2)-O(5)	1.528(4)
P(2)-O(1)	1.533(4)
P(4)-O(8)	1.520(4)
P(4)-O(9)	1.530(4)
P(4)-O(7)	1.528(5)
P(4)-O(10)	1.529(4)
P(6)-O(12)	1.524(4)
P(6)-O(2)	1.520(4)
P(6)-O(6)	1.517(4)
P(6)-O(11)	1.532(4)

Table 8.5. Selected bond distances for Ni-CoAlPO-STA-7 synthesised with TMC and TEAOH.

Atom- Atom- Atom-	Angle, °
O(2)-Al(1)-O(3)	104.9(2)
O(2)-Al(1)-O(1)	110.7(2)

O(3)-Al(1)-O(1)	109.6(2)
O(2)-Al(1)-O(10)	110.7(2)
O(3)-Al(1)-O(10)	110.5(2)
O(1)-Al(1)-O(10)	110.3(2)
O(2)-Co(1)-O(3)	104.9(2)
O(2)-Co(1)-O(1)	110.7(2)
O(3)-Co(1)-O(1)	109.6(2)
O(2)-Co(1)-O(10)	110.7(2)
O(3)-Co(1)-O(10)	110.5(2)
O(1)-Co(1)-O(10)	110.3(2)
O(4)-P(2)-O(5)	109.4(2)
O(4)-P(2)-O(3)	111.2(3)
O(3)-P(2)-O(5)	107.4(2)
O(4)-P(2)-O(1)	111.8(2)
O(3)-P(2)-O(1)	107.6(3)
O(5)-P(2)-O(1)	109.3(2)
O(7)-Al(3)-O(8)	106.0(2)
O(7)-Al(3)-O(6)	110.8(2)
O(8)-Al(3)-O(6)	110.1(2)
O(7)-Al(3)-O(4)	110.8(2)
O(8)-Al(3)-O(4)	110.2(2)
O(6)-Al(3)-O(4)	108.9(2)
O(7)-Co(3)-O(8)	106.0(2)
O(7)-Co(3)-O(6)	110.8(2)
O(8)-Co(3)-O(6)	110.1(2)
O(7)-Co(3)-O(4)	110.8(2)
O(8)-Co(3)-O(4)	110.8(2)
O(6)-Co(3)-O(4)	108.9(2)
O(8)-P(4)-O(9)	108.3(3)
O(8)-P(4)-O(10)	110.6(3)
O(9)-P(4)-O(10)	110.5(2)
O(8)-P(4)-O(7)	109.7(3)
O(9)-P(4)-O(7)	109.9(2)

O(10)-P(4)-O(7)	107.9(3)
O(5)-Al(5)-O(12)	106.8(2)
O(5)-Al(5)-O(9)	112.3(2)
O(12)-Al(5)-O(9)	109.0(2)
O(5)-Al(5)-O(11)	108.7(2)
O(12)-Al(5)-O(11)	109.5(2)
O(9)-Al(5)-O(11)	110.4(2)
O(5)-Co(5)-O(12)	106.8(2)
O(5)-Co(5)-O(9)	112.3(2)
O(12)-Co(5)-O(9)	109.0(2)
O(5)-Co(5)-O(11)	108.7(2)
O(12)-Co(5)-O(11)	109.5(2)
O(9)-Co(5)-O(11)	110.4(2)
O(6)-P(6)-O(2)	111.7(2)
O(6)-P(6)-O(12)	108.9(3)
O(2)-P(6)-O(12)	107.0(2)
O(6)-P(6)-O(11)	111.7(2)
O(2)-P(6)-O(11)	107.8(2)
O(12)-P(6)-O(11)	109.7(2)

Table 8.6. Selected bond angles for Ni-CoAlPO-STA-7 synthesised with TMC and TEAOH.

8.3. Ni-SAPO-TMC-TEAOH

Atom	x	y	z	U_{eq}	Occ.
Al(1)	0.93528(10)	0.33443(10)	0.41636(18)	0.0149(6)	1
Al(3)	0.83509(10)	0.54510(10)	0.34137(19)	0.0135(6)	1
Al(5)	1.05226(10)	0.56488(10)	0.16402(18)	0.0138(6)	1
Si(2)	0.83356(9)	0.43367(9)	0.59139(17)	0.0140(5)	0.25
Si(4)	0.95079(9)	0.66627(9)	0.34009(17)	0.0146(5)	0.25
Si(6)	0.93502(9)	0.44360(9)	0.16254(16)	0.0138(5)	0.25
P(2)	0.83356(9)	0.43367(9)	0.59139(17)	0.0140(5)	0.75
P(4)	0.95079(9)	0.66627(9)	0.34009(17)	0.0146(5)	0.75
P(6)	0.93502(9)	0.44360(9)	0.16254(16)	0.0138(5)	0.75
O(1)	0.8644(3)	0.3688(3)	0.5112(5)	0.0277(13)	1
O(2)	0.9411(2)	0.3758(2)	0.2549(5)	0.0230(11)	1
O(3)	0.9179(3)	0.2459(2)	0.3803(5)	0.0274(12)	1
O(4)	0.8428(3)	0.5021(3)	0.5042(5)	0.0274(13)	1
O(5)	0.8713(2)	0.4430(2)	0.7354(5)	0.0223(12)	1
O(6)	0.8711(2)	0.4911(2)	0.2118(5)	0.0259(12)	1
O(7)	0.8775(2)	0.6274(2)	0.3434(5)	0.0242(12)	1
O(8)	0.7459(2)	0.5625(2)	0.3061(5)	0.0246(12)	1
O(9)	0.9990(2)	0.6345(2)	0.2226(5)	0.0266(12)	1
O(10)	0.9864(2)	0.6577(3)	0.4875(5)	0.0271(13)	1
O(11)	1.0064(2)	0.4848(3)	0.1712(5)	0.0237(12)	1
O(12)	0.9211(2)	0.4194(2)	0.0090(4)	0.0227(12)	1
Ni(1)	1.2500	0.2500	0.1429(3)	0.0369(8)	1
N(1A)	1.1746(6)	0.1761(6)	0.1389(11)	0.077(3)	0.50
C(1A)	1.1155(15)	0.1877(15)	0.047(3)	0.100(8)	0.50
C(2A)	1.0684(16)	0.2492(14)	0.088(5)	0.151(15)	0.50
C(3A)	1.1121(14)	0.3133(13)	0.048(3)	0.082(7)	0.50
C(4A)	1.1523(15)	0.1502(15)	0.280(3)	0.087(8)	0.50
N(1B)	1.1746(6)	0.1761(6)	0.1389(11)	0.077(3)	0.50
C(1B)	1.107(4)	0.199(2)	0.195(7)	0.22(2)	0.50
C(2B)	1.107(3)	0.279(2)	0.175(5)	0.173(17)	0.50

C(4B)	1.167(3)	0.159(3)	-0.024(6)	0.184(19)	0.50
N(21)	0.7500	0.2500	1.0000	0.071(5)	1
C(21A)	0.8015(14)	0.2083(15)	0.911(3)	0.097(9)	0.50
C(21B)	0.8022(12)	0.2928(13)	0.912(3)	0.078(7)	0.50
C(22)	0.8428(8)	0.2491(7)	0.7993(16)	0.096(4)	1
O(31)	0.7500	0.2500	0.441(3)	0.092(9)	0.40
O(32)	1.2500	0.2500	-0.207(6)	0.042(14)	0.20

Table 8.7. Atomic coordinates and thermal parameters for Ni-SAPO-STA-7 synthesised with TMC and TEAOH from single crystal X-ray data refined in space group P4/n, with lattice parameters a = 18.726(2) Å, c = 9.4487(11) Å.

Atom-Atom	**Distance, Å**
Al(1)-O(2)	1.714(5)
Al(1)-O(3)	1.723(5)
Al(1)-O(1)	1.727(5)
Al(1)-O(10)	1.732(5)
Al(3)-O(7)	1.734(5)
Al(3)-O(8)	1.734(5)
Al(3)-O(6)	1.725(5)
Al(3)-O(4)	1.742(5)
Al(5)-O(5)	1.725(5)
Al(5)-O(12)	1.734(5)
Al(5)-O(11)	1.729(5)
Al(5)-O(9)	1.732(5)
Si(2)-O(4)	1.534(5)
Si(2)-O(5)	1.543(5)
Si(2)-O(3)	1.541(5)
Si(2)-O(1)	1.543(5)
Si(4)-O(8)	1.544(5)
Si(4)-O(9)	1.550(5)
Si(4)-O(10)	1.552(5)
Si(4)-O(7)	1.554(5)

Si(6)-O(11)	1.546(5)
Si(6)-O(12)	1.542(5)
Si(6)-O(6)	1.562(5)
Si(6)-O(2)	1.541(5)
P(2)-O(4)	1.534(5)
P(2)-O(3)	1.541(5)
P(2)-O(5)	1.543(5)
P(2)-O(1)	1.543(5)
P(4)-O(8)	1.544(5)
P(4)-O(9)	1.550(5)
P(4)-O(7)	1.554(5)
P(4)-O(10)	1.552(5)
P(6)-O(12)	1.542(5)
P(6)-O(2)	1.545(5)
P(6)-O(6)	1.562(5)
P(6)-O(11)	1.546(5)

Table 8.8. Selected bond distances for Ni-SAPO-STA-7 synthesised with TMC and TEAOH.

Atom- Atom- Atom-	**Angle, °**
O(2)-Al(1)-O(3)	105.7(2)
O(2)-Al(1)-O(1)	110.0(2)
O(3)-Al(1)-O(1)	108.4(3)
O(2)-Al(1)-O(10)	112.0(2)
O(3)-Al(1)-O(10)	110.2(2)
O(1)-Al(1)-O(10)	110.3(2)
O(4)-Si(2)-O(1)	110.6(3)
O(4)-Si(2)-O(5)	109.1(3)
O(1)-Si(2)-O(5)	110.5(3)
O(4)-Si(2)-O(3)	111.3(3)
O(1)-Si(2)-O(3)	107.2(3)

O(5)-Si(2)-O(3)	108.1(3)
O(4)-P(2)-O(5)	109.1(3)
O(4)-P(2)-O(3)	111.3(3)
O(3)-P(2)-O(5)	108.1(3)
O(4)-P(2)-O(1)	110.6(3)
O(3)-P(2)-O(1)	107.2(3)
O(5)-P(2)-O(1)	110.5(3)
O(7)-Al(3)-O(8)	106.0(2)
O(7)-Al(3)-O(6)	110.5(2)
O(8)-Al(3)-O(6)	110.5(2)
O(7)-Al(3)-O(4)	111.3(2)
O(8)-Al(3)-O(4)	109.6(2)
O(6)-Al(3)-O(4)	108.9(2)
O(8)-Si(4)-O(9)	108.4(3)
O(8)-Si(4)-O(7)	108.3(3)
O(9)-Si(4)-O(7)	110.4(3)
O(8)-Si(4)-O(10)	110.8(3)
O(9)-Si(4)-O(10)	110.7(3)
O(7)-Si(4)-O(10)	108.2(3)
O(8)-P(4)-O(9)	110.8(3)
O(8)-P(4)-O(10)	110.8(3)
O(9)-P(4)-O(10)	110.7(3)
O(8)-P(4)-O(7)	108.3(3)
O(9)-P(4)-O(7)	110.4(3)
O(10)-P(4)-O(7)	108.2(3)
O(5)-Al(5)-O(12)	107.2(2)
O(5)-Al(5)-O(9)	111.5(2)
O(12)-Al(5)-O(9)	109.8(2)
O(5)-Al(5)-O(11)	108.5(2)
O(12)-Al(5)-O(11)	109.1(2)
O(9)-Al(5)-O(11)	110.7(3)
O(12)-Si(6)-O(11)	110.0(3)
O(12)-Si(6)-O(2)	107.6(3)

O(11)-Si(6)-O(2)	108.5(3)
O(12)-Si(6)-O(6)	108.6(3)
O(11)-Si(6)-O(6)	111.3(3)
O(2)-Si(6)-O(6)	110.9(3)
O(6)-P(6)-O(2)	110.9(3)
O(6)-P(6)-O(12)	108.6(3)
O(2)-P(6)-O(12)	107.6(3)
O(6)-P(6)-O(11)	111.3(3)
O(2)-P(6)-O(11)	108.5(3)
O(12)-P(6)-O(11)	110.0(3)

Table8.9. Selected bond angles for Ni-SAPO-STA-7 synthesised with TMC and TEAOH.

8.4. Rh-TMC-ZnAlPO-STA-7

Atom	x	y	z	U_{eq}	Occ.
Al(1)	0.0657(2)	-0.0508(2)	0.3343(4)	0.080(7)	0.80
Al(2)	0.04498(13)	0.16435(12)	0.1573(3)	0.052(13)	0.80
Al(3)	-0.1656(2)	0.0648(2)	0.0825(3)	0.013(2)	0.80
Zn(1)	0.0657(2)	-0.0508(2)	0.3343(4)	0.000(3)	0.20
Zn(2)	0.04498(13)	0.16435(12)	0.1573(3)	0.000(24)	0.20
Zn(3)	-0.1656(2)	0.0648(2)	0.0825(3)	0.085(11)	0.20
P(1)	0.1661(2)	0.0486(2)	0.1589(4)	0.0290(10)	1
P(2)	-0.0672(2)	0.1658(2)	-0.0931(4)	0.0331(11)	1
P(3)	-0.0552(2)	0.0651(2)	0.3359(4)	0.0314(10)	1
O(1)	0.0784(6)	-0.0741(6)	0.5067(11)	0.059(3)	1
O(2)	0.0610(6)	-0.1273(5)	0.2375(11)	0.056(3)	1
O(3)	0.1367(6)	0.0006(6)	0.2760(12)	0.061(3)	1
O(4)	-0.0131(6)	-0.0055(6)	0.3189(13)	0.066(3)	1
O(5)	0.1564(6)	0.0120(6)	0.0142(12)	0.068(3)	1
O(6)	0.2468(6)	0.0629(6)	0.1907(13)	0.071(4)	1
O(7)	0.1275(5)	0.1229(5)	0.1582(14)	0.066(3)	1

O(8)	0.0018(6)	0.1535(6)	-0.0064(13)	0.069(3)	1
O(9)	-0.0088(6)	0.1300(6)	0.2919(13)	0.071(4)	1
O(10)	-0.1318(5)	0.1382(6)	-0.0118(12)	0.064(3)	1
O(11)	-0.0813(6)	0.2466(5)	-0.1239(11)	0.060(3)	1
O(12)	-0.1246(6)	0.0598(6)	0.2437(11)	0.060(3)	1
Rh(1)	0.2500	0.2500	0.6296(6)	0.049(2)	0.50
N(1)	0.3273(13)	0.1722(13)	0.6403(27)	0.048(6)	0.50
C(2)	0.3849(34)	0.1995(34)	0.5587(69)	0.139(21)	0.50
C(3)	0.3916(40)	0.2912(40)	0.5761(79)	0.177(27)	0.50
C(4)	0.3481(32)	0.1550(32)	0.7817(66)	0.137(20)	0.50
C(5)	0.3334(89)	0.1625(84)	0.4898(170)	0.174(52)	0.25
O(20)	0.2500	0.2500	0.1241(104)	0.191(37)	0.50
O(30)	-0.2500	0.2500	-0.1097(102)	0.126(32)	0.25

Table 8.10. Atomic coordinates and thermal parameters for Rh-ZnAlPO-STA-7 synthesised with TMC from single crystal X-ray data refined in space group P4/n, with lattice parameters a = 18.7461(4) Å, c = 9.4215(4) Å.

Atom-Atom	**Distance, Å**
Zn(1), Al(1)-O(2)	1.701(10)
Zn(1), Al(1)-O(4)	1.709(11)
Zn(1), Al(1)-O(1)	1.699(10)
Zn(1), Al(1)-O(3)	1.732(11)
Zn(2), Al(2)-O(6)	1.727(11)
Zn(2), Al(2)-O(7)	1.732(10)
Zn(2), Al(2)-O(8)	1.754(13)
Zn(2), Al(2)-O(9)	1.743(12)
Zn(3), Al(3)-O(5)	1.712(12)
Zn(3), Al(3)-O(10)	1.756(11)
Zn(3), Al(3)-O(11)	1.720(10)
Zn(3), Al(3)-O(12)	1.705(10)
P(1)-O(3)	1.526(12)
P(1)-O(5)	1.537(12)

P(1)-O(6)	1.565(11
P(1)-O(7)	1.569(10)
P(2)-O(2)	1.545(11)
P(2)-O(8)	1.547(12
P(2)-O(10)	1.524(11)
P(2)-O(11)	1.564(10)
P(3)-O(1)	1.554(11)
P(3)-O(4)	1.549(11)
P(3)-O(9)	1.554(12)
P(3)-O(12)	1.568(10)

Table8.11. Selected bond distances for Rh-ZnAlPO-STA-7 synthesised with TMC.

Atom- Atom- Atom-	**Angle, °**
O(2)-Al(1)-O(4)	109.2(6)
O(2)-Al(1)-O(1)	107.6(6)
O(4)-Al(1)-O(1)	109.2(6)
O(2)-Al(1)-O(3)	109.8(5)
O(4)-Al(1)-O(3)	111.1(6
O(1)-Al(1)-O(3)	109.8(6)
O(5)-P(1)-O(3)	109.6(6)
O(5)-P(1)-O(6)	111.1(6)
O(3)-P(1)-O(6)	108.2(6)
O(5)-P(1)-O(7)	109.7(7)
O(3)-P(1)-O(7)	111.1(6)
O(6)-P(1)-O(7)	107.2(6)
O(6)-Al(2)-O(7)	105.0(5)
O(6)-Al(2)-O(9)	109.6(6)
O(7)-Al(2)-O(9)	110.3(6)
O(6)-Al(2)-O(8)	111.2(5)
O(7)-Al(2)-O(8)	111.4(6)

O(9)-Al(2)-O(8)	109.3(6)
O(10)-P(2)-O(8)	110.4(7)
O(10)-P(2)-O(2)	110.1(6)
O(8)-P(2)-O(2)	109.4(6)
O(10)-P(2)-O(11)	106.8(6)
O(8)-P(2)-O(11)	112.6(6)
O(2)-P(2)-O(11)	107.6(6)
O(12)-Al(3)-O(11)	103.8(5)
O(12)-Al(3)-O(5)	112.5(6)
O(11)-Al(3)-O(5)	111.6(6)
O(12)-Al(3)-O(10)	109.3(5)
O(11)-Al(3)-O(10)	108.6(5)
O(5)-Al(3)-O(10)	110.7(6)
O(1)-P(3)-O(4)	109.5(6)
O(1)-P(3)-O(9)	109.0(7)
O(4)-P(3)-O(9)	110.8(6)
O(1)-P(3)-O(12)	107.7(6)
O(4)-P(3)-O(12)	108.2(6)
O(9)-P(3)-O(12)	111.5(6)

Table8.12. Selected bond angles for Rh-ZnAlPO-STA-7 synthesised with TMC.

8.5 Ni(deta)$_2$(F)-AlPO-5

Atom	x	y	z	U_{eq}	Occ.
Al(2)	0.1009(4)	0.05937(19)	1.1580(4)	0.0342(13)	1
Al(4)	0.2156(5)	0.1777(2)	0.6693(7)	0.060(2)	1
Al(6)	0.6066(4)	0.2277(3)	0.6944(5)	0.0483(16)	1
P(1)	0.2110(4)	0.15956(19)	1.3053(5)	0.0484(14)	1
P(3)	0.1064(3)	0.06602(15)	0.7893(4)	0.0315(11)	1
P(5)	0.3998(4)	0.2241(2)	0.8248(5)	0.0534(15)	1
F(11)	0.2500	0.2500	0.5805(12)	0.063(4)	1
O(1)	0.1899(9)	0.1032(5)	1.2234(16)	0.082(5)	1
O(2)	0.2050(7)	0.1513(3)	1.4824(15)	0.067(3)	1
O(3)	0.1401(9)	0.2049(5)	1.2493(19)	0.070(4)	1
O(4)	0.3136(12)	0.1761(5)	1.2665(19)	0.093(5)	1
O(5)	0.0962(9)	0.0580(5)	0.9618(13)	0.069(3)	1
O(6)	-0.0105(11)	0.0829(4)	1.2325(19)	0.094(5)	1
O(7)	0.1842(8)	0.1087(5)	0.7539(17)	0.065(3)	1
O(8)	0.1350(8)	0.0073(6)	0.725(2)	0.105(6)	1
O(9)	0.3305(9)	0.1788(4)	0.7678(13)	0.052(4)	1
O(10)	0.1216(8)	0.2164(5)	0.7642(18)	0.074(4)	1
O(12)	0.4977(10)	0.2066(4)	0.776(2)	0.089(5)	1
O(13)	0.3959(9)	0.2239(6)	0.9958(18)	0.114(5)	1
Ni(1)*	0.5000	0.0000	0.7557(7)	0.0522(17)	0.5
N(1)*	0.513(4)	-0.0737(17)	0.960(6)	0.141(15)	0.5
N(4)*	0.568(3)	0.0587(13)	1.047(4)	0.217(14)	1
C(2)*	0.593(3)	-0.0495(14)	1.049(4)	0.179(12)	1
C(3)*	0.639(2)	0.0119(17)	0.986(7)	0.211(13)	1
C(1)**	1.09740	0.54760	-0.01010	-	1
C(2)**	1.12560	0.48510	-0.01040	-	1
C(3)**	0.88530	0.52570	0.50900	-	1
C(4)**	0.90810	0.46250	0.50910	-	1
C(5)**	1.11460	0.53260	0.51110	-	1
C(6)**	0.91650	0.53930	-0.03970	-	1

C(7)**	1.08840	0.47020	0.53010	-	1
C(8)**	0.89360	0.47620	-0.02780	-	1
N(1)**	1.11200	0.54580	0.34220	-	1
N(2)**	1.00090	0.55420	0.06090	-	1
N(3)**	1.00290	0.45460	0.43280	-	1
N(4)**	0.89350	0.46020	0.13990	-	1
N(5)**	0.90670	0.55170	0.35510	-	1
N(6)**	1.09480	0.45520	0.13440	-	1

Table 8.13. Atomic coordinates and thermal parameters for as-prepared Ni(deta)$_2$(F)-AlPO-5 from single crystal X-ray data refined in space group Ccc2, with lattice parameters a =13.8603(5) Å, b =23.1285(5) Å and c = 8.5420(4) Å.(*) Disordered scattering modelled as N and C atoms. (**) Coordinates of the computer simulated energy minimised position of the template.

Atom-Atom	**Distance, Å**
Al(2)-O(5)	1.677(12)
Al(2)-O(8)	1.712(13
Al(2)-O(6)	1.757(13)
Al(2)-O(4)	1.716(13)
Al(4)-O(7)	1.806(12)
Al(4)-O(2)	1.716(13)
Al(4)-O(10)	1.777(14)
Al(4)-O(9)	1.801(13)
Al(4)-F(11)	1.896(6)
Al(6)-O(12)	1.734(13)
Al(6)-O(13)	1.699(16)
Al(6)-O(3)	1.693(13)
Al(6)-O(4)	1.739(16)
P(1)-O(4)	1.509(16)
P(1)-O(3)	1.515(11)
P(1)-O(2)	1.527(14)
P(1)-O(1)	1.508(11)

P(3)-O(6)	1.467(14)
P(3)-O(7)	1.493(11)
P(3)-O(8)	1.517(13
P(3)-O(5)	1.492(12)
P(5)-O(9)	1.502(11)
P(5)-O(12)	1.474(13)
P(5)-O(10)	1.501(14)
P(5)-O(13)	1.462(16

Table8.14. Selected bond distances for as-prepared $Ni(deta)_2(F)$-AlPO-5.

Atom- Atom- Atom-	**Angle, °**
O(1)-P(1)-O(4)	107.5(8)
O(1)-P(1)-O(3)	109.0(8)
O(4)-P(1)-O(3)	111.5(8)
O(1)-P(1)-O(2)	110.0(7)
O(4)-P(1)-O(2)	107.5(8)
O(3)-P(1)-O(2)	111.3(8)
O(5)-Al(2)-O(1)	111.6(7)
O(5)-Al(2)-O(8)	109.3(8)
O(1)-Al(2)-O(8)	103.1(8)
O(5)-Al(2)-O(6)	109.5(7)
O(1)-Al(2)-O(6)	109.6(7)
O(8)-Al(2)-O(6)	113.6(6)
O(6)-P(3)-O(5)	105.9(9)
O(6)-P(3)-O(7)	114.3(6)
O(5)-P(3)-O(7)	110.5(7)
O(6)-P(3)-O(8)	110.9(8)
O(5)-P(3)-O(8)	105.6(9)
O(7)-P(3)-O(8)	109.3(7)
O(2)-Al(4)-O(10)	122.7(7)
O(2)-Al(4)-O(9)	121.0(7)

O(10)-Al(4)-O(9)	115.4(7)
O(2)-Al(4)-O(7)	92.1(6)
O(10)-Al(4)-O(7)	94.9(7)
O(9)-Al(4)-O(7)	92.2(6)
O(2)-Al(4)-F(11)	87.9(5)
O(10)-Al(4)-F(11)	85.6(5)
O(9)-Al(4)-F(11)	87.3(4)
O(7)-Al(4)-F(11)	179.4(6)
O(3)-Al(6)-O(13)	109.2(7)
O(3)-Al(6)-O(12)	112.7(7)
O(13)-Al(6)-O(12)	111.8(9)
O(3)-Al(6)-O(4)	111.0(7)
O(13)-Al(6)-O(4)	109.4(7)
O(12)-Al(6)-O(4)	102.6(8)
O(13)-P(5)-O(12)	108.3(10)
O(13)-P(5)-O(9)	107.4(7)
O(12)-P(5)-O(9)	107.9(8)
O(13)-P(5)-O(10)	109.8(9)
O(12)-P(5)-O(10)	109.7(8)
O(9)-P(5)-O(10)	113.7(7)

Table8.15. Selected bond angles for as-prepared Ni(deta)$_2$(F)-AlPO-5.

8.6 Calcined Ni-TMC-SAPO-STA-6

Atom	x	y	z	U_{iso}	Occ.
Al(1)	.2737400(0)	.1061290(0)	.0000000(0)	0.04919	1
Al(2)	.3897660(0)	-.1102340(0)	-.2500000(0)	0.04919	1
P(1)	.5974750(0)	-.0974740(0)	-.2500000(0)	0.04919	1
P(2)	.2605810(0)	-.1078180(0)	.0000000(0)	0.04919	1
O(1)	.2257810(0)	-.0069820(0)	.0000000(0)	0.04919	1
O(2)	.3177890(0)	-.1417390(0)	-.1129040(0)	0.04919	1
O(3)	.4995130(0)	-.1275660(0)	-.2171500(0)	0.04919	1

O(4)	.1736710(0)	-.1603820(0)	.0000000(0)	0.04919	1
O(5)	.6698570(0)	-.1392340(0)	-.1503340(0)	0.04919	1
Ni(1)	.2669870(0)	.2330130(0)	.2500000(0)	0.025	0.082

Table 8.16. Atomic coordinates and thermal parameters for the calcined Ni-SAPO-STA-6 synthesised with TMC from Rietveld profile refinement of powder X-ray diffraction data in space group P 4/m n c, with lattice parameters a = 14.3038(9) Å, c = 10.2481(5) Å.

Atom-Atom	**Distance, Å**
Al(1)-O(1)	1.75735(11)
Al(1)-O(4)	1.88746(12)
Al(1)-O(5)	1.80242(10)
Al(1)-O(5)	1.80242(10)
Al(2)-O(2)	1.79917(9)
Al(2)-O(2)	1.79917(9)
Al(2)-O(3)	1.62453(10)
Al(2)-O(3)	1.62453(10)
P(1)-O(3)	1.50402(9)
P(1)-O(3)	1.50402(9)
P(1)-O(5)	1.57225(8)
P(1)-O(5)	1.57225(8)
P(2)-O(1)	1.52583(10)
P(2)-O(2)	1.49794(7)
P(2)-O(2)	1.49794(7)
P(2)-O(4)	1.45284(9)

Table 8.17. Selected bond distances for calcined Ni-SAPO-STA-6 synthesised with TMC.

Atom- Atom- Atom-	Angle, °
O(1)-Al(1)-O(4)	96.4(8)
O(1)-Al(1)-O(5)	115.0(8)
O(1)-Al(1)-O(5)	115.0(8)
O(4)-Al(1)-O(5)	104.4(9)
O(4)-Al(1)-O(5)	104.4(9)
O(5)-Al(1)-O(5)	117.4(4)
O(2)-Al(2)-O(2)	108.8(5)
O(2)-Al(2)-O(3)	108.4(5)
O(2)-Al(2)-O(3)	108.4(5)
O(2)-Al(2)-O(3)	108.4(5)
O(2)-Al(2)-O(3)	108.4(5)
O(3)-Al(2)-O(3)	109.7(5)
O(3)-P(1)-O(3)	125.6(9)
O(3)-P(1)-O(5)	108.1(1)
O(3)-P(1)-O(5)	108.1(1)
O(3)-P(1)-O(5)	108.1(1)
O(3)-P(1)-O(5)	108.1(1)
O(5)-P(1)-O(5)	85.5(1)
O(1)-P(2)-O(2)	119.7(2)
O(1)-P(2)-O(2)	119.7(2)
O(1)-P(2)-O(4)	100.5(2)
O(2)-P(2)-O(2)	101.1(5)
O(2)-P(2)-O(4)	107.4(5)
O(2)-P(2)-O(4)	107.4(5)

Table 8.18. Selected bond angles for calcined Ni-SAPO-STA-6 synthesised with TMC.

8.7. $Ni(deta)_2$-$AlPO_4$-UT-6

Atom	x	y	z	U_{iso}	Occup.
P(1)	0.377(2)	0.200(2)	0.891(2)	0.025	1
P(2)	0.820(2)	0.333(2)	0.850(2)	0.025	1
P(3)	0.630(2)	0.376(2)	0.314 (2)	0.025	1
Al(1)	0.633(2)	0.154(2)	0.071(2)	0.025	1
Al(2)	0.138(2)	0.446(2)	0.901(2)	0.025	1
Al(3)	0.586(2)	0.368(2)	0.661(2)	0.025	1
O(1)	0.781(3)	0.173(3)	0.919(3)	0.025	1
O(2)	0.463(3)	0.203(4)	0.014 (3)	0.025	1
O(3)	0.347(4)	0.033(2)	0.892(4)	0.025	1
O(4)	0.480(3)	0.230(4)	0.743(3)	0.025	1
O(5)	0.233(3)	0.265(3)	0.956(3)	0.025	1
O(6)	0.775(2)	0.457(4)	0.018(4)	0.025	1
O(7)	0.761(3)	0.394(4)	0.712(3)	0.025	1
O(8)	0.988(4)	0.359(4)	0.807(4)	0.025	1
O(9)	0.766(5)	0.472(5)	0.271(3)	0.025	1
O(10)	0.649(4)	0.346(4)	0.477(3)	0.025	1
O(11)	0.624(5)	0.235(4)	0.239(4)	0.025	1
O(12)	0.500(4)	0.473(5)	0.315 (5)	0.025	1
F(1)	-0.004(3)	0.384 (3)	0.083(3)	0.025	1
Ni(1)*	0.009	0.020	0.520	0.1	0.48
C(1)**	0.739	0.981	0.415	0.04(1)	1
C(2)**	0.826	0.856	0.339	0.04(1)	1
C(3)**	0.190	0.166	0.639	0.04(1)	1
C(4)**	0.278	0.040	0.571	0.04(1)	1
C(5)**	0.161	0.228	0.310	0.04(1)	1
C(6)**	0.744	0.912	0.678	0.04(1)	1
C(7)**	0.268	0.103	0.310	0.04(1)	1
C(8)**	0.846	0.783	0.674	0.04(1)	1
N(1)**	0.012	0.165	0.345	0.04(1)	1

N(2)**	0.794	0.013	0.549	0.04(1)	1
N(3)**	0.222	0.002	0.439	0.04(1)	1
N(4)**	0.998	0.838	0.642	0.04(1)	1
N(5)**	0.032	0.143	0.644	0.04(1)	1
N(6)**	0.983	0.865	0.348	0.04(1)	1

Table 8.19. Selected bond distances for Ni(deta)$_2$-AlPO$_4$-UT-6 from Rietveld profile refinement of powder X-ray diffraction data in space group P $\bar{1}$, with lattice parameters a=9.283(1) Å, b=9.091(1)Å, c=9.357(1) Å.(*)Occupancy of Ni(deta)$_2$ complex in energy minimised position= 0.48(2), i.e. ca. 1 per cage. (**) Coordinates of the μ-fac isomer of the nickel complex obtained from energy minimisation were used but not refined during the analysis.

Atom-Atom	**Distance, Å**
Al(1)-O(1)	1.789(22)
Al(1)-O(2)	1.803(22)
Al(1)-O(3)	1.748(22)
Al(1)-O(11)	1.739(21)
Al(2)-O(5)	1.886(21)
Al(2)-O(6)	1.929(21)
Al(2)-O(8)	1.968(21)
Al(2)-O(9)	1.823(22)
Al(3)-O(4)	1.683(22)
Al(3)-O(7)	1.804(22)
Al(3)-O(10)	1.721(22)
Al(3)-O(12)	1.639(22)
P(1)-O(2)	1.523(21)
P(1)-O(3)	1.542(21)
P(1)-O(4)	1.543(21)
P(1)-O(5)	1.443(20)
P(2)-O(1)	1.585(22)
P(2)-O(6)	1.522(22)

P(2)-O(7)	1.583(22)
P(2)-O(4)	1.559(22)
P(3)-O(9)	1.534(22)
P(3)-O(10)	1.579(22)
P(3)-O(11)	1.484(21)
P(3)-O(12)	1.481(21)

Table 8.20. Selected bond distances for $Ni(deta)_2$-$AlPO_4$-UT-6.

Atom- Atom- Atom-	**Angle, °**
O(1)-Al(1)-O(2)	109.1(18)
O(1)-Al(1)-O(3)	98.3(17)
O(1)-Al(1)-O(11)	125.4(20)
O(2)-Al(1)-O(3)	114.0(19)
O(2)-Al(1)-O(11)	105.8(18)
O(3)-Al(1)-O(11)	104.3(18)
O(5)-Al(2)-O(6)	93.3(14)
O(5)-Al(2)-O(8)	94.4(15)
O(5)-Al(2)-O(9)	106.6(15)
O(6)-Al(2)-O(8)	160.1(13)
O(6)-Al(2)-O(9)	103.2(16)
O(8)-Al(2)-O(9)	92.1(15)
O(4)-Al(3)-O(7)	117.8(20)
O(4)-Al(3)-O(10)	114.2(19)
O(4)-Al(3)-O(12)	111.3(21)
O(7)-Al(3)-O(10)	97.6(17)
O(7)-Al(3)-O(12)	105.8(20)
O(10)-Al(3)-O(12)	108.9(23)
O(2)-P(1)-O(3)	99.2(21)
O(2)-P(1)-O(4)	110.4(23)
O(2)-P(1)-O(5)	113.8(23)
O(3)-P(1)-O(4)	103.9(21)

O(3)-P(1)-O(5)	103.8(21)
O(4)-P(1)-O(5)	122.2(23)
O(1)-P(2)-O(6)	114.3(21)
O(1)-P(2)-O(7)	122.4(21)
O(1)-P(2)-O(8)	112.8(20)
O(6)-P(2)-O(7)	101.0(19)
O(6)-P(2)-O(8)	100.5(17)
O(7)-P(2)-O(8)	102.9(18)
O(9)-P(3)-O(10)	95.7(18)
O(9)-P(3)-O(11)	118.7(23)
O(9)-P(3)-O(12)	106.9(22)
O(10)-P(3)-O(11)	111.0(22)
O(10)-P(3)-O(12)	108.6(23)
O(11)-P(3)-O(12)	114.1(23)

Table 8.20. Selected bond angles for $Ni(deta)_2$-$AlPO_4$-UT-6.